

**Investigation of Transient Flow and Dispersion
Phenomena Resulting from Possible Hazmat Releases
at Research Facilities of CERN**

Dissertation

with the aim of achieving a doctoral degree
at the Faculty of Mathematics, Informatics and Natural Sciences
Department of Earth Sciences
at Universität Hamburg

submitted by
Uwe Kai Käuflin

Hamburg, 2024

Department of Earth Sciences

Date of Oral Defense:

06.12.2024

Reviewers:

Prof. Dr. Bernd Leitl
Dr. Oriol Rios

Members of the Examination Commission:

Chair Prof. Dr. Bernd Leitl
Dr. Oriol Rios
Prof. Dr. Matthias Hort
Prof. Dr. Jürgen Böhner
Prof. Dr. Martina Neuburger

Chair of the Subject Doctoral Committee
Earth Sciences:

Prof. Dr. Hermann Held

Dean of the Faculty MIN

Prof. Dr.-Ing. Norbert Ritter

Eidesstattliche Versicherung | Declaration on Oath

Hiermit erkläre ich an Eides statt, dass ich die vorliegende Dissertationsschrift selbst verfasst und keine anderen als die angegebenen Quellen und Hilfsmittel benutzt habe.

I hereby declare upon oath that I have written the present dissertation independently and have not used further resources and aids than those stated.

A handwritten signature in black ink, appearing to be 'H. Weitz', written in a cursive style.

München, **04.06.2024** | Munich, **06/04/2024**

Abstract

The dissertation delineates a comprehensive methodology for the development of Computational Fluid Dynamics (CFD) simulations of atmospheric boundary layer (ABL) flows pertinent to pollutant dispersion scenarios, specifically within the context of hazardous material (hazmat) releases at CERN research facilities. The optimal configuration of the computational domain was ascertained to be an octagonal shape with a medium diagonal of three kilometers and a height of 500 meters, which ensures a robust flow transition and mitigates backflow complications. Detailed modeling of terrain, edifices, and vegetation was identified as critical to high-fidelity simulation of turbulent structures. The relaxation of the domain boundaries, executed via CAD software or programming tools, proved to be effective in facilitating smooth flow transitions. Boundary conditions, encompassing velocity profiles, surface roughness parameters, and a combination of inlet and outlet conditions, were meticulously selected on the basis of meteorological data, regulatory standards, and flow characteristics to precisely define flow behavior and pollutant dispersion in simulations. The meshing strategy employed for the large-eddy simulations yielded favorable results, featuring a ground resolution of one meter and half a meter in areas of interest. The selection of modeling methods for pollutant dispersion is contingent on the nature of the pollutants, with the Lagrangian particle model recommended for larger pollutants and the species transport model for gaseous substances. The simulation approach should be chosen judiciously based on factors such as geometry preparation, meshing, temporal discretization, and consideration of atmospheric flow fluctuations during pollutant release. The outcomes derived from Gaussian Plume Models (GPMs) and LES for pollutant dispersion may be analogous for simplistic scenarios but can diverge significantly for more intricate release scenarios. GPMs are computationally expedient and advantageous for far-field assessments, whereas LES offers more realistic results for near-field or densely built environments. Sensitivity analysis of the boundary conditions revealed their direct impact on concentration values, with increased turbulence at the inlet and features such as arboreal elements in the geometry influencing plume dimensions and downstream concentrations. In general, the dissertation provides a thorough methodology for establishing CFD simulations of ABL flows for pollutant dispersion scenarios, incorporating considerations such as domain configuration, precise terrain and building modeling, meshing strategy, boundary conditions, and the selection of appropriate modeling techniques. The findings of this study enhance the understanding and prediction of pollutant dispersion in realistic scenarios, providing valuable insights for environmental assessments, emergency preparedness, and air qual-

ity management decision-making.

Keywords: Computational Fluid Dynamics (CFD), Atmospheric Boundary Layer (ABL), Large Eddy Simulation (LES), Pollutant Dispersion, Radionuclide Releases, Hazmat Safety, CERN Research Facilities, Gaussian Plume Model (GPM), Turbulence Modeling Environmental Safety, Near-field Dispersion, Mesh Resolution, Boundary Conditions, Simulation Workflow, Emergency Preparedness, CFD vs Analytical Models, LES vs Traditional Dispersion Models, Advanced Turbulence Techniques, High-Resolution Environmental Simulations, Comparative Analysis of Dispersion Models, Industrial and Research Facility Safety, Simulation Accuracy in Complex Terrains, Modeling Environmental Impacts, Cutting-edge CFD Applications

Kurzfassung

Die Dissertation beschreibt eine umfassende Methodik für die Entwicklung von Strömungssimulationen in der atmosphärischen Grenzschicht, die für Schadstoffausbreitungsszenarien, insbesondere im Zusammenhang mit der Freisetzung von Gefahrstoffen in CERN Forschungseinrichtungen, relevant sind. Die optimale Konfiguration des Rechengebiets wurde als achteckigen Form mit einer mittleren Diagonale von drei Kilometern und einer Höhe von 500 Metern bestimmt, die einen robusten Strömungsübergang gewährleistet und Komplikationen durch Rückströmung reduziert. Eine detaillierte Modellierung des Geländes, der Gebäude und der Vegetation hat sich als entscheidend für eine realitätsgetreue Simulation der turbulenten Strukturen herausgestellt. Die Anpassung der Ränder des Rechengebiets, die mit Hilfe von CAD-Software oder Programmierertools durchgeführt wurde, erwies sich als effektiv, um sanfte Strömungsübergänge zu ermöglichen. Die Randbedingungen und die Geschwindigkeitsprofile und die Kombination von Einlass- und Auslassrandbedingungen wurden auf der Grundlage meteorologischer Daten, gesetzlicher Normen und Strömungseigenschaften sorgfältig ausgewählt, um das Strömungsverhalten und die Schadstoffausbreitung in den Simulationen realitätsnah abzubilden. Die Auswahl der Modellierungsmethoden für die Schadstoffausbreitung hängt stark von der Art der Schadstoffe ab, wobei das Lagrangesche Partikelmodell für partikelförmige Feststoffe und das Speziestransportmodell für gasförmige Schadstoffe empfohlen wird. Der Simulationsansatz sollte auf der Grundlage von Faktoren wie Geometrievorbereitung, Vernetzung, zeitliche Diskretisierung und Berücksichtigung der atmosphärischen Strömungsschwankungen während der Schadstofffreisetzung mit Bedacht gewählt werden. Die Ergebnisse von Gaußschen Fahnenmodellen und Large Eddy Simulationen für die Schadstoffausbreitung können bei einfachen Szenarien ähnlich sein, bei komplizierteren Freisetzungsszenarien jedoch erheblich voneinander abweichen. Gaußsche Fahnenmodelle sind rechnerisch zweckmäßig und vorteilhaft für Fernfeldbewertungen, während LES realistischere Ergebnisse im Nahfeld oder in dicht bebauten Umgebungen liefert. Eine Sensitivitätsanalyse der Randbedingungen ergab, dass sich diese direkt auf die Konzentrationswerte und das betroffene Gebiet auswirken, wobei eine erhöhte Turbulenz am Einlass und baumartige Elemente in der Geometrie die Abmessungen der Abgasfahne und die stromabwärts gelegenen Konzentrationen beeinflussen. Generell bietet die Dissertation eine gründliche Methodik für die Erstellung von CFD-Simulationen von ABL-Strömungen für Schadstoffausbreitungsszenarien, die Überlegungen zur Domänenkonfiguration, zur präzisen Gelände- und Gebäudemodellierung, zur Vernetzungsstrategie, zu den Randbedingungen und zur Auswahl ge-

eigneter Modellierungsmethoden einbezieht. Die Ergebnisse dieser Studie verbessern das Verständnis und die Vorhersage der Schadstoffausbreitung in realistischen Szenarien und liefern wertvolle Erkenntnisse für die Umweltbewertung, die Notfallvorsorge und die Entscheidungsfindung beim Luftqualitätsmanagement.

Acknowledgement

I would like to express my heartfelt gratitude to the following individuals, without whom I would not have been able to complete this research and navigate my doctoral journey successfully.

First and foremost, I extend my deepest appreciation to the FIRIA & CFD team at CERN, especially to my supervisors Dr. S. La Mendola, Dr. Oriol Rios and Mr. M. Battistin. Their unwavering support and guidance paved the way for me to conduct my doctoral research at CERN, and their expertise in fire-related topics has been invaluable throughout my work. I also acknowledge Dr. Oriol Rios, Dr. P. Vojtila and Mr. S. Melhem for their assistance with radiological impact assessment, which greatly contributed to my research.

The author thanks Prof. B. Leidl, my professor at the University of Hamburg, whose vision and encouragement made this project possible. His profound insights and extensive knowledge of the subject guided me through the research process.

In addition, I extend my deepest thanks to my family and friends, but especially to my daughter Mila. I apologize for being preoccupied with this thesis and I am grateful for your understanding and support.

Lastly, I would like to thank all those who have supported me but were not specifically mentioned in this acknowledgment. I am truly proud and grateful to be surrounded by such wonderful people who have allowed me to focus on the most important things in life.

Contents

Eidesstattliche Versicherung - Declaration on Oath	i
Abstract	iii
Kurzfassung	v
Acknowledgement	vii
Nomenclature	xiii
1. Introduction	1
1.1. Justification for Research	1
1.2. Research Approach	3
1.3. Thesis Outline	5
2. Atmospheric Boundary Layer Meteorology	7
2.1. ABL Structure	7
2.2. ABL Characteristics	9
2.3. Modeling Mechanical Turbulence	10
2.4. Scope for Simulations	12
2.5. Gaussian Plume Models	15
3. Numerical Modeling Theory	17
3.1. Governing Equations	18
3.2. Turbulence Modeling	20
3.2.1. Reynolds Averaged Navier Stokes Equations (RANS)	21
3.2.2. Large Eddy Simulations	23
3.3. Transport Modeling	27
3.3.1. Lagrangian Particle Dispersion	28
3.3.2. Species Transport Model	32
3.3.3. Comparison	35
4. Comprehensive Methodology Evaluation	37
4.1. Geometry	37
4.1.1. Shape and Size	38
4.1.2. Topography Models	40

4.1.3. Relaxation	41
4.1.4. Modelling Challenges	44
4.2. Meshing Strategy	48
4.2.1. Mesh Type	49
4.2.2. Mesh Refinement Study	51
4.2.3. Final Selected Mesh	61
4.2.4. Evaluation of Mesh Size	66
4.2.5. Meshing Challenges	71
4.3. Simulation Setup	71
4.3.1. Boundary Conditions	71
4.3.2. Turbulent Inlet Specification Method	76
4.3.3. Review of Boundary Conditions	84
4.3.4. Solver Settings	85
4.3.5. Particle Dispersion Modeling	88
4.3.6. Soot Properties	89
4.3.7. Gas Dispersion Modeling	90
4.4. Simulation Approach	91
4.4.1. Steady Solution	92
4.4.2. Transient Solution	93
4.4.3. Pollutant Release	95
4.5. Simulation Results	98
4.5.1. Time-Step Size	98
4.5.2. Wall Resolution	100
4.5.3. Atmospheric Turbulence	103
5. Discussion - Findings and Guidelines	113
5.1. Comparison of GPM and LES	113
5.1.1. Similarities of GPM and LES	114
5.1.2. Differences of GPM and LES	123
5.2. Sensitivity Analysis on Boundary Conditions	136
5.2.1. Atmospheric Turbulence at Monitoring Lines	141
5.2.2. Monitoring-Planes - Dispersion Parameter	157
5.2.3. Monitoring-Points - Ground Concentration	161
5.2.4. Sensitivity Analysis - Conclusions	164
6. Summary and Conclusion	167
6.1. Comprehensive Approach to Domain Setup	167
6.2. Meshing Strategy	168
6.3. Crucial Role of Boundary Conditions	169
6.4. Dispersion Modeling: Lagrangian vs. Eulerian Models	169
6.5. Simulation Methods and Models	170

6.6. Gaussian Plume Models and Large-Eddy Simulations	170
6.7. Sensitivity on Boundary Conditions	171
6.8. Turbulent Inlet Specification Method	172
6.9. Outlook	173
6.10. Scientific Summary	173
A. Python Relaxation Procedure	177
B. ANSYS Fluent Meshing Functionalities	183
C. GPM at CERN - Differences from the Swiss Guideline ENSI G-14	185
C.1. Assumptions	185
C.2. Gaussian Atmospheric Dispersion Model	185
C.3. Deposition Factors	187
D. Sensitivity Analysis on Boundary Conditions	189
D.1. Mean Velocity Profiles	190
D.1.1. DTM-NF-MO-1	190
D.1.2. DTM-STG-MO-1	191
D.1.3. DTM-STG-MO-025	192
D.1.4. DEM-STG-MO-1	193
Bibliography	195
List of Figures	203
List of Tables	207

Nomenclature

Acronyms & Abbreviations

ABL Atmospheric Boundary Layer

ASCII American Standard Code for Information Interchange

ATLAS A Toroidal LHC ApparatuS

BCD Boundary Central Differencing

CAD Computer Aided Design

CD Central Differencing

CERN European Organization for Nuclear Research

CFD Computational Fluid Dynamics

CFL Courant–Friedrichs–Lewy

DEM Digital Elevation Model

DTM Digital Terrain Model

ESDU Engineering Sciences Data Unit

FDS Fire Dynamic Simulator

FFT Fast Fourier Transform

FIRIA Fire-Induced Radiological Integrated Assessment

GPM Gaussian Plume Model

ISOLDE Isotope Separator On Line Device

LAD Leaf Area Density

LAI Leaf Area Index

LES Large Eddy Simulation

LHC Large Hadron Collider

LPM	Lagrangian Particle Model
MNS	Modele Numerique de Surface - see DTM
MNT	Modele Numerique de Terrain - see DEM
PSD	Particle Size Distribution
RANS	Reynolds Averaged Navier-Stokes (Equations)
SBL	Surface Boundary Layer
SITG	Le <u>S</u> ystème d' <u>I</u> nformation du <u>T</u> erritoire de <u>G</u> enève
SS	Synthetic Synthesizer
STG	Synthetic Turbulence Generator
TKE	Turbulence Kinetic Energy
VDI	Verein Deutscher Ingenieure (Association of German Engineers)
VM	Vortex Method
WALE	Wall-Adapting Local Eddy-Viscosity
WMLES	Wall-Modeled Large Eddy Simulation
WRLES	Wall-Resolved Large Eddy Simulation

Greek Symbols

α_i	Volume fraction of the i -th species
Δt	Time-step size
Δt_{avg}	Average time-step size
Δt_{est}	Estimated time-step size
Δt_{fin}	Finally selected time-step size
Δt_{max}	Maximum time-step size
Δt_{min}	Minimum time-step size
Δx	Cell length
Δz	Height difference vs. reference value
Δ	LES filter width
Δ_{avg}	Average LES filter width

δ_{ij}	Kronecker delta
Δ_{max}	Maximum LES filter width
Δ_{min}	Minimum LES filter width
η	Kolmogorov length scale
Γ_h	Turbulent thermal diffusivity
Γ_m	Turbulent mass diffusivity
κ	Von Kármán constant
μ	Dynamic viscosity
μ_t	Turbulent viscosity
μ_{air}	Dynamic viscosity of air
μ_{Ar}	Dynamic viscosity of Argon gas
μ_m	Dynamic viscosity of the mixture
ν	Kinematic viscosity
ν_t	Turbulent kinematic viscosity
ν_{air}	Kinematic viscosity of air
ν_{sgs}	Sub-grid scale viscosity
ϕ_p	Volume fraction of the dispersed second phase (particles)
ϕ_{air}	Volume fraction of the continuous phase (air)
Ψ_m	Similarity function
ρ	Fluid density
ρ_1	Fluid density at the edge of the domain
ρ_2	Fluid density in the center of the domain
ρ_i	Density of the i -th species
ρ_m	Mass averaged density of the mixture
ρ_p	Particle density
ρ_{air}	Air density
ρ_{Ar}	Argon gas density

σ_{ij}	Viscous stress tensor
σ_u	Variance of velocity u
σ_v	Variance of velocity v
σ_w	Variance of velocity w
τ_r	Relaxation time
τ_w	Wall shear stress
τ_{ij}	Reynolds stress tensor
θ	Potential temperature
ε	Dissipation rate of turbulence kinetic energy
C_κ	Kolmogorov constant
C_μ	k- ε turbulence model constant

Operators, Superscripts & Subscripts

\int	Integral operator
∇T	Gradient of temperature
∇Y_i	Gradient of the mass fraction of the i -th species
∇	Vector differential operator
∂	Partial derivative

Roman Symbols

\dot{m}_s	Mass flow rate of the particle stream
\dot{m}_1	Mass flux at the edge of the domain
\dot{m}_2	Mass flux in the center of the domain
\dot{v}_1	Volume flow rate at the edge of the domain
\dot{v}_2	Volume flow rate in the center of the domain
$\langle U_i \rangle$	Time averaged velocity in i -direction
\bar{k}	Time-averaged turbulent kinetic energy
$\bar{k}_{ave,lv}$	Surface-averaged mean turbulent kinetic energy for each distance from the release point x and refinement level

$\bar{k}_{ave,vf}$	Surface-averaged mean turbulent kinetic energy for each distance from the release point x and the very fine refinement level
$\bar{k}_{max,lvl}$	Maximum turbulent kinetic energy of a certain mesh refinement level
$\bar{k}_{max,vf}$	Maximum turbulent kinetic energy of the very fine mesh refinement level
\bar{u}	Time-averaged velocity of a plane in x -distance from release point
$\bar{u}_{ave,lvl}$	Surface-averaged mean velocity for each distance from the release point x and refinement level
$\bar{u}_{ave,vf}$	Surface-averaged mean velocity for each distance from the release point x and the very fine refinement level
\bar{y}	Total concentration weighted plume center-line displacement in y -direction
\bar{z}	Average plume rise from sea level
\bar{z}_0	Average plume height from ground level
\mathbf{U}	Velocity magnitude
\tilde{c}	Integrated and normalized concentration
$\tilde{c}_{max,lvl}$	Integrated and normalized maximum concentration of a certain mesh refinement level
$\tilde{c}_{max,vf}$	Integrated and normalized maximum concentration of the very fine mesh refinement level
\tilde{c}_{max}	Maximal integrated and normalized concentration
\tilde{f}_{max}	Normalized maximal frequency
u_i	Velocity of the i -th species
\vec{A}_i	Normal vector for the i -th face of a polyhedral cell
\vec{c}_i	Vector from the cell centroid of a polyhedral cell to its i -th centroid of each surrounding polyhedral cell
\vec{f}_i	Vector from the cell centroid of a polyhedral cell to its i -th centroid of each face
\vec{F}_{drag}	Drag force
\vec{F}_{grav}	Gravitation force
\vec{F}_{other}	Other force
\vec{g}	Gravitation acceleration vector

\vec{J}_i	Diffusion flux of the i -th species
\vec{u}_{air}	Directed air velocity
\vec{u}_p	Directed particle velocity
\vec{v}_m	Mass averaged velocity of the mixture
$\vec{v}_{dr,k}$	Drift velocity of the secondary phase k
\vec{v}_{k-1}	Velocity of the primary phase $k - 1$
A_+	Shape control constant
A	Plume cross-section surface
A_1	Cross section of the domain at the edge of the domain
a_1	Coefficient after Morsi and Alexander (1972) for calculating the drag coefficient depending on Reynolds number
A_2	Cross section of the domain in the center of the domain
a_2	Coefficient after Morsi and Alexander (1972) for calculating the drag coefficient depending on Reynolds number
a_3	Coefficient after Morsi and Alexander (1972) for calculating the drag coefficient depending on Reynolds number
A_{domain}	Domain area
A_{door}	Surface of the smoke release door of the ATLAS surface building
c	Speed of light
C_+	Constant for the logarithmic wall function
C_d	Drag coefficient
C_s	Smagorinsky constant
C_W	WALE constant
C_w	Wall damping constant in the Van Driest damping function
$c_{max,n}$	Maximal normalized concentration \tilde{c}
CFL	CFL number
CFL_{avg}	Volume-averaged CFL number
D	Van Driest damping coefficient

d_p	Particle diameter
D_t	Turbulent eddy diffusivity
D_{Ar}	Diffusivity of Argon gas in Nitrogen gas
$D_{i,m}$	Mass diffusion coefficient for the i -th species
d_{pad}	Particle aerodynamic diameter
$D_{T,i}$	Thermal diffusion coefficient for the i -th species
E_{ii}	Auto-spectral energy density
E_{ij}	Cross-spectral energy density
f	Frequency
f_{max}	Maximal frequency
H	Total height of the simulated domain
I_u	Turbulence intensity in x -direction
I_v	Turbulence intensity in y -direction
I_w	Turbulence intensity in z -direction
inc	Smoothing increment
k	Turbulence kinetic energy
L	Obukhov length
l	Wave length
l_0	Integral/sub-grid length scale
l_m	Mixing length for subgrid scales
L_{cha}	Characteristic length
m_p	Particle mass
M_{air}	Molecular weight of air
m_{air}	Mass of air
M_{Ar}	Molecular weight of Argon gas
m_{parcel}	Mass of the parcel
$m_{release}$	Total released pollutant mass in one scenario

Ma	Mach Number
N	Total number of time-steps per simulation
n	Total number of i -species
n_p	Number of particles within one parcel
n_{faces}	Number of faces on an inlet boundary
N_{reg}	Total number of regular squared cells
$n_{vortices}$	Number of vortices needed on an inlet boundary
Pr_t	Turbulent Prandtl number
Re	Reynolds number
S_{ij}^*	Differing part of the strain-rate tensor of the mean flow
S_m	Source term in the mass conservation
S_{ii}	Two-sided auto-spectral energy density
s_{ij}	Strain-rate tensor
Sc_t	Turbulent Schmidt number
T	Total simulation time
t	Time
t_{amb}	Ambient temperature
$tke_{ave,n}$	Normalized averaged mean turbulent kinetic energy
$tke_{max,n}$	Maximum mean turbulent kinetic energy
u'	Fluctuating velocity in x -direction
u_*	Friction velocity in flow direction
U	Time-averaged velocity in x -direction
u	Instantaneous velocity in x -direction
u_+	Dimensionless velocity
u_1	Velocity at the edge of the domain
u_2	Velocity in the center of the domain
U_i	Velocity components: u, v, w

u_τ	Shear velocity
$u_{ave,n}$	Normalized surface-averaged mean velocity
u_{door}	Constant release velocity at the ATLAS door
u_{ref}	Reference velocity at z_{ref}
v'	Fluctuating velocity in y -direction
V	Time-averaged velocity in y -direction
v	Instantaneous velocity in y -direction
V_{cell}	Cell volume
w'	Fluctuating velocity in z -direction
W	Time-averaged velocity in z -direction
w	Instantaneous velocity in z -direction
w_p	Mass fraction of particles
w_{air}	Mass fraction of air
x_i	Spatial components: x,y,z
x_{max}	Maximal spatial coordinate for x -direction
x_{min}	Minimal spatial coordinate for x -direction
y	Distance from closest wall
y_+	Dimensionless wall distance
Y_i	Local mass fraction of the i -th species
y_{max}	Maximal spatial coordinate for y -direction
y_{min}	Minimal spatial coordinate for y -direction
z	Height from ground level
z_0	Aerodynamic roughness length
z_{ref}	Reference height
$z_{terrain}$	Terrain height at corresponding x, y -coordinates

1. Introduction

This research investigates the transient flow and dispersion phenomena of possible releases of hazardous material (hazmat) in the research facilities of CERN, the European Organization for Nuclear Research in Geneva, Switzerland. It is one component of the broader Fire-Induced Radiological Integrated Assessment (FIRIA) project at CERN, which aims to define the fire safety requirements applicable to the Organization's research facilities. The contribution of this dissertation to the FIRIA project is the development of a novel methodology to simulate the release of radioactive substances as a consequence of a fire. Multiple computational fluid dynamics (CFD) simulation methods were utilized to predict the dispersion of pollutants. The results are partially validated using existing literature on mean and turbulent quantities of atmospheric boundary layer (ABL) flows and analytical data on pollutant dispersion tracking, such as Gaussian plume models (GPM).

1.1. Justification for Research

In recent years, microscale modeling of pollutant dispersion in urban environments has become increasingly important, and large-eddy simulation (LES) has emerged as a widely used computational tool for this task. LES is a numerical modeling technique used to simulate turbulent flow in complex systems by directly resolving the large-scale structures in the flow, resulting in the need for adequate mesh resolution and small time-step sizes, which traditionally makes LES computationally expensive. However, with recent advances in computing resources and the implementation of parallel computing for LES, it has become feasible for applications where flow-averaged solutions are insufficient to capture the level of detail required to characterize turbulent flows. This trend is reflected in the increasing number of LES publications in the last 20 years, as shown in Figure 1.1 (excluding citations) based on a Google Scholar search¹.

During the past two decades, there has been a notable increase of 400 % in LES-related publications, although a slight decline in 2020/2021 attributed to the COVID-19 pandemic. Numerous international conferences were postponed by one or two years in order to facilitate in-person gatherings. Despite the progress made in the realm of large-scale LES, particularly in obstacle-resolving models, its popularity has been steadily growing in the field of environmental flows. This shift is due to the realization that a well-executed

¹Search results in Google scholar for the keyword "large-eddy simulation" for the relevant period of time excluding citations.

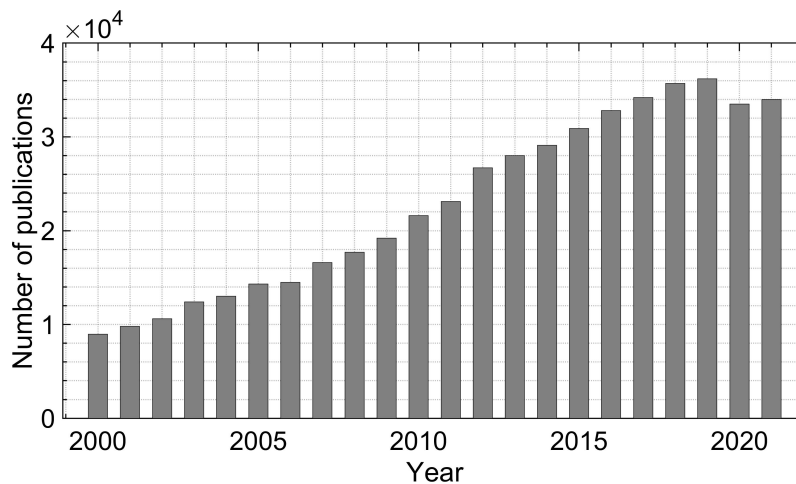


Figure 1.1.: Number of publications with the keywords "large-eddy simulation" for the last two decades.

Reynolds-Averaged Navier–Stokes (RANS) approach does not exhibit significant differences from LES in terms of computational requirements. Consequently, LES can be effectively employed to address more complex problems associated with the determination of precise inflow and boundary conditions.

Thus, large-eddy simulations (LES) are gaining popularity not only in technical flows but also in large-scale simulations of the atmospheric boundary layer. In this context, it is crucial to limit the domain size to accurately capture turbulent structures while addressing flow dynamics within volumes as large as 100 cubic kilometers (100 km³). When weather or urban climate models are used to forecast flow and weather conditions, they typically operate at a minimum domain size of 1 cubic kilometer (1 km³). In contrast, the numerical LES solver is capable of resolving the flow down to a much smaller scale, reaching 0.1 cubic meters (0.1 m³).

However, understanding the transient nature of vortices and their formation remains a challenging task. When it comes to modeling such flows, steady Reynolds-Averaged Navier-Stokes (RANS) approaches fall short of providing the same level of detail. One prominent application of large-eddy simulation (LES) and also for Unsteady Reynolds-Averaged Navier-Stokes (URANS) approaches in atmospheric flows is the prediction of wind loads on buildings. This is particularly critical because fluctuating winds and the transient drag forces they exert on buildings have a significant impact on the results. However, LES not only allows for accurate capture of the interaction between wind and buildings but also takes into account the influence of approaching flows from the surrounding areas. This influence becomes evident in the sensitivity analysis of boundary conditions, detailed in Chapter 5.2. In this analysis LES demonstrates its superiority over transient RANS models. Excel in modeling the effects on flow separation and vortex shedding, as well as improving the representation of the fluid-structure interaction.

Modeling the dynamic wake field of buildings and the dispersion of pollutants re-

leased in their vicinity poses a challenge when relying on averaged solutions. As highlighted in Gousseau et al. (2011), the accuracy of RANS solutions is highly dependent on the choice of the turbulent Schmidt number (Sc_t), a parameter that cannot be predetermined prior to simulations. To be precise, the turbulent Schmidt number (Sc_t) is defined as the ratio of the turbulent kinematic viscosity of a scalar (ν_t) to its turbulent eddy diffusivity (D_t) as outlined in Pope (2000).

$$Sc_t = \nu_t / D_t \quad (1.1)$$

In contrast, LES is generally less reliant on empirical constants compared to RANS models. However, it is important to note that LES does not entirely avoid input parameters. Although LES reduces the dependency on such parameters, it still requires careful setup, including choices like grid resolution and subgrid-scale models, to ensure accurate results. However, many studies have demonstrated the effectiveness of LES in modeling transient turbulent-flow simulations.

This dissertation aimed to explore the feasibility of using commercially available large-eddy simulation (LES) software to model pollutant dispersion scenarios within the atmospheric boundary layer (ABL), and applying it to realistic release scenarios present at research facilities of CERN. The research was conducted in the context of the FIRIA project, which sought to establish fire safety requirements for CERN's research facilities. The specific scenario considered in this study was anticipated to have a minimal dosimetric impact on the population, making microscale modeling of atmospheric flows the preferred approach.

The primary objective of microscale modeling was to accurately resolve turbulent structures within atmospheric flows, encompassing horizontal length scales ranging from approximately one to hundreds of meters. In this endeavor, LES was employed to estimate pollutant concentrations in the vicinity of release points. Analytical models were also used to provide initial estimates of the directions and sizes of the plume.

The significance of this research lies in its application of LES to real-world scenarios, which allows the assessment of its feasibility and identification of potential limitations.

1.2. Research Approach

The investigation focuses on near-field pollutant dispersion scenarios in close proximity to the emission source, specifically within a 500-meter range. In such short distances, the main factor that influences dispersion is the mechanical turbulence generated by the roughness of the surface that forms buildings, vegetation, or other obstacles to flow. Many other factors relevant for the long-distance transport of pollutants can be simplified or ignored in this context.

Meteorological models excel at predicting the transport of pollutants over longer distances. These models take into account critical processes and phenomena, such as the

impact of thermal stratification of air and the Coriolis force resulting from the Earth's rotation. However, traditional atmospheric modeling often involves much larger domain sizes, which comes at the expense of significantly lower spatial resolution, particularly when applied outside the field of atmospheric science.

Real-time weather forecasts are frequently employed to estimate plume movements over extended distances, considering up-to-date weather data and changing atmospheric conditions. However, meteorological models cannot provide the high spatial resolution necessary to accurately trace pollutant paths, estimate concentrations, assess human exposure close to the source, or determine the affected area for specific wind directions.

Analytical models like the Gaussian plume model (GPM) simplify complex conditions near the source to provide a straightforward statistical model description. Note that the GPM is an exact solution of the advection-diffusion equation but under highly simplified release and dispersion conditions. This limitation renders these models unsuitable for near-source dispersion modeling and exposure assessment.

The objective of this project was to employ more sophisticated models, such as large-eddy simulation (LES), along with simplified methods to examine the influence of relevant parameters on the dispersion model. To pursue a pragmatic approach given limited resources, the following assumptions and simplifications were applied.

- The logarithmic wind profile is modeled using Monin-Obukhov similarity theory, as proposed by Monin and Obukhov (1954).
- Wind directions are assumed to remain constant at different heights above ground, in contrast to the Ekman spiral.
- A well-mixed and thermally neutral stratification of the lowest layer of the atmosphere is assumed, which means that there are no temperature-induced buoyant forces.
- Mechanical turbulence induced by vegetation is either not explicitly considered or is only partially considered.
- Mountains and hills, which could potentially affect larger-scale wind flow, are not taken into account.
- The effects of precipitation on pollutant dispersion and deposition are not taken into account.
- Low-level jets that form during stable conditions at night are not included in the analysis.
- Restriction of the simulations to the lower decameter of the atmospheric boundary layer, which is why the Coriolis force, is not a significant factor for the calculations.

Pollutants released in realistic scenarios at CERN from a heating, ventilation, and air conditioning (HVAC) stack typically remain below an altitude of 100 meters when travel distances range from 500 to 1000 meters from the release point. Consequently, the plume disperses within the roughness layer, also known as the Prandtl layer, of the atmospheric

boundary layer. This layer is primarily influenced by viscous and drag forces. Hence, the simplifications listed above can be applied when conducting pollutant dispersion simulations in the near field.

For a more comprehensive understanding of why these simplifications are appropriate, refer to Chapter 2.4 for a detailed justification. The investigation was carried out using the commercial software ANSYS® Fluent, which was licensed by CERN. This accessibility allows researchers without access to university-specific codes to conduct simulations for similar scenarios and benefit from the knowledge acquired through this research.

1.3. Thesis Outline

Previous studies have established large-eddy simulation (LES) as a reliable method for modeling pollutant dispersion in urban areas within the atmospheric boundary layer (ABL) (Vasaturo et al. (2018), Zheng et al. (2021), Cheng and Porté-Agel (2015), Antoniou et al. (2017), Lateb et al. (2016)). This dissertation focuses on applying LES to specific pollutant dispersion scenarios at CERN. It places particular emphasis on the selection and definition of terrain, geometry, mesh, boundary conditions, and turbulent inlet specifications, as well as the evaluation of the characteristics of the released particulate matter and potential simplification methods.

The primary goal of this research is to contribute to improvements in safety in industrial and research settings by conducting simulations in the vicinity of buildings and exploring potential changes and simplifications of boundary conditions that could impact safety. The dissertation comprises six chapters.

- Chapter 1: Introduction to the topic.
 - Chapter 2: Summary of relevant meteorological aspects for pollutant release scenarios and a description of simplifications in meteorological conditions for the chosen simulation approach.
 - Chapter 3: Introduction to basic numerical models and laws used in simulations presented in Chapters 4 and 5.
 - Chapter 4: Detailed description of the methodology to prepare and run pollutant dispersion simulations, including geometry preparation, meshing strategy, selection of boundary conditions, and numerical model settings. The chapter concludes with an evaluation of the mesh and solver setup.
 - Chapter 5: Comparison of a Gaussian Plume Model (GPM) employed at CERN with the numerical LES method in specific scenarios. It also provides guidelines for conducting LES simulations in the context of pollutant release scenarios within ABL flows.
-

- Chapter 6: Summarizes the conclusions from previous chapters and offers an outlook on future projects.

Together, these chapters provide a comprehensive exploration of pollutant dispersion modeling using LES and its implications for safety and environmental considerations.

2. Atmospheric Boundary Layer Meteorology

The atmospheric boundary layer (ABL) is the lowest part ($\sim 10\%$) of the troposphere, which ranges from ground level to an altitude as high as 11 km depending on the location and weather conditions. The top of the ABL reaches altitudes up to ~ 1 km from ground level. Depending on location, weather conditions, and time of day, the ABL could extend up to 3 km or down to 100 m to the ground. In the ABL, surface interactions between air flow and ground play a strong role, affecting processes such as frictional drag, evaporation, transpiration, heat transfer, pollutant emission, and terrain-induced flow effects, see Stull (1988).

2.1. ABL Structure

Following Stull (1988), the atmospheric boundary layer (ABL) can be further divided into three main regions: the Prandtl layer or surface boundary layer (SBL), the inertial sublayer and the outer layer. The Prandtl layer extends from the ground surface to approximately 2-3 times the height of urban buildings and constitutes approximately 10% of the total depth of the ABL. This layer is characterized by a high intensity of turbulence, which usually ranges from 10% to 30%, depending on the height above the ground z_0 , as stated in VDI 3783/12 (2000). The intensity of the turbulent flux is a critical factor that influences the dispersion of pollutants near the release point and plays a central role in the simulations presented in this thesis.

According to Tennekes et al. (1972), the influence of the Coriolis force on the direction of the wind within the Prandtl layer is considered negligible. Please note that Stull (1988) serves as a reference for several statements in this chapter.

The inertial sublayer, also referred to as the mixing layer or convective boundary layer of the ABL, lies above the Prandtl layer and extends up to approximately 100 meters from the ground. Within this height range, surface effects become less pronounced as you move higher.

In this part of the ABL, the stratification of the flow undergoes significant changes over the diurnal cycle. During the day, momentum exchange results primarily from the alternating heating and cooling of the surface due to sunlight. Solar heating, coupled with cooling, generates not only horizontal but also more pronounced vertical turbulence, often leading to unstable stratification. When the stratification is neutral, the temperature

remains relatively constant with height. This situation can occur when clouds or fog cover the lower part of the ABL, resulting in negligible temperature gradients.

In contrast, nighttime conditions give rise to stability within the first few hundred meters of the ABL. Consequently, the ABL shallows and stable stratification may develop. In this reduced surface layer, the formation of low-level jets is possible. Figure 2.1 illustrates the potential temperature gradients within the ABL and their corresponding stability classes or types of stratification.

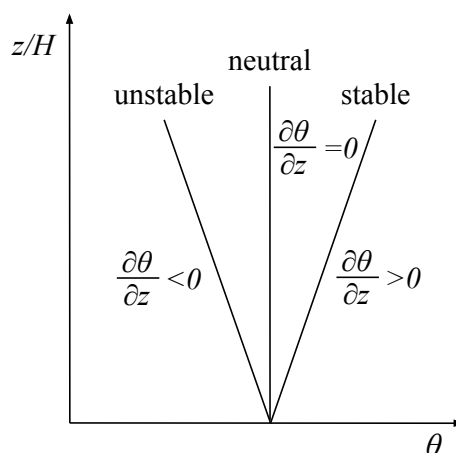


Figure 2.1.: Categorisation of stratification classes as function of the potential temperature θ with respect to the total ABL depth H : Unstable, neutral and stable conditions.

When a negative potential temperature gradient is observed, it signifies that the surface has a higher potential temperature compared to the upper regions of the ABL. This condition results in unstable stratification. In contrast, positive gradients indicate that the surface potential temperature is lower than that of the atmosphere, a more typical scenario during the night, leading to stable stratification.

The primary factors influencing the horizontal and vertical dispersion of pollutants within the ABL are mean wind, mechanical turbulence, and local variations in terrain and buildings, among other factors. In instances of neutral stratification where thermal turbulence is minimal, airflow is primarily influenced by mechanical turbulence, commonly referred to as forced convection. Buoyancy forces can either enhance or hinder the vertical growth of pollutant plumes, depending on the prevailing stability conditions and the characteristics of the pollutant release. This dynamic interplay serves as an additional factor shaping plume size and, notably, plume rise.

Although the focus of the simulations is primarily on neutral stratification, it is important to recognize that evaluating worst-case scenarios for pollutant dispersion is a multifaceted endeavor. In meteorology, (elevated) inversions and stable atmospheric conditions are often considered challenging scenarios due to their potential for trapping pollutants near the surface. The choice of the worst-case scenario depends on a variety of factors, including the height of the release, the conditions of the release, and the local

dispersion environment.

In the context of this study, which considers the atmospheric flow patterns around the CERN site, and in accordance with the pre-established research goals, as well as an initial assessment of various stratification types and wind conditions (as illustrated in Figures 4.25 and 4.24), the dissertation predominantly delves into the realm of neutral stratification. This selection aligns with the specific aim of gaining a comprehensive understanding of the dynamics of pollutant dispersion within the lower ABL, which commonly experiences neutral stratification.

However, it is essential to recognize that real-world scenarios can vary significantly and that the environmental conditions surrounding a pollutant release are dynamic. As such, the results and insights gained in this dissertation should be considered in the context of the specific research objectives and simulation constraints.

2.2. ABL Characteristics

The turbulence level within the atmospheric boundary layer (ABL) can be quantified using the Reynolds number Re , as described in Equation 2.1. This dimensionless number is defined as:

$$Re = \frac{U \cdot L_{cha}}{\nu_{air}} \quad (2.1)$$

Where:

- U represents the mean velocity at a specific measurement location.
- L_{cha} corresponds to the characteristic length, typically determined as the height above the ground where the velocity measurement is taken.
- ν_{air} represents the viscosity of air. For standard conditions at 0°C and at atmospheric pressure of 1013.25 hPa, the value of ν_{air} is approximately $1.46 \cdot 10^{-5} \text{ m}^2\text{s}^{-1}$.

An illustrative example is provided in the following equation, considering typical values present in this dissertation.

$$Re = \frac{(1 \text{ ms}^{-1}) \cdot (10 \text{ m})}{1.46 \cdot 10^{-5} \text{ m}^2\text{s}^{-1}} \approx 685'000 \quad (2.2)$$

In the realm of fluid dynamics, atmospheric flows are distinguished by having one of the highest Reynolds numbers (Re) compared to a wide range of other applications. This signifies that the flow dynamics within the Earth's atmosphere exhibit exceptionally complex and turbulent behaviors, rendering atmospheric flow simulations and analyses a challenging and critical area of study.

The turbulent behavior within the ABL is notably intricate and subject to variation influenced by several factors, including time of day, season, terrain, and atmospheric stability. Despite this variability, there are consistent characteristics associated with ABL

turbulence. These characteristics encompass a high degree of unpredictability and intermittency, as evidenced by the continual formation, interaction, and decay of eddies and vortices of varying sizes and shapes.

ABL turbulence is further influenced by the Coriolis force, which contributes to the development of large-scale circulations, and by the presence of obstacles capable of generating turbulent wakes and structures. Consequently, the study of ABL turbulence presents both a compelling challenge and a significant area of inquiry, offering implications that span multiple fields, including atmospheric science, engineering, and environmental monitoring.

More characteristics of the turbulent behavior of the ABL are listed below.

- According to Wyngaard (2010), turbulent eddy sizes during daytime range $10^{-3} \leq \delta \leq 10^{+3}$ m.
- Energy containing eddies can reach sizes up to $\delta \sim 100$ m.
- Inertial sub-range eddies range from $0.3 \leq \delta \leq 30$ m.
- Dissipating eddy sizes are smaller than $\delta \leq 10^{-1}$ m.

Van der Hoven (1957) classified disturbances at an altitude of ~ 100 m into three different levels: Macro-scale and meso-scale phenomena and microscale turbulence. Macro-scale phenomena can influence the local wind speed within several days (~ 4 d), while meso-scale phenomena are characterized by diurnal cycles (~ 12 h) and have a non-negligible effect on the turbulent kinetic energy. microscale turbulence is typically characterized by higher frequencies within the turbulent spectrum, often occurring at shorter time intervals compared to larger-scale turbulence. The so called spectral gap in the context of turbulence refers to a range of spatial or temporal scales within turbulent flow where there is a noticeable absence of energy or significant fluctuations. In other words, it represents a gap or a break in the spectrum of energy distribution across different scales of turbulence.

Since macro-scale and meso-scale phenomena persist for longer periods, their behavior can be studied by using measurements of wind speed direction at weather stations performed several times per day. Assuming that large-scale fluctuations can be approximated as quasistationary cases of varying wind conditions, the focus is set on short-duration releases (approximately 1 hour) combined with near-field dispersion (around 500 meters) and a microscale turbulence modeling approach. This approach effectively captures the dynamic variations in wind conditions while maintaining the computational efficiency required for the analysis.

2.3. Modeling Mechanical Turbulence

The depth of the Prandtl-layer, a vital component of the atmospheric boundary layer, is a parameter heavily influenced by the characteristics of the surrounding terrain. In areas

with low ground roughness, such as expansive grasslands or coastal regions, the Prandtl-layer assumes a more modest dimension. Conversely, in regions characterized by high roughness, including urban environments, this layer extends to greater depths (Andrews (2010)).

Within the atmospheric surface layer, a phenomenon of paramount significance is encountered: the logarithmic increase in wind velocity with height above the Earth's surface. Under specific conditions delineated by Kaimal and Finnigan (1994), this logarithmic wind profile manifests itself, defining the understanding of wind behavior near the Earth's surface. These conditions encompass:

- **Steady, homogeneous flow:** The logarithmic wind profile is applicable to steady and homogeneous atmospheric flow, where the wind varies primarily with height and not laterally or over time.
- **Neutral atmospheric stability:** The logarithmic wind profile is most pronounced under neutral atmospheric stability conditions. Neutral stability implies that there is no significant temperature difference between the ground and the air, resulting in minimal buoyancy forces influencing the wind profile.
- **Flat, open terrain:** The logarithmic wind profile is often observed over flat and open terrain, where the effects of surface roughness are relatively uniform and do not vary significantly with direction.
- **No obstructions:** The profile assumes an absence of significant obstructions or obstacles that could disrupt the flow pattern. It is typically valid well above the height of any obstructions, such as buildings or vegetation.
- **Within the atmospheric surface layer:** The logarithmic wind profile is a characteristic of the lower portion of the atmospheric boundary layer, typically extending up to a few hundred meters above the Earth's surface.

This logarithmic increase in wind velocity represents a foundational concept within the realm of atmospheric science. It plays an indispensable role in the comprehension of wind dynamics close to the Earth's surface. The pursuit of this understanding often relies on the methodology established by Monin and Obukhov (1954), which is described in greater detail in Chapter 4.3.1. This method hinges on the assumption of horizontally homogeneous and stationary flow conditions, incorporating a stability parameter derived from turbulence and mean velocity fields dependent on height above ground (z), kinematic momentum, potential temperature flux, and buoyancy. In cases of neutral stability, a common occurrence near the Earth's surface in the vicinity of CERN, the potential temperature flux becomes negligible as the Obukhov length (L) approaches infinity.

The Prandtl layer, situated within the atmospheric surface layer, serves as a critical arena where the intricate processes of pollutant transport and mixing unfold. Within this context, the dissertation places substantial emphasis on the precise modeling of mechanical turbulence. Simultaneously, it is delved into the intricate flow conditions necessary to

effectively capture near-ground eddies, thereby ensuring the attainment of high-quality results.

2.4. Scope for Simulations

Large-eddy simulations (LES) are computationally expensive, necessitating constraints on the simulation scope. Firstly, the study area is confined to the Meyrin-site at CERN and its immediate environs. Secondly, the simulations exclusively consider neutral stratification within the relevant meteorological conditions. This choice is substantiated by the earlier discussions in Section 2.1, where it is assumed that temperature remains relatively constant with height. Consequently, there is no requirement to model potential temperature, and the energy equation does not need be solved. As a result, the computational load is reduced, focusing on solving four key Navier-Stokes equations: mass conservation and the three momentum equations, with the potential inclusion of passive scalar transport equations. This simplification exclusively applies to releases with temperatures akin to the ambient temperature. Despite these simplifications, the simulations remain computationally demanding due to the considerable simulated area in LES and the requisite high grid resolution for accurate resolution near the ground to resolve relevant turbulence, flow and dispersion obstacles sufficiently.

Domain Height

Preliminary investigations utilizing steady-state RANS equations have indicated that in scenarios where pollutants are released from ground-level sources, the dispersion height reaches a maximum of approximately 100 meters at a distance of 400 meters. It is important to emphasize that these simplifications exclusively pertain to ground-level release scenarios. In cases of elevated releases, such as those from higher stacks, pollutants can easily reach the mixed layer. Neglecting thermal turbulence or focusing solely on the first 100 meters of altitude (the Prandtl layer) for dispersion modeling could yield incorrect outcomes.

To streamline the simulation process, a Neumann boundary condition was applied to the top wall boundary, replacing open wall or pressure conditions. It is worth noting that this approach may introduce artificial flows in scenarios where the terrain altitude varies significantly across the computational domain. However, for the Meyrin site, characterized by relatively flat terrain within a range of approximately ± 50 meters, this is not a concern. To ensure numerical stability in ANSYS[®] Fluent, the terrain was adjusted at the domain edges (illustrated in Figure 4.4), and the domain height was set at 500 meters above ground, exceeding the anticipated dispersion height. This higher portion of the computational domain functions as a buffer region, effectively decoupling any potential effects arising from the simplified top boundary conditions from the plume dispersion

simulations conducted near the ground. For a comprehensive description of the geometry setup, please refer to Chapter 4.3.1.

Simulation of Prandtl-Layer

Turbulence within the Prandtl-layer primarily originates from sources such as friction, wake turbulence, and wind shear. Wake turbulence typically forms in the vicinity of obstacles like buildings or trees. However, at the CERN Meyrin site, where the surroundings mainly consist of grasslands and vineyards, vegetation is not a significant factor for the model, while the CAD modelling of the buildings were of particular importance.

To address the effects of surface friction, a wall modeling approach is adopted instead of fully simulating eddies as small as a few millimeters. These small-scale eddies, while not significantly altering overall wind characteristics, do contribute to the logarithmic wind profile. By employing a wall modeling technique like wall-modeled large-eddy simulation (WMLES) in the simulations, the required grid resolution can be significantly reduced near solid surfaces. Larsson et al. (2016) summarize the use of WMLES for methods where LES equations are solved down to the wall to model the wall stress directly.

Without this approach, simulating an extensive area of 9 square kilometers with a resolution of 1 millimeter at ground level would necessitate an impractical 900 million computational cells to accurately represent the first ground layer. The following layers extending up to a height of 500 meters across the entire domain would require even more computational cells. For a more comprehensive explanation of the meshing procedure, please refer to Chapter 4.2.3, where the definition of the final selected mesh is described.

Diurnal Cycle

Another factor contributing to turbulence production, particularly in the mixed layer, is the diurnal cycle. This cycle causes temperature gradients, humidity variations, and wind changes at different heights. At night, the stable boundary layer usually forms near the ground, with a residual layer above, leading to low turbulence levels. During the day, the turbulent mixed layer with temperature gradients and high turbulence forms about half an hour after sunrise. During the day, water from plants evaporates, and the air at ground level reaches a higher specific humidity, whereas at night, humidity decreases close to the ground, leading to frost or condensation. However, humidity is not a relevant factor for pollutant dispersion in the selected scenarios. Wind speed also varies with the diurnal cycle. At ground level, wind speed is always zero due to the no-slip condition, while above the ABL, the geostrophic wind persists throughout the day. In the intermediate layer, wind may reach higher values due to the Coriolis force.

To account for wind variations conservatively, the measured mean wind speed at CERN is reduced from 2 ms^{-1} at 10 m height to 1 ms^{-1} to follow with Swiss federal specifications ENSI-G14 (2009). More details on this adjustment can be found in Chapter 2.5. This re-

duction in wind speed results in higher pollutant concentrations near the ground due to slower transport.

Impact of Changing Weather Conditions

The results of a release can be significantly affected by changes in weather conditions and corresponding wind patterns, especially during continuous releases over an extended period. These changes may include variations in wind direction, wind speed, and thermal effects. Predicting these variations accurately is challenging, as local conditions can differ over large areas. To simplify the simulation, the wind conditions have been defined as steady, without temporal modifications. This is considered a conservative approach, as wind gusts or changing directions would only increase the spread of pollutants. This approach is appropriate when assessing the maximum concentration of pollutants in areas close to the release point.

However, when evaluating the affected areas, it is essential to consider the impact of changing wind directions. Furthermore, it would be valuable to examine the influence of transient boundary conditions on pollutant dispersion during long-term releases to assess their effect on ground-level concentrations.

Simulated Time Period

The time required to simulate a pollutant release scenario using LES is influenced by various factors, such as the size and complexity of the modeled area, atmospheric and meteorological conditions, and the physical and chemical properties of the pollutant. It is important to select the simulated time period that is long enough to capture the relevant transport and dispersion processes. A typical duration for such a simulation can range from several hours to several days, depending on the specific requirements of the simulation.

The simulated time period has a significant impact on the evaluation of flow properties. The duration of the pollutant release directly affects the dispersion of pollutants and corresponding ground concentrations. For example, if the release takes a longer time, the weather conditions may change more dramatically. In many cases, the typical release time for the investigated scenarios is measured in minutes or hours, making it possible to neglect the diurnal cycle and variations over the day.

Additionally, the results of the simulation may change when injecting pollutants at different times during the passing of a large eddy. This change occurs because the mean wind, and therefore the dispersion of pollutants, varies. These variations also impact the evaluation of mean flow characteristics, such as mean velocities, turbulence intensity, and energy density. Depending on the simulated scenarios and the type of wind characteristics assessed, these flow properties converge within the total simulated time period of 90 minutes or earlier. The mean wind profile was the property that first converged, while the energy density was the last. The total simulation duration is limited by the

computational effort required for the full simulation run. For transient LES with a total simulation time of 120 minutes, a standard computing time of approximately one week using 200 cores is needed.

2.5. Gaussian Plume Models

The article by Sutton (1947) discusses the theoretical distribution of airborne pollution from factory chimneys. The author proposes a mathematical model to estimate the dispersion of pollutants released from industrial chimneys and assesses the impact of various factors such as wind direction, atmospheric stability, and chimney height. The results of the model show that the distribution of pollutants depends on the weather conditions and other factors, and the author concludes that it is essential to consider these factors in the planning and regulation of industrial emissions.

The idea of a Gaussian distribution of pollutants dispersion in air was already proposed by Sutton (1947). The author's mathematical model estimates the dispersion of pollutants released from industrial chimneys and assesses the impact of various factors such as wind direction, atmospheric stability, and chimney height. The model assumes a Gaussian distribution for the concentration of the pollutant.

$$C(x, y, z) = \frac{Q}{2\pi} \cdot \frac{1}{\sigma_x \sigma_y \sigma_z} \exp \left[-\frac{1}{2} \left(\frac{x^2}{\sigma_x^2} + \frac{y^2}{\sigma_y^2} + \frac{z^2}{\sigma_z^2} \right) \right] \quad (2.3)$$

where C is the concentration of the pollutant, Q is the total amount of the pollutant released, x is the downwind distance from the source, y is the crosswind distance from the centerline of the plume, z is the height above the ground, $\sigma_{x,y,z}$ are the standard deviations of the concentration in the x , y and z -direction.

These kind of models for the concentration of pollutants, called Gaussian plume models (GPMs) are widely used for a variety of applications, including the assessment of the impact of industrial emissions on air quality, the prediction of the dispersion of hazardous materials (hazmat) in the event of an accident, and the design of air pollution control systems. They are relatively simple to use, and can provide quick and inexpensive estimates of the potential impact of a pollutant release.

However, GPMs have several limitations and may not provide accurate predictions in complex atmospheric conditions, such as in the presence of terrain, buildings, or other obstacles that can disrupt the plume. In these cases, more sophisticated models, such as the large-eddy simulation (LES) or the Reynolds-Averaged Navier-Stokes (RANS) models, may be more appropriate. These models will be further discussed in the next chapters.

The simplicity of Gaussian plume models allows to integrate several processes like dry and wet deposition of particles due to precipitation, radioactive decay or plume rise due to the buoyancy forces. Moreover, several different types of stratification of the atmo-

sphere can be taken into account, which lead to different dispersion coefficients. This allows to see within seconds of computing time the impact of the stratification. It should be mentioned, however, that GPMs do not depict ground release scenarios in urban areas in a satisfactory way, and alternative models would be required for these scenarios. In fact, changing topography around the release point, as it often happens in urban areas, might have a big impact on pollutant concentrations, since the plume might be deflected from the ground at certain slopes. Also changes in the surface roughness, even when localized in areas of few meters squared, could strongly affect the plume direction and dispersion. Channeling of the plume in street canyons and therefore the deflection from the wall cannot be accounted for. Also the impact of the building wake for releases from low stacks on the roof cannot be easily accounted for. All these aspects impact in a negative way the accuracy of the simulations close to the release point, and since studying the short range dispersion is one of the main goal of this project, CFD simulations were used instead of GPMs for the atmospheric dispersion modelling at CERN. For distances with less impact (≥ 500 m) due to the wider dispersion of the plume and lower pollutant concentrations the GPM is still used. GPMs have been nonetheless useful as a term of comparison for the simulation approach taken in this project. In fact, validating the simulation results with real data has not been possible during the COVID pandemic and, hence, the only way to assess the goodness of the LES based simulation used in this project has been comparing it to the GPM based analytical approach, which has been used since a long time and has been proven and validated for several cases. The results of such comparison is reported in Chapter 5.1.

The GPM used at CERN follows the ENSI-G14 from the Swiss government ENSI-G14 (2009), which defines the exposition of radiation from emissions of pollutants from nuclear power plants. CERN is listed as nuclear research institute, which is why Swiss guidelines for nuclear power plants also apply for CERN. The ENSI-G14 follows the German "Guidelines for assessing the design of nuclear power plants with pressurized water reactors against accidents" from 1983, the IAEA Safety Series No. 50-SG-S3, the IAEA Safety Standard NS-G-3.2, and the IAEA Safety Report Series No. 19.

3. Numerical Modeling Theory

This chapter elucidates the foundational principles of numerical modeling for the computational fluid dynamics solver. It encompasses an explanation of the governing equations, turbulence modeling, and transport modeling, all of which are extensively employed in this dissertation to simulate the dispersion of pollutants. Understanding this numerical modeling theory is crucial to achieving accurate representations of pollutant behavior in the environment.

Without a solid grasp of the theory of numerical modeling, it becomes challenging to precisely simulate the intricate physical processes involved in the dispersion of pollutants. These processes encompass turbulence, chemical reactions, and particle behavior, all of which exert a significant influence on the spread and concentration of pollutants in the environment. Consequently, they have direct implications for human health and the environment.

Understanding numerical modeling theory is fundamental as it empowers the selection of appropriate models and parameters, facilitating precise simulations of various processes and predictions concerning pollutant behavior across different release and dispersion scenarios. For a comprehensive exploration of numerical modeling theory in computational fluid dynamics, two notable references are "Turbulent Flows" by Tennekes et al. (1972) and "Turbulent Flows" by Pope (2000). These texts provide an in-depth overview of turbulent flows, including the fundamental transport equations.

The key premises for simulations in this context are as follows.

- The analysis focuses on studying the motion of fluid portions.
- Newtonian fluids are considered, characterized by a molecular viscosity μ , which may vary with temperature or pressure, but not by external forces.
- The Eulerian solver is employed to describe fluid motion, where the reference coordinate system remains fixed, and the quantities being solved are functions of both position (x) and time (t).
- Alternatively, the Lagrangian approach, in which the reference system is the fluid element itself along with its trajectory, are used to track particles within the fluid.

For ANSYS® users, the ANSYS® Fluent Theory Guide, accessible in ANSYS Inc. (2022), serves as a valuable and direct resource within the software environment.

3.1. Governing Equations

The Navier-Stokes equations represent a system of partial differential equations that provide insights into the behavior of viscous fluids, as detailed in Batchelor (2000). These equations stem from the second law of motion and were independently formulated by Claude-Louis Navier (1785-1836) and George Gabriel Stokes (1819-1903) through the application of Newton's second law of motion to fluid flows. Their primary purpose is to characterize the viscosity and stress of the fluid, necessitating the utilization of numerical techniques for solution derivation.

Traditionally, the three Navier-Stokes equations capture the conservation of momentum for fluid motion in each spatial direction, typically denoted as x , y , and z . Moreover, mass conservation is inherent to complement the analysis of fluid motion.

This clarification highlights that the primary focus of the Navier-Stokes equations is on momentum conservation, with mass conservation being an integral component of the broader understanding of fluid behavior.

The fluid velocity, denoted as \mathbf{U} , is expressed as a function of position x and time t in a fixed, non-rotating Eulerian reference system. The velocity components u , v , and w in the x , y , and z directions, respectively, are used to describe \mathbf{U} , as shown in Equation 3.1. Furthermore, the spatial coordinates x , y , and z are represented as x_i and are defined in Equation 3.2.

$$\mathbf{U}(x, t) = (u, v, w) \quad (3.1)$$

$$x_i = (x, y, z) \quad (3.2)$$

This representation clarifies that the velocity of the fluid \mathbf{U} depends on both position and time in an Eulerian framework, with u , v , and w denoting the velocity components and x , y , and z representing the spatial coordinates.

The conservation of mass is governed by the continuity equation, which is expressed as follows.

$$\frac{\partial \rho}{\partial t} + \frac{\partial \rho U_i}{\partial x_i} = 0 \quad (3.3)$$

Here, ρ represents the density of the fluid.

In the context of multiphase flows, there are two phases: the dispersed phase and the continuous phase. The dispersed phase consists of small droplets, bubbles, or particles suspended within the continuous phase Crowe et al. (2011). In scenarios similar to those used in this dissertation, such as pollutant dispersion simulations, solid smoke particles represent the dispersed phase, while the surrounding air serves as the continuous phase. In cases involving dispersed phases, such as liquid droplets, droplet evaporation and sublimation can affect mass conservation. To account for this, a source term S_m is

introduced into the mass conservation Equation 3.3.

The simplified continuity equation, expressed as Equation 3.4, represents the conservation of mass for an incompressible fluid. It states that the rate of change of mass within a control volume is equal to the net mass flux through its boundaries. When the density of the fluid is constant and the fluid is both incompressible and divergence-free, the derivative of velocity with respect to the spatial coordinates sums up to zero.

$$\frac{\partial U_i}{\partial x_i} = 0 \quad (3.4)$$

The assumption of incompressible fluid motion is valid when the maximum velocity of the fluid remains below a Mach number of $Ma = u/c < 0.3$, as referenced in Young et al. (2010). In air, the speed of sound depends on the temperature and is approximately 343 ms^{-1} at 293.15 degrees Kelvin. Under typical atmospheric conditions, the critical velocity for the use of compressible Navier-Stokes equations is approximately 103 ms^{-1} . Given that the atmospheric dispersion simulations conducted in the context of this dissertation do not involve fluid speeds that approach these values, the assumption of incompressible fluid behavior remains appropriate for this research.

The ∇ operator is introduced as the vector differential operator to describe the divergence of the velocity component U_i with respect to the spatial coordinates x_i .

$$\nabla U_i = \frac{\partial U_i}{\partial x_i} = \frac{\partial u}{\partial x} + \frac{\partial v}{\partial y} + \frac{\partial w}{\partial z} = 0 \quad (3.5)$$

The momentum conservation equation, as expressed in Equation 3.6, elucidates how the velocity of a fluid evolves over time due to external influences (Batchelor (2000)). On the left-hand side of the equation the acceleration of the fluid is observed. This acceleration is determined by two main terms: the rate of change in velocity vector time, $\partial U_i / \partial t$, and the convective term, $U_j \cdot \partial U_i / \partial x_j$, which accounts for the effects of advection.

In contrast, the right-hand side of the equation includes the forces exerted on the fluid. These forces can be categorized into two components: the pressure gradient, denoted as $-\partial p / \partial x_i$, and the viscous forces, represented as $1/\rho \cdot \partial \sigma_{ij} / \partial x_j$, where ρ signifies the density of the fluid.

This equation encapsulates the fundamental principles that govern the change in fluid velocity, encompassing the effects of acceleration, advection, pressure, and viscous forces.

$$\frac{\partial U_i}{\partial t} + U_j \cdot \frac{\partial U_i}{\partial x_j} = -\frac{1}{\rho} \frac{\partial p}{\partial x_i} + \frac{1}{\rho} \frac{\partial \sigma_{ij}}{\partial x_j} \quad (3.6)$$

The viscous forces are described by the viscous stress tensor, σ_{ij} , which is related to the strain rate tensor, s_{ij} , through a linear relationship known as the constitutive equation, as stated in Landau and Lifshitz (1987). For Newtonian fluids, the constitutive equation is given by Equation 3.7, where μ is the dynamic viscosity of the fluid.

$$\sigma_{ij} = 2\mu s_{ij} \quad (3.7)$$

The strain rate tensor, s_{ij} , represents the rate of fluid deformation and is defined by Equation 3.8. The term $\partial U_i / \partial x_j$ represents the rate of deformation in the j -th direction caused by the velocity gradient in the i -th direction, while the term $\partial U_j / \partial x_i$ represents the rate of deformation in the i -th direction caused by the velocity gradient in the j -th direction. The factor of $1/2$ is included to account for the fact that the deformation is symmetric in two directions.

$$s_{ij} = \frac{1}{2} \left(\frac{\partial U_i}{\partial x_j} + \frac{\partial U_j}{\partial x_i} \right) \quad (3.8)$$

Together, equations 3.6-3.8 represent a subset of the fundamental equations of fluid mechanics, which govern the motion of a fluid in response to external forces. These equations can be solved numerically using various techniques, such as finite difference, finite element, or spectral methods, to simulate the behavior of fluid flows in different scenarios.

For an incompressible Newtonian fluid, the definition of kinematic viscosity ($\nu \equiv \mu / \rho$) can be combined with the definition of the viscous stress tensor in Equation 3.7 to write the momentum conservation Equation 3.6 as:

$$\frac{\partial U_i}{\partial t} + U_j \frac{\partial U_i}{\partial x_j} = -\frac{1}{\rho} \frac{\partial p}{\partial x_i} + \nu \frac{\partial^2 U_i}{\partial x_j \partial x_j}, \quad (3.9)$$

where additional forces such as gravitational force, see Equation 3.33 can also be added to the momentum conservation equation if needed.

3.2. Turbulence Modeling

Turbulence is a ubiquitous phenomenon in fluid flows, characterized by chaotic and unpredictable fluctuations in velocity and pressure. Among others, it plays a pivotal role in various engineering applications, including aircraft design, combustion, and dispersion of pollutants in the atmosphere. The intricate and multiscale nature of turbulence, particularly in atmospheric flows, presents a formidable challenge for accurate modeling and simulation using computational methods.

Turbulence models provide an approach to approximate the effects of turbulence while mitigating the computational burden of simulations. They achieve this by employing different strategies, including the resolution of larger eddies and parameterization of smaller ones. Two primary approaches to turbulence modeling are commonly employed. Reynolds-average Navier-Stokes (RANS) and Large-Eddy Simulation (LES). It is essential to note that RANS, while commonly used, is not a turbulence model in the strict sense; instead, it is an approach that addresses the closure problem associated with turbulence

modeling.

RANS models are known for their computational efficiency, but their assumptions and limitations can compromise their accuracy, especially when predicting complex turbulence phenomena. In contrast, LES models offer higher accuracy by directly resolving a range of eddies, but come with higher computational demands Pope (2000).

The choice of an appropriate turbulence modeling approach depends on the specific requirements of the application, achieving a balance between the desired level of accuracy and computational effort. In this section, the primary turbulence modeling approaches commonly used in atmospheric boundary layer simulations are introduced and their respective strengths and limitations are discussed, with particular attention to the closure problem in turbulence modeling.

RANS modeling is used to establish a realistic flow within the domain. The advantage of utilizing RANS modeling lies in its ability to efficiently solve fluid dynamics before transitioning to large-eddy simulation (LES), which entails significantly more computational effort. Thus, RANS serves as a valuable tool for preconditioning and initializing the flow. Once the RANS solver, equipped with the k - ε turbulence model, converges, the resulting initial solution can be used to evaluate turbulence characteristics and determine appropriate cell sizes for subsequent LES simulations. Further insights into this procedure are elaborated in Chapter 4.3.

3.2.1. Reynolds Averaged Navier Stokes Equations (RANS)

In RANS models, the equations describing fluid flow are averaged over numerous time steps to represent the turbulent characteristics present in the flow Pope (2000). These time-averaged equations are then solved using numerical methods to predict the velocity, pressure, and temperature fields within the flow Pope (2000). The continuity equation in the context of RANS can be expressed as:

$$\frac{\partial \langle U_i \rangle}{\partial x_i} = 0 \quad (3.10)$$

Here, $\langle U_i \rangle$ denotes the time-averaged velocity in the i -direction, which is represented as $\langle U \rangle$, $\langle V \rangle$, and $\langle W \rangle$ for the respective directions. When the flow is statistically stationary, the time average velocity $\langle U_i \rangle$ can be calculated by:

$$\langle U_i \rangle = \frac{1}{T} \int_{t_0}^{t_0+T} U_i(x_i, t) dt \quad (3.11)$$

The Reynolds decomposition, as stated in Equation 3.12, denotes the separation of a turbulent quantity, i.e. the instantaneous velocity U_i into a mean value $\langle U_i \rangle$ and a fluctuating part u'_i . Whenever the term mean velocity is used in this dissertation, the time-averaged velocity is meant, and not the spatial averaged velocity. In case the spatial-averaged velocity is used, it is explicitly mentioned.

$$U_i(x_i, t) = \langle U_i \rangle + u'_i \quad (3.12)$$

The Reynolds equation, which describes the mean flow of an incompressible fluid in the context of RANS, introduces the Reynolds stress tensor $\tau_{ij} \equiv -\rho \langle u'_i u'_j \rangle$ to account for the temporal and spatial behavior of flow involving velocity fluctuations. It is expressed as

$$\rho \frac{\partial \langle U_i \rangle}{\partial t} + \rho \langle U_j \rangle \frac{\partial \langle U_i \rangle}{\partial x_j} = -\frac{\partial \langle p \rangle}{\partial x_i} + \mu \frac{\partial^2 \langle U_i \rangle}{\partial x_j \partial x_j} + \frac{\partial}{\partial x_j} \left(\rho \langle u'_i u'_j \rangle \right) \quad (3.13)$$

In this equation, the operator $\langle \dots \rangle$ signifies the Reynolds averaging of derivatives, and the Reynolds stress tensor τ_{ij} represents the transfer of momentum due to velocity fluctuations.

In high Reynolds number flows, the dominant factor contributing to momentum transfer is typically turbulence, which far outweighs the viscous effects. To compute Reynolds stresses in such flows, various eddy-viscosity models can be employed. Among these models, the k- ϵ and k- ω SST models (Shear-Stress Transport) are the most commonly used approaches Spalart and Allmaras (1992).

In this dissertation, a two-step approach was adopted. Initially, Reynolds-Averaged Navier-Stokes (RANS) steady-state simulations were employed to obtain an approximate mean velocity field, which served as the starting point for subsequent large-eddy simulation (LES). Consequently, the k- ϵ model was utilized as the turbulence model for the RANS simulations without further investigation into the choice of a different viscosity model. The k- ϵ model is discussed in more detail in the following.

It is essential to note that in eddy viscosity models, such as the k- ϵ model, the velocity fluctuations u'_i are not directly computed but are modeled by relating them to the mean flow. These models make the assumption that the fluctuations are random, which considerably simplifies turbulence modeling. However, it is important to recognize that, in reality, the motion and formation of eddies are not truly random. This assumption leads to a significant simplification of turbulence modeling for most applications and, as a result, it does not precisely capture the complex behavior of eddies as they exist in the real world.

The Boussinesq model, first introduced by Boussinesq (1877), is the simplest eddy viscosity model. It adds a turbulent viscosity μ_t as an artificial term to control the strength of the diffusion of momentum. The resulting equation is given by:

$$-\rho \langle u'_i u'_j \rangle + \frac{2}{3} \rho k \delta_{ij} = \rho \nu_t \left(\frac{\partial \langle U_i \rangle}{\partial x_j} + \frac{\partial \langle U_j \rangle}{\partial x_i} \right) = 2 \rho \nu_t S_{ij}^*, \quad (3.14)$$

where S_{ij}^* is the different part of the strain-rate tensor of the mean flow. Equation 3.15 defines the differing part of the strain rate tensor of the mean flow, denoted by S_{ij}^* . It is given by:

$$S_{ij}^* = \frac{1}{2} \left(\frac{\partial \langle U_i \rangle}{\partial x_j} + \frac{\partial \langle U_j \rangle}{\partial x_i} - \frac{2}{3} \frac{\partial \langle U_k \rangle}{\partial x_k} \delta_{ij} \right), \quad (3.15)$$

where δ_{ij} is the Kronecker delta, which allows normal and shear stresses to be combined into a single formula. Equation (3.14) shows that increasing turbulent viscosity leads to higher diffusion.

The turbulence kinetic energy (TKE) is defined as half the normal fluxes of the Reynolds stress tensor and can be written as:

$$k \equiv \frac{1}{2} \langle u'_i u'_i \rangle \quad (3.16)$$

The Boussinesq model uses the gradient diffusion hypothesis, which can also be applied to heat and mass transfer using the turbulent Prandtl number $Pr_t = \nu_t / \Gamma_h$ and the turbulent Schmidt number $Sc_t = \nu_t / \Gamma_m$. Here, Γ_h is the turbulent thermal diffusivity and Γ_m is the turbulent mass diffusivity. Using the eddy viscosity model, an approximate numerical solution for the RANS equations can be found. For the k- ϵ turbulence model, the turbulent viscosity ν_t is calculated using the following equation:

$$\nu_t = C_\mu \frac{k^2}{\epsilon}, \quad (3.17)$$

where the constant of the turbulence model is $C_\mu = 0.09$ and ϵ is the dissipation rate. This equation is derived by assuming a balance between the production of TKE and its dissipation, also called local equilibrium.

3.2.2. Large Eddy Simulations

As discussed in the introduction chapter, large-eddy simulation presents a formidable simulation method, particularly when dealing with turbulent flows such as those found in the atmospheric boundary layer. The primary objective of LES is to directly resolve the energy-containing eddies that span all turbulence length scales critical for modeling a given turbulent flow. Typically, this involves using a grid resolution that is approximately four times smaller than the size of the smallest eddies, while employing a turbulence model to parameterize smaller ones by a corresponding turbulence model.

In this process, certain aspects of the flow, especially the smaller energy-containing eddies, are subject to modeling. These smaller eddies are assumed to exhibit isotropic behavior and are thus modeled using subgrid-scale models. In contrast, the larger eddies are resolved at the finest grid resolution possible because they exert a significant influence on the trajectories of transported fluid and particles.

The modeling of very small-sized eddies becomes less significant when considering the transport of particles. This is because the movement of particles within these smaller eddies has a smaller amplitude, resulting in a less pronounced effect on particle trajectories. In addition to a smaller wavelength of these eddies and a corresponding higher

frequency, these movements can also be predicted with random-walk models taking into account the modeled turbulent kinetic energy.

To ensure that simulation results closely approximate reality, a crucial factor to consider is the resolution of the majority of energy-containing eddies. The recommended level of resolution can vary between researchers, Pope (2000) advocating for resolving approximately 80 % of turbulent kinetic energy. However, depending on the specific problem to be addressed, it may be justifiable to aim for a resolution of around 90 %. An evaluation of the robustness of the solution under varying mesh sizes is discussed in Chapter 4.2.4.

The computational effort of transient simulations is significantly influenced by both the time step size and spatial resolution. Opting for a smaller mesh size can lead to a notable reduction in computational effort. It is worth noting that reducing spatial resolution also permits the use of larger time-step sizes. In Chapter 4.5, you will find guidance in determining the appropriate cell size and time step size based on considerations such as eddy sizes and energy cascade/density plots.

To represent turbulent eddy viscosity μ_t in LES simulations, several subgrid-scale modeling types are commonly used, including the following four dominant models, among others.

- **Smagorinsky-Lilly Model:** Named after American meteorologist Joseph Smagorinsky and Douglas Lilly, this model is described in Smagorinsky (1963).
- **Dynamic Smagorinsky-Lilly Model:** Conceived by Germano et al. and subsequently by Lilly, this model employs a procedure in which the Smagorinsky model constant is dynamically computed based on information provided by the resolved scales of motion. Details can be found in Germano et al. (1991) and Lilly (1998).
- **Wall-Adapting Local Eddy-Viscosity (WALE) Model:** This model, designated to adapt to near-wall turbulence, is described in Nicoud and Ducros (1999).
- **Dynamic Kinetic Energy Subgrid-Scale Model:** Detailed information about this model, which focuses on the dynamic aspects of kinetic energy at the subgrid scale, can be found in Kim and Menon (1997).

Among these methods, the Wall-Adapting Local Eddy-Viscosity (WALE) model was selected, which incorporates a modification to the velocity scales. Although a general overview of these models is provided in the following, for more detailed information, it is recommended to consult the literature, particularly Pope (2000) and Nicoud and Ducros (1999).

As in RANS models, the Boussinesq hypothesis is applied to subgrid-scale turbulence models. This involves introducing a subgrid eddy viscosity term denoted as ν_{sgs} into the calculated viscous stress. The inclusion of this subgrid eddy-viscosity term leads to an increase in the viscous stress, resulting in higher dissipation of energy. Equation 3.18 outlines the calculation of the Smagorinsky constant, C_s :

$$C_s = \frac{1}{\pi} \left(\frac{2}{3C_\kappa} \right)^{0.75} \quad (3.18)$$

Here, $C_\kappa = 1.5$ represents the Kolmogorov constant, a fundamental parameter in turbulence theory named after the Russian mathematician and physicist Andrei Kolmogorov, who made significant contributions to the study of turbulence. Lilly derived a specific value for the Smagorinsky constant, which is widely accepted as $C_s = 0.173$. This value is considered valid for describing homogeneous isotropic turbulence within the inertial subrange.

The Kolmogorov constant κ is associated with the Kolmogorov length scale (η), which characterizes the smallest eddies in a turbulent flow. It plays a crucial role in the scaling of turbulence and is related to turbulence quantities such as the turbulent kinetic energy (k) and the turbulence dissipation rate (ε) through the equation:

$$\varepsilon = C_\kappa \frac{k^{3/2}}{\eta} \quad (3.19)$$

Here, k is the turbulent kinetic energy and ε represents the rate of dissipation of the turbulence. The Kolmogorov constant helps to understand the scaling of turbulence at small scales, particularly in the inertial subrange of turbulence, where the energy cascade follows a power-law behavior.

The Smagorinsky constant C_s can then be used to estimate the subgrid length scale l_0 within a cell, using the LES filter width or cell size Δ :

$$l_0 = C_s \Delta \quad (3.20)$$

The viscosity of the subgrid scale ν_{sgs} for the initial solution is then modeled using the following equation:

$$\nu_{sgs} = (C_s \Delta)^2 \sqrt{2S_{ij}S_{ij}} \quad (3.21)$$

It is important to note that the Smagorinsky model is derived for homogeneous isotropic turbulence, and its validity is limited to conditions far from walls without shear, such as in a free-stream condition. However, in practical applications, it is often necessary to adapt the model to various flow conditions. Lilly's simplified approach, proposed in 1966 Lilly (1966), introduces damping of turbulence for large-scale fluctuations. As a result, the model has been continuously refined and adapted over time to better suit different flow scenarios.

It is important to note that different simulation codes may use varying values for the Smagorinsky constant C_s . ANSYS® Fluent employs a value of $C_s = 0.1$ based on empirical data. This choice is made to reduce the damping effect on the wall, as detailed in ANSYS Inc. (2022). Furthermore, most simulation software allows users to modify the Smagorinsky constant C_s to tailor it to their specific simulation requirements.

Various methods have been developed to enhance wall modeling, with the primary goal of reducing the kinematic viscosity of the sub-grid ν_{sgs} near the wall. One of the most popular and widely used approaches is the dynamic Smagorinsky model, often also referred to as Van Driest Damping, named after the Dutch physicist and engineer Johannes van Driest (1956). This method leverages information on the resolved scales of motion to dynamically adapt the Smagorinsky constant C_s .

The dynamic adjustment, both in space and time, of the Smagorinsky constant aims at accounting for the logarithmic part of the wall function. To achieve this, the length scale of the subgrid l_0 is calculated using a mixing length l_m for the scales of the subgrid. This mixing length depends on various factors, including the distance to the nearest wall y , the von Karman constant κ , the local grid size Δ , and the Smagorinsky constant C_s .

When cells are close to the wall, the coefficient κy decreases proportionally due to the decreasing value of y . Consequently, the sub-grid length scale l_0 decreases near the wall:

$$l_0 = \min(l_m, C_s \Delta) = \min(\kappa y, C_s \Delta) \quad (3.22)$$

It can therefore also be called the damping function for the sub-grid length scale l_0 . Van Driest (1956) proposed a continuous solution over the full domain or boundary layer (including viscous sublayer and buffer layer), so there is no modification over time for changing flow conditions.

$$l_0 = \min(l_m, C_s \Delta) = \min(\kappa y \cdot D, C_w \Delta) \quad (3.23)$$

The van Driest damping coefficient can be calculated using the dimensionless wall distance y^+ and a shape control constant A^+ :

$$D = 1 - \exp\left(-\frac{y^+}{A^+}\right) \quad (3.24)$$

In Launder and Spalding (1974) it is described that the shape control constant $A^+ = 26$ provides the best correlations with experiments.

The WALE model then further applies the ideas developed and accounts for the reduction of the subgrid length scale l_0 close to the wall but also on the changing conditions over time, see Equation 3.25:

$$l_0 = \min(l_m, C_s \Delta) = \min(\kappa y, C_W \Delta) \quad (3.25)$$

The WALE constant, represented as C_W , was initially defined as $C_W = 0.5$ according to Nicoud and Ducros (1999). However, it has been adjusted to $C_W = 0.35$ based on research findings, particularly in studies such as Sufra and Steiner (2020), where it demonstrated satisfactory performance. In the WALE turbulence model, the viscosity of the subgrid scale ν_{sgs} is modified to account for the influence of the strain and rotation rate on turbulence production. In particular, rotation rate turbulence production is considered more

significant than shear production. It is important to note that in pure viscous shear flows, such as laminar flows, the rotation rate turbulence production is zero. Therefore, even in these flow scenarios, viscous forces are accurately taken into account.

3.3. Transport Modeling

Transport modeling of particles is a vital aspect of computational fluid dynamics that allows us to understand how various substances, such as pollutants, dust or droplets, disperse and move within a fluid medium, often air. This modeling plays a crucial role in applications such as environmental studies, industrial processes, and safety assessments, where predicting the behavior of particles is of paramount importance.

One of the fundamental considerations in particle transport modeling is how the particles interact with the surrounding fluid, typically air. This interaction is governed by the concept of coupling, which defines how information is exchanged between the particle phase and the continuous phase (the fluid) during simulation.

Predicting the wind flow field is not the only factor crucial to simulating pollutant dispersion scenarios in the atmospheric boundary layer. The choice of transport model depends on various factors, including the type of pollutant, the release characteristics, the duration, and the parameters to be evaluated. In the field of atmospheric science and environmental engineering, several well-established pollution dispersion modeling approaches have been developed and rigorously tested. These models serve as valuable tools for understanding and predicting the dispersion of pollutants in various scenarios.

In the context of this study and within the field of computational fluid dynamics, two primary pollutant dispersion models are highlighted.

- **Euler-Lagrange Model:** Two phases are calculated with the Discrete Phase Model (DPM): continuous phase (air) and dispersed phase (particles)
- **Euler-Euler Model:** Two phases are calculated as mixture in the species transport model, where the two continua are interpenetrating each other with a corresponding volume fraction.

Both CFD modeling approaches are well-established and widely used in the field and are known for their ability to provide accurate and comprehensive insights. They are often chosen for investigations and risk assessments, particularly in scenarios involving safety-critical pollutant releases. Lagrangian models excel in representing scenarios involving dilute particle-laden flows, while Eulerian models are more adept at handling situations characterized by higher particle concentrations.

The following chapters will provide an in-depth exploration of these two approaches. To offer a broader perspective beyond CFD, this work also discusses the analytical solution using the Gaussian plume model (GPM). Later in this study, a comparison will be made between the analytical and CFD results to assess their respective merits.

In Chapter 3.3.1 and Chapter 3.3.2, both methods will be explained in detail. Subsequently, in Chapter 3.3.3, a comparative analysis of both models will be presented. This analysis will highlight their respective advantages and disadvantages while also addressing the limitations of each method.

3.3.1. Lagrangian Particle Dispersion

The Euler-Lagrange approach is implemented in ANSYS® Fluent as the Discrete Phase Model (DPM). This approach introduces a discrete second phase that is simulated along with the transport equations for the continuous phase. In DPM, the second phase is represented by spherical particles dispersed within the continuous phase. The model computes the trajectory of these particles considering factors such as inertia, hydrodynamic drag, and gravitational effects.

The choice of coupling method depends on the specific characteristics of the problem being studied. For instance, one-way coupling simplifies simulations but may not capture complex interactions. However, two-way and four-way coupling provide a more detailed understanding of the interplay between particles and fluid, making them suitable for scenarios with significant mutual influences.

The ratio between the volume fraction of the dispersed second phase (particles), denoted as ϕ_p , and the volume fraction of the continuous phase (air), denoted as ϕ_{air} , can significantly impact the outcome of the transport model.

$$\phi_p + \phi_{air} = 1 \quad (3.26)$$

In Elghobashi (1994) particle-laden turbulent flows are investigated and an overview of different coupling methods is given. In the following, a summary of the coupling methods is provided, depending on the particle volume fraction.

- **One-way coupling:**
 $\phi_p \leq 10\%$; The particles are passive and do not influence the behavior of the fluid. They are transported by the fluid, and their effects on the fluid are neglected.
- **Two-way coupling:**
 $\phi_p > 10\%$; Also known as bidirectional coupling, it accounts for the mutual interaction between the particles and the fluid. Here, the particles affect the fluid flow by introducing forces (e.g., drag, lift, and virtual mass) that impact the fluid's motion. Moreover, the particles are influenced by the fluid velocity field.
- **Four-way coupling:**
 $\phi_p > 10\%$; In some advanced modeling scenarios, it is necessary to consider additional complexities, such as particle-particle interactions. Four-way coupling extends two-way coupling by including interactions between particles themselves.

Other references like the one from Schütz et al. (2007) state that the maximum volume fraction should only be 5% to apply the one-way coupling method. In addition to the

coupling method, the way in which particles interact with surfaces should also be defined. This is done by specifying the boundary condition. Three possibilities or a mixture of these could be identified:

- **Escape:** The particle leaves the flow domain through surface (outlets).
- **Trap:** The particle is deposited on the surface.
- **Reflect:** The particle bounces off the surface (walls and inlet).

In the following chapters, insights are given for the DPM and how it is applied in ANSYS® Fluent.

Particle Size

The choice between Lagrangian and Eulerian modeling approaches depends not only on particle diameter but also on factors such as particle density and shape. When considering particles with diameters greater than $5\mu\text{m}$, gravity typically exerts a substantial influence on their motion and trajectory. However, it is essential to note that, for significantly larger particles or those with specific shapes, density can become a more critical factor. In contrast, even smaller particles might exhibit a settling velocity that cannot be completely neglected, especially when considering their density, shape, and low wind speeds.

Experimental studies, such as those conducted in Sjöholm et al. (2001), have demonstrated that particles of different sizes exhibit an imbalanced behavior due to various forces acting on them. In this study, the authors investigated the removal of particles from gases using the higher inertia of larger particles. In particular, they observed significant differences in behavior between particles smaller than $1\mu\text{m}$ and those larger than $10\mu\text{m}$. A similar phenomenon was also observed in aerosols that disperse in the air, particularly in expiratory droplets containing airborne particles smaller than $10\mu\text{m}$, as reported in Wei and Li (2015):

- $d_p \ll 5\mu\text{m}$; particles closely follow the streamlines due to their limited inertia.
- $d_p \gg 5\mu\text{m}$; particles detach from the streamlines due to their higher inertia.

However, it is important to acknowledge that the behavior of pollutants in the air is complex and can be influenced by multiple factors, including density ρ_p , which directly affects their mass m_p and inertia. As the density of the particles increases, their mass and inertia also increase, causing them to deviate from the flow streamlines.

Particle Forces

The DPM model describes particle (solid, droplet, or bubble) trajectories by considering the particle force balance, as found in the ANSYS Fluent theory guide ANSYS Inc. (2022), see Equation 3.27. This balance takes into account several factors, including the mass

of the particle m_p and density ρ_p , the acceleration of the particle at a specific time step $d\vec{u}_p/dt$, and the forces affecting the trajectory of the particle. These forces encompass the drag force \vec{F}_{drag} , gravitational force \vec{F}_{grav} , and possible other forces \vec{F}_{other} .

$$m_p \frac{d\vec{u}_p}{dt} = \vec{F}_{drag} + \vec{F}_{grav} + \vec{F}_{other} \quad (3.27)$$

The drag force \vec{F}_{drag} is calculated using the following relation:

$$\vec{F}_{drag} = m_p \frac{\vec{u}_{air} - \vec{u}_p}{\tau_r} \quad (3.28)$$

To calculate the drag force, the difference between the velocity of the surrounding fluid (air) \vec{u}_{air} and the velocity of the particles \vec{u}_p is required. Furthermore, the relaxation time τ_r is necessary, as defined in Gosman and Ioannides (1983), which represents the time required for the particle to accelerate to 63 % of the free stream velocity:

$$\tau_r = \frac{\rho_p d_p^2}{18 \mu_{air}} \frac{24}{C_d Re} \quad (3.29)$$

Here, the particle density ρ_p , the diameter of the particle d_p , the dynamic viscosity of the air μ_{air} , the drag coefficient C_d and the Reynolds number Re are essential for the calculation. The Reynolds number can be estimated with the diameter of the particles d_p as representative length, with the density and dynamic viscosity of the air ρ_{air} , μ_{air} and with the velocities:

$$Re = \frac{d_p \rho_{air}}{\mu_{air}} \cdot |\vec{u}_{air} - \vec{u}_p| \quad (3.30)$$

Using the just-provided definitions of relaxation time and Reynolds number, the drag force can be expressed as:

$$\vec{F}_{drag} = m_p \frac{18 \rho_{air} C_d}{24 \rho_p d_p} \cdot |\vec{u}_{air} - \vec{u}_p| \cdot (\vec{u}_{air} - \vec{u}_p) \quad (3.31)$$

Equation 3.32 provides the drag coefficient C_d for a spherical particle as a function of the Reynolds number Re . The coefficients a_1 , a_2 , and a_3 , which depend on the Reynolds number range, can be found in Morsi and Alexander (1972), a widely recognized source of drag coefficient formulations in particle dynamics.

$$C_d = a_1 + \frac{a_2}{Re} + \frac{a_3}{Re} \quad (3.32)$$

The gravitational force acting on a particle, denoted as \vec{F}_{grav} , can be calculated using the following equation:

$$\vec{F}_{grav} = m_p \frac{\vec{g} (\rho_p - \rho_{air})}{\rho_p} \quad (3.33)$$

where m_p is the mass of the particle, \vec{g} is the acceleration due to gravity, ρ_p is the density

of the particle, and ρ_{air} is the density of the surrounding air.

The Saffman lift force is typically used for sub-micron particle sizes and small particle Reynolds numbers. However, it is not considered in the representative scenarios of the present study, despite the aerodynamic diameter of the particle being a constant $d_p = 0.3 \mu\text{m}$, which falls into this category. The Saffman lift force is calculated using a generalization of the expression established by Saffman (1965), as described in Li and Ahmadi (1992). Other forces, such as the Magnus or rotational lift force, thermophoretic forces, Brownian force, and virtual mass force, may also exist. However, they are not applicable to the scenarios in the present study and are therefore irrelevant for calculating the trajectory of the particles.

Stochastic Tracking

The stochastic tracking model is used to predict particle dispersion based on the kinetic energy of the turbulence within the fluid phase, taking into account the influence of instantaneous turbulent velocity on particle trajectories. By default, for steady solvers, the trajectory of the particles is calculated using the mean velocity exclusively. For LES instead, the instantaneous part of the velocity field is available for each time step. This means that only the subgrid-scale fluctuations need to be modeled to create much smaller random fluctuations, as stated in Innocenti et al. (2016) and Marchioli (2017). The implementation of ANSYS[®] Fluent is in close alignment with the principles described in Gosman and Ioannides (1983). Within this framework, the DRW model, often referred to as the "eddy lifetime" model, offers insights into particle behavior as it interacts with a sequence of discrete, idealized turbulent eddies within the fluid phase. Each of these eddies is characterized by two key attributes:

- A Gaussian distributed random velocity fluctuation, denoted as u'_i .
- A specific time scale τ_e

To determine the values of u'_i that endure throughout the lifetime of the turbulent eddy, it is assumed that these values conform to a Gaussian probability distribution. This assumption is represented by the following equation.

$$u'_i = \zeta \sqrt{u'^2} \quad (3.34)$$

In this equation, ζ stands for a normally distributed random number, while the remaining part of the equation represents the local RMS (root mean square) value of the velocity fluctuations. This RMS value can be computed based on the known turbulent kinetic energy at each point in the flow, assuming isotropy:

$$\sqrt{u'^2} = \sqrt{v'^2} = \sqrt{w'^2} = \sqrt{2k/3} \quad (3.35)$$

It is worth noting that within the LES model, the velocity fluctuations are treated as equivalent in all directions. The characteristic lifetime of the eddy can be defined in two ways: either as a constant,

$$\tau_e = 2T_L \quad (3.36)$$

where T_L is computed based on Equation 3.38, or as a random variation around T_L ,

$$\tau_e = -T_L \ln(r) \quad (3.37)$$

Here, r represents a uniform random number greater than zero and less than 1, and is also determined using Equation 3.38. The option of calculating τ_e randomly provides a more realistic representation of the correlation function.

$$T_L \approx 0.15 \frac{k}{\varepsilon} \quad (3.38)$$

Parcels

In the Discrete Phase Model (DPM), parcels, which are clusters of particles, are tracked throughout the simulation domain. This approach, commonly used in atmospheric Lagrangian dispersion modeling, involves either fixing the number of particles in each parcel (constant-mass option) or varying it to maintain the specified mass flow rate and particle mass. This practice helps reduce computational efforts while ensuring sufficiently accurate results. The number of parcels significantly impacts the statistical quality of the simulation: using fewer parcels increases statistical uncertainties, whereas employing more parcels improves the results, but also increases computational effort. When choosing the number of parcels to track, it is essential to consider the distance from the release point, as the number of parcels decreases as they disperse throughout the domain.

The number of particles within one parcel, denoted as n_p , directly depends on the particle mass m_p and the constant parcel mass m_{parcel} :

$$n_p = m_{parcel} / m_p \quad (3.39)$$

In contrast, the number of parcels, denoted as n_{parcel} , can be calculated based on the mass flow rate of the particle stream \dot{m}_s , the mass of the parcel m_{parcel} , and the size of the time step Δt :

$$n_{parcel} = \dot{m}_s / m_{parcel} \cdot \Delta t \quad (3.40)$$

3.3.2. Species Transport Model

The species transport model, also known as the mixture model, is a simplified multiphase model that involves solving the Eulerian velocity field and conservation equations for

advection and diffusion. In the context of turbulent flows, it calculates the mass diffusion between two or more species using the following equation:

$$\vec{J}_i = - \left(\rho D_{i,m} + \frac{\mu_t}{Sc_t} \right) \nabla Y_i - D_{T,i} \frac{\nabla T}{T} \quad (3.41)$$

In Equation 3.41, the diffusion flux \vec{J}_i of the i -th species results from both molecular (see Fick (1855), $(\rho D_{i,m} \nabla Y_i)$) and turbulent diffusion $(\frac{\mu_t}{Sc_t} \nabla Y_i)$, with ∇Y_i representing the mass fraction of the i -th species, and ∇T indicating the temperature gradient.

The notation ∇ is the nabla operator, which represents the gradient in three dimensions. It is a vector operator that returns a vector that points in the direction of the greatest rate of increase of a scalar function, which in this case either the mass fraction of the species or the temperature. The equation also includes the local mass fraction of the i -th species Y_i , the mass diffusion coefficient of the species i in the mixture $D_{i,m}$, and the thermal diffusion coefficient $D_{T,i}$. The turbulent diffusion term is proportional to the turbulent Schmidt number Sc_t and the turbulent viscosity μ_t .

In turbulent flows, the influence of turbulent diffusion greatly outweighs that of molecular diffusion, rendering the latter negligible. Furthermore, when the temperature difference between the two species is minimal, the energy equation becomes redundant, allowing us to set the thermal diffusion coefficient $D_{T,i}$ to zero. Moreover, to simplify the species transport model, the Schmidt number Sc_t is often assumed to be a constant value, typically $Sc_t = 0.7$. However, a more recent approach proposed by Longo et al. (2020) calculates the turbulent Schmidt number locally, accounting for variations within the flow field. Applying these three assumptions to Equation 3.41 results in the following simplified form:

$$\vec{J}_i = - \frac{\mu_t}{0.7} \nabla Y_i \quad (3.42)$$

The diffusion flux \vec{J}_i is directly proportional to the turbulent viscosity μ_t and the local mass fraction of each species Y_i , indicating a strong correlation between the diffusion flux and the turbulent viscosity, as observed in simulations. Specifically, a higher turbulent kinetic energy k results in greater diffusion.

The continuity equation directly incorporates the advection of the two species by calculating the mass-averaged velocity \vec{v}_m and the density ρ_m of the mixture based on the volume fraction α_i , the density ρ_i , and the velocity \underline{u}_i of each of the $n = 2$ species:

$$\rho_m = \sum_{i=1}^n \rho_i \alpha_i \quad (3.43)$$

$$\vec{v}_m = \frac{1}{\rho_m} \sum_{i=1}^n \rho_i \alpha_i \underline{u}_i \quad (3.44)$$

The mass-averaged velocity \vec{v}_m and density ρ_m are then used in the species transport equation to account for the advection of the two species. The mass conservation equation

for the mixture model is a modification of the continuity equation, as shown in Equation 3.45:

$$\frac{\partial}{\partial t} (\rho_m) + \nabla \cdot (\rho_m \vec{v}_m) = 0 \quad (3.45)$$

This equation considers the conservation of mass for the entire mixture, where the velocity of the mixture \vec{v}_m and the density of the mixture ρ_m are calculated based on the volume fractions α_i , the densities ρ_i , and the velocities \underline{u}_i of each species i , assuming a total of two species ($n = 2$). The momentum Equation 3.6 is modified to account for the presence of multiple species in the mixture:

$$\begin{aligned} \frac{\partial}{\partial t} (\rho_m \vec{v}_m) + \nabla \cdot (\rho_m \vec{v}_m \vec{v}_m) = & -\nabla p + \nabla \cdot \left[\mu_m \left(\nabla \vec{v}_m + \nabla \vec{v}_m^T \right) \right] \\ & + \rho_m \vec{g} + \vec{F} - \nabla \cdot \left(\sum_{i=1}^n \alpha_i \rho_i \vec{v}_{dr,k} \vec{v}_{dr,k} \right) \end{aligned} \quad (3.46)$$

The modified Equation 3.46 includes additional terms that represent the drag force caused by the movement of each species relative to the mixture. These terms are expressed in terms of the volume fraction α_i , the density ρ_i , and the velocity of each species $\vec{v}_{dr,k}$. The remaining terms of the equation, such as the pressure gradient, the forces of the body due to gravity, and the external forces \vec{F} , are analogous to those of the original equation. The viscosity term now represents the dynamic viscosity of the mixture μ_m , which is a function of the viscosities of individual species and their respective volume fractions.

Equation 3.47 shows the expression for the dynamic viscosity μ_m of the mixture, which is calculated as a weighted sum of the dynamic viscosities of the individual species μ_i , where the weight factor is the volume fraction of each species α_i .

$$\mu_m = \sum_{i=1}^n \alpha_i \mu_i \quad (3.47)$$

On the other hand, Equation 3.48 gives the drift velocity $\vec{v}_{dr,k}$ of species k relative to the previous species $k - 1$ in the series, where \vec{v}_m represents the mass-averaged velocity of the mixture:

$$\vec{v}_{dr,k} = \vec{v}_m - \vec{v}_{k-1} \quad (3.48)$$

The energy equation is not presented in this chapter due to the simplification applied to the simulations in the context of this dissertation.

3.3.3. Comparison

Both the Euler-Lagrange and Euler-Euler approaches utilize the discrete phase model and the mixture model, which are available in ANSYS® Fluent. Each approach has its own set of benefits and limitations. Table 3.1 provides a summary of the features of both models:

Table 3.1.: Characteristics of different transport modelling approaches

Tracking Type	Euler-Lagrange	Euler-Euler
modeling type	discrete phase model	mixture model
computational efforts	high	low
uncertainty	high, depends on parcel amount	low
particle aerodynamics	high flexibility	low flexibility
size limitations	particle size distribution	small particles only
particle interactions	agglomeration & breakup	neglected
volume fraction	smaller 12 %	not limited
coupling	two-way-coupling	one-way-coupling
deposits	feasible	not feasible

This table highlights several differences between the two approaches, including computational efforts, uncertainty, particle aerodynamics, size limitations, particle interactions, volume fraction, coupling, and deposits.

Advantages and Limitations

The Euler-Lagrange model provides several distinct advantages over the Euler-Euler model. These advantages include:

- **Agglomeration and Breakup Modeling:** The Euler-Lagrange model allows the modeling of particle agglomeration and breakup in addition to the calculation of particle trajectories. This feature is especially valuable when dealing with scenarios in which particles tend to stick together or fragment.
- **Variable Particle Size Distribution:** This model offers the flexibility to consider variable particle size distributions (PSDs), enabling the simulation to account for the wide range of particle sizes that exist in real-world applications. As a result, it can provide more accurate representations of particle behavior under varying conditions.
- **Consideration of Particle Properties:** Particle inertia and gravitational forces can significantly influence particle trajectories. The Euler-Lagrange model is well suited for scenarios involving larger particle diameters and substantial particles, where these forces play a pivotal role in dispersion.
- **Deposit Assessment:** The Euler-Lagrange model is suitable for simulating scenarios where particle deposition on surfaces or within a system needs to be assessed.

By tracking particle trajectories, the model can provide valuable insight into the locations and patterns of particle deposition, which is crucial to understanding and mitigating issues related to fouling, erosion, or contamination in industrial or environmental settings.

However, it is important to note that the Euler-Lagrange model is not without limitations and disadvantages. Some key considerations include:

- **Computational Demands:** Simulating a large number of discrete particles can be computationally intensive, particularly when modeling complex, three-dimensional turbulent flows. This can lead to increased simulation time and resource requirements.
- **Limitations in Dilute Flows:** Although the Euler-Lagrange model excels in scenarios with larger particles and higher particle loads, it may not be the best choice for extremely dilute flows, where particle-particle interactions are negligible.
- **Limited Insight into Continuous Phase:** The model's primary focus is on the dispersed phase (particles), which can provide less insight into the continuous phase (fluid) dynamics. If a comprehensive understanding of the entire flow field is necessary, a combined Eulerian-Lagrangian approach might be more suitable.
- **Complex Setup:** Setting up Euler-Lagrange simulations, especially in cases involving intricate physics, can be challenging and may require extensive calibration and validation to ensure accurate results.

These considerations underscore the need to carefully evaluate the specific requirements of a simulation before selecting any of these two models. After careful investigation of the scenarios investigated in this dissertation, it was determined that the Euler-Lagrange model is the most appropriate approach; more details on this choice can be found in Chapter 4.3. Under the premise that particles reach larger diameters and a distribution with different behavior shall be modeled in the simulation, the Lagrangian particle model is the preferred model. Also, when the particles are occupying an increased amount of the volume fraction, then the choice of the Lagrangian particle model might be beneficial, since the coupling between discrete solid phase and continuous fluid phase will influence the continuous fluid phase.

4. Comprehensive Methodology Evaluation

In this chapter, a comprehensive evaluation of the methodology to perform large-eddy simulations for realistic scenarios is carried out. The methodology serves as the basis for all subsequent analyses in this dissertation and encompasses several critical components, including geometry setup, meshing strategy including a refinement, the setup for boundary conditions, solver settings, simulation approach, and the assessment of atmospheric turbulence. The objective is to systematically assess each facet of this methodology to ensure its robustness, reliability, and suitability for the research at hand. The methodology presented here applies to the further assessments described in Chapters 4 and 5.

4.1. Geometry

The geometry comprises two main components: CAD data representing buildings and obstacles within the CERN area and topographical data. The topographical data, dated February 25, 2020, are obtained in raster format (ASCII grid data) and offer an altimetric accuracy of 15 centimeters and a planimetric accuracy of 50 centimeters, see Figure 4.1. This topographic information is taken from the "Le Système d'Information du Territoire de Genève" (SITG) website Direction de l'information du territoire (2022).

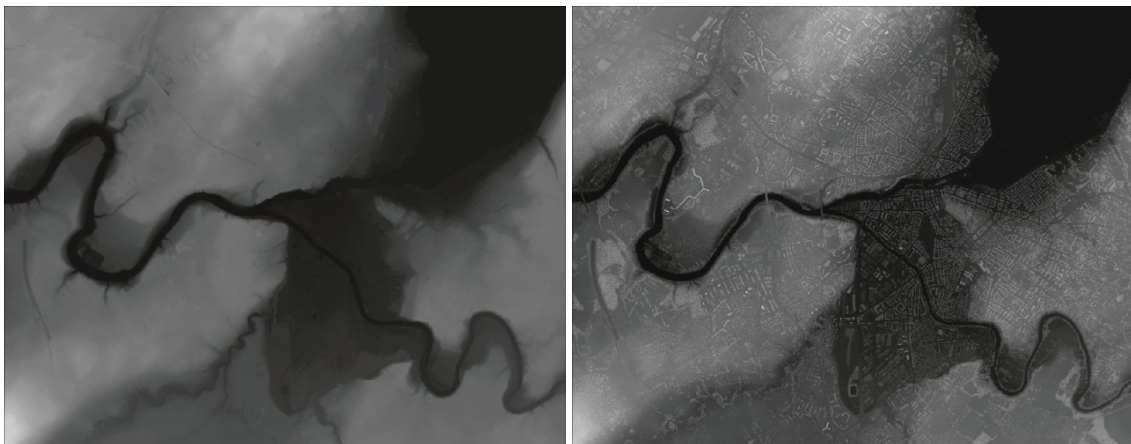


Figure 4.1.: Exemplary terrain data shown for the Geneva city center: digital terrain model on the left and digital elevation model on the right. Source: Direction de l'information du territoire (2022)

The buildings, on the other hand, are modeled in CAD and integrated into the terrain. This integration is crucial to achieving high-quality representations of buildings with sharp edges. Importantly, since these data sources are distinct and independent of each

other, they can be easily manipulated prior to the meshing process. This flexibility allows for the addition or removal of buildings, which might be necessary due to factors such as new construction projects or the removal of existing structures.

4.1.1. Shape and Size

The geometry takes the form of an octagon, a deliberate choice to ensure that, for each 45 degree angle, there is at least one inlet boundary perpendicular to the inlet surfaces. In addition, the edges of the domain are strategically located at a considerable distance from the release point. This arrangement ensures a substantial separation between the boundaries and the release point, eliminating the influence of boundary conditions on pollutant dispersion in the near-field of the release location.

In studies including generic street canyons, as for example performed by Zheng et al. (2021), the direction of the wind is often restricted to a single direction, resulting in smaller domains. However, this enables the application of periodic boundary conditions, treating the flow as homogeneous in the span. Most best-practice guidelines, such as the one presented in COST Action 732 (2007), provide recommendations for domain size in the context of RANS simulations. Zheng et al. (2021) confirmed in their work the applicability also for large-eddy simulations.

Optimal simulation outcomes are attained when the release point is located within a 1-kilometer radius of the domain center, enabling effective tracking of pollutant dispersion across a considerable distance. The domain size and configuration are determined by several factors, including the release type (continuous, short-term, puff) and the area affected by the plume. In the upcoming investigations, the domain spans an area of $A_{domain} = 7.5, km^2$, with a maximum longitudinal extent of 3 kilometers, facilitating the exploration of multiple release scenarios within CERN surroundings. The CERN site measures 1.8 kilometers in one direction and one kilometer in the other.

It is important to note that this configuration necessitates defining a larger number of cells due to the expansive area, resulting in higher computational costs. This disagrees with the recommendations of Zheng et al. (2021), who recommend a domain size of:

- Domain width - 2.5H (H = roof height of the street canyon)
- Domain height - 7.5H
- Upstream domain length - 5H
- Downstream domain length - 10H

As emphasized by Zheng et al. (2021), it is of paramount importance to minimize the blockage ratio of the flow, with an ideal upper limit that does not exceed 13.3%. However, in this study, depending on the location of the release point within the domain, the minimum recommended values for blockage and domain size, as proposed by Zheng et al. (2021), are significantly exceeded.

The decision to model multiple potential release points simultaneously, along with the simplification of employing a single geometric model for various simulations, substantially reduces the simulation effort. Furthermore, the objective was not only to represent a small section of the CERN site but to encompass the entire area potentially affected.

The types of releases in this work vary between ground-level and elevated fire exhaust gas releases, as well as elevated dense gas releases. The primary focus is on the area around the release point, with a maximum distance of 400 meters. To accommodate this, an additional length of 500 meters was added to create an intermediate area, ensuring flow normalization. This intermediate area, shown in Figure 4.2, is strategically centered around the release point to facilitate the precise follow-up of the flow. This means that any terrain features, such as hills, are not smoothed out but are retained as obstacles, generating wake fields downstream.

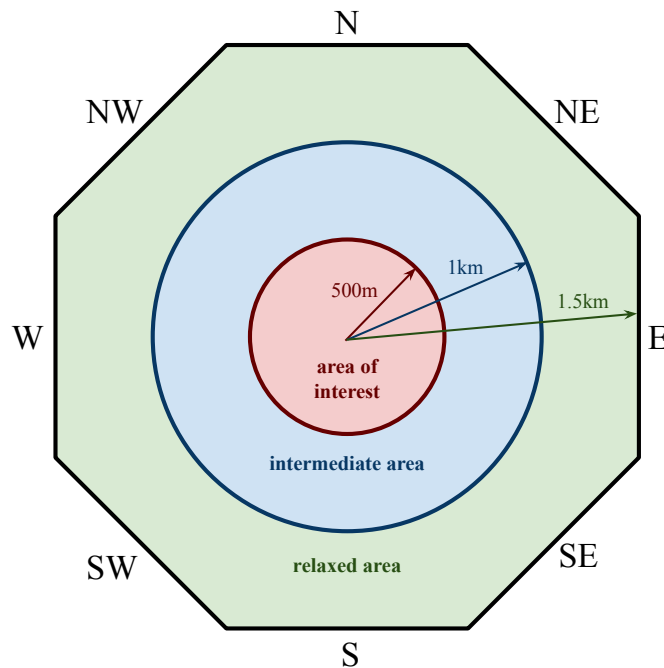


Figure 4.2.: Bird's eye view of the domain extends and its subdivision in areas: area of interest, intermediate area, relaxed area.

The domain relaxation process extends from the outer edges of the intermediate area to the domain boundaries, as shown in Figure 4.2. This process, known as geometry relaxation, focuses on adjusting the altitude of the terrain near the edges. The objective is to improve numerical stability and create a consistent inflow and outflow area, thus preventing flow acceleration or deceleration. Detailed insights into this process will be provided in Chapter 4.1.3.

4.1.2. Topography Models

Two different topography models were used to account for the variations in elevation of the terrain within the chosen domain size. The terrain data, which covers an area of nine square kilometers, was extracted from the SITG website Direction de l'information du territoire (2022). In cases requiring larger areas, terrain data must be extracted in multiple files and can subsequently be merged using tools like Python. In particular, the website offers two distinct terrain models for selection:

- **MNS - Modele Numerique de Surface:**
This refers to the Digital Terrain Model (DTM), which provides ground altitudes without any obstructions (such as buildings, trees, hedges, etc.).
- **MNT - Modele Numerique de Terrain:**
This is the Digital Elevation Model (DEM), encompassing all terrain features, including obstacles.

Both grid datasets offer area-averaged heights with an altimetric accuracy of 15 cm and a planimetric accuracy of 50 cm. As an illustration, Figure 4.3 displays the CERN site between Meyrin (Switzerland) and Saint-Genis-Pouilly (France). These topography models were obtained from the SITG website in a grid raster format of 0.5 meters Direction de l'information du territoire (2022).

To prepare the terrain data for integration into CAD/CFD tools, it is essential to triangulate the grid format. This triangulation can be achieved through various options, including Python, for instance, by using the "numpy2stl" package or by utilizing the Feature Manipulation Engine (FME), a versatile geospatial extract, transformation, and load software platform.

Once the ASCII grid data are successfully converted into stereolithography data (.stl) through this process, it becomes readily compatible with ANSYS[®] SpaceClaim and Fluent for further utilization.

An illustrative example, although not the final selection, is detailed in the script presented in the Appendix A. This Python-based script manipulates the terrain altitude, as visually represented in Figure 4.3. In this particular case, the terrain relaxation process took place at a certain distance from the edges, resulting in an elevation adjustment to an average of 460 meters. The relaxation length was configured at 500 meters, which means the distance over which the altitude modifications extended from the edges. The raw digital elevation model (DEM) is visually demonstrated on the left side of Figure 4.3 and the relaxed DEM is shown on the right side.

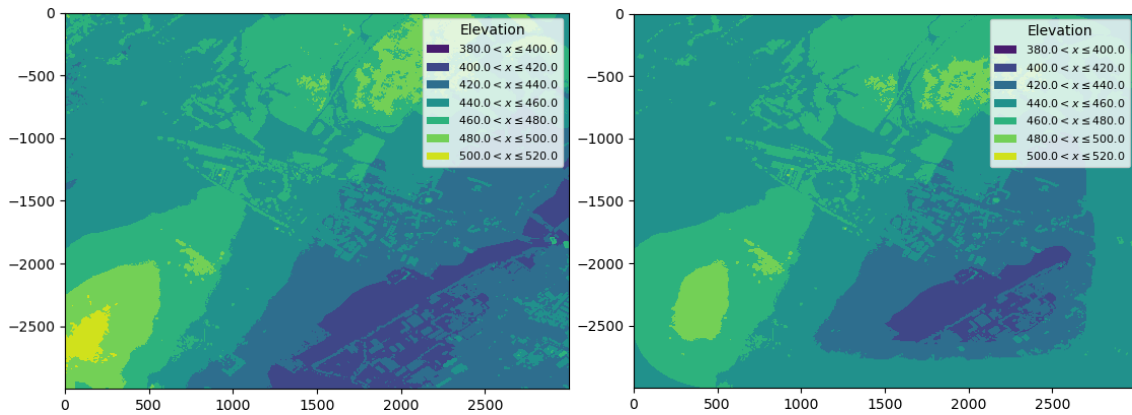


Figure 4.3.: Raw DEM (left) and relaxed DEM (right).

4.1.3. Relaxation

The selected approach differs from script-based modifications and instead involves CAD-based manipulations. Specifically, the geometry relaxation was executed within the relaxed area of the domain, ensuring uniform altitudes at the domain's sides, including inlets and outlets.

In this CAD procedure, solid ground was added or removed with a linear slope and circular shape, effectively altering the terrain altitude from a diameter of 2 to a diameter of 3 km from the center of the domain, as depicted in Figure 4.4. This slope maintains a maximum angle of 5.1 degrees to facilitate a smooth transition of airflow from the exterior to the interior of the domain and vice versa. Notably, all the domain's edges are set to the same altitude.

To achieve the desired terrain altitude, the CAD manipulation process involves adding volume if the actual terrain height is lower than the target value and, conversely, removing volume if the actual terrain height exceeds the desired altitude.

Here is an overview of the necessary steps.

1. Import of triangulated surface data into ANSYS[®] SpaceClaim.
2. Create a volume extending from the imported surface to sea level (0 m).
3. Adding two revolved volumes with a slope of 5.1 degrees, descending/ascending from the desired relaxation height, here 460 m, from the maximum diameter (3 km) to the minimum diameter (2 km), specifically in areas requiring relaxation.
4. Remove volume in regions where the terrain altitude is excessively high.
5. Adding volume in regions where the terrain altitude is too low.
6. The surface is now prepared for subsequent stages.

An alternative approach involves modifying the terrain before importing it into ANSYS[®] SpaceClaim, as demonstrated in Figure 4.3. The script for this procedure can be found in the Appendix A. In this method, the terrain is processed in Python and adjustments are made on the basis of the distance from the domain edges.

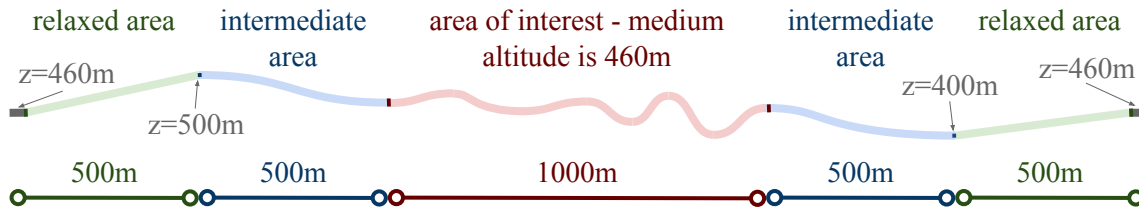


Figure 4.4.: Relaxation of the geometry shown in a cross-section through the full terrain.

A cosine function can be applied to uniformly modify the terrain along all edges. The height change, denoted as Δz , is calculated as the difference between the real and target heights, multiplied by one. In mathematical terms, this adjustment is represented as $\cos(x_{max,min}, y_{max,min}) = 1 \cdot \Delta z$.

As one moves closer to the center of the domain, the function gradually reduces its manipulation factor (cosine). When the distance of 500 meters from the edge is reached, the function values become $\cos(x_{max,min} \pm 500, y_{max,min} \pm 500) = 0 \cdot \Delta z$. This approach allows for a smooth transition from the domain's edges to its center.

If implemented correctly, this method offers a simpler alternative to CAD manipulation. The type of function (linear, logarithmic, sine, etc.), the distance from the edges for relaxation, and the relaxation height can be readily adjusted. However, it is important to note that this approach becomes more complex when dealing with an octagonal shape. In such cases, the manipulation must be performed not only in the x and y directions but also in their combinations. Employing a circular pattern from the domain center may help achieve effective relaxation for octagonal shapes.

In this section a more detailed explanation of the terrain relaxation steps using CAD is provided. Refer to Figure 4.5, which illustrates all the solid objects used to manipulate the geometry. The upper part of Figure 4.5 shows the terrain in green, solidified up to sea level, and solid blue, as previously mentioned. In the lower part, the terrain has already been modified in step one (green), and a red solid is introduced.

The initial step involves removing the intersection of both solids from the terrain, effectively reducing ground elevation in certain areas to attain a maximum altitude of 460 meters along the edges. This process involves the removal of terrain material at specific locations, and the slope chosen for this modification is 5.1 degrees. The second step entails adding ground to the existing terrain where the terrain's altitude falls below the desired value. In this step, the two solids can be easily merged to achieve the necessary modifications.

Geometry relaxation was performed to ensure that the volume flow within the area of interest (the inner red region in Figure 4.4) closely matches the volume flow defined at the inlets. Additionally, it was essential to guarantee that the velocity near the edges starts at zero, close to the ground. This is needed to make sure that the solver works in a stable way and functions for the velocity profile can be applied.

This approach was necessitated by the specific definition of boundary conditions (as

detailed in Chapter 4.3.1) and the principle of mass conservation, as articulated in Equation 4.1. According to this principle, the flow through the geometry would accelerate ($u_2 > u_1$) with a decreasing cross-section ($A_2 < A_1$) or decelerate with an increasing cross-section ($A_2 > A_1$). Such variations could adversely affect the atmospheric boundary layer profile and consequently the dispersion patterns, the pollutant concentration, and other results obtained.

It should be noted that the relaxation altitude was chosen relatively high, at $z = 460$ meters, compared to the average altitude of the CERN Meyrin site (ranging from 420 to 460 meters), as depicted in Figure 4.6, which provides an illustration of the terrain and building altitudes.

$$\begin{aligned} \dot{m}_1 &= \dot{m}_2 \\ \rho_1 \cdot \dot{v}_1 &= \rho_2 \cdot \dot{v}_2 \\ \rho_1 \cdot u_1 \cdot A_1 &= \rho_2 \cdot u_2 \cdot A_2 \end{aligned} \quad (4.1)$$

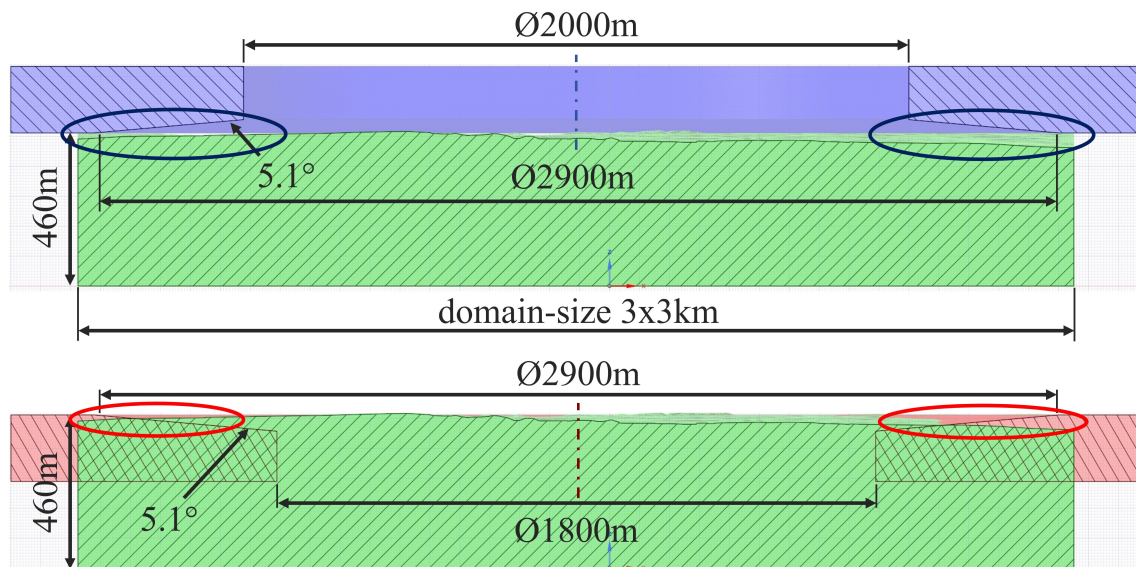


Figure 4.5.: Cross-sectional depiction of the domain center illustrating the two stages of the relaxation procedure: 1. At the top, a blue volume is used to remove overlapped ground from the underlying green solid (not visible in the cross-section). 2. At the bottom, a red volume is merged with the green terrain extracted from the surface STL file to achieve the desired relaxation height of 460 meters along the domain's edges. Both solids feature a 5.1-degree slope.

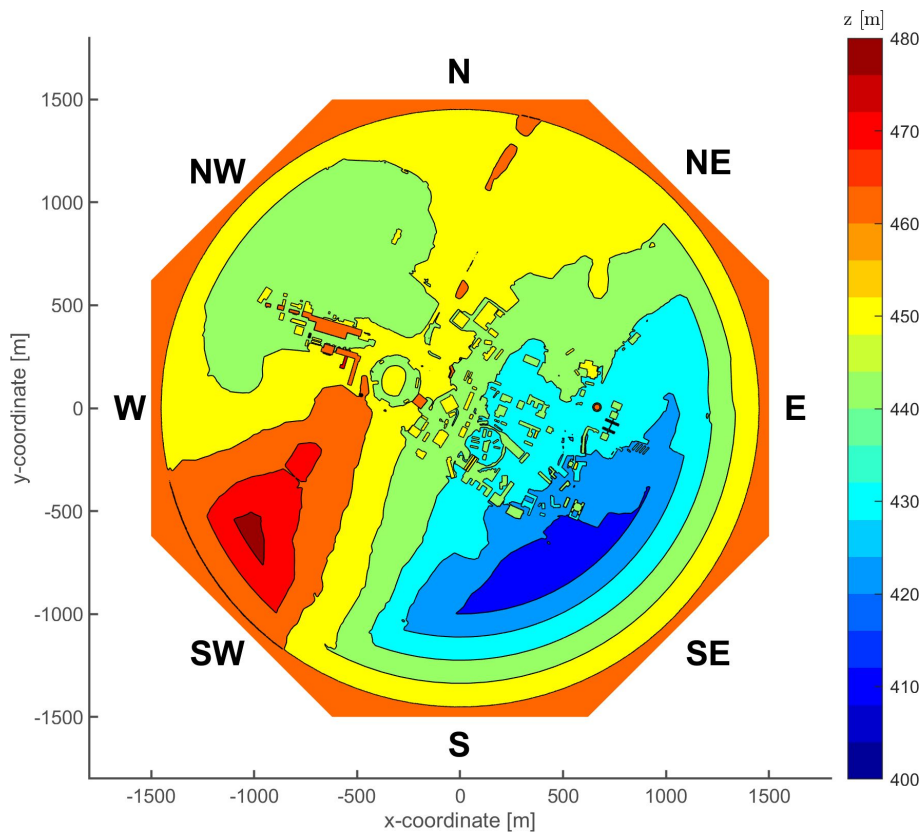


Figure 4.6.: Contour plot showing the altitude of the final geometry including the relaxation and the elevation of the terrain and the buildings.

4.1.4. Modelling Challenges

In the realm of computational fluid dynamics and environmental modeling, several modeling challenges can arise when simulating complex domains and phenomena. These challenges encompass diverse aspects, from the interaction of flow patterns with geometric shapes to the consideration of various terrain and land-use characteristics.

This section delves into the modeling hurdles encountered and the strategies employed to tackle them effectively. From managing backflow issues to optimizing domain shapes and ensuring the fidelity of building and vegetation representation, a comprehensive understanding of these challenges is vital for successful simulations in the field of environmental modeling.

Backflow is a phenomenon in which the flow direction deviates from the expected wind direction, often observed at the pressure outlet of a computational domain. When backflow occurs, it can lead to violations of mass conservation, rendering the simulation results inaccurate. This issue can have a significant impact on the flow dynamics, affecting not only regions near the boundaries but also the center of the computational domain. Consequently, preventing backflow at the edges of the domain is of paramount importance. One potential factor contributing to backflow is relaxation of the domain edges. Addressing this challenge requires careful consideration: The domain edges should not

undergo excessive relaxation to lower altitudes, and the transition from the central area to the sides should be as gradual as possible. While increasing the relaxation length may offer a solution, it is crucial to strike a balance, as overly large geometries may hinder the goal of achieving a small mesh size with uniform grid resolution.

Another significant challenge lies in the selection of the domain shape. When opting for a quadratic shape instead of an octagonal one, issues related to backflow may emerge over the full computational domain, worsening over time. This phenomenon becomes evident when geometry boundaries are placed in cardinal wind directions, but the flow needs to be simulated in ordinal directions, such as North East, North West, South East and South West, and is exemplified in Figure 4.7. In the case of a quadratic geometry, problems arise when introducing fluctuations to the mean velocity at the inlet, leading to a potential backflow issue at the pressure outlets, as indicated by the red arrow in Figure 4.7. This challenge can be attributed to the proximity of the velocity-inlet and pressure-outlet boundaries, which can disrupt the flow. In contrast, such issues do not typically arise with an octagonal shape, where at least two boundaries act as transition points for the flow, obviating the need for turbulent fluctuations at these boundaries. This is illustrated by the blue arrows in Figure 4.7. An alternative approach involves segmenting the inlet boundary into three parts and introducing fluctuations primarily in the segments farthest from the pressure outlets to mitigate the risk of inducing backflow.

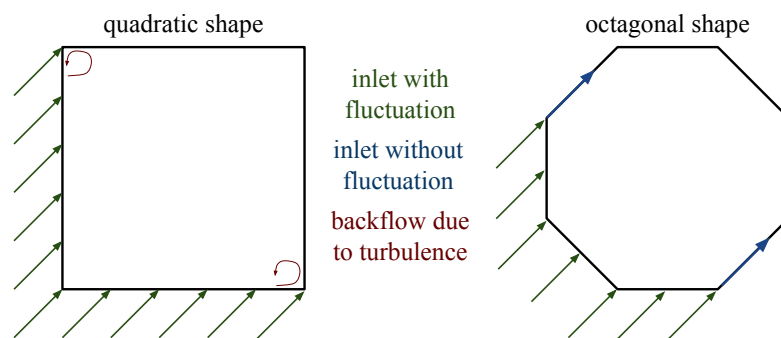


Figure 4.7.: Choice of geometry shape resulting in backflow issues.

Selecting the right level of detail in simulations presents another notable challenge. Attempting to replicate the precise surface structures of buildings, including features such as corrugated iron sheets, concrete walls, and intricate elements such as ladders, lamps, or roof ventilation systems, would require a considerable increase in surface mesh resolution. In far reaches beyond the area of interest, it is advisable not to opt for excessively small cell sizes. Doing so would lead to a significant increase in computational workload without commensurate benefits, as high mesh resolution is unnecessary for managing inflow and outflow at the domain boundaries.

It is imperative to model each building using CAD because relying solely on elevation data from a Digital Elevation Model (DEM) to simulate obstacles is insufficient for precise simulations. Extensive research, such as the studies conducted by Wilson (1979),

has highlighted the importance of accurately representing sharp buildings with upright walls to simulate the dynamics around structures. These considerations encompass phenomena such as frontal vortex, recirculation cavity, wake cavity, and roof wake boundary, as illustrated in Figure 4.8. Using a DEM model alone does not capture these dynamics accurately. Instead, an algorithm capable of detecting abrupt variations in terrain height and adjusting the nodes to create straight building walls should be employed, especially if the DEM is used as a primary model. Without this correction, when triangulating the ASCII grid data, the modeled walls will inevitably deviate from reality due to the combination of building height and grid resolution. To provide an example, with a grid resolution of 0.5 m and a building height of 3 m, the resulting angular misalignment would be approximately 9.5 degrees, significantly affecting the flow pattern compared to buildings with upright walls. For taller structures, such as a 100 m high building with the same grid resolution, the angular misalignment becomes less consequential, approximately 0.3 degrees.

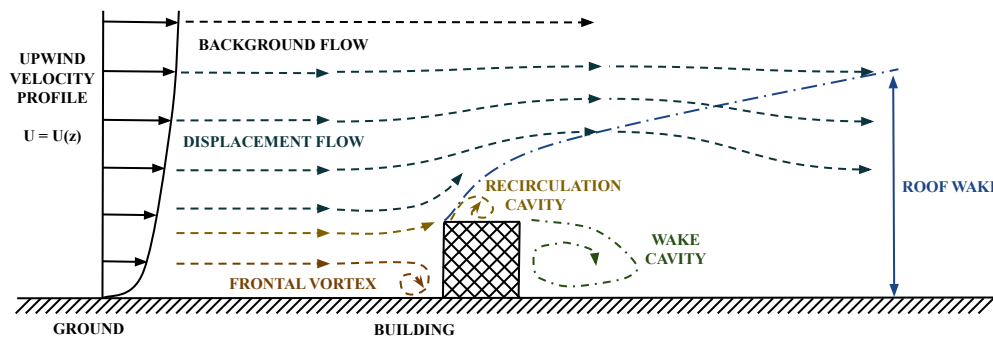


Figure 4.8.: Flow around a sharp-edged building, based on Wilson (1979).

Forests or woodlands contribute to increased shear and turbulence within the atmospheric boundary layer compared to flat land, as observed in Chaudhari et al. (2016). Consequently, when larger areas contain woodlands, vineyards, or other vegetation near the release point, it is advantageous to model them as surface roughness elements or porous regions. Attempting to achieve a geometric and numerical resolution of the effects of forests and forests on the flow field for large domains is impractical. Instead, employing porous media representations for these areas stands out as the most efficient method. In particular, studies that use large-eddy simulation (LES), such as those mentioned in Nebenführ and Davidson (2015) and Chaudhari et al. (2016), have reported reasonable agreement with the actual conditions. Although these studies correctly predict mean velocity over the forest canopy, they face challenges in estimating turbulent kinetic energy, especially resolved turbulent kinetic energy with respect to lateral and vertical variances, which often appear under-predicted, as noted in Nebenführ and Davidson (2015). The suggested remedy, according to Nebenführ and Davidson (2015), is to employ finer mesh resolutions, but this approach may not be feasible for large domains due to the associated computational efforts. In future studies, it would be worthwhile to explore the impact of

forests and their role in the dispersion of pollutants, both upstream and downstream of a release point.

Moreover, Adedipe et al. (2020) emphasize the importance of accurately estimating parameters such as Leaf Area Density (LAD) or Leaf Area Index (LAI) when assessing the impact of forests and forests on the flow field. Turbulence levels are observed to increase up to a certain forest density before subsequently decreasing. However, due to the higher computational demands and the lack of precise parameters for LAD, the decision was made not to model woodlands as a porous medium in this study, as doing so would introduce complexity and uncertainties into the simulation. It is also worth noting that the forests with the most significant impact on flow, compared to vineyards and grassland, are relatively scarce around the CERN site and are located far from the two potential release points. A bird's-eye view of the CERN Meyrin site and its surrounding areas is presented in Figure 4.9. The CERN Meyrin site is flanked by grasslands and forests to the north, the villages of Meyrin and Saint-Genis-Pouilly to the east and west, and vineyards dominate the southern landscape. Among the most relevant wind directions, both in terms of probability and impact, are North-East, South-West, and South, as depicted in Figures 4.9 and 4.24. Given the combined factors of potential release points and the prevailing wind directions, the presence of grasslands and vineyards creates relatively low ground roughness values, making the inclusion of vegetation impact less significant in the geometry dataset.

If the release point were located closer to the forest or if the forests were considerably larger, exerting a significant impact on particle dispersion, an alternative approach might involve employing uniformly spaced solid obstacles or increasing the surface roughness in these areas. This configuration would result in reduced mean velocity in the lower layer and increased turbulent kinetic energy. Alternatively, a Digital Elevation Model (DEM) could be employed for the outer domain to impede air flow through the forest, thereby generating turbulence and reducing mean velocity in those areas.



Figure 4.9.: CERN Meyrin site and its neighboring environment. Forest areas are indicated in green, while the two potential release points under investigation are marked in red.

4.2. Meshing Strategy

This chapter describes the meshing process for the final mesh, which has been generated using ANSYS[®] Fluent Meshing. Before defining the final mesh, a comprehensive mesh refinement study was conducted, as detailed in Chapter 4.2.2. This study involved an evaluation of the meshing parameters to ensure optimal performance of the selected mesh. In particular, the size of the computational domain significantly influences the mesh size, even when employing a modest ground-mesh resolution. Therefore, this chapter delves into the crucial aspects of achieving accurate flow predictions while maintaining computational efficiency.

During the meshing procedure, ANSYS[®] Fluent Meshing adapts its initial layer of cells to the geometrical surface, effectively creating a numerical mesh on the modeled geometry. For ground surfaces, the only simplification needed is a curvature approximation for round shapes, reducing the number of cells required. It is worth noting that other software tools, often designed for research purposes rather than commercial engineering applications, utilize hexagonal meshes or Cartesian grids, which may not accurately represent the geometry's surface, especially for round shapes, resulting in a staggered representation.

4.2.1. Mesh Type

The selection of cell types plays a crucial role in the meshing process, affecting the quality, flexibility, and computational efforts of the mesh. In the context of atmospheric boundary layer flows, the choice of cell type is of particular significance. This work considers three primary cell types commonly used in computational fluid dynamics: hexahedral, tetrahedral, and polyhedral cells.

Hexahedral meshes are a popular choice in research due to their favorable computational efficiency compared to other cell types, as documented in Wang et al. (2021). The efficiency comes from their fewer faces and nodes relative to polyhedral cells, making them well suited for straightforward geometries that align with the predominant flow direction. According to Wang et al. (2021) a polyhedral mesh requires approximately 1.58 times more computational time than a hexahedral mesh, while a tetrahedral mesh requires about 1.29 times the computational time for a hexahedral mesh with an equivalent cell count.

However, the application of a hexahedral mesh can be impractical for complex geometries because of its limited flexibility. In contrast, polyhedral meshes offer significantly more flexibility. Even in the case of very basic geometries, the total cell count can be reduced by approximately 65%, while maintaining the same minimum cell size on specific surfaces and the same stretching ratio. This finding is derived from a comparative analysis presented in reference Wang et al. (2021), which evaluated the total cell count needed to simulate channel flow with a single obstacle. The study in Wang et al. (2021) also demonstrated that both hexahedral and polyhedral meshes exhibit comparable performance. Given the reduced number of polyhedral cells in this conclusion (where $n_{poly} = 0.358 n_{hexa}$), and the resulting lower computational time required to achieve similar solutions ($t_{poly} = 0.57 t_{hexa}$), polyhedral meshes appear advantageous for handling complex geometries.

Furthermore, it is essential to consider that hexahedral meshes result in larger cells in the same locations compared to polyhedral meshes due to their decreased flexibility. To facilitate meaningful comparisons between different cell types, a viable approach is to maintain consistent computational efforts or total cell counts. With this approach, the results become more directly comparable and it becomes evident that polyhedral meshes may outperform hexahedral meshes. For instance, doubling the number of polyhedral cells, while preserving the same computational efforts as hexahedral meshes, may lead to a better-resolved solution, particularly near walls, and enhance the accuracy of polyhedral meshes compared to hexahedral ones. The key findings of the study conducted by Wang et al. (2021), where the quality of the mesh, computational efforts, profiles and contours of the mean velocity and kinetic energy of turbulence, the characteristic length of flow features, and spectral distribution of the turbulence kinetic energy are analyzed, are summarized below for polyhedral meshes:

- **Polyhedral mesh is the most economical** (to retain the minimum cell size):
 - 35.8% polyhedral cells compared to hexahedral cells
 - 21.3% polyhedral cells compared to tetrahedral cells
- **No boundary-layer mesh needed, resulting in:**
 - Improved orthogonality
 - Enhanced skewness
 - Better prediction of vortices in the vicinity of buildings
- **Polyhedral mesh is recommended due to:**
 - Low computational efforts
 - High accuracy
 - High flexibility

The results of the numerical simulations conducted by Wang et al. (2021) have been validated through wind tunnel experiments. The study concludes that the advantages of the polyhedral mesh outweigh its disadvantages. Its flexibility, particularly in the handling of complex geometries, offers potential savings in computational effort while retaining the same minimum surface cell size as other meshing types. The primary requirements and challenges for the mesh are outlined in the list below.

Flexibility:

- The ability to adapt well to the geometry surface and smoothly transition between rough and fine grids is crucial. This includes:
- Maintaining a small minimum mesh size near the ground and around buildings to capture vortex generation.
- Implementing refinement areas around the urban region of the simulation domain to adequately resolve built areas.
- Ensuring refinement near the release point to capture the interaction of the flow with the buildings.
- Creating smooth transitions between different regions within the simulation domain.

Accuracy:

- For large-eddy simulation (LES) in particular, maintaining aspect ratios of cells close to one at all times is recommended. Smooth transitions play a critical role in obtaining accurate results.

Flow alignment:

- Aligning hexahedral cells in the flow direction is vital. Even slight deviations can yield different solutions. The polyhedral mesh, with its flexible shape, is more suitable.
-

In summary, the selected software and meshing approach offer the advantage of accurately representing geometric features such as corners and building curvatures within the mesh. The mesh fully resolves the entire domain, ensuring smooth transitions. Compared to other mesh types, such as immersed boundary meshes or hexahedral meshes, the polyhedral mesh provides superior resolution and more seamless transitions.

4.2.2. Mesh Refinement Study

The objective of this investigation is to evaluate the sensitivity of the simulations to the resolution of the computational mesh and to establish an optimal balance between precision and computational efficiency. The assessment focuses primarily on key flow characteristics and pollutant concentration values, integral parameters studied using large-eddy simulation (LES). Specifically, mean velocity and turbulent kinetic energy in the monitoring planes are critical flow characteristics that guide the selection of the final meshing procedure, detailed in Chapter 4.2.3.

The dispersion of pollutants released from the ATLAS surface building is simulated using the Discrete Phase Model (DPM), as presented in Chapter 3.3.1. Two wind directions, north-east and south, were considered to analyze the required mesh size in the outer regions of CERN and the mesh size between buildings. The evaluation focuses on quantities derived from the instantaneous velocity field, necessitating caution when comparing turbulent kinetic energy values for different mesh sizes. Finer meshes generally resolve smaller vortices, while coarser meshes model these vortices, given their inability to resolve finer-scale features in LES. This distinction is crucial in interpreting and comparing turbulent kinetic energy values. Additionally, the Lagrangian particle tracking method provides a partial basis for comparison, considering that too few tracked parcels, especially at large distances from the release point, may lead to parcel movement strongly influenced by fluctuating velocity terms within specific cells, impacting statistical significance.

The mesh refinement study encompassed five distinct mesh resolutions, spanning from 2.2 million polyhedral cells to 21.6 million polyhedral cells:

- Very coarse: 2.2 million cells
- Coarse: 4.3 million cells
- Medium: 9.8 million cells
- Fine: 16.1 million cells
- Very fine: 21.6 million cells

The mesh resolution, global sizing controls, and surface sizing functions were precisely adjusted to achieve the desired mesh refinement level, whether finer or coarser. Table 4.1 offers a summary of the meshing properties associated with the sizing functions. Please consider inspecting details of the scoped size controls in Appendix B. Global scoped sizing controls for the mesh were configured with specific values: The minimum cell size

is set to half a meter, the maximum cell size, primarily observed near the top boundary, ranges from 50 to 100 meters, and the global growth rate varies between 1.1 and 1.2.

Table 4.1.: Mesh refinement properties for five levels of mesh refinement.

<i>refinement level</i>	<i>growth rate</i>	<i>ground-special</i>	<i>ground-inner</i>	<i>ground-outer</i>	<i>buildings-special</i>	<i>buildings</i>	<i>boi-buildings-special</i>	<i>boi-buildings</i>	<i>wall</i>	<i>edges</i>
very coarse	1.2	0.5m	5m	10m	0.5m	3m	0.5m	10m	100m	0.5-100m
coarse	1.2	0.5m	3m	6m	0.5m	3m	0.5m	6m	100m	0.5-100m
medium	1.2	0.5m	1.5m	3m	0.5m	1.5m	0.5m	4m	50m	0.5-50m
fine	1.15	0.5m	1m	3m	0.5m	1.5m	0.5m	3m	50m	0.5-50m
very fine	1.1	0.5m	1m	3m	0.5m	1m	0.5m	3m	50m	0.5-50m

The most important control of scope size in Table 4.1 is the ground-inner control together with the boi-buildings, which are, respectively, a surface control and a volumetric control in the inner area. These parameters play a pivotal role in determining the resolution of the mesh within the built area of the ground domain, exerting a strong influence on the overall mesh size. Alongside boi-buildings, which specifically refine the vicinity of the buildings, these controls collectively govern the mesh resolution in the inner area. Notably, the very fine mesh achieves a high-resolution flow representation with a minimum cell size of one meter, whereas the very coarse mesh maintains a minimum cell size of five meters on the same surface.

Throughout the mesh refinement study, continuous monitoring of pollutant concentration and fluctuating velocities was conducted during the simulation. The collected data encompassed the mean velocity integrated in time for the three components of the velocity vector and the turbulent kinetic energy at each location on the monitoring planes, as illustrated in Figure 4.38. The detailed methodology for data analysis is expounded in Chapter 4.5.3. Subsequent procedures were then applied to these quantities for each cell in the monitoring planes.

- A comparative analysis was conducted on the data collected from each monitoring plane to identify localized differences or similarities between different mesh sizes.
- Quantities, including velocity and turbulent kinetic energy, were averaged over the entire plane size to evaluate global variations and similarities as mesh sizes were altered.
- Normalization of quantities was performed using the solution obtained for the very fine mesh as a reference to obtain relative errors.

To assess the various levels of mesh refinement, the initial step involved the identification of localized differences in the monitoring planes, strategically placed at specific

distances, as illustrated in Figure 4.38. Notable variations were observed mainly in concentration values, revealing significant deviations in plume position and maximum values across the five refinement levels, as illustrated in Figure 4.10.

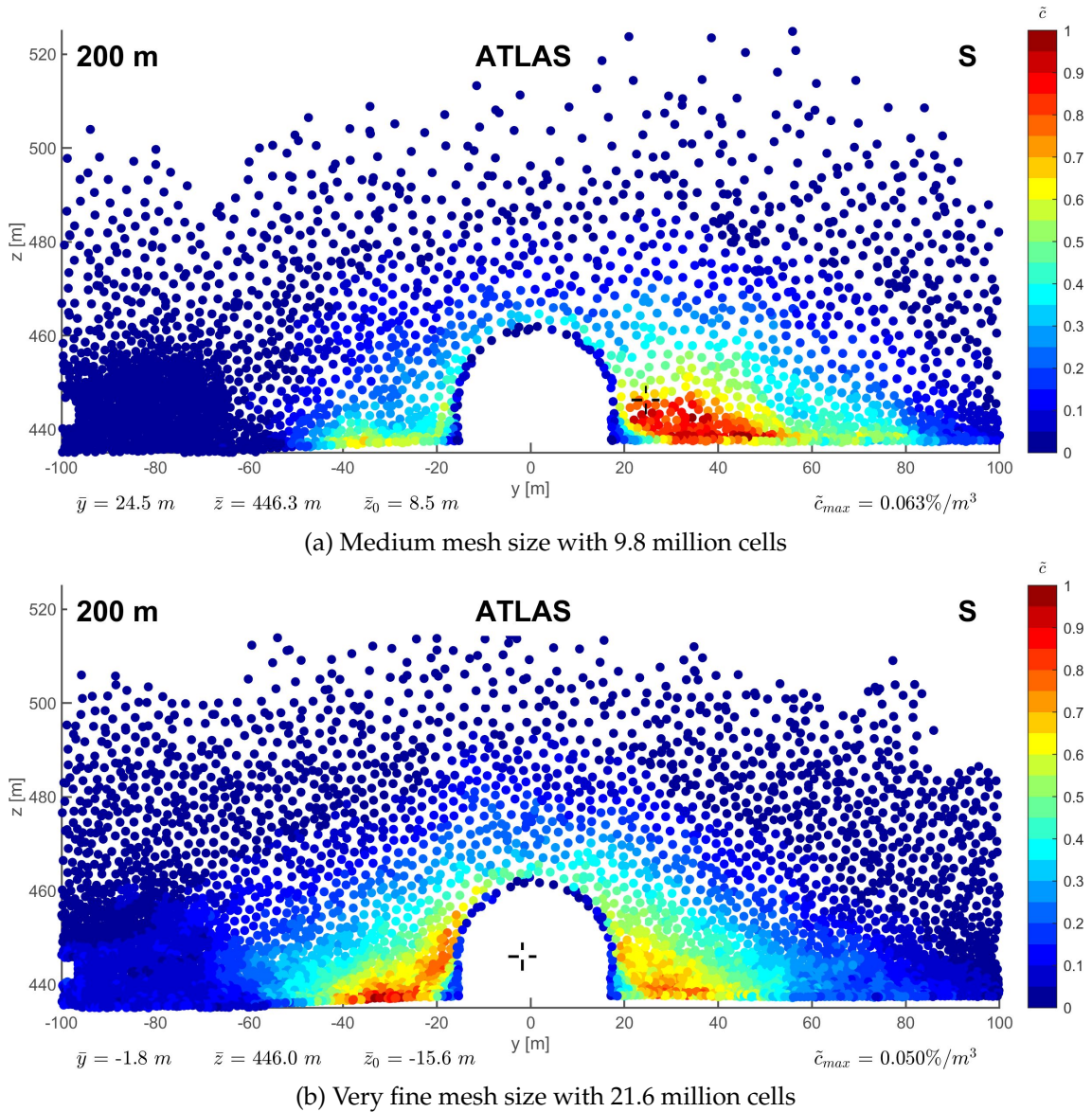


Figure 4.10.: Scatter plots showing the normalized maximum concentration $c_{max,n}$ at the cross-wind monitoring planes at $x = 200$ m distance from the release point and with wind blowing into south.

The discrepancy between the coarser mesh (top) and finer mesh (bottom) manifests itself in the plume distribution across the CERN Globe monitoring plane. In the coarser mesh, the plume is predominantly situated on the right side, while the finer mesh presents a more symmetric plume distribution on both sides of the CERN Globe.

This difference arises from the inadequacy of time averaging in the pollutant tracking process, particularly with respect to large eddies that influence particle movement over an extended period, notably near the release point. These large eddies are not fully aver-

aged during the release period, leading to disparities in plume distribution. Insufficient parcel release time and quantity further hinder statistically accurate evaluations of pollutant concentrations, introducing uncertainty into the solution due to the limited number of parcels released.

For short release durations, the results are highly sensitive to the positions of large eddies in the domain. Consequently, for puff releases or brief periods, it is advisable to conduct multiple releases at different times to estimate the uncertainty of the solution and its impact on the results. In this dissertation, release durations range from 20 minutes to 1 hour, still classified as short-term releases. Thus, the findings herein establish a robust foundation for practical investigations of flow around buildings in the atmospheric boundary layer.

Another notable observation from Figure 4.10 is the variation in concentration values between cell neighbors. This phenomenon stems from the choice of the pollutant dispersion method, with the mesh refinement study using the DPM model. The uncertainty in the concentration predictions for distant cell neighbors is influenced by the total number of tracked parcels. In a worst-case scenario, where only a single parcel containing the entire release mass is tracked, the parcel's trajectory could follow a specific direction, potentially resulting in an unrealistically high concentration in just one cell of the cross-wind planes. This outcome would not align with the concept of turbulent dispersion.

Although a higher number of released parcels enhances statistical accuracy, this approach is constrained by elevated computational costs and cannot completely eliminate the inherent Lagrangian nature of statistical uncertainty. In contrast, species models, as described in 3.3.2, primarily carry the statistical uncertainty of larger eddies moving along the release point and eliminate the uncertainty associated with the limited number of tracked parcels. Consequently, the species-transport model emerges as a more reliable and preferred method for pollutant dispersion in the ABL. However, the advantages of Lagrangian particle tracking methods are still evident in scenarios involving aerodynamic lift forces or gravity forces influencing the trajectory of pollutants.

However, fully eliminating the described effect while maintaining a low computational effort poses a challenge. To address this, the Eulerian species transport model can be employed, effectively eliminating the statistical dependency introduced by the DPM. In light of this, for subsequent investigations, the pollutant tracking method was changed from DPM to the species transport model. This change not only reduces the impact of statistical uncertainties, but also provides a more robust and reliable representation of pollutant dispersion.

The results of the pollutant release scenario, coupled with the variations in pollutant concentration observed in the air, underscore the importance of recognizing and addressing these challenges in simulation studies. Highlights the importance of choosing an appropriate pollutant dispersion model that aligns with the specific characteristics and goals of the simulation, ensuring more accurate and reliable results.

It was observed that increasing the number of injected parcels by one order of magnitude, from 60 to 600 million parcels, in the Lagrangian particle tracking method could alleviate the challenges described earlier. However, this approach proved impractical due to a significant escalation in computational demands, extending the simulation duration from several days to weeks on a high-performance cluster (HPC) until completion. Furthermore, extending the simulation time to facilitate a thorough comparison of concentration values, even for short-term releases or puff-release scenarios, presented practical limitations.

Figures 4.11 and 4.12 confirm a substantial variation in concentration values by $\pm 50\%$ across different levels of mesh refinement, a variation not attributable to the size of the mesh. Consequently, it was concluded that trying to compare concentration values using the DPM model in ANSYS® Fluent for short-term releases with a low number of tracked parcels is not a viable and meaningful approach.

Quantities such as mean velocity and turbulent kinetic energy, derived from continuously available instantaneous velocity, converge to a stable level after numerous iterations. Differences in the averaged data over the entire plane and the identification of maximum values reveal a clear trend, particularly by showcasing the behavior of these quantities with a finer mesh. It is crucial to prioritize the validation of flow simulations before validating dispersion models, especially in scenarios involving complex flows. Therefore, the mean velocity values and turbulent kinetic energy are averaged over all cross-wind monitoring planes. These planes, which are consistent in size across all refinement levels, employ a regular grid to evaluate these quantities. An overall comparison of the results of the mesh refinement study in the north-east and south wind directions is illustrated in Figures 4.11 and 4.12, respectively.

The evaluated quantities are normalized with respect to the highest grid resolution, which serves as the reference case and is determined by the results obtained from the very fine mesh. These quantities encompass the maximum concentration $c_{max,n}$, the spatially averaged mean velocity in the monitoring plane $u_{ave,n}$, the spatially averaged turbulent kinetic energy in the monitoring plane $tk_{ave,n}$, and the maximum turbulent kinetic energy $tk_{max,n}$, each as a function of the distance x from the release point.

To achieve normalization, the maximum concentration is derived by dividing the time-integrated maximum concentration ($\tilde{c}_{max,lv}$) of each mesh refinement level by the integrated maximum concentration ($\tilde{c}_{max,vf}$) of the very fine mesh. Similarly, the normalization process is applied to the other quantities. Consequently, the very fine mesh exhibits a normalized value of one for each quantity and position, serving as the baseline for comparison. The following equations outline the methodology used to derive these normalized variables.

$$c_{max,n} = \frac{\tilde{c}_{max,lv}}{\tilde{c}_{max,vf}} \quad (4.2)$$

$$tke_{max,n} = \frac{\bar{k}_{max,lvl}}{\bar{k}_{max,vf}} \quad (4.3)$$

The remaining parameters undergo a similar normalization process, although with some differences in the approach for each parameter. For the maximum turbulent kinetic energy and maximum concentration, only the locations on each cross-wind plane where these quantities reach their maximum are considered for evaluation. In contrast, the mean velocity \bar{u} and the turbulent kinetic energy \bar{k} are initially averaged over each crosswind plane, yielding surface average values $\bar{u}_{ave,lvl}$ and $\bar{k}_{ave,lvl}$ for each distance and refinement level.

This approach is adopted to preserve the significance of the maximum values, which should not be diluted by plane averaging. Instead, for mean velocity and turbulent kinetic energy, full-plane averaging is performed to assess the resolved turbulence kinetic energy and the consistency of mean velocity across different mesh refinement levels. Initially, differences are identified at specific locations among different mesh refinement levels, followed by an investigation into the overall performance on each plane near the release point, which is crucial for pollutant dispersion.

Equations 4.4 and 4.5 illustrate the normalization process for the mean velocity $u_{ave,n}$ and the turbulent kinetic energy $tke_{ave,n}$:

$$u_{ave,n} = \frac{\bar{u}_{ave,lvl}}{\bar{u}_{ave,vf}} \quad (4.4)$$

$$tke_{ave,n} = \frac{\bar{k}_{ave,lvl}}{\bar{k}_{ave,vf}} \quad (4.5)$$

Figure 4.11 presents the results regarding the parameters discussed above plotted against the distance x from the release point for all mesh refinement levels. As discussed earlier, the normalized maximum concentration $c_{max,n}$ (top left graph) fails to converge with finer meshes due to the pollutant tracking method selected as Lagrangian particles and a very limited number of injected parcels. The concentration values for the coarser meshes show variations of up to $\pm 50\%$ compared to those obtained with the very fine mesh. In particular, the concentration graph does not show a clear correlation.

The graph on the top right of Figure 4.11 illustrates the results for the normalized averaged mean velocity $u_{ave,n}$. It should be mentioned that the total height of the monitoring planes varies from smaller distances from the release point $x = 40\text{-}200\text{ m}$, and is defined with a height $z = 100\text{ m}$, while for larger distances from the release point $x = 300\text{-}400\text{ m}$ the height is $z = 150\text{ m}$. In Figure 4.11, it was found that the overall averaged values exhibit a significant dependency on the resolution of the grid. Although the lower segment displays variation across mesh refinement levels, an approximate 5% difference in mean velocity values persists. Notably, the very coarse and coarse grid resolutions diverge from the predictions of the medium, fine, and very fine meshes. The medium mesh

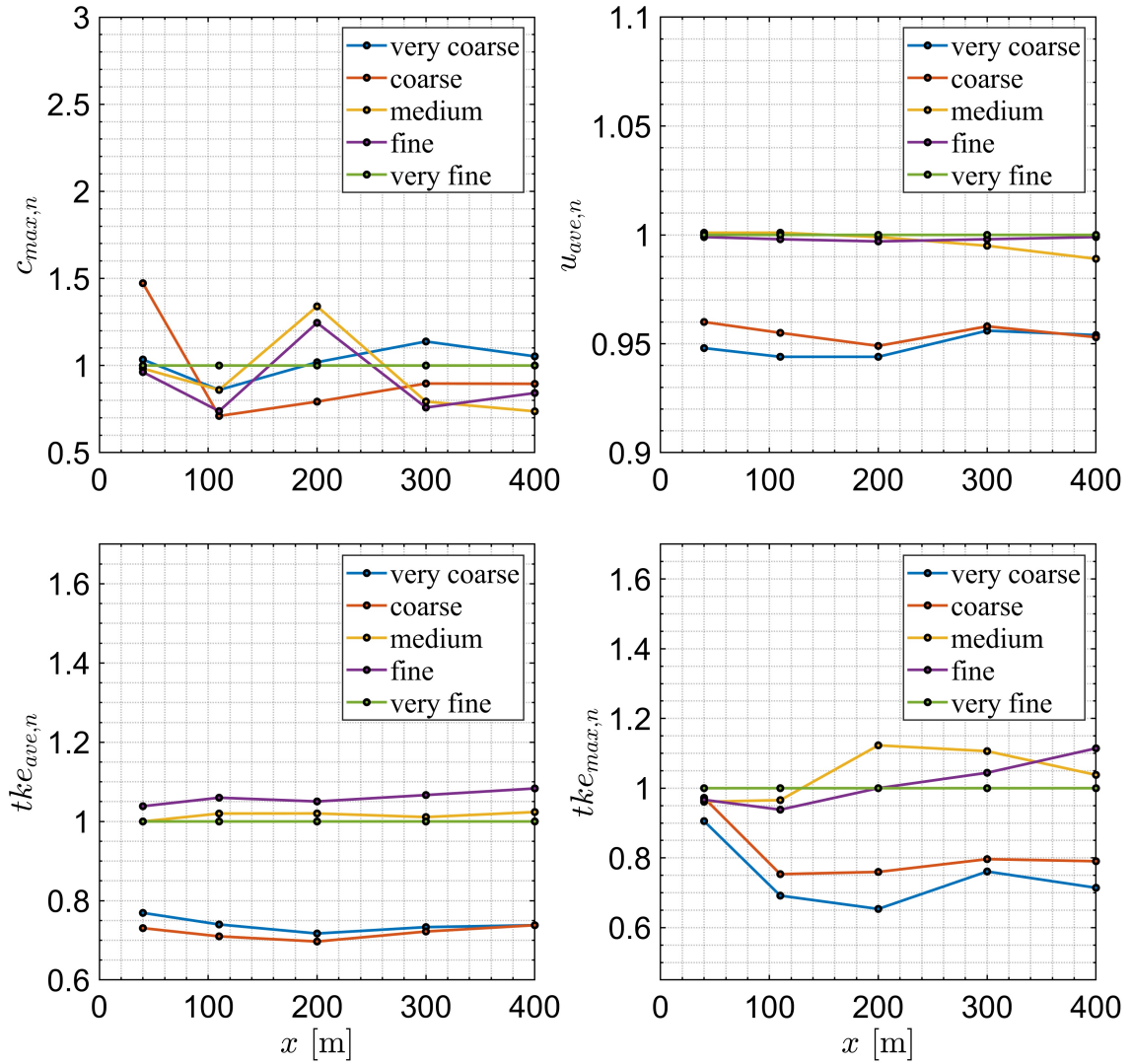


Figure 4.11.: The comparison illustrates the normalized maximum concentration $c_{max,n}$, normalized plane-averaged mean velocity $u_{ave,n}$, normalized plane-averaged turbulent kinetic energy $tke_{ave,n}$ and normalized maximum turbulent kinetic energy $tke_{max,n}$ as a function of the distance from the release point x . These parameters are depicted for monitoring planes positioned in the north-east, where the wind blows in this direction.

shows a slight deviation of 1% from the fine and very fine mesh results at a distance of $x = 400$ m from the release point. This observation suggests that the mean velocity field converges for the medium or fine mesh, indicating a good grid resolution of the immediate vicinity of the release point for these refinement levels.

In the bottom-left graph of Figure 4.11, the normalized average turbulence kinetic energy $tke_{ave,n}$ is shown. Notably, there is a pronounced deviation in the observed normalized turbulence kinetic energy for very coarse and coarse meshes compared to medium, fine and very fine meshes, which display similar performances. This consistency suggests a comparable resolution of vortices across these refined meshes. The uniformity in resolution could be attributed to the identical grid resolution on the ground, as indicated

in Table 4.1, specifically in the surface control (ground-outer). The lack of variation in grid resolution from medium to very fine meshes, along with a similar ground growth rate (1.1 to 1.2), probably contributes to the similarity in the resolved vortices. The average turbulence kinetic energy typically undergoes changes from coarser to finer meshes, especially when there is interaction with upstream obstacles. However, it is essential to note the nature of large-eddy simulation (LES), where vortices can only explicitly be resolved down to the grid resolution. In LES, the kinetic energy of the turbulence tends to be higher for finer grid resolution than for coarser ones due to subgrid-scale modeling. Thus, comparing the averaged turbulence kinetic energy provides only partial insights into the performance of the meshes.

In the bottom right graph of Figure 4.11, the normalized maximum mean turbulent kinetic energy $tk_{e_{max,n}}$ is presented. In close proximity to the release point, where each level's grid resolution is defined with the same cell size of 0.5 m for the surface of the ATLAS building (as indicated by "ground-special" and "boi-buildings-special" in Table 4.1), the observed maximum values are comparable. However, as the distance from the release point increases, the discrepancies become more pronounced. At farther distances (100-400 m), medium, fine, and very fine meshes predict similar values for $tk_{e_{max,n}}$, while for coarse and very coarse meshes, the disparity is more significant. This underscores a direct correlation between the maximum turbulent kinetic energy and the cell size. Similarly to the discussion above relating the averaged turbulent kinetic energy, the resolution of vortices also influences the maximum turbulent kinetic energy. Considering this relationship and the mesh definitions in the planes, it can be inferred that the ground sizing function for "ground-outer", which is set to 3 m for the medium, fine, and very fine meshes, directly impacts the values obtained on the monitoring planes.

In Figure 4.12, the results of the calculated quantities corresponding to the wind blowing towards the south are depicted. In the top-left graph, the normalized maximum concentration values $c_{max,n}$ are presented. Similarly to the results discussed earlier concerning the wind blowing toward the northeast direction, here, too, the comparison of maximum concentration values evaluated on the monitoring plane does not facilitate a comparison across different refinement levels. This limitation stems from the uncertainty associated with the Lagrangian tracking method and the use of only a limited number of injected parcels.

The normalized mean velocity $u_{ave,n}$ in the direction of the south wind, depicted in the top right graph of Figure 4.12, demonstrates minimal variation between different levels of mesh refinement. Alterations in mesh conditions are primarily applied to the "ground-inner" surface, "buildings", and "boi-buildings", the refinement body for buildings. In contrast to the north-east wind direction, where the "ground-outer" surface size remains consistent across medium, fine, and very fine grid resolutions, adjustments are made to all parameters mentioned above based on the refinement level for the south wind direction. Particularly noticeable is the impact on the very coarse grid resolution, where

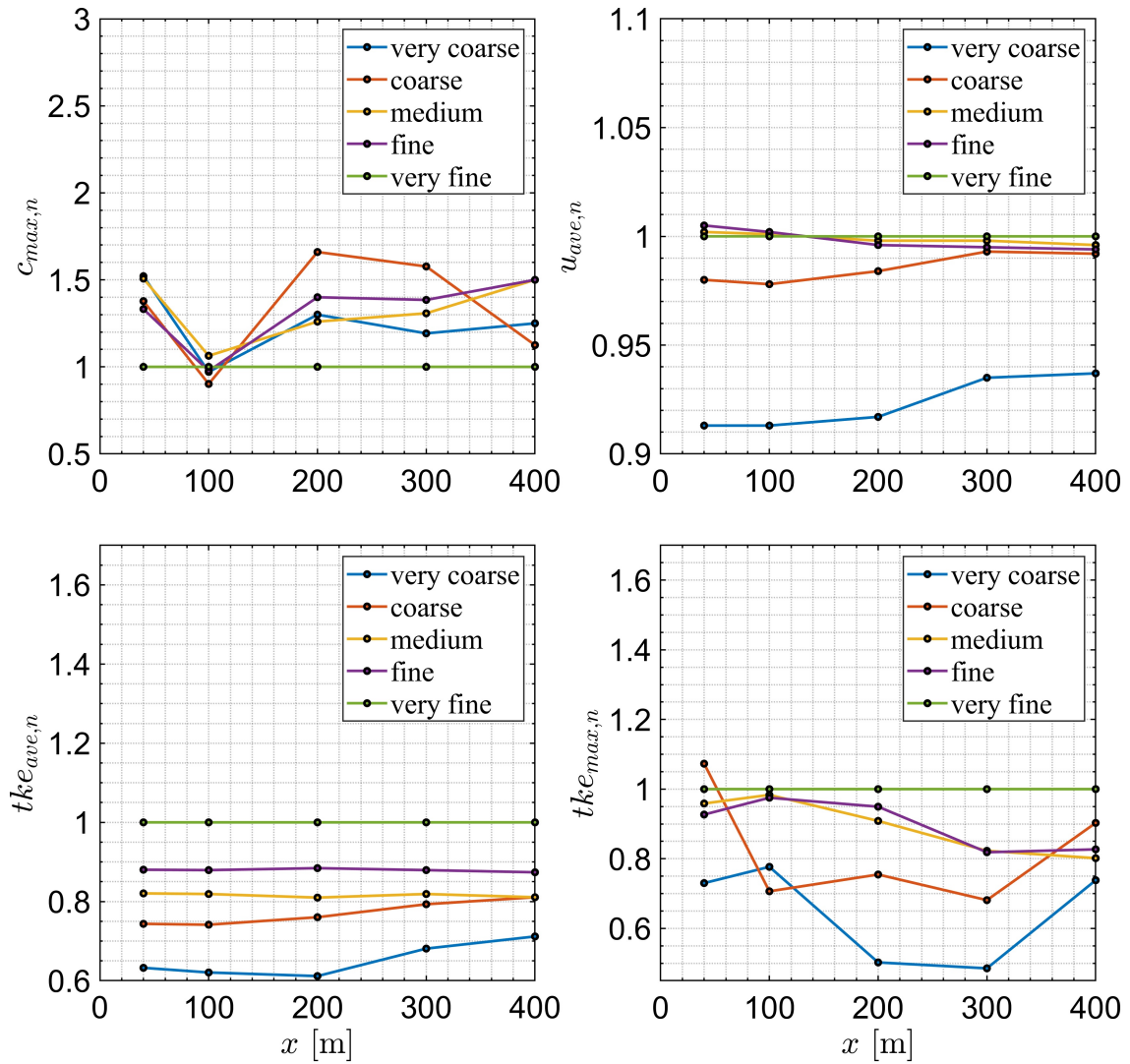


Figure 4.12.: The comparison illustrates the normalized maximum concentration $c_{max,n}$, normalized plane-averaged mean velocity $u_{ave,n}$, normalized plane-averaged turbulent kinetic energy $tk_{e_{ave,n}}$ and normalized maximum turbulent kinetic energy $tk_{e_{max,n}}$ as a function of the distance from the release point x . These parameters are depicted for monitoring planes positioned in the south, where the wind blows in this direction.

the mean velocity registers significantly lower (6-9%) than for the medium, fine, and very fine grid resolutions. The coarse grid exhibits a slight deviation, especially within the distances $x = 40-200$ m. Consequently, the results suggest that the medium mesh size begins to accurately predict the mean velocity with only slight deviations (0.5%).

In the bottom-left graph of Figure 4.12, the results of the normalized plane-averaged turbulent kinetic energy $tk_{e_{ave,n}}$ in the south wind direction are shown. A noticeable discrepancy is evident among the results obtained from various mesh refinements. Higher values of plane-averaged turbulent kinetic energy are observed with finer grid resolutions. Finer meshes have the capability to resolve smaller-scale turbulent structures, a feat beyond the capability of coarser meshes. Consequently, coarser meshes tend to underes-

timate the turbulent kinetic energy. In large-eddy simulation (LES), where the small-scale turbulent motions are not explicitly resolved, subgrid-scale (SGS) models are employed to represent their impact, if any, on the flow.

In the bottom right graph of Figure 4.12, the normalized maximum mean turbulence kinetic energy $tke_{max,n}$ is depicted for the different levels of mesh refinement with wind blowing in the south direction. Near the release point, the observed maximum values are quite similar for medium, fine, and very fine meshes. However, as the distance from the release point increases, the disparity between the mesh refinements becomes more pronounced. This can be attributed to the lower resolution of the grid at the positions of the monitoring planes. The very fine mesh exhibits the highest turbulence kinetic energy, since it has the capability to resolve even small-scale vortices.

The turbulence kinetic energy graphs, depicting both the maximum value and the plane-averaged value, illustrate that finer mesh sizes in large-eddy simulation (LES) lead to the resolution of smaller vortices and therefore to more energy. This prompts the question of how much turbulence kinetic energy resolution is necessary to accurately predict the turbulent diffusion of pollutants. More precisely, the question is when do concentration values, which are time-integrated on monitoring-planes and monitoring-points, converge to a certain threshold. Unfortunately, this question remained unanswered in the mesh refinement study conducted. The limitation was due to the choice of the pollutant tracking method. Instead of employing the Lagrangian particle model with its restricted number of tracked parcels, the Eulerian scalar method for species dispersion should have been utilized. This alternative method would have eliminated the uncertainty associated with Lagrangian particles traversing the domain. The impact of the grid resolution for turbulent diffusion is therefore not answered.

Advection, which serves as the primary mechanism for pollutant transport, converges noticeably at medium to fine grid resolutions, depending on the wind direction and the associated grid resolutions. Advection, intricately linked to mean velocity, emerges as the second crucial parameter that influences the dispersion of the pollutant. In terms of turbulent diffusion, finer grid resolutions typically result in a more accurate dispersion of pollutants. This is because smaller vortices, influenced by grid resolution, play a significant role in determining pollutant trajectories, leading to a more realistic dispersion pattern. Failing to fully resolve these turbulent eddies can lead to reduced spreading of pollutants, making finer grid resolutions generally more conservative in their predictions. The results obtained for the maximum and plane-averaged turbulent kinetic energy ($tke_{max,n}$ and $tke_{ave,n}$) highlight the importance of refining specific areas critical for accurately predicting flow dynamics. Especially near the emission source, where peak velocity, wake regions, and turbulent eddies exert a strong influence, precise resolution is essential to accurately simulate pollutant dispersion.

4.2.3. Final Selected Mesh

This chapter serves as an introduction to the meshing procedure, highlighting the key factors that must be considered. The choices made are based on the mesh refinement study, which is described in the previous section. The focus here is on addressing the elements and considerations necessary for successful meshing and setting the stage for a comprehensive understanding of the meshing strategy.

In wall-resolved large-eddy simulations (WRLES), the precise modeling of flow near walls and boundary layers is crucial. However, applying WRLES to atmospheric boundary layer flows can be cost-prohibitive because of the extensive domain size. To illustrate a domain of 7.5 square kilometers, achieving a dimensionless wall distance of $y_+ = 1$ and using cells with an aspect ratio equal to one would lead to a cell size of 1 millimeter in the ground layer, resulting in a total count of 7.5 trillion cells. Even if the aspect ratio for the initial cell layer is increased to 100 (although not advised, according to Wang et al. (2021)), the number of cells would still be impractical at 750 million, given a domain depth of 500 meters, the number of cells needed would increase even more with an assumed growth rate of 1.2 in the vertical direction.

In ABL flows, it is therefore common to model the ground layer rather than resolving it. A detailed geometric model that includes grass is not needed and is also not recommended. The approach followed in this work includes a subdivision of the domain into several zones, where cell sizes are varied, and the so-called size functions are defined prior to the mesh generation.

As illustrated in Figure 4.13, the terrain is divided into two segments: ground-inner (light green) and ground-outer (dark green). These surfaces represent the ground in the inner and outer zones, respectively. The buildings are shown in gray, and special buildings, such as the ISOLDE facility in red and the ATLAS surface building in blue, are distinguished from standard buildings. These special buildings serve as release points for pollutant dispersion scenarios, either in the building stack or through specific doors for the use of the fire brigade in case of an emergency.

The two separate terrain parts facilitate independent meshing. The choice of these terrain segments is greatly influenced by the built environment. The inner zone surrounds the buildings and potential release points with a minimum distance of 500 m to ensure that the resolution of the mesh is fine enough to produce meaningful results, as shown in Figure 4.13. This resolution is essential for accurately modeling the dispersion of pollutants, considering that the wind directions might change for the same scenario and that the proximity to release points should be better resolved than surrounding areas. The inner zone is a crucial area for the pollutant dispersion and tracking simulations because it has the biggest impact on the solution. To accurately capture the details in the central part of the domain, most size controls are applied in this area.

The inner zone plays an essential role in the refinement procedure, serving as a reference point for the volumetric refinement zone, as shown in Figure 4.14. One of these

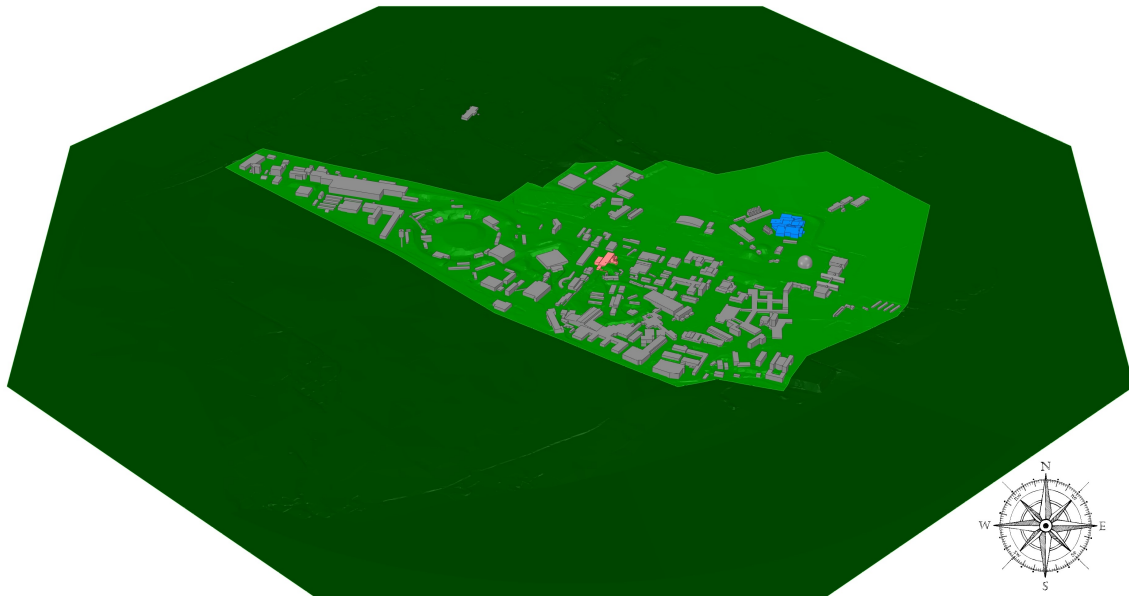


Figure 4.13.: Ground of the domain is divided into two parts: ground-inner (light green) and ground-outer (dark green). Buildings are represented in grey and special buildings (ISOLDE facility in red and ATLAS surface building in blue).

refinements, known as BOI-buildings, extends up to an altitude of 480 meters above sea level. This corresponds to a height range of 30-70 meters above ground, depending on the terrain's elevation. Consequently, the control of polyhedral cell size is maintained up to this specified elevation above the ground.

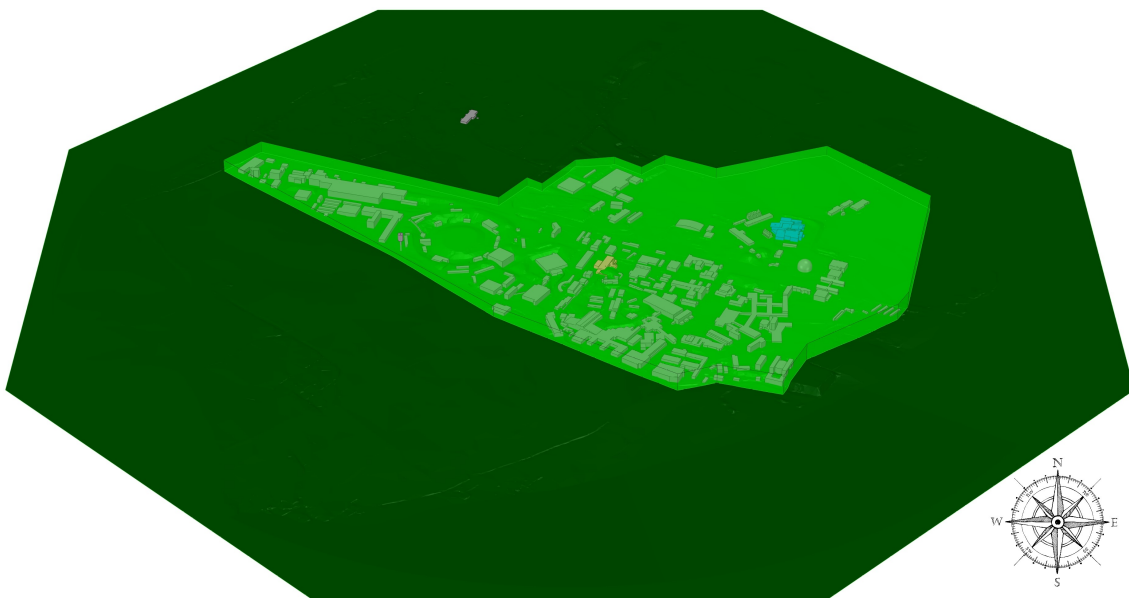


Figure 4.14.: Relaxed terrain with buildings and BOI-buildings, shown as light green body with a top altitude of $z = 480$ m.

Two additional specialized volumetric refinement zones, referred to as BOI-buildings-special, were delineated around the potential release points, the ISOLDE and ATLAS

facilities. These BOI-buildings-special zones, shown in Figure 4.15, were configured to extend 1 meter from the original facilities, ensuring a comprehensive resolution of the immediate vicinity of the release points. The surface mesh resolutions for these release buildings were additionally adjusted to 0.5 meters with a growth rate of 1.2, which is consistent with the growth rate in the rest of the domain. Consequently, the volumetric mesh reaches a cell size of approximately 1 meter at a distance of 4 meter from these refined surfaces, which corresponds to the resolution of the ground cell surface size. The maximum cell size within the BOI-buildings, which is 3 meters, is reached at a distance of approximately 16 meters from the BOI-buildings-special zones.

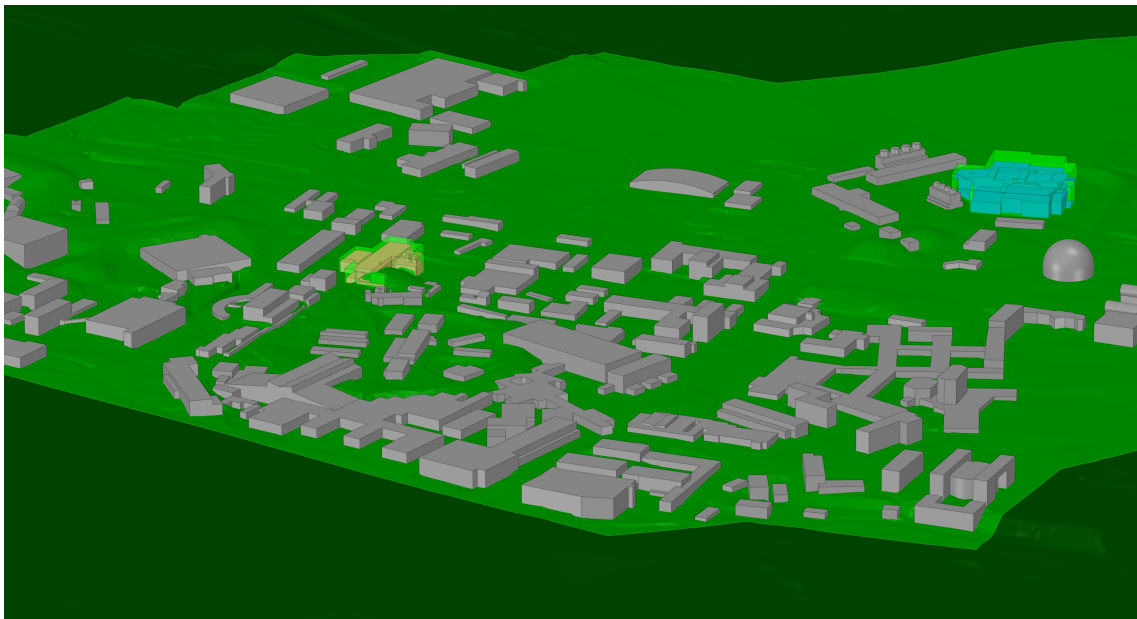


Figure 4.15.: Enlarged view of terrain, buildings and BOI-buildings, shown as light green bodies.

A summary of these functions can be found in the list below. A detailed description of these functions and their definitions are described in the Appendix B.

- **Global scoped sizing**
 - Minimum cell size of 0.5 m;
 - Maximum cell size of 80 m;
 - Growth rate of 1.2.
- **Scoped sizing controls**
 - Ground-special with a surface cell size of 0.5 m (hard);
 - Ground-inner with a surface cell size of 1 m (hard);
 - Ground-outer with a surface cell size of 3 m (soft);
 - Buildings-special with a surface cell size of 0.5 m (hard);
 - Buildings with a surface cell size of 3 m (soft);
 - Wall with a maximum surface cell size of 80 m (soft);

- BOI-buildings-special with a maximal volume cell size of 0.5 m;
- BOI-buildings with a maximal volume cell size of 3 m;
- Edges with a size of 0.5-50 m (curvature).

As mentioned in this section, the volume mesh can accumulate a significant number of cells if appropriate surface sizing is not utilized. With the specified scoped size controls mentioned above, the volume mesh comprises a total of 15.4 million polyhedral cells. Figures 4.16 and 4.17 show a cross-section through the center of the meshed domain. Three-dimensional polyhedral cells show the highest resolution close to the ground (1-3 meters) and the smallest resolution on the top boundary (80 meters). In addition, a constant growth factor of 1.2 from ground level can be observed. In Figure 4.16 a red zone is highlighted, which shows the area for the enlarged view of Figure 4.17. In this, the constant volumetric cell size close to the building can be seen, as well as the constant volumetric cell size of the building refinement zone.

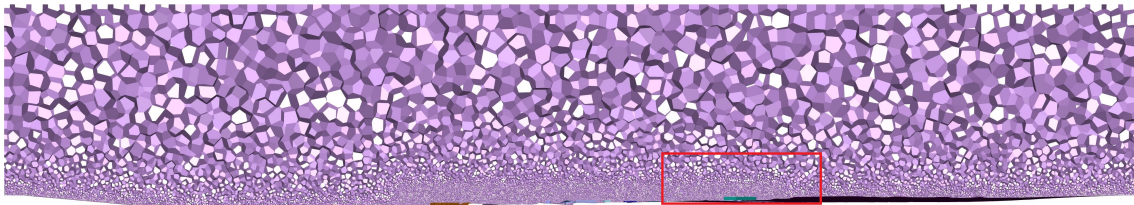


Figure 4.16.: Cross section in N-S direction through the center of the meshed domain showing polyhedral cells in the cross-section. In red the area of the enlarged view in Figure 4.17 is shown.

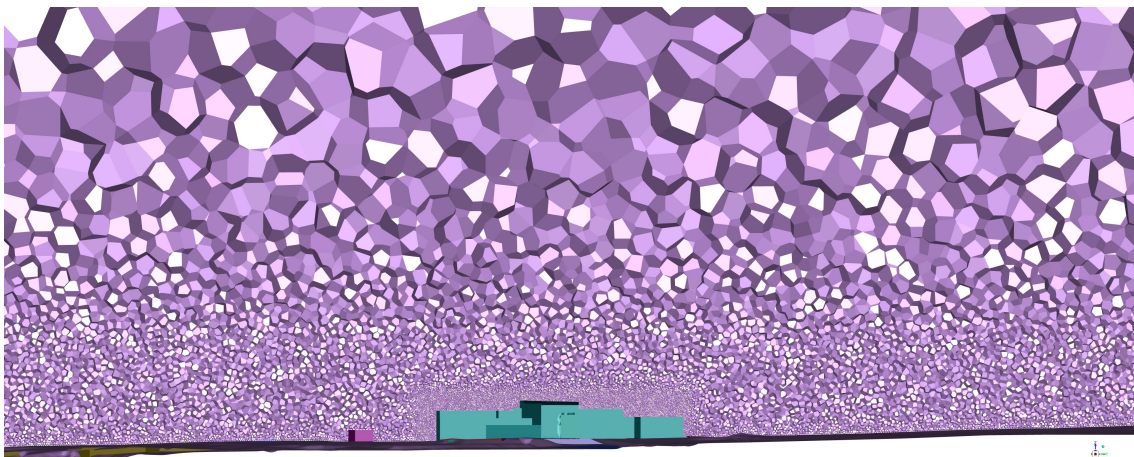


Figure 4.17.: Enlarged view of the cross-section in N-S direction through the BOI-buildings-special.

The quality of the mesh plays a pivotal role in the accuracy and stability of the numerical solution. Therefore, two key quality parameters were evaluated: orthogonality and aspect ratio for polyhedral cells. Figure 4.18 illustrates an ideal mesh on the left and a slightly deformed mesh on the right, with the vectors required to assess orthogonal

quality and aspect ratio. The orthogonal quality is determined using the normal vector of the face for each face (denoted as \vec{A}_i), the vector from the centroid of the cell to the centroid of each surrounding cell (denoted as \vec{c}_i), and the vector from the cell centroid to the centroid of each face (denoted as \vec{f}_i). For each face, the cosine values between \vec{A}_i and \vec{c}_i , as well as between \vec{A}_i and \vec{f}_i , are determined. The smallest of these values represents the cell's orthogonality.

The aspect ratio is calculated as the ratio between the maximum and minimum values of the normal distances between the cell centroid and the face centroids (C_i) and the distances between the cell centroid and nodes (D_i). An ideal mesh, as shown on the left side of Figure 4.18, exhibits an orthogonality quality of 1 and an aspect ratio of 1.19 for all cells. However, as the quality of the mesh deteriorates, as illustrated on the right side of Figure 4.18, the orthogonality declines and the aspect ratio increases to 2.26. ANSYS Fluent Meshing ANSYS Inc. (2022) classifies the orthogonality quality of polyhedral cells into various ranges and assigns the corresponding ratings:

- Orthogonal quality
 - 0.00 - 0.001: Unacceptable
 - 0.001 - 0.14: Bad
 - 0.15 - 0.20: Acceptable
 - 0.20 - 0.69: Good
 - 0.70 - 0.95: Very good
 - 0.95 - 1.00: Excellent

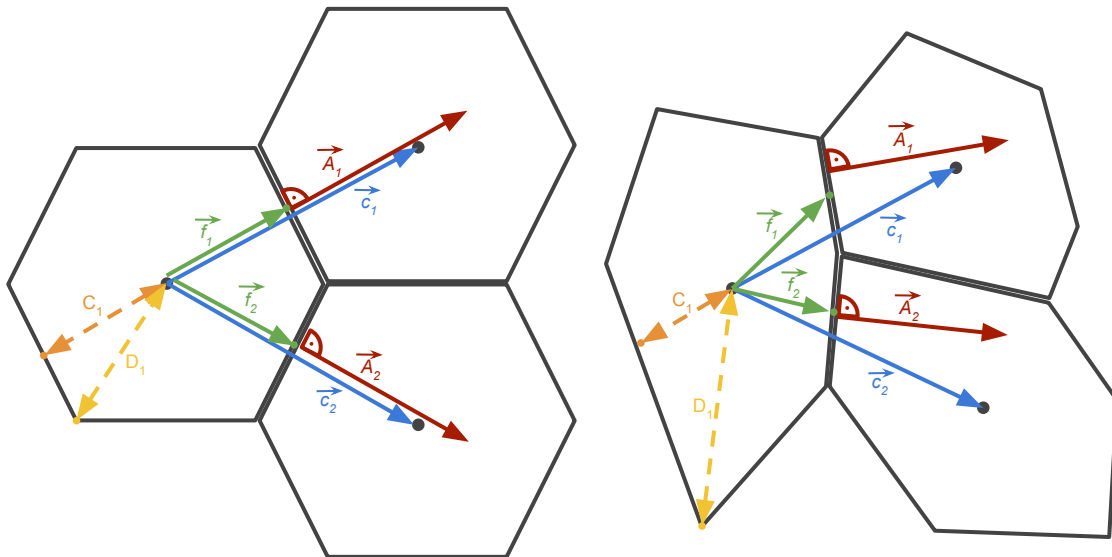


Figure 4.18.: An ideal mesh on the left and deformed mesh on the right is shown to identify the positioning of parameters and their relation to bad mesh quality.

In Figure 4.19, the orthogonal quality and aspect ratio of the final mesh with 15.4 million polyhedral cells are shown. The orthogonal quality is rated as excellent or very good

for most of the cells, indicating that the mesh is of high quality. Furthermore, most cells have an aspect ratio that is smaller than 4, further confirming the high performance of ANSYS® Fluent Meshing. Thus, it can be concluded that only minor improvements are required to further enhance the quality of the mesh.

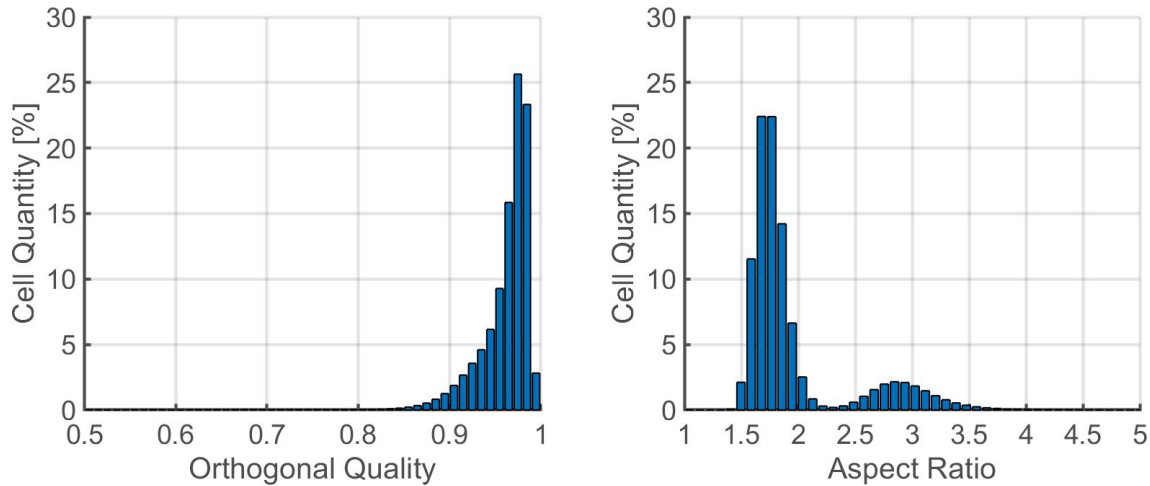


Figure 4.19.: Polyhedral mesh quality evaluated with orthogonal quality (left) and aspect ratio (right).

4.2.4. Evaluation of Mesh Size

The size of the mesh plays a key role in determining the amount and size of vortices resolved during the simulation. It directly influences the scale of vortices that the simulation is capable of capturing. Opting for a mesh with smaller cells requires a higher temporal resolution, thereby demanding greater computational resources. This establishes a delicate trade-off between mesh resolution and the ability to resolve turbulent eddies effectively.

In particular, vortices larger than the chosen cell size (set at 1 meter) exert a significant impact on the transport and dispersion of particles because of their heightened momentum. In contrast, vortices smaller than 1 meter possess less energy and contribute minimally to particle movement within the flow. To accurately predict pollutant transport, it becomes imperative to resolve the transport and generation of vortices induced by obstacles within the simulation geometry.

As eddies persist, they undergo a process of fragmentation, dividing into smaller sizes over time until they reach Kolmogorov microscales. At this scale, viscosity takes precedence, leading to the dissipation of turbulent kinetic energy into heat Kolmogorov (1941). The Kolmogorov length scale is defined as a fraction of the kinematic viscosity of the fluid ν and the average dissipation rate ε according to Landahl and Mollo-Christensen (1992):

$$\eta_{Kolmogorov} = \left(\frac{\nu^3}{\varepsilon} \right)^{1/4} \quad (4.6)$$

Researchers often adopt an approach to resolve more than 80 % of turbulent kinetic energy using LES, as stated in Zhiyin (2015). Consequently, less than 20 % of the turbulent kinetic energy is left to be modeled by SubGrid-Scale (SGS) models. This strategy is rooted in the principles elucidated in Pope (2000).

The schematic representation of the energy cascade plot in Figure 4.20 illustrates the intricate process of energy transfer across various length scales in a turbulent flow. The x-axis conventionally represents the natural logarithm of the wavelength l , while the y-axis illustrates the natural logarithm of the energy associated with the corresponding wavelength $E(l)$.

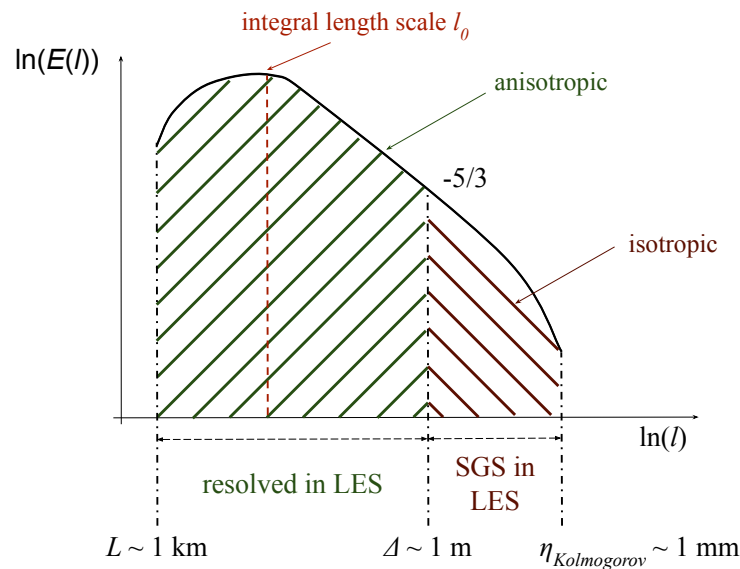


Figure 4.20.: Schematic view of resolved and modelled vortices shown in an energy cascade plot.

The integral length scale, denoted l_0 , characterizes turbulent eddies that harbor the highest energy within the flow. In atmospheric flows, the largest turbulent eddies L can extend up to approximately one kilometer. These sizable eddies, coupled with smaller ones down to sizes of about one meter, significantly contribute to the overall turbulent energy. In regions marked by anisotropic flow characteristics in Figure 4.20, turbulence exhibits variations in different directions. Anisotropy in the energy cascade plot manifests itself as discernible fluctuations in energy distribution across various wavenumbers or length scales. As the scale decreases below a certain size, the flow tends toward isotropy. In an isotropic flow, the turbulence is uniformly and equally distributed in all directions. This change in characteristics is reflected in the lower portion of the energy cascade plot in Figure 4.20.

The Kolmogorov scale $\eta_{Kolmogorov}$ is a critical marker, representing the smallest scale in a turbulent flow where viscosity dominates over turbulence. This scale becomes particularly pronounced in the smallest scales of the turbulent cascade, reflecting the region

where turbulent kinetic energy is dissipated into heat.

In large-eddy simulation (LES), the simulation is designed to resolve larger turbulent structures, such as the integral length scale l_0 . The resolved range typically extends from larger scales ($L = 1$ km) to smaller scales ($\Delta = 1$ m). SubGrid-Scale (SGS) models come into play for scales smaller than what is resolved in LES. For atmospheric flows, these could include vortices up to $\eta_{Kolmogorov} 1$ mm, corresponding to the Kolmogorov scale.

Figure 4.21 depicts the normalized cumulative turbulent kinetic energy (k) in relation to the wavelength $l = 2 \cdot \pi / \kappa$ and the integral length scale (l_0), following the methodology outlined in Pope (2000). This visualization provides valuable insight into the distribution of turbulent kinetic energy across diverse length scales within a turbulent flow.

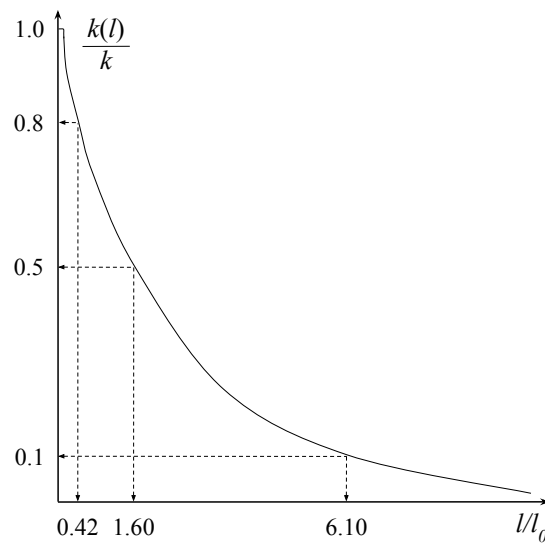


Figure 4.21.: Normalized cumulative turbulent kinetic energy k against wavelength l and integral length-scale l_0 according to Pope (2000).

The graph serves as a guide, offering an understanding of the critical length scales that need to be resolved to capture a specific portion of energy in the turbulent spectrum. For example, resolving the eddy sizes approximately 6.1 times larger than the integral length scale (l_0) accounts for only 10 % of the resolved turbulent kinetic energy (k). In contrast, solving the eddy sizes approximately 0.42 times the integral length scale (l_0) produces an impressive 80 % of the resolved turbulent kinetic energy. This information helps to make informed decisions about the spatial resolutions required in the domain to accurately capture and represent turbulent energy contributions across various length scales.

Figure 4.22 visually represents the numerical requirements for resolving an eddy for the smallest possible wavelength $l_{min} = 2\Delta$. The illustration underscores that a minimum of four cells is essential to effectively resolve an eddy in two dimensions of this specified wavelength l .

In essence, the selection of an appropriate mesh size demands careful consideration, striking a balance between computational efficiency and the ability to detail resolved

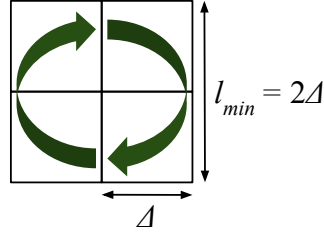


Figure 4.22.: Illustration of the minimal number of cells to resolve an eddy for the smallest possible wavelength $l_{min} = 2\Delta$.

turbulent eddies. Given the paramount role of large vortices in particle transport and dispersion, a key focus lies in accurately resolving the transport and generation of vortices induced by obstacles in the simulation geometry. Consequently, the refinement of these specific areas becomes crucial.

To assess the extent to which turbulent eddies are captured by a designated mesh, steady RANS simulations serve as a widely employed methodology. In these simulations, the integral length scale (l_0) emerges as a valuable metric, offering an indication of the smallest resolved turbulent eddies. As described in Pope (2000), the integral length scale (l_0) is calculated from the turbulent kinetic energy (k) and the dissipation rate (ϵ) using the equation:

$$l_0 = \frac{k^{3/2}}{\epsilon} \quad (4.7)$$

Following the rule, which was presented in Figure 4.21, Table 4.2 shows the same relationship and additionally the ratio of the integral length scale to the cell size (l_0/Δ), which is important for the evaluation of the mesh. To resolve 90% of the turbulent kinetic energy (k) a l_0/Δ ratio of 12.5 or higher must be reached.

Table 4.2.: Cumulative turbulent kinetic energy k against integral length scale l_0 with wavelength l and mesh size Δ . Based on the Kolmogorov energy spectrum.

	l/l_0	l_0/Δ
$k(l) = 0.1k$	6.10	0.33
$k(l) = 0.5k$	1.60	1.25
$k(l) = 0.8k$	0.42	4.76
$k(l) = 0.9k$	0.16	12.50

The precise calculation of the length (Δ) of a polyhedral cell is inherently challenging due to its irregular shape and non-systematic composition, distinguishing it from the more straightforward calculations applicable to hexahedral meshes. Instead, an estimation method is used for the mesh size considerations, taking advantage of the cubic root of the cell volume (V_{cell}), as illustrated in Equation 4.8.

$$\Delta \approx \sqrt[3]{V_{cell}} \quad (4.8)$$

In this context, assuming a sphere with an equivalent volume to that of the polyhedral cell, the diameter of the sphere would be approximately 1.5 times longer than the estimated length derived from Equation 4.8. In contrast, when comparing the estimated length with the radius of the sphere, the length would be reduced by a factor of 0.75. This comparison highlights the rationality of the approximation outlined in Equation 4.8.

The ratio of the integral length scale to cell size (l_0/Δ), as illustrated in Figure 4.23 for the cross-section in the wind direction at the release point, serves as a valuable metric to evaluate and compare mesh resolutions with the corresponding values detailed in Table 4.2. In this representation, the values of l_0/Δ generally exceed 12.5 in the vicinity of the CERN Meyrin site and at higher altitudes. This observation implies that more than 90% of the naturally occurring turbulence is effectively resolved in these regions.

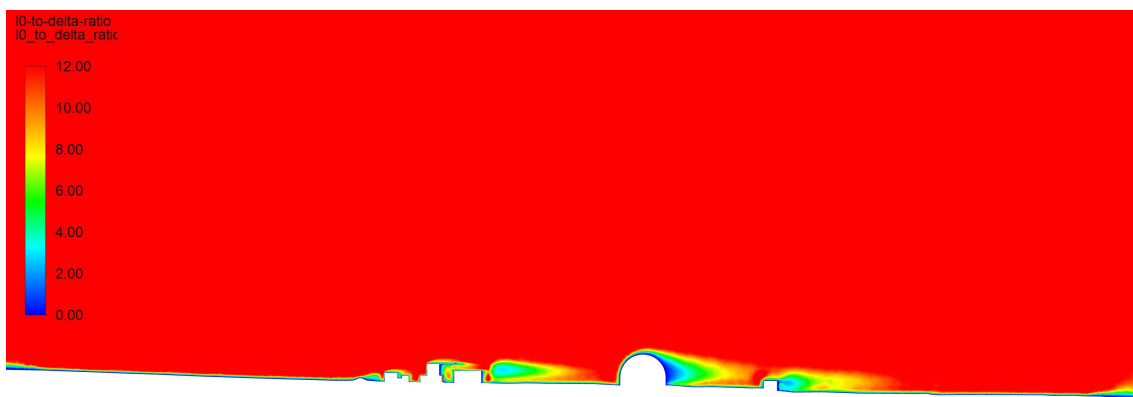


Figure 4.23.: Example for l_0/Δ ratio in a cross-section as enlarged view of the regions close to the release point.

In contrast, in areas directly influenced by buildings, the values often fall below the suggested threshold. However, a substantial majority of cells still exhibit a ratio of the integral length scale to the cell size (l_0/Δ) that exceeds 4.8, corresponding to a resolution of more than 80% of all turbulent eddies in these zones. The minimum ratio of the integral length scale to the cell size (l_0/Δ), $l_0/\Delta_{min} = 0.01$, is located near the ground, indicating insufficient mesh resolution to resolve the flow near the wall. At the other extreme, the maximum value, $l_0/\Delta_{max} = 1166$, is located at the periphery of the body-of-interest, where refinements are applied and velocities are high. The volume-averaged value, $l_0/\Delta_{avg} = 607$, is relatively high, reflecting the fact that the wake regions in the flow field constitute a minority of cells.

Figure 4.23 indicates that turbulent eddies are resolved sufficiently, especially in areas far from buildings and at high altitudes. However, areas close to buildings, particularly the regions between buildings and their immediate surroundings, could benefit from better resolution. Although most of these areas achieve at least 80% resolution of turbulent eddies with a grid resolution of 1 m near walls at the ground, further investigation of the mesh has been performed in the refinement study discussed in Chapter 4.2.2.

4.2.5. Meshing Challenges

Meshing challenges arise when the domain is divided into distinct regions. Dividing the domain into separate regions, such as an essential inner domain and a constant outer domain, can be advantageous when specific mesh modifications are required. For example, you might want to alter the terrain of the outer zone due to changes in vegetation while keeping the inner zone unchanged. This approach allows you to retain the mesh of the inner zone and only re-mesh the outer zone. In cases where new constructions in the area need investigation, modifying the inner zone can be done without the need for extensive re-meshing of the outer zone.

Furthermore, when dealing with porous zones, it is possible to mesh these regions separately, simplifying the application of sink terms for momentum and providing a clear separation between these zones. Although these options were considered during the simulation setup, ANSYS® Fluent Meshing encountered challenges in correctly combining these regions. Even with highly precise CAD geometry, issues such as overlapping zones occurred during separate meshing due to the wrapping procedure used for surface mesh generation.

This problem is particularly pronounced for large geometries where the terrain is extracted as a stereolithography file and a CAD model is used for buildings. Combining these two different data types into a single surface requires the use of the wrapping procedure, as ANSYS® SpaceClaim cannot perform volume extraction. Unfortunately, the wrapping procedure lacks the precision needed to accurately define the surfaces. Even when a CAD surface is wrapped from both sides, the surfaces may not be identical, resulting in small gaps at the edges or even surface overlapping.

This presents challenges when defining interfaces between two regions in the solver. Consequently, the domain was not divided into multiple regions, and an alternative scripting approach was adopted for the meshing procedure. This approach minimizes user input, making it easier to generate a new mesh, and allows the meshing procedure to be carried out efficiently.

4.3. Simulation Setup

The following sections delve into the details of boundary conditions, solver settings, and the implementation of particulate and gas dispersion modeling.

4.3.1. Boundary Conditions

The complexity of the environment surrounding CERN posed challenges in defining in-flow boundary conditions. The ground roughness values vary depending on the direction of the wind. The eastern area, which encompasses Meyrin and the city of Geneva, exhibits a distinct flow profile compared to winds blowing from the South-West or North-

East. This variation is attributed to the predominance of farmland, vineyards, and occasionally woodland, resulting in fluctuating turbulence levels in the lower atmospheric boundary layer. Providing a highly detailed representation of the inflow conditions at the CERN site went beyond the scope of this study. As a result, a single roughness length is assumed that characterizes the mean inflow wind profile, associated turbulence, and a consistent reference wind speed, regardless of the wind direction.

To effectively manage the number of simulations, the focus was set on wind directions with high probabilities and significant potential impacts on releases at the CERN site reaching the public. Specifically, the South (S), North East (NE), and South West (SW) wind directions have been considered. These wind conditions were examined using data from an ultrasonic anemometer near CERN collected over several years. In Figure 4.24, the probability of wind directions in five-degree sectors and their corresponding wind speeds at a height of ten meters can be observed. The emphasis was placed on surrounding farmland since the most significant dosimetric impact on individuals is expected when pollutants deposit on plant surfaces. This exposure pathway is of utmost importance, considering the possible ingestion of vegetables, milk, and meat from cattle fed grasses from the area of interest.

The wind rose served as a tool to initially comprehend the potential wind speeds and directions. Although different wind speeds were observed, the investigation was simplified to focus on a singular wind speed, specifically $u_{ref} = 1 \text{ m/s}$, in accordance with Swiss regulations for pollutant particle transport in the event of accidental releases (ENSI-G14 (2009)). This chosen wind speed provides a basis for scalability, allowing the extrapolation of pollutant concentration in specific areas under varying wind speeds. The investigation further restricted itself to a single atmospheric stability class, opting for the frequently encountered stability class "D" characterized by neutral stratification, as illustrated in Figure 4.25. This choice also facilitates simplification of the analysis by disregarding potential temperature variations.

The selected wind speed values at a specific height were used to estimate the mean velocity at the desired height using the logarithmic law. This law, derived from Prandtl's mixing length theory (Tollmien et al. (1961)), is elucidated by Monin and Obukhov in the Monin-Obukhov similarity theory (Monin and Obukhov (1954)). In this context, the velocity follows an increase with altitude, denoted as z , as expressed by the following equation:

$$u(z) = \frac{u_*}{\kappa} \left[\ln \left(\frac{z}{z_0} \right) - \Psi_m \left(\frac{z}{L} \right) \right] [m/s] \quad (4.9)$$

In this equation, u_* represents the friction velocity, κ is the Von Kármán constant with a value of $\kappa = 0.41$, and the aerodynamic roughness length is indicated as $z_0 = 1 \text{ m}$, corresponding to the value for the center of large towns / cities, low mountains or forests, as described in Stull (1988). The Obukhov length L is determined based on the recommendations provided in McGrattan et al. (2020), as outlined in Table 4.3.

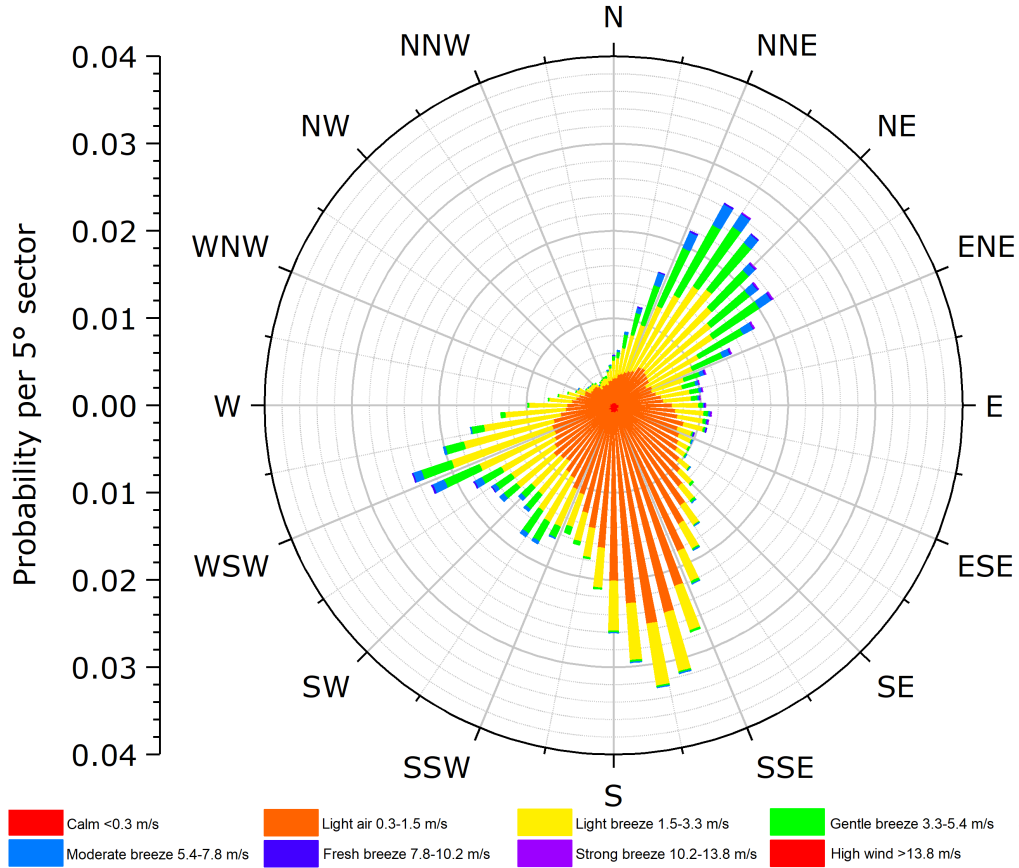


Figure 4.24.: Wind rose showing the probability of the wind direction per five degree sector and their corresponding wind speeds with slightly adapted Beaufort scale measured by an ultrasonic anemometer in 2018 and 2019 at 10 m height in a field Easterly of CERN (Maisonnex).

Table 4.3.: Suggested values for the Obukhov Length L in meter.

Stability class	Value range	Suggested value
Very unstable	$-200 \leq L < 0$	-100
Unstable	$-500 \leq L < -200$	-350
Neutral	$ L > 500$	1000000
Stable	$200 < L \leq 500$	350
Very stable	$0 < L \leq 200$	100

In situations of near-neutral stratification, the similarity function Ψ_m tends toward zero, allowing its exclusion from the calculation in Equation 4.9. For completeness, the similarity function Ψ_m is presented in Equation 4.10, following the law of Dyer (1974) for stable cases where $L \geq 0$:

$$\Psi_m \left(\frac{z}{L} \right) = -5 \frac{z}{L} \quad (4.10)$$

The friction velocity u_* is determined using the reference velocity u_{ref} at a specific height z_{ref} , along with the Von Kármán constant κ and the roughness length classification

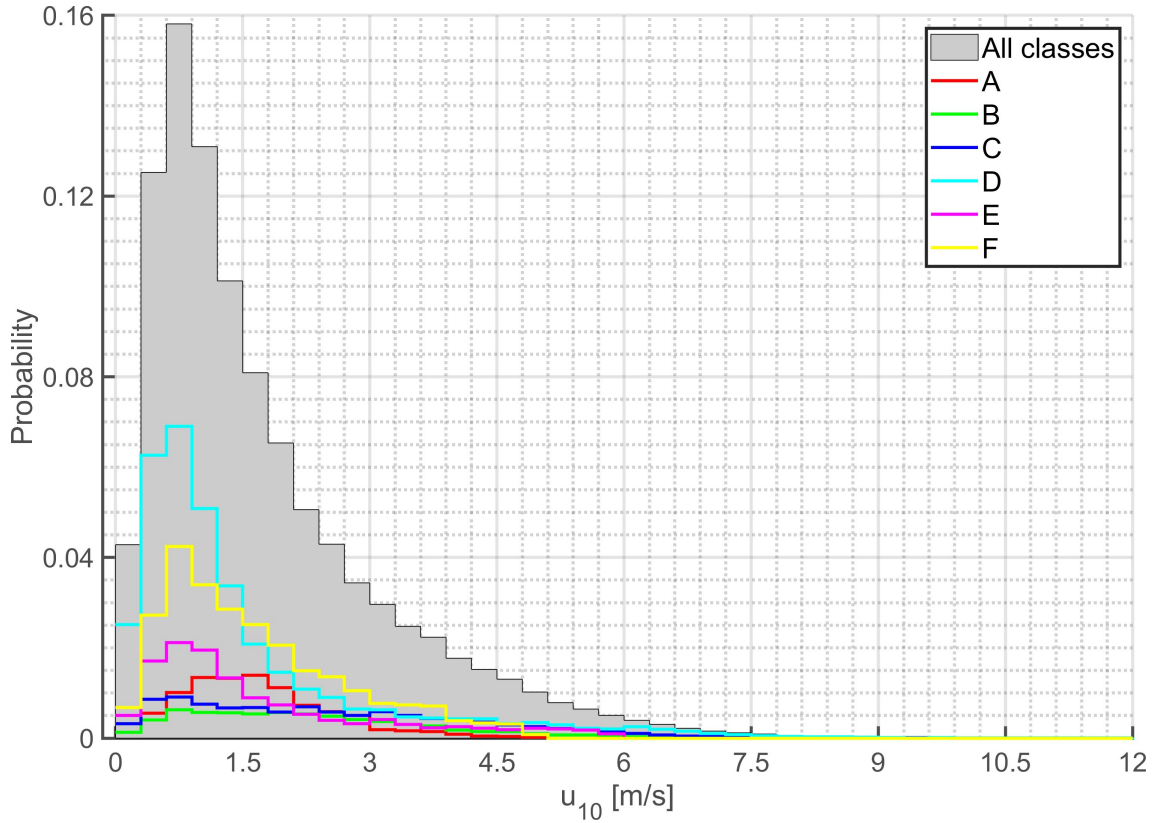


Figure 4.25.: Probability of wind speeds for the atmospheric stability classes measured by an ultrasonic anemometer in 2018 and 2019 at 10 m height East of CERN. A: very unstable, B: moderately unstable, C: slightly unstable, D: neutral, E: slightly stable, F: stable.

z_0 .

$$u_* = \frac{\kappa u_{ref}}{\ln\left(\frac{z_{ref}}{z_0}\right)} [m/s] \quad (4.11)$$

Fluctuating velocity inlets, introduced for specific inlet surfaces, as illustrated in Figure 4.7, take advantage of the synthetic turbulence generator (STG) in their implementation. Both the vortex method (VM) and the synthetic turbulence generator (STG) play crucial roles in this context. The VM generates vortices on the inlet surfaces, with a specific equation expressing the relationship between the faces of the inlet surface and the vortices (Equation 4.12):

$$n_{vortices} = n_{faces} / 4 \quad (4.12)$$

The STG, on the other hand, is used to introduce fluctuations in velocity inlets, offering advantages over the VM in terms of face-handling capability and computational effort. The foundation of STG lies in the concept introduced by Shur et al. (2014), and its superiority over VM is documented in Sergent (2002). For the chosen mesh size, the minimum required number of faces n_{faces} at the inlet is 3300, resulting in the recommended number

of 825 vortices $n_{vortices} \approx 825$. A mesh refinement analysis in this study results in a significantly higher number of vortices at the inlet (refer to Chapter 4.2.2). However, ANSYS® Fluent imposes a limit of 1000 vortices on a single surface. Consequently, synthetic models, such as the STG, are favored for the mesh refinement study. The STG is chosen over the Spectral Synthesizer (SS) because of its lower computational effort and its ability to generate high-quality turbulence fluctuations.

The performance of synthetic models, extensively investigated by Vasaturo et al. (2018), requires a dedicated section within the computational domain for the development of turbulence, although at the cost of increased computational effort (Bazdidi-Tehrani et al. (2016)). While the implementation of STG in ANSYS® Fluent is relatively recent and lacks detailed studies, it is considered the most potent model among the available turbulent inlet specification methods, following ANSYS Inc. (2022). Chapter 4.3.2 provides an in-depth exploration of the STG's performance, with a specific focus on atmospheric turbulence assessed through energy cascade plots.

To prevent flow deceleration in the center of the domain and minimize the likelihood of backflow at the pressure outlet faces, the lateral faces have been designated as inlets without fluctuations, as shown in Figure 4.7. This choice not only enhances convergence, but also promotes solution stability. By not defining fluctuations on these faces, the risk of backflow at the intersection point of the inlet and outlet boundary conditions is effectively mitigated. In addition, the potential for backflow at the outlets due to the wake of buildings or ground inclination has been addressed. This concern is alleviated by situating all buildings and release points in the central region of the domain and maintaining a relaxed elevation of the terrain. In general, the decisions made in this dissertation align with established guidelines, such as those outlined in COST Action 732 (2010) and VDI 3783/12 (2000).

To define a turbulent inlet at the boundaries using a synthetic model in large-eddy simulations (LES), evaluation and comparisons should be application-specific, as emphasized by Patruno and Ricci (2018). Consequently, Chapter 4.3.2 of this dissertation includes an investigation to directly compare established methods, including the vortex method (VM), which was recently reviewed by Vasaturo et al. (2018) and confirmed as a potential turbulent inlet specification method. The results of two synthetic turbulence generation methods are juxtaposed and distinctions are discussed.

The conclusion drawn from the comparison is that the synthetic turbulence generator (STG) is the preferred method over the vortex method (VM). Therefore, STG has been adopted as the standard turbulence generation method based on this evaluation.

To prescribe inlet fluctuations for large-eddy simulation (LES) at the boundaries using a synthetic model, the turbulent kinetic energy k [$\text{m}^2 \text{s}^{-2}$] and turbulent dissipation rate ε [$\text{m}^2 \text{s}^{-3}$] are required, similar to approaches used in k - ε turbulence models. Hence, the methodology described in Hargreaves and Wright (2007) was adopted. The turbulent kinetic energy k is estimated using the friction velocity u_* [m, s^{-1}] and the turbulence

viscosity coefficient c_μ according to the formula:

$$k = \frac{u_*^2}{\sqrt{c_\mu}} \quad (4.13)$$

The turbulent dissipation rate ε is computed using the friction velocity u_* , the von Karman constant κ , the height above the ground z [m], and the surface roughness height z_0 [m], represented as:

$$\varepsilon(z) = \frac{u_*^3}{\kappa \cdot (z + z_0)} \quad (4.14)$$

As the friction velocity and the von Kármán constant κ remain constant, the turbulent dissipation rate exhibits a pronounced increase near the ground and decreases with altitude. According to Richards (1993), the viscosity coefficient of the turbulence (c_μ) can be set to 0.09, a widely accepted default value in the context of k- ε turbulence models. With $c_\mu = 0.09$, the turbulent kinetic energy (k) yields approximately $0.105 \text{ m}^2\text{s}^{-2}$. This results in a constant turbulent kinetic energy for each altitude, while the turbulent dissipation rate (ε) varies with altitude.

For the walls, which include both the ground and the buildings, a non-slip condition is enforced, according to the guidelines outlined in COST Action 732 (2007).

4.3.2. Turbulent Inlet Specification Method

This chapter explores turbulent inlet specification methods in ANSYS® Fluent, crucial for the accurate simulation of turbulent flow in the atmospheric boundary layer. Conventional methods, such as the Spectral Synthesizer (SS) and vortex method (VM), are standard, but a newer technique, the synthetic turbulence generator (STG), is introduced and warrants investigation.

An efficient inlet turbulence specification is vital. The in literature widely used vortex method has limitations, particularly in scenarios with a larger number of surface cells (as defined by Equation 4.12), since computational effort is increasing and vortices can be restricted to a specific maximum. In contrast, the synthetic turbulence generator (STG) emerges as a promising alternative, offering computational advantages and higher flexibility for meshing the inlet. This chapter aims to unravel the intricacies of these turbulent-inlet specification methods, shedding light on their merits and demerits in computational fluid dynamics.

This study comprehensively examines these two turbulent inlet specification methods, focusing on critical parameters for both the vortex method (VM) and the synthetic turbulence generator (STG). The core of this investigation centers on the impact of these parameters on the prediction of pollutant dispersion, a key outcome in the simulations in this dissertation.

Drawing from previous studies, including Mathey et al. (2006), Bazdidi-Tehrani et al. (2016), and Vasaturo et al. (2018), which evaluated the effectiveness of the vortex method

(VM) and the Spectral Synthesizer (SS) in generating turbulent flows, this analysis aims to improve the understanding of the STG method. Vasaturo et al. (2018) demonstrated that VM outperforms SS in various aerodynamic roughness lengths and that VM performance approaches the Precursor Method (PM). VM exhibits mean streamwise velocity deviations below 2% for any terrain, while the PM shows even smaller deviations (<1%) and SS deviations are <8%. For longer domains, the decay in mean velocity might be higher. The decay of VM's turbulence kinetic energy ranges from 18.5% to 23.5% (rural to urban), while SS is inappropriate with a decay of approximately 79.3%. Under the premises set by Vasaturo et al. (2018), VM proves robust, making it a versatile tool for simulating turbulent atmospheric boundary layer flows, providing swift and reliable results, as confirmed by Bazdidi-Tehrani et al. (2016).

Examining the synthetic turbulence generator (STG) alongside the well-established vortex method requires nuanced conclusions, given inherent limitations in directly comparing these two methods. If the effectiveness of the STG aligns with that of the VM, it could signal its potential applicability in the scenarios under study. However, caution is needed to draw definitive conclusions considering the unique attributes and constraints associated with each method. However, a validation with wind tunnel experiments or real test case data would be much more suitable, but did not exist at this moment.

To allow a meaningful comparison, the ATLAS release scenario at CERN with pollutant release from the door and northern winds was chosen, using a digital elevation model (DEM) with surface roughness $z_0 = 1$, detailed in Chapter 5.2. This comparative study focuses on the analysis of VM and STG for turbulent inlet conditions. This approach allows a direct assessment of substituting STG with VM within a realistic scenario.

It is essential to clarify that this comparison does not validate the STG inlet specification method, lacking a benchmark against wind tunnel or real-world tests. However, it provides insight into the relevance and performance of STG in ABL flow scenarios, laying the foundation for potential future studies. These findings can be correlated with the results of the sensitivity analysis in Chapter 5.2, offering information on the sensitivity of the result to different methods of turbulent inlet specification or without perturbations.

Figure 4.26 offers a comparative view of averaged mean velocity along the six monitoring-lines, depicted in Figure 4.37, for the two turbulent inlet methods, STG and VM, along with their respective theoretical definitions at the inlet.

Examining the mean velocity U for both inlet specification methods reveals varying results with height above the ground. In proximity of the ground at $z/H < 0.2$ or $z < 100$ m, the inlet turbulent specification method has a low impact due to the presence of obstacles. Beyond $z/H > 0.2$, the velocity profile at the inlet in combination with the inlet specification method becomes the main contributor to the mean flow. In this region, the mean velocity shows a slight variation between the VM and the STG. The disparity in mean velocity profiles between VM and STG and the theoretical curve can be attributed to the relaxation of the terrain, as shown in Figure 4.6. The monitoring lines positions

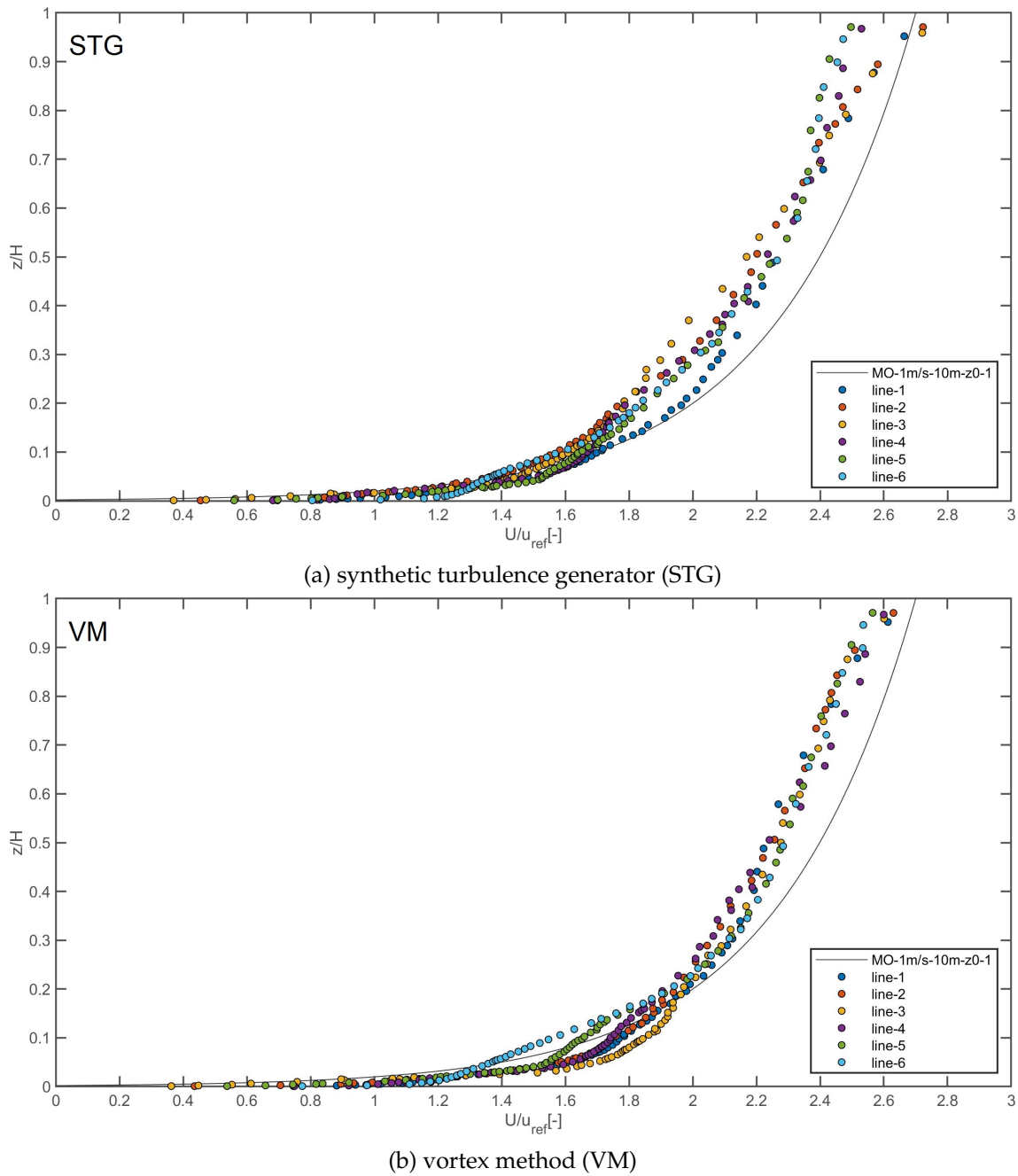


Figure 4.26.: Comparison of STG and VM as turbulent inlet specification method with wind blowing into south direction. The normalized mean velocity U/u_{ref} is presented for both methods for the total domain depth with $z = 500$ m and $z_{ref} = 1 \text{ ms}^{-1}$.

are not directly comparable to theoretical values because of differences in altitude at the positions. Consequently, the values for STG and VM should mainly be compared to each other rather than to the theoretical curve. Near the ATLAS surface building, where the terrain reaches a height of $z = 440$ m above sea level and the edges of the domain are relaxed to $z = 460$ m, the constant volume flow decelerates with an increasing cross-section of the domain. Figure 4.26 illustrates how the mean velocity profile is defined at

the inlet. The flat top boundary, which does not follow the altitude of the ground in the terrain, contributes to this effect.

The mean velocity profiles for the two turbulent inlet specification methods show minor differences, indicating similar performance in averaging fluctuations. The maximum deviation from the theoretical curve is less than 10%, occurring at heights of $0.25 < z/H < 0.4$ and $0.8 < z/H < 0.9$. Within the monitoring lines for the same turbulent inlet specification method (STG or VM), fluctuations are more pronounced for the VM than for the STG. For the STG, the largest deviations, around 10%, dominate in $z/H = 0.2$. In contrast, at height $z/H = 0.1$ for the VM, the mean velocity for different monitoring lines fluctuates strongly, reaching up to 20%.

The results of the turbulence intensity (TI) are illustrated in Figure 4.27 and compared to reference literature values for different ground roughness values from ESDU (1985). The results reveal a similarity in the bottom part of the domain for both turbulent inlet specification methods. The TI curves exhibit comparable slopes in general. In the lateral and vertical directions to the flow, the TI values ($I_{v,w}$) remain identical up to an altitude of 200 m or $z/H < 0.4$. Beyond this height, the STG method shows slightly higher TI values. In the main flow direction, TI (I_u) decreases steadily with increasing altitude for STG, while VM exhibits an oscillating progression at $z/H = 0.1$ and $z/H = 0.4$. Furthermore, at altitudes above $z/H > 0.5$, the STG method predicts uniformly TI values of 0.1, while the TI decreases further with the VM to 0.05. This behavior is consistent in all directions ($I_{u,v,w}$). In particular, TI at the inlet was defined as 0.1, indicating that the values at ML-6 should asymptotically approach this value. The STG method appears to perform slightly better in maintaining TI, especially near the ground. According to ESDU (1985), the TI values should only slightly decrease above an altitude of $z/H > 0.4$, further supporting the superior performance of the STG turbulence inlet generation method.

In Figure 4.28, the turbulence kinetic energy (TKE) is depicted for the STG at the top and the VM at the bottom. The observed trend in the TI plots is reaffirmed. TKE for the VM decreases sharply above $z/H = 0.4$, compared to the more stable values for the STG. Both inlet specification methods predict a higher TKE near the domain top. Vasaturo et al. (2018) reported a 20% reduction of TKE for the turbulent inlet specification of the VM along the stream direction of the domain for a short length (4H). This reduction, significantly higher than in the precursor method, is evident in Figure 4.28, where the monitoring lines are positioned in the stream-wise direction (line-6 to line-1).

Lines six to four show lower TKE values for the VM, indicating a weaker turbulent-inlet specification compared to the STG. In the area of the inlet surface to the first monitoring line (line 6) the flow has passed the distance around 1 km, while it was significantly reduced for the VM. Upon reaching the built environment, the TKE increases due to shear production on the ground, coupled with a general velocity increase as the domain depth slightly decreases. This results in a higher TKE in the lower and central parts of the domain. However, for the upper part of the domain, the TKE does not reach the

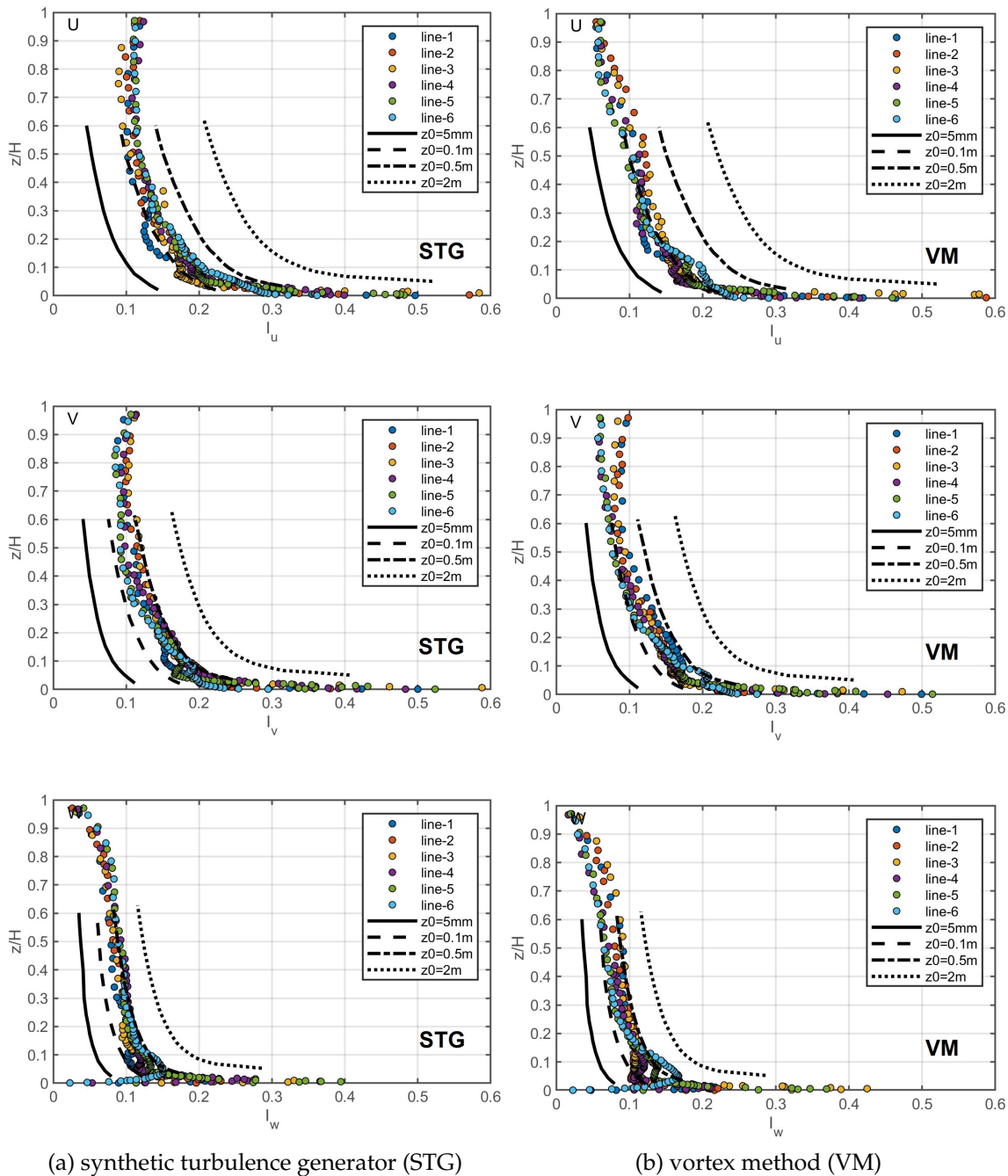


Figure 4.27.: Comparison for turbulence intensity $I_{u,v,w}$ of the STG and the VM as turbulent inlet specification method with wind blowing into south direction.

same values as in the STG method. This discrepancy is attributed to the absence of visible ground interaction influence, which prevents an increase in TKE in this region. It should be mentioned that the TKE is defined with 10% at the inlet, which corresponds to the values found in the STG. Close to the ground vortices are produced as a result of the interaction with obstacles.

The next parameter under analysis is the spectral distribution of turbulence kinetic energy, an important factor in understanding the size of generated vortices and ensur-

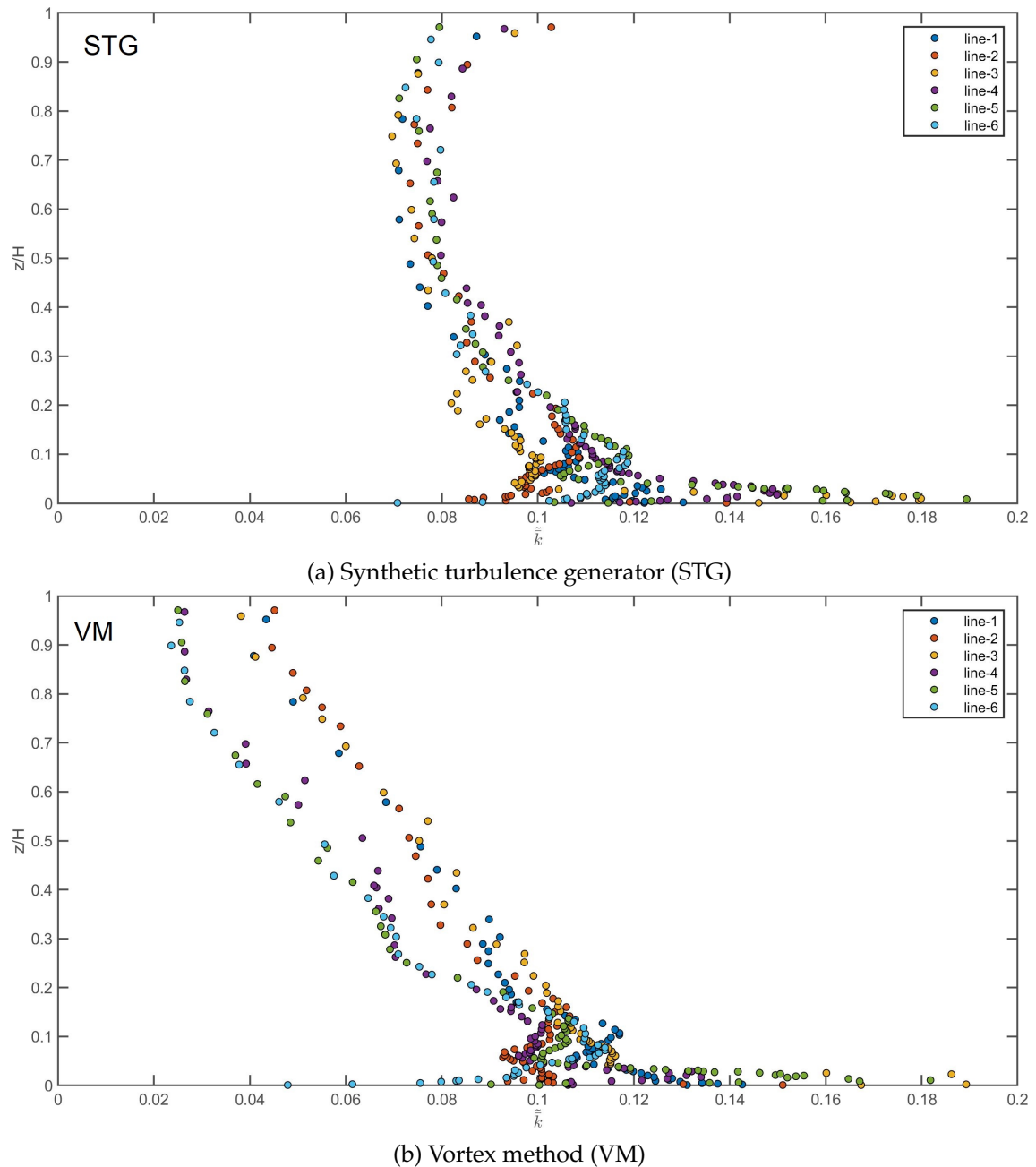


Figure 4.28.: Comparison for turbulence kinetic energy \bar{k} of STG and VM as turbulent inlet specification method with wind blowing into south direction.

ing the efficacy of the STG. Figure 4.29 presents a comparison of the performance of the two inlet specification methods along monitoring line number six at a representative altitude of $z = 95.51$ m above ground, where the effects of the shear ground production are minimized. Although the spectral distribution of turbulence kinetic energy for various heights were examined, only the representative altitude is shown here to simplify the presentation. The mentioned reference range will be further described in Chapter 4.5. Here the focus shall be set on the comparison between both turbulence inlet specification models.

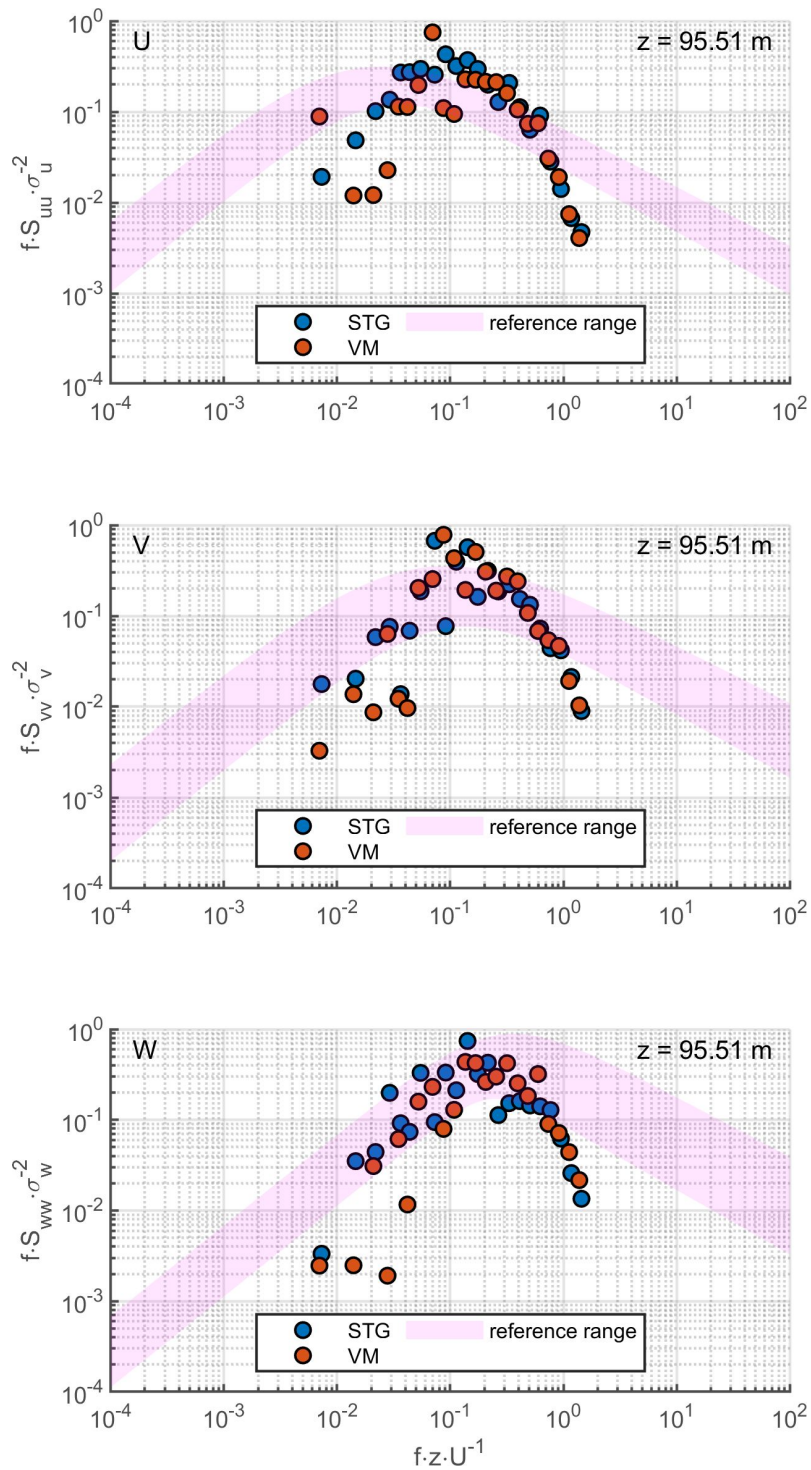


Figure 4.29.: Comparison of the performance of STG and VM in direct comparison for ML-6 with wind blowing into south direction. Spectral distribution of turbulence kinetic energy is presented for both methods.

At lower altitudes, where ground effects and ground shear production are prominent, both methods exhibit similar predictions, aligning well with the reference range, further described in Chapter 4.5.3. However, for a more meaningful assessment of the performance of the inlet specification method, comparisons at higher altitudes are more rele-

vant, as indicated by the trends observed in the turbulence intensity graphs. The altitude of $z = 95.51$ m serves as a representative height, demonstrating a comparable performance between the two methods in all directions. Both high-frequency small vortices and low-frequency large vortices show similar tendencies. Notably, the larger vortices display slightly more energy with the STG inlet specification than with the VM, though the difference remains minor.

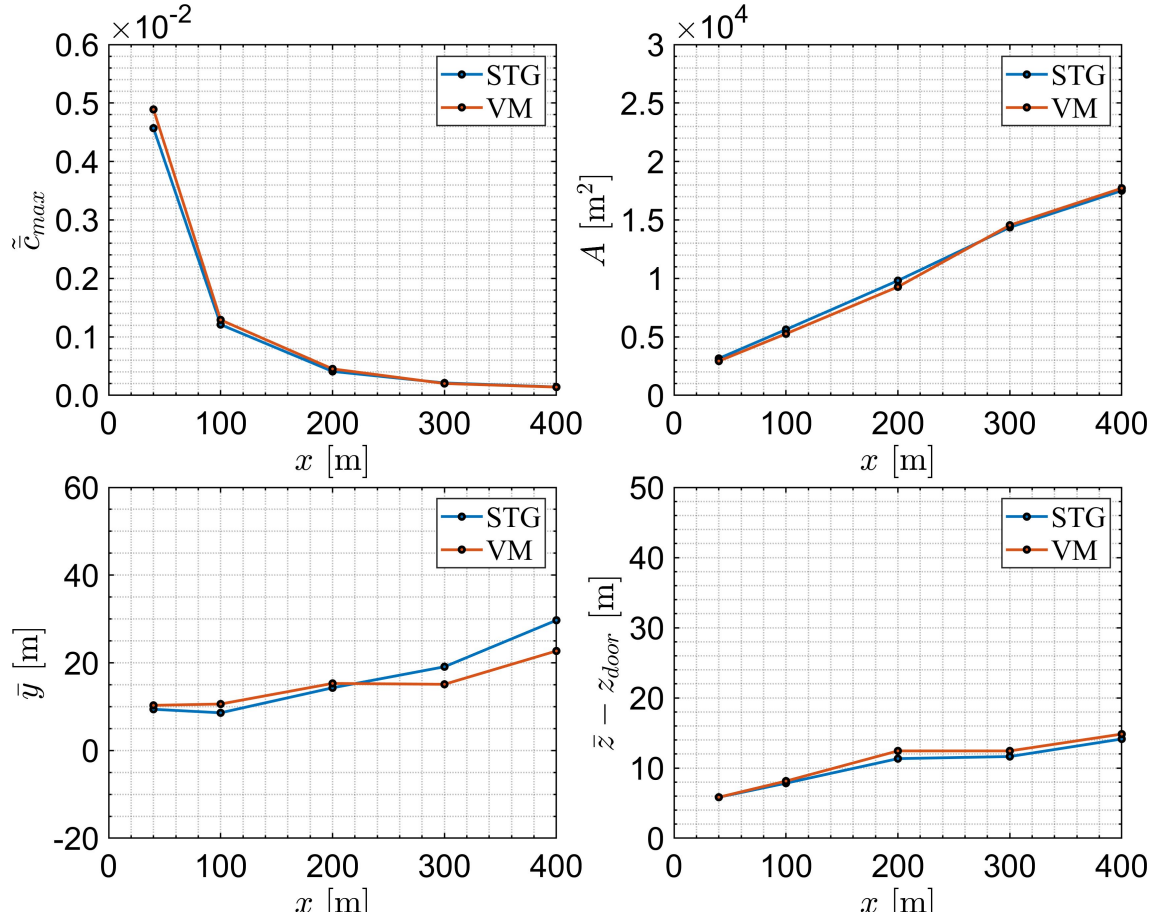


Figure 4.30.: Comparison of displacement parameters \bar{y} and $\bar{z} - z_{door}$, the plume cross-section A and the maximum concentration \tilde{c}_{max} as function of the distance from the release point for the two inlet turbulence generation methods: STG and VM.

Figure 4.30 illustrates a comparison of the plume's displacement parameter between the two turbulent inlet generation methods: STG and VM. The displacement parameters \bar{y} and $\bar{z} - z_{door}$, the plume cross-section A , and the maximum concentration \tilde{c}_{max} show similar predictions for both methods. Consequently, the impact of the synthetic inlet turbulence generation method on pollutant dispersion is minimal. This suggests that the synthetic turbulence generator performs comparable to the vortex method for this specific scenario.

In addition to performance, computing efficiency is also essential. In Table 4.4 the computation time needed is juxtaposed:

Table 4.4.: Computing efficiency of the two investigated turbulent inlet specification methods: vortex method (VM) and synthetic turbulence generator (STG).

	VM	STG
Inner-iterations	13.3	7.1
Time for one inner-iteration [%]	100	62.5
Computing time [%]	100	33.9

The total computing time in the CERN internal cluster amounted to 4256 hours for the VM and 1420 hours for the STG. These resources were used to simulate an internal simulation time of 2 hours, maintaining a consistent time step size of 0.2 seconds. The simulations were conducted on more than 2000 available cores, with most runs utilizing 256 cores, resulting in a computational duration of a few days considering parallel scaling effects. Saving two thirds of the total runtime in the case of running with STG and reaching very similar results in terms of pollutant concentrations and flow characteristics lead to a general use of the STG.

In summary, the results obtained from both the VM and STG methods are largely identical in numerous parameters, with only minor variations observed in the turbulence intensity at specific altitudes and the variation in the kinetic energy of the turbulence, potentially indicative of the decay described by Vasaturo et al. (2018). In contrast, the STG consistently demonstrated superior performance. Considering the notable reduction in computational resources required by the STG method compared to VM, it is recommended to simulate atmospheric boundary layer flows with pollutant dispersion in urban settings. Further investigations and validation efforts are advisable for the STG in ABL flows. This blind test suggests its suitability as a viable replacement for the VM in such simulations. Importantly, changing the inlet specification method did not show a discernible impact on pollutant dispersion simulations, as the proximity of the pollutant release to ground level and surrounding buildings overshadowed any potential deviations in TI, TKE, eddy sizes and mean velocity. In particular, the omission of turbulent inlet specification had a substantial impact on pollutant dispersion, as will be discussed in Chapter 5.2.

4.3.3. Review of Boundary Conditions

As discussed in Chapter 3.2, both RANS with a $k-\epsilon$ turbulence model and large-eddy simulation (LES) are employed as initial or subsequent models to finally simulate the dispersion of pollutants in the atmospheric boundary layer. It is crucial to note that the boundary conditions exhibit slight variations between the steady and transient phases of the simulations.

In the steady state solution, the turbulence is modeled using the $k-\epsilon$ model, and consequently the $k-\epsilon$ turbulence specification method is applied. In contrast, in the transient phase of the solution, LES is utilized, necessitating the specification of a fluctuating tran-

sient velocity. It should be noted that, while the roughness height (often denoted as the equivalent sand grain roughness, k_s) can be utilized to define the roughness of the wall in the steady solution, specifying a rough wall is not an option in the transient solution.

The following list summarizes the most important specifications for boundary conditions.

- Upstream surfaces:
 - Type: Velocity-inlet
 - Velocity specification method: Magnitude and direction
 - Velocity magnitude: Monin-Obukhov vertical profile
 - Fluctuating velocity algorithm: STG
- Side and top surfaces:
 - Type: Velocity-inlet
 - Velocity specification method: Magnitude and direction
 - Velocity magnitude: Monin-Obukhov vertical profile
 - Fluctuating velocity algorithm: No perturbations
- Downstream surfaces:
 - Type: Pressure-outlet
 - Prevent reverse flow: Yes
 - Average pressure specification: No
 - Target mass flow rate: No
- Ground and buildings:
 - Type: Wall
 - Shear condition: No slip

4.3.4. Solver Settings

In this chapter, the intricacies of the solver settings are employed in the simulations carried out for this study. The solver settings play a pivotal role in determining the accuracy, stability, and convergence of the computational fluid dynamics simulations. Various aspects, including the pressure-velocity coupling scheme, spatial discretization methods, transient formulations, and other key settings that shape the numerical solution, have been explored.

Pressure-Velocity Coupling Scheme: The choice of a suitable pressure-velocity coupling scheme significantly influences the efficiency and robustness of the solver. For steady-state simulations, a coupled pressure-velocity algorithm is employed. This choice ensures a more robust and efficient single-phase implementation by addressing the interdependence between the pressure and velocity fields.

Spatial Discretization: Spatial discretization methods are tailored to different variables within the simulation. The bounded central differencing (BCD) method takes prece-

dence over central differencing (CD) in transient simulations. This strategic selection improves stability and effectively resolves backflow issues on outlet surfaces. BCD is an improvement over CD designed to mitigate the issues of numerical oscillations. It incorporates limiting functions that restrict the difference to a certain range, preventing nonphysical oscillations in the solution. BCD is commonly used in more complex simulations, such as those involving turbulent flows, shocks, or other scenarios with rapid changes in the solution.

Transient Formulation: For transient simulations, the choice of a suitable transient formulation is paramount. A second-order implicit scheme is adopted, striking a balance between numerical accuracy and stability. This formulation enables the use of larger time steps while maintaining the required level of numerical robustness.

Pseudo-Transient Formulation for Steady Solutions: The pseudo-transient formulation is introduced to enhance the convergence behavior of steady-state simulations. This technique transforms the steady-state equations into a pseudo-time-dependent form, allowing for iterative updates within each pseudo-time step. Fictitious time steps are introduced to facilitate iterative updates. While there is no actual physical time progression, the solver iteratively refines the solution in pseudo-time, mimicking the convergence process of transient simulations. This approach enhances the solver's adaptability in navigating complex solution spaces. Pseudo-transient formulations prove valuable in scenarios where standard steady-state solvers face challenges in convergence. The introduction of pseudo-time enhances the solver's flexibility and adaptability during iterative convergence.

Warped-Face Gradient Correction: The application of warped-face gradient correction enhances solution accuracy by accounting for non-uniformities in the mesh. This correction ensures precise calculations of the gradients at the faces of the cells, contributing to the overall reliability of the results.

High Order Term Relaxation: Although not utilized in this study, high-order term relaxation is a consideration for stabilizing certain numerical schemes. This setting provides control over the influence of high-order terms in the discretized equations, affecting the stability of the solution.

In Chapter 4.4, more detailed information on time discretization is provided. Gravity plays a role especially for pollutant dispersion and was defined as an acceleration in the negative z direction, with a value of $g = 9.81 \text{ m/s}^2$.

Table 4.6 provides an overview of the solution controls for steady and transient setups, specifically focusing on the relaxation factors for various variables. Break down each entry in the table and discuss the implications of choosing specific values.

Pressure Relaxation Factor: The pressure relaxation factor influences the coupling between pressure and velocity fields. A lower value (0.30 in transient) indicates a stronger influence of pressure on velocity in each iteration. This can enhance stability, but might require more iterations for convergence.

Table 4.5.: Overview of solver settings for both steady and transient setups.

SOLVER SETTINGS		STEADY	TRANSIENT
pressure-velocity coupling scheme		coupled	SIMPLE
spatial discretization	gradient	least squares cell based	
	pressure	second order	second order
	momentum	second order upwind	BCD
	tke	second order upwind	✗
	ε	second order upwind	✗
pseudo transient formulation		✓	✗
transient formulation		✗	second order implicit
warped-face gradient correction		✓	✓
high order term relaxation		✗	✗

Momentum Relaxation Factor: The momentum relaxation factor affects the coupling between the momentum and velocity fields. A higher value (0.70 in transient) allows for a more gradual update of momentum, potentially improving stability. However, an excessively high value can lead to slower convergence.

Density Relaxation Factor: The density relaxation factor controls the update of the density. A value of 1.00 indicates that the density is fully updated in each iteration, maintaining a strong coupling with other variables. This is typical for incompressible flows.

Body Forces Relaxation Factor: The body forces relaxation factor governs the influence of external forces on the flow. A value of 1.00 implies a full update of body forces in each iteration, maintaining consistency with the other variables.

Turbulent Kinetic Energy (TKE) Relaxation Factor: TKE represents the energy associated with turbulent fluctuations. A relaxation factor of 0.75 in steady simulations moderates the update of TKE, striking a balance between stability and convergence. In transient simulations, direct updating of the TKE is not applicable.

Turbulent Dissipation Rate (ε) Relaxation Factor: Similar to TKE, ε represents the rate of dissipation of turbulent energy. A relaxation factor of 0.75 in steady simulations controls the update of ε , balancing stability and convergence. In transient simulations, the direct update of ε is not applicable.

Turbulent Viscosity Relaxation Factor: The turbulent viscosity relaxation factor controls the update of turbulent viscosity. A value of 1.00 implies a full update in each iteration in steady simulations. In transient simulations, direct updating of turbulent viscosity may not be applicable.

Choice of Values: The choice of relaxation factors depends on the specific characteristics of the flow and the desired trade-off between stability and convergence speed. Larger relaxation factors generally lead to more stable simulations, but may require more iterations for convergence. Smaller relaxation factors can accelerate convergence, but might make the simulation more susceptible to instability.

The selected values strike a balance tailored to the nature of steady- and transient-simulations, aiming for stability while maintaining reasonable convergence rates. Ad-

justments may be necessary on the basis of the specific requirements and behavior of the simulated flow.

Table 4.6.: Overview of solution controls for both steady and transient setups.

SOLUTION CONTROLS		STEADY	TRANSIENT
relaxation factors	pressure	0.50	0.30
	momentum	0.50	0.70
	density	1.00	1.00
	body forces	1.00	1.00
	tke	0.75	✗
	ε	0.75	✗
	turbulent viscosity	1.00	✗

4.3.5. Particle Dispersion Modeling

The chosen method for particle dispersion modeling is tailored to scenarios involving combustion particles, which are partially composed of pollutants. This method employs the discrete phase model, selected for its capacity to intricately simulate deposition, accurately track particle mass, specify particle size and distribution based on release type, and facilitate coupled interactions between the discrete and continuous phases. Parcels, representing clusters of particles, are injected and meticulously tracked at each time step, ensuring precise synchronization with the airflow. Statistical values, such as mean and RMS, are recorded for each cell to capture essential information.

For efficient computational tracking, the maximum number of steps for parcel movement is capped at 50'000, corresponding to a maximum transport time of around 2 hours and 46 minutes. The tracking distance is set to 3 km, equivalent to the total length or width of the computational domain. The release point, strategically located in the center of the domain, maintains a distance of approximately 1.5 km from the edges of the domain. This ensures that parcels have sufficient space to traverse the full length from the release point to the pressure-outlets of the domain.

To facilitate continuous tracking of parcels as they traverse the domain, monitoring points and planes are strategically placed to coincide with the paths of interest. In addition, parcels are tracked upon entering and exiting the domain. In particular, certain additional forces available in the properties of the discrete phase model, such as the Saffman lift force, the virtual mass force, and the pressure gradient force, are deemed inapplicable for this scenario. This is mainly due to significant variations in aerodynamic parameters and particle shape compared to the standard spherical model implemented in ANSYS®, making these specific forces irrelevant in the context of combustion particles.

4.3.6. Soot Properties

At Lund University, an extensive investigation was carried out by Malmberg (2019) to characterize the properties of soot generated from the combustion of flammable materials such as cables and oil. The findings of this study are the basis for the selection of parameters for particle dispersion modeling in computational fluid dynamics. Specifically, a constant particle size of $0.3\ \mu\text{m}$, accompanied by a density of $1800\ \text{kg m}^{-3}$, was derived. Figure 4.31 illustrates the size distribution of soot particles generated from burning oil, serving as a representative example of a specific fire scenario.

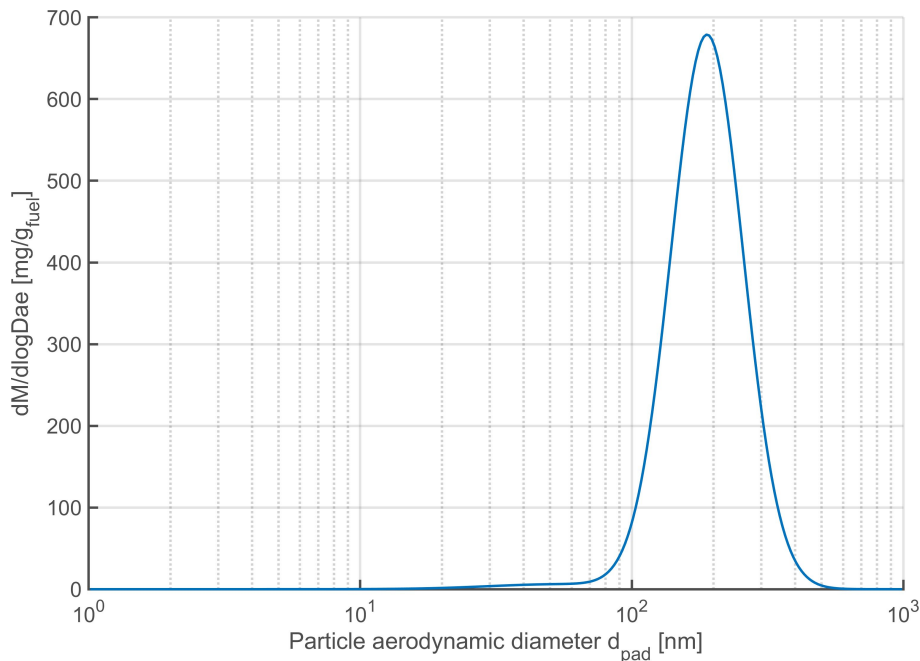


Figure 4.31.: Averaged aerosol size distributions following the report from Malmberg (2019).

In anticipation of accurately predicting the quantity and composition of soot released into the atmosphere, a filtration process analogous to that occurring within the facilities was taken into account. The accumulation of aerosols within the system results in larger particle sizes before their eventual release into the atmosphere. Consequently, a slightly larger mean size of $0.3\ \mu\text{m}$ was selected, deviating from the test results by approximately plus 50 %.

Various potential sources of indoor fires that encompass a range of fire scenarios within buildings have been identified. Colleagues from the FIRIA project (Fire-Induced Radiological Integrated Assessment), operating within the HSE (Health Safety & Environment) group, conducted indoor fire simulations using the Fire Dynamics Simulator (FDS), as detailed in the reference Pascual et al. (2020). Using the insights from these simulations, an intervention plan was developed for the fire brigade. The plan includes typical mass-flow and volume-flow soot rates, which serve as release terms for subsequent atmospheric boundary layer simulations. The release points for the combusted particles are strategi-

cally placed on the stack or fire-safety doors of the relevant surface buildings.

Figure 4.32 presents two representative mass flow rates for the release scenarios corresponding to the ISOLDE and ATLAS particle detectors. The total time to extinction was estimated using tools within fire risk assessment terminology. For the ISOLDE release scenario, the intervention time until fire extinction was evaluated to be shorter than for the ATLAS release scenario (15 vs. 60 min). The combination with a smaller release mass flow rate leads to an integrated total released mass over 15 minutes of 0.231 kg for the ISOLDE release scenario, while for the ATLAS release scenario, the integrated mass over 60 minutes was 0.934 kg. In the FIRIA project, these time estimates were derived using tools such as Pathfinder, considering the response time of the fire brigade to reach the source inside the building. This calculation takes into account factors such as fire and smoke propagation, as well as the time needed for fire extinction.

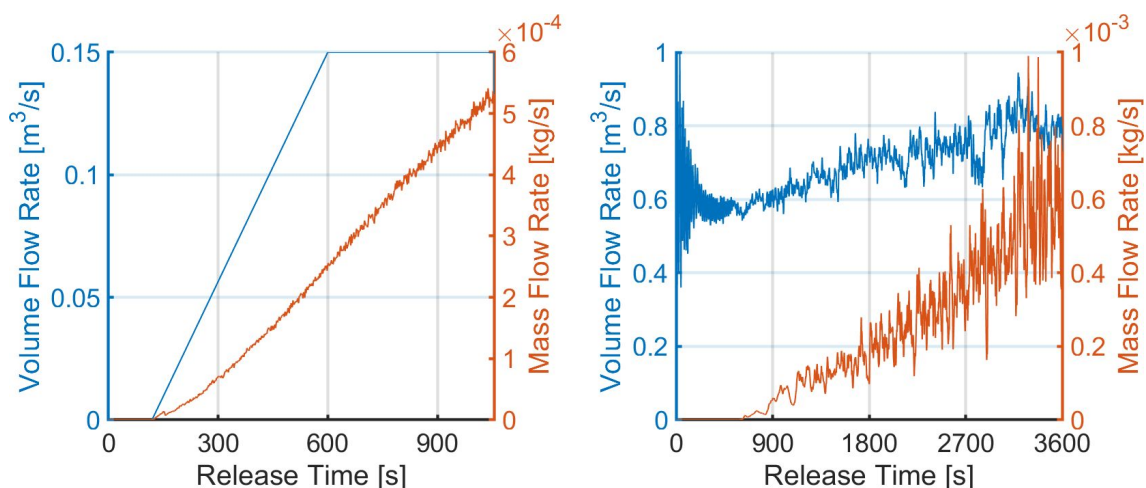


Figure 4.32.: Volume flow rate of the released air and mass flow rate of soot released into the atmosphere on the basis of FDS indoor simulations and estimated time to a complete fire extinction: ISOLDE facility on the left and ATLAS detector on the right. Time to fire extinction: ISOLDE 15 min and ATLAS 60 min.

4.3.7. Gas Dispersion Modeling

To simulate the release of toxic or radioactive gases, the Eulerian approach was used for scenarios involving the atmospheric dispersion of noble gas argon in the air. In this context, no chemical reactions between the two phases were assumed, and a multiphase model was deemed unnecessary. The mixture of the two gases was contingent on the turbulent quantities and the mass diffusivity of the two phases, where diffusivity plays a minor role in turbulent flows.

Air, a mixture of several gases, was treated as a single phase with a density of ρ_{air} equal to 1.23 kg m^{-3} . On the other hand, argon gas, with a density of ρ_{Ar} equal to 1.62 kg m^{-3} , is 1.3 times denser than air. The dynamic viscosity of air μ_{air} was set to $1.79 \cdot 10^{-5} \text{ kg m}^{-1} \text{ s}^{-1}$ and the dynamic viscosity of argon μ_{Ar} was set to $2.13 \cdot 10^{-5} \text{ kg m}^{-1} \text{ s}^{-1}$. The molecular

weights of the two fluids are $M_{\text{air}} = 28.97 \text{ kg kmol}^{-1}$ for air and $M_{\text{Ar}} = 39.95 \text{ kg kmol}^{-1}$ for argon.

The buoyancy significantly influences the dispersion of argon gas in the air as a result of the density disparity between the two fluids. The momentum equations account for the gravity forces within the mixture. A volume-weighted mixing law was chosen to calculate the density of the gas mixture, dependent on the volume occupied by each gas in each volume cell. The viscosity specification for the mixture is based on a mass-weighted mixing law utilizing the mass of each gas in each volume cell for the viscosity calculation. A constant dilute approximation was applied for mass diffusivity, with its value determined by diffusion coefficients for argon in nitrogen and oxygen, which are the main components that make up approximately 99% of the air mixture. According to Roberts R. C. (1963), the diffusivity for argon in both nitrogen and oxygen is $D_{\text{Ar}} = 2.0 \cdot 10^{-5} \text{ m}^2 \text{ s}^{-1}$, justifying a constant approximation under minor temperature and pressure changes.

4.4. Simulation Approach

The simulation approach for large-eddy simulation (LES) introduces complexities that are not encountered in relatively more straightforward procedures of steady Reynolds-average Navier-Stokes (RANS) simulations. Although LES offers a superior representation of the turbulent flow field, its implementation demands a higher investment in resources and expertise compared to steady RANS simulations. The challenges in pre-processing and post-processing contribute significantly to this demand.

To embark on an LES simulation, meticulous preparation is essential. This involves the generation of an appropriate mesh and the determination of initial/boundary conditions. Furthermore, a preliminary steady-state RANS simulation is often conducted to establish a starting point for the LES simulation. In particular, near-wall boundary conditions pose a specific challenge in LES and require careful consideration, contrasting with the relative ease of obtaining such conditions in steady RANS simulations. The mesh employed in LES must be fine-tuned to a degree that ensures the resolution of relevant turbulent vortices without resorting to modeling. It is crucial to emphasize the interconnected nature of the mesh, the boundary conditions, and the simulation approach. Consequently, the following points encapsulate the pivotal steps necessary to conduct meaningful LES simulations.

The initial phase of the simulation process involves the preparation of the geometry. Subsequently, the first mesh is generated, incorporating estimated sizes for surfaces, surface growth, and areas of interest, where finer mesh resolutions may be applied. With the foundational mesh in place, the simulation setup unfolds, marking the first application of boundary conditions, reference frames, monitoring points/lines/planes, expressions, and custom field functions. A preliminary steady Reynolds-Averaged Navier-Stokes

(RANS) simulation is initiated, providing insights for further mesh refinement.

This iterative process extends to the creation of subsequent meshes, where size functions are adapted based on feedback from preceding simulations. The cycle of steady RANS simulations and mesh refinement repeats until a mesh is defined, aligning with the dynamic needs of the simulation. Once the mesh configuration is established from steady RANS simulations, the simulation proceeds to initialize the turbulence. Synthetic fluctuations, represented by the variables k and ε , are introduced to superimpose the characteristics of the transient flow on the mean flow within the computational domain. This step enhances the transition between steady-state and transient solutions.

Attention turns to the critical Courant-Friedrichs-Lewy (CFL) criterion in the LES phase. This criterion, expressed by Equation (4.15), governs the time-stepping methods, ensuring that the time step remains sufficiently small to capture rapid flow variations. The adaptive CFL-based time-stepping method is employed, dynamically adjusting the time-step size to maintain $CFL < 1$ during the first LES run.

$$CFL = \frac{|u| \cdot \Delta t}{\Delta x} \quad (4.15)$$

Where $|u|$ is the maximum flow velocity in each cell, Δt the time-step size, and Δx the cell length. The CFL number must be kept below 1 for numerical stability. This criterion prevents the accumulation of numerical errors and ensures that the simulation accurately represents the dynamic behavior of turbulent flows.

In subsequent LES runs, the convergence criteria are adjusted, and the time-step sizes are varied, examining their impact on solution accuracy, particularly in relevant areas and output parameters. Once a verified strategy is established, the final simulations are set up, incorporating the chosen mesh, the time-step size, and the convergence criteria.

Before releasing pollutants into the domain, a comprehensive domain flush is performed, a process that takes approximately 30 minutes of simulation time. Following the flush, the pollutant release scenario unfolds, transporting pollutants throughout the domain within a time frame ranging from 15 to 60 minutes. After release, additional time is allocated for the pollutants to exit the domain or, at the very least, the area of interest.

In conclusion of this intricate simulation process, the monitored results are subjected to a thorough evaluation. Using either integrated tools within the simulation software or external programming languages, the data analysis illuminates the intricate details of LES with turbulent dispersion of pollutants within the ABL. In the sections of this chapter 4.4 the approach is further detailed.

4.4.1. Steady Solution

In this section, the steady solution is discussed, which serves as the initial assessment of both the mesh size and the boundary conditions. The application of the Monin-Obukhov similarity theory is instrumental in defining velocity-inlet boundary conditions, as elab-

orated in Chapter 4.3.1. These prescribed settings, detailed in the same chapter, are similarly extended to the walls and outlets. Beyond accounting for terrain and buildings, monitoring points, lines, and planes are strategically defined to monitor pollutant concentration in specified areas of interest.

The steady RANS simulations employ the realizable k - ϵ model with standard wall functions. A phased approach is adopted to solve the flow, in which a first-order upwind spatial discretization is initially applied, succeeded by second-order upwind spatial discretization for momentum equations, and finally extends to second-order upwind spatial discretization for momentum, turbulent kinetic energy (tke), and dissipation rate (ϵ) equations. This phased strategy was implemented in response to the challenges (divergence of momentum equations) encountered during direct simulation with second-order spatial discretization. The adoption of a phased approach was deemed more robust, providing a stable and effective solution to the encountered issues.

The resultant steady solution proves to be valuable in estimating the appropriate mesh size. This is achieved by evaluating the Kolmogorov length scale, the integral length scale, and the non-dimensional wall distance for a wall-bounded flow y_+ across the domain or in cross sections, as expounded upon in Chapter 4.2.4. Figure 4.33 illustrates an example of the velocity magnitude contour plot for a cross-section in the north-east wind direction of the final steady-state RANS solution. Due to domain size (500 meters depth and 3 kilometer length), the detail in the center around the buildings is not visible. The figure shows the definition of the velocity profile with 1 m/s at 10 meters altitude and its propagation throughout the domain.

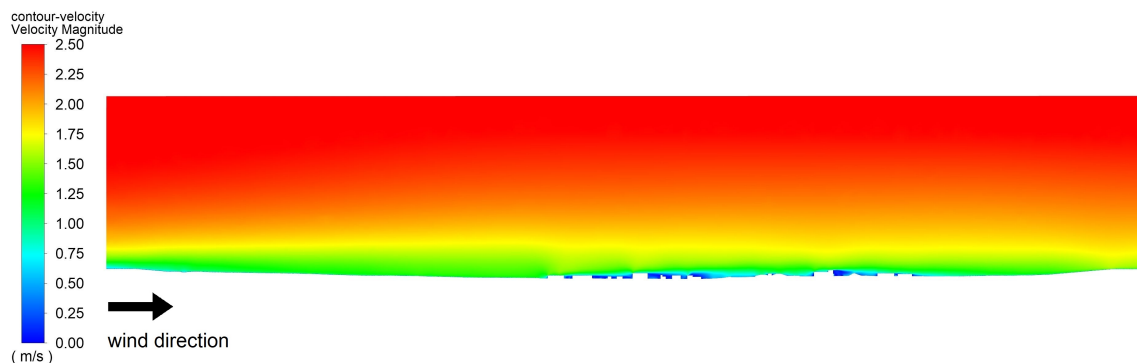


Figure 4.33.: Contour plot shown for a cross-section in flow direction and coloured with the velocity magnitude of the final steady-state RANS solution.

4.4.2. Transient Solution

To address the flow dynamics, including fluctuations in the velocity field, a transient solution becomes imperative. The conclusive steady-state Reynolds-average Navier-Stokes (RANS) solution serves as the initial condition for the transient large-eddy simulation (LES). The initialization process involves estimating time-dependent velocity fluctuations

($k, \varepsilon \rightarrow u'(t)$) utilizing mean velocity, turbulent kinetic energy, and dissipation rate data extracted from the steady-state RANS solution.

This initialization step is critical in transforming the mean flow field from steady solution to induce turbulence, as visualized in Figure 4.34. The discrepancy between Figures 4.33 and 4.34 lies in the described initialization process. In the latter figure, the velocity undergoes a modification, evident in regular fluctuations at the same altitude compared to the results shown in Figure 4.33.

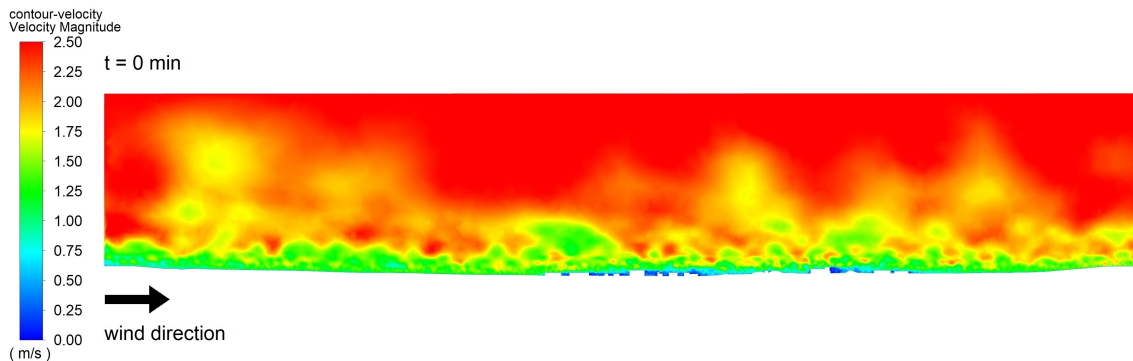


Figure 4.34.: Contour plot shown for a cross-section in flow direction and coloured with the velocity magnitude of the initialized turbulent fluctuating velocity field. $t = 0$ min

Following the introduction of a turbulent flow field, the transient LES is initiated. A comprehensive domain flush, spanning 30 minutes simulation time, is conducted to facilitate adequate development of the flow field within the LES framework. The duration of this flushing period depends on factors such as the size of the domain and the prevailing wind speed, ensuring that the release of pollutants starts within a fully developed ABL, as illustrated in Figure 4.35. In instances where computational efforts are not a limiting factor, an extended flushing period is advisable for more robust simulation results.

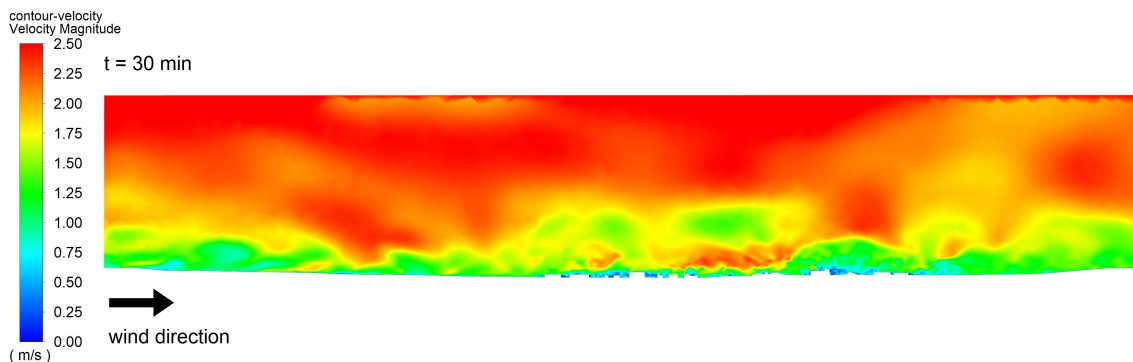


Figure 4.35.: Contour plot shown for a cross-section in flow direction and coloured with the velocity magnitude of the flushed transient solution. $t = 30$ min

In summary, the velocity fluctuations obtained from the steady state RANS solution, derived from the turbulent kinetic energy (k) and the turbulent dissipation rate (ε), as shown in Figure 4.34, exhibit a more predictable pattern compared to the fluctuations

observed in the flushed domain with LES, illustrated in Figure 4.35.

4.4.3. Pollutant Release

In transient large-eddy simulation (LES), various quantities averaged over time play a crucial role in the analysis and comprehension of flow field dynamics. These quantities offer valuable insight into the averaged characteristics of turbulent flows over time. Some key mean quantities routinely assessed include:

- Mean velocity (\bar{u} , \bar{v} , \bar{w})
- Turbulent kinetic energy ($\overline{u'u'}$, $\overline{v'v'}$, $\overline{w'w'}$)
- Reynolds stresses ($\overline{u'v'}$, $\overline{u'w'}$, $\overline{v'w'}$)
- Mean pressure (\bar{p})
- Mean scalar concentration (\bar{c})
- Shear stress (τ_{ij})

For scenarios involving pollutant release, it is often not necessary to assess the concentration of pollutant across the entire domain. To optimize simulation efforts, especially for the Lagrangian tracking method, specific areas of interest can be defined, such as monitoring points, lines, and planes. These defined areas are particularly crucial in transient simulations, enabling the tracking of pollutants over time.

In this study, the monitoring points are meticulously chosen for each scenario. Figure 4.36 illustrates a representative scenario involving a release from the ATLAS surface building. The monitoring points are strategically placed one meter above the ground, approximating the typical breathing height of the individuals. These points span various distances from a few meters to 200 meters from the release point, as illustrated in Figure 4.36.

Six monitoring lines are established to assess atmospheric flow, capturing time-resolved velocity data. This approach facilitates the computation of mean velocity, turbulent kinetic energy, and energy cascade plots at specific altitudes. Unlike monitoring points, these lines are independent of the release scenario and are strategically positioned throughout the domain where the dispersion pollutants are most prominent. The positions of these six monitoring lines are shown in Figure 4.37.

Furthermore, a set of up to five cross-wind planes is delineated at distances ranging from 40 to 400 meters from the release point. These planes serve as observation zones where the concentration of pollutants and the time-resolved velocities are monitored. The objective is to meticulously track the transport of pollutants along with the prevailing atmospheric wind conditions.

The dimensions of these planes are deliberately chosen to be sufficiently large in width and height, ensuring that 99.9% of the released parcels or species traverse through them. Note that the larger the planes, the larger the file sizes exported for each time step, leading to increased storage space usage. This results in a longer time for writing values at each

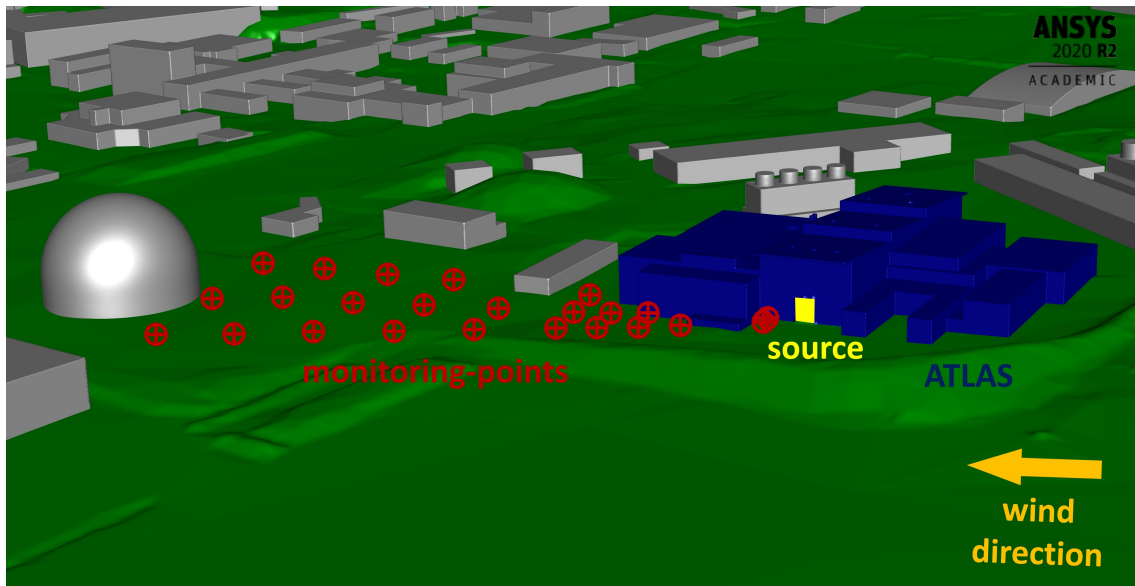


Figure 4.36.: Monitoring points, which are positioned at one meter above ground and which span various distances from a few meters to 200 meters from the release point.



Figure 4.37.: Monitoring lines, which are defined from ground level to the top of the domain.

iteration and a longer post-processing time for a large amount of data. Consequently, it is recommended to carefully select the plane size, opting for dimensions as compact as possible while retaining effective pollutant tracking. This recommendation holds for both particle and gas dispersion release scenarios.

In the case of dense gas releases, a meticulous choice of plane size is imperative. The

plane dimensions are adjusted, with the width significantly widened and the height reduced. This adjustment is made in consideration of the high density of gases, which induces a negative buoyancy effect, particularly in close proximity to the source. It is important to note that at larger distances, the effective density difference approaches zero.

For scenarios involving factors such as plume downwash due to wind suction on the downwind side of a building or plume rise resulting from high exhaust speeds, the selection of plane sizes demands careful adjustments. In these cases, the interplay of various atmospheric effects necessitates a thoughtful approach to ensure meaningful simulation results.

A tracking distance of up to 500 meters is determined for monitoring pollutants, aligning with the model setup's capability to accurately predict pollutant dispersion within this range. This choice is consistent with the microscale pollutant modeling approach adopted for dispersion studies. The dimensions of the plume, including its vertical stretching, reach an altitude of approximately 100 meters, corresponding to the height of the atmospheric surface layer under neutral stability conditions (as per Arya (2001)). Up to this height, the applicability of Monin-Obukhov similarity theory and other simplifications is maintained, allowing for streamlined consideration of meteorological conditions. It should be noted that obstacle-induced shear production and mechanical turbulence remain the predominant driving forces in the atmospheric surface layer within this altitude range.

Illustrated in Figure 4.38 is an example showcasing the placement of crosswind planes for the ATLAS scenario, where the wind direction is from the south. These planes not only serve as monitoring points for assessing pollutant concentrations and time-resolved velocities but can also be instrumental in validating mass conservation within the particle dispersion modeling approach.

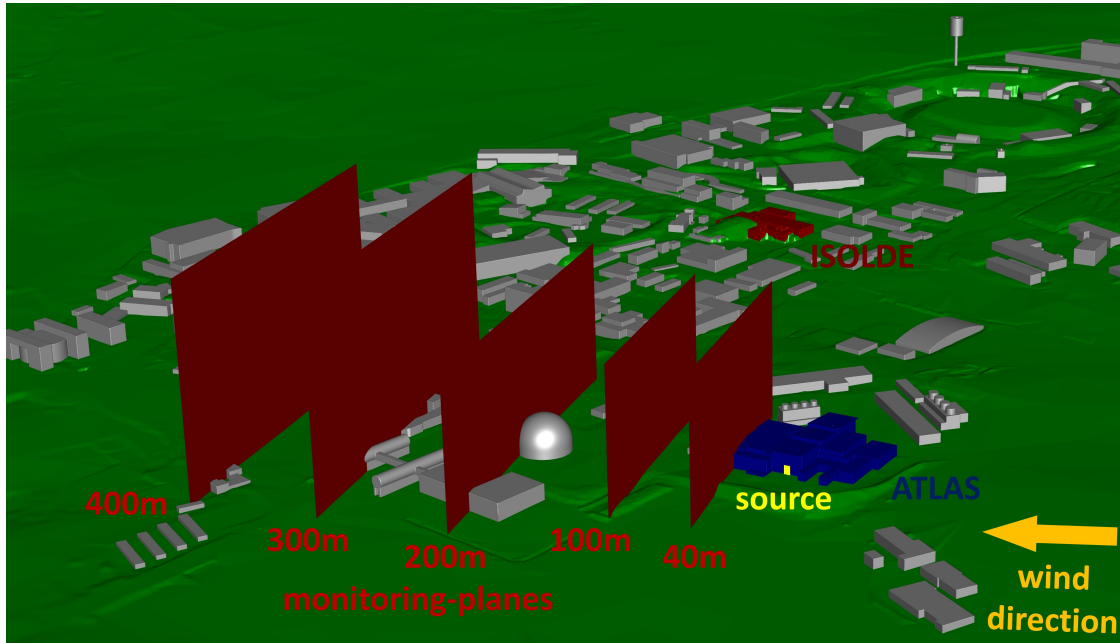


Figure 4.38.: Monitoring planes, which are defined in cross-wind direction at specific distances downstream from the release point.

4.5. Simulation Results

This section presents the simulation results for the boundary conditions and the simulation approach described in sections 4.1 to 4.4.

4.5.1. Time-Step Size

This chapter delves into the critical aspect of determining the size of the time-step, an essential element in attaining a dependable solution within large-eddy simulations (LES). The size of the time-step in LES plays a fundamental role in sustaining numerical stability, and its assessment revolves around the Courant-Friedrichs-Lewy (CFL) number, as elucidated by Courant et al. (1928). The CFL number, depicted in Equation 4.15, serves as a benchmark for evaluating the size of the time-step in the simulation. According to the equation for the CFL number, the time-step size (Δt) can be computed using the peak flow velocity ($|u|$) and the cell length (Δ):

$$\Delta t \leq \frac{\Delta}{|u|} \quad (4.16)$$

For the determination of cell length (Δ), the cube root of the polyhedral cell volume ($\sqrt[3]{V_{cell}}$) and the velocity magnitude $|V|$ are used. Consequently, the formula for estimating the time-step size Δt_{est} in the simulation takes the form:

$$\Delta t_{est} = \frac{\sqrt[3]{V_{cell}}}{|V|} \quad (4.17)$$

Adherence to the recommended time step size (Δt_{est}) ensures numerical stability for transient LES. As illustrated in Figure 4.39, the evaluation of the time-step size (Δt) suggests that a time-step size of ten seconds would be sufficiently small to meet the CFL condition for the outer part of the domain. In the inner zone, where mesh refinements are implemented as volumetric size controls, and a finer mesh resolution is applied on the ground, the estimated time step size is considerably smaller, ranging from approximately 0.2 to 2 seconds with the simulation specific velocity of 1 m/s at 10 meters height above the ground. The report derived from the estimated time-step size indicates that the minimum value is $\Delta t_{min} \approx 0.08$ seconds.

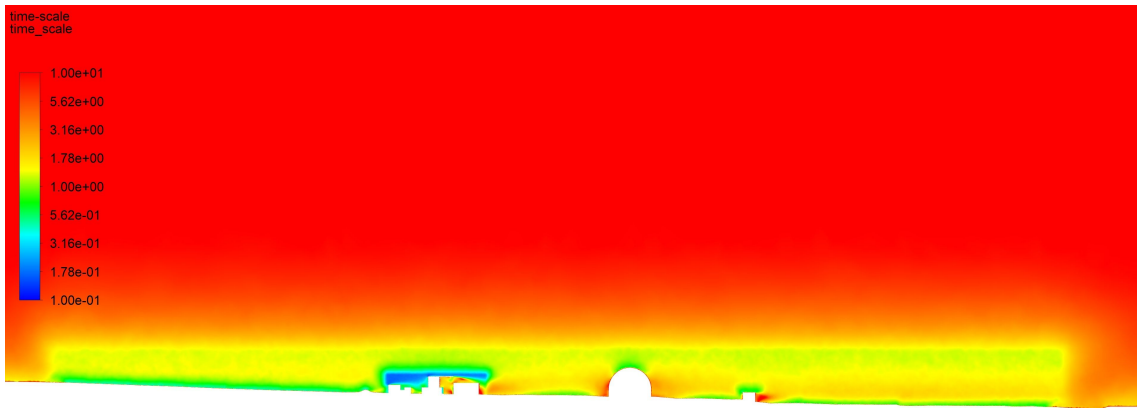


Figure 4.39.: Example for the time-step size Δt in a cross-section as enlarged view of the regions close to the release point.

Figure 4.39 illustrates the time step size (Δt) in a cross-section, with a detailed focus on regions near the release point. In order to ensure both numerical stability, the time-step size was incrementally adjusted, starting from an initial value of $\Delta t = 0.01$ seconds. The progression involved a systematic increase until a final time-step size was determined, considering factors such as the quality of the result, computational efficiency, and the amount of inner iterations. Each time step necessitates a certain amount of inner iterations until the solver achieves sufficient convergence. As the time-step size increases, the solver typically requires more inner iterations until the solution converges to the same extent. Hence, a trade-off between time-step size and inner iterations should be carefully considered to minimize the total iterations needed for a given simulation time. The final time-step size, $\Delta t_{fin} = 0.2$ seconds, emerged as the optimal choice, demonstrating good performance considering the above mentioned factors. Subsequently, the CFL number was calculated using the final time step size and continuously monitored throughout the LES to ensure that the CFL condition was met for the full simulation.

To verify the estimated time step size of the steady state simulations, the CFL number is checked in the transient LES, as shown in Figure 4.40. The observed CFL number ranges between $1.3 \cdot 10^{-3} \leq CFL \leq 9.1$, and the CFL number averaged in volume is $CFL_{avg} = 0.026$. Only a few cells in the very refined areas (body-of-interest around release points) have $CFL > 1$.

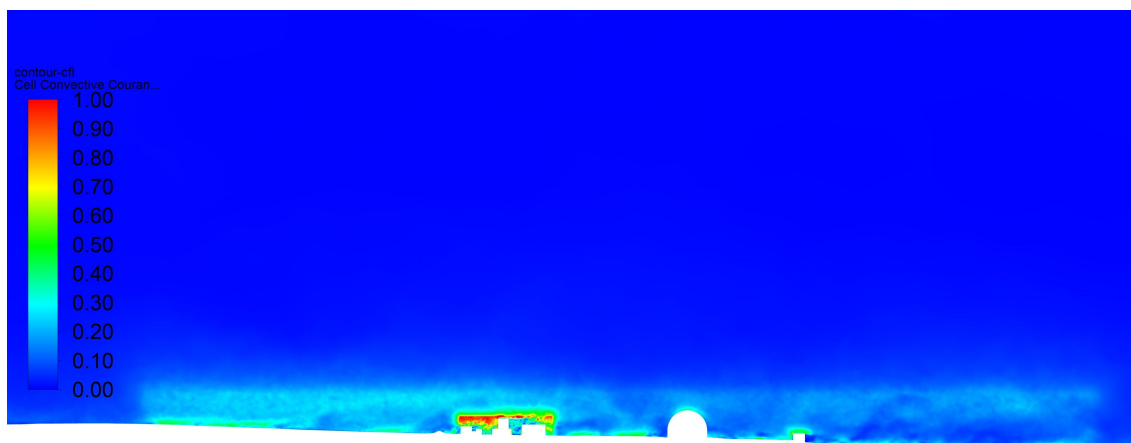


Figure 4.40.: Example of the CFL number obtained with a time-step size $\Delta t = 0.2\text{ s}$ in a cross-section as enlarged view of the regions close to the release point.

The areas where the CFL condition was not met underwent careful analysis. Key parameters and outputs were monitored to identify signs of instability, such as erratic behavior, divergence, or extreme values. In addition, the convergence behavior of the solution was examined to ensure that it remained within acceptable limits. The mesh independence study, detailed in Chapter 4.2.2, demonstrated the consistency of the results even when the CFL number varied significantly from the mesh presented in this chapter while maintaining wind speed and time-step size.

If the CFL number was exceeded, potentially impacting the flow, several options were considered. Adjustments could be made to the mesh, a specific body-of-interest, where mesh refinements are applied, could be removed from the simulation or modify the surface sizing on buildings. Alternatively, changes in the way the mesh size grows from the surfaces of buildings involved in the release were considered to ensure a smooth transition from the ground to the top of the simulation domain. This approach would result in larger cell sizes several meters above the roof, where the wind speed is higher, leading to a lower CFL number. However, it is important to note that employing a coarser mesh might negatively impact the amount of resolved turbulent kinetic energy.

Another option was to reduce the time-step size, although this might increase simulation run-times. The decision between adjusting the mesh or the time-step size depended on finding the right balance between computational efficiency and maintaining simulation stability.

4.5.2. Wall Resolution

Addressing wall resolution poses challenges in flows where wall effects are substantial. However, for atmospheric boundary layer flows, complete resolution of walls is not imperative due to terrain simplifications made during geometry preparation. Objects such as grass, small hedges, trees, and even distant buildings are not represented in the CAD models, allowing simplifications in inlet boundary conditions. The Monin-Obukhov ve-

locity profile, discussed in Chapter 4.3.1, specifies zero velocity at ground, with a velocity that increases with altitude. As long as the inlet flow profile remains uniform across the domain, the impact of not fully resolving the flow at the wall, as noted in von Kármán (1930), should be minor in the outer regions, as detailed in Chapter 4.5.3. Small vortices generated far from the release point or in the outer region are often irrelevant for pollutant dispersion in the central domain because eddies produced on the ground in the outer area dissipate relatively quickly.

In the inner part, where the flow is mainly disturbed by buildings and decelerated, an approximation is viable, given that the velocity at the ground and forces close to the ground are not substantial. Alternatively, rough walls for the ground or wall-modeled large-eddy simulation (WMLES) could be utilized to apply forces in the momentum equations for flow deceleration. Vasaturo et al. (2018) outlined an alternative approach to the standard ANSYS® Fluent method to implement these wall modeling conditions using user-defined functions.

$$\begin{aligned} u_+ &= y_+ \\ \frac{U}{u_\tau} &= \frac{u_\tau \cdot y}{\nu} \end{aligned} \quad (4.18)$$

In this context, the dimensionless velocity u_+ is obtained by dividing the mean velocity parallel to the wall U by the shear velocity u_τ . The dimensionless wall coordinate y_+ is defined as the product of the fraction of shear velocity u_τ and the distance from the wall y , divided by the kinematic viscosity ν . The shear velocity u_τ can be calculated by taking the square root of the wall shear stress τ_w divided by the fluid density ρ , as expressed below:

$$u_\tau = \sqrt{\frac{\tau_w}{\rho}} \quad (4.19)$$

In cases where the mesh lacks the fineness to resolve the viscous sublayer, the logarithmic law is applied within the height range of $30 \leq y_+ \leq 300$:

$$u_+ = \frac{1}{\kappa} \cdot \ln(y_+) + C^+ \quad (4.20)$$

In these equations, the von Kármán constant is denoted by $\kappa = 0.41$, and the constant $C^+ \approx 5.57$. The constant C^+ is an empirical constant that depends on the specific conditions and characteristics of the flow. It is determined through experimental data or calibration based on numerical simulations.

In the buffer layer (height range $5 < y_+ < 30$), located between the viscous sublayer and the log-law region, the two laws are blended. For the height range $5 < y_+ < 20$ an alternative approach is available to calculate the wall shear stress. An overview of the models used according to the dimensionless wall distance y_+ is given in Figure 4.41.

Since the near-ground cells are between one and three meters large, the cells are rather

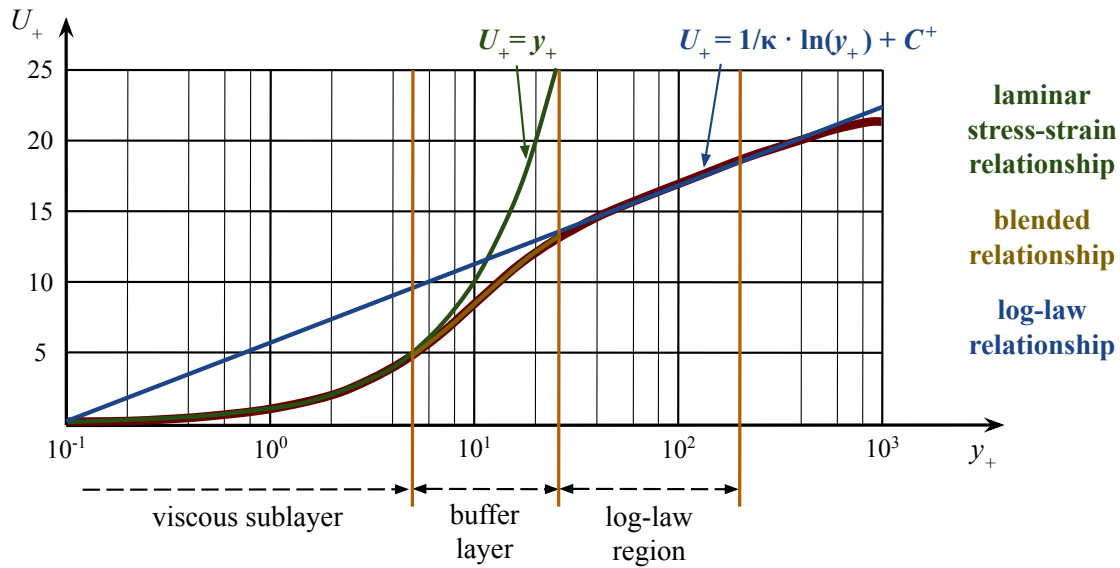


Figure 4.41.: Schematic example of the dimensionless wall distance y_+ values on walls.

coarse and lead to values for the dimensionless wall distance y_+ between 300 and approximately 3000, as shown in Figure 4.42. The logarithmic law can be applied in a suitable way in the inner part of the domain, where the dimensionless wall distance y_+ is within the maximum applicable range of $y_+ \approx 300$. In LES, the guiding principle for turbulence resolution is that a finer mesh resolves smaller eddy sizes, generally leading to a higher-quality solution. However, achieving a finer mesh comes at the cost of significantly increased computational resources and time. In practical terms, a compromise between solution quality and computational feasibility is essential, which is why the ground in the outer region was resolved with only three meters cell size. It should be mentioned that dispersion phenomena are solely tracked in the inner region, where the ground resolution with a cell size of one meter is sufficient to apply the log-law.

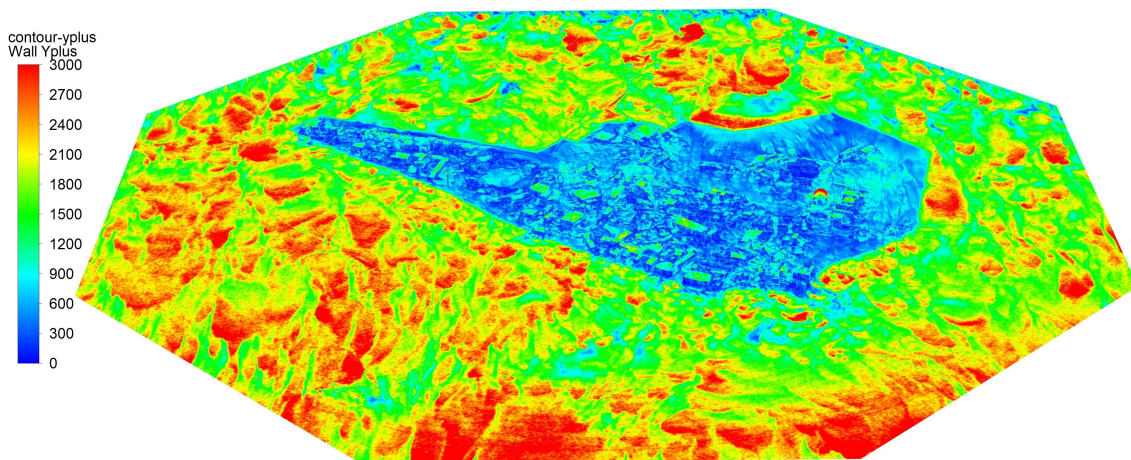


Figure 4.42.: Example for the dimensionless wall distance y_+ values on the ground and the buildings of the full domain.

4.5.3. Atmospheric Turbulence

In the examination of the simulation results, atmospheric turbulence and velocity emerge as pivotal factors influencing the transport and dispersion of pollutants. Consequently, these aspects are meticulously assessed and compared against theoretical profiles and references. To verify the consistency of the mean velocity profile applied at the boundaries within the inner domain, velocity profiles are scrutinized along six monitoring lines, as detailed in Chapter 4.3.1. Each assessment encompasses various wind directions and boundary conditions to ensure comprehensive coverage. The presented values undergo cross-verification to confirm their representativeness for each scenario.

Mean Velocity Magnitude

To evaluate the mean velocity profiles, time-dependent velocities are continuously monitored throughout the transient LES simulation. Instantaneous velocity components $u_i(z, t_n) = u, v, w(z, t_n)$ at a given altitude z above ground and at each time step t_n (where n is the total number of time steps) are used to calculate the time-averaged or mean velocity components $U_i = U, V, W$ for each monitoring location. The velocity components are defined such that u is the velocity component in the main wind direction, v is the velocity component perpendicular to the main wind direction, and w is the vertical velocity component.

$$U_i(z) = \frac{1}{n} \cdot \sum_{n=1}^n u_i(z, t_n) \quad (4.21)$$

Using the mean velocity components U, V, W , the mean velocity magnitude $|V|$ can be calculated as follows:

$$|V|(z) = \sqrt{U(z)^2 + V(z)^2 + W(z)^2} \quad (4.22)$$

The mean velocity magnitude $|V|$ is then compared to the velocity profile at the inflow boundaries, where the Monin-Obukhov similarity theory is employed. In Figure 4.43, an exemplary case is presented to illustrate the effectiveness of the applied boundary conditions. The theoretical profile serves as an approximation of how the wind may be distributed at specific altitudes and is influenced by the terrain and the presence of obstacles such as buildings, trees, and other structures. This comparison allows for the evaluation of the performance of the synthetic turbulent inlet conditions and the overall correlation between the theoretical profile and the simulation results. A minor discrepancy is observed in line-1, where the wind flow exhibits a slightly higher speed near the ground compared to other positions. Examining the location of line-1, shown in Figure 4.37, reveals its placement on the hill in the center of the domain, where the flow experiences acceleration in proximity to the ground.

In Figure 4.43, the mean velocity magnitude profile $|V|$ is normalized with the reference

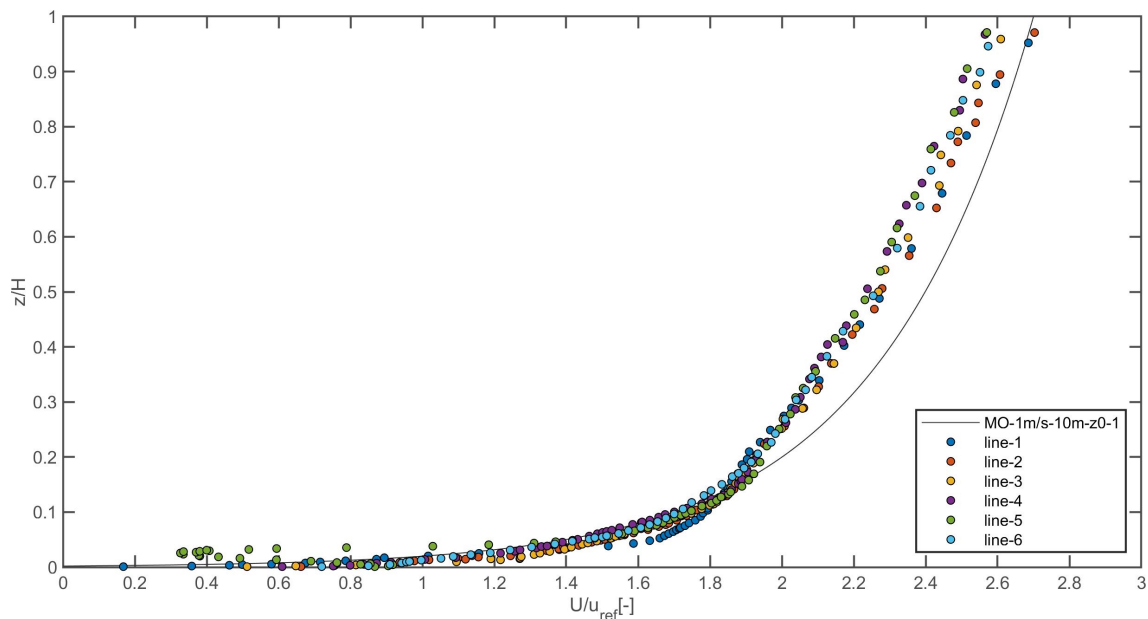


Figure 4.43.: Mean velocity magnitude profile $|V|$, obtained from a LES, performed for the ATLAS scenario, with south-west winds with $H=500$ m and $u_{ref}=1$ m/s.

velocity $u_{ref} = 1$ m/s, and the altitude z is normalized with the height of the domain $H = 500$ m. The black line represents the Monin-Obukhov theory, with conditions set for the neutral stability class, including a reference velocity $u_{ref} = 1$ m/s at a reference height $z_{ref} = 10$ m and terrain roughness $z_0 = 1$ m. The velocity close to the ground shows consistency across all line positions compared to the theoretical profile. A slight deviation of approximately 10% is noticeable at higher altitudes, starting at $z/H = 0.2$ m, where the flow is less influenced by terrain and obstacles. ground. Given that pollutant tracking occurs primarily in the surface boundary layer and the Monin-Obukhov similarity theory is not universally applicable to all geometries, this discrepancy is deemed acceptable. Moreover, the deviation is consistent for both the synthetic turbulent inlet and the inlet with no perturbations, indicating the acceptable performance of the synthetic turbulence generator (STG) at the inlet in terms of stable mean quantities.

In the context of particle transport, the mean velocity plays a crucial role, particularly in the near-ground region, where a significant concentration of pollutants tends to accumulate. The speed of particle movement directly impacts the concentration integrated in time within cells. Slower particle movement results in a longer residence time in a specific region, leading to higher concentrations incorporated over time. This extended duration allows particles to accumulate and persist, contributing to an overall increase in concentration over time. Consequently, when particles move more slowly under the same release mass-flow conditions, it can lead to elevated concentration levels in specific areas.

Turbulence Intensity

In addition to the mean velocity, turbulent motion plays a crucial role in tracking the dispersion of pollutants. Turbulent flow contributes to the enlargement of the plume and a wider distribution of particles, driven by high fluctuating velocities in transverse and vertical directions. Therefore, it is imperative to examine the intensity of the turbulence as a key characteristic of the turbulent atmospheric flow. This involves calculating the fluctuating velocity components $u'_i(z, t_n) = u', v', w'(z, t_n)$ derived from the instantaneous velocity components $u_i(z, t_n) = u, v, w(z, t_n)$ and their corresponding mean velocity components $U_i(z) = U, V, W(z)$.

$$u'_i(z, t_n) = u_i(z, t_n) - U_i(z) \quad (4.23)$$

To calculate the turbulent kinetic energy k , the initial step involves determining the variance $\sigma_{u_i}^2(z)$. This is achieved using the components of fluctuating velocity $u'_i(z, t_n)$ and the total simulation time T , which results from the constant time step size Δt multiplied by the total number of time steps n . The equation for calculating the variance of velocity fluctuations is provided by Equation 4.24:

$$\sigma_{u_i}^2(z) = \frac{1}{n \cdot \Delta t} \cdot \sum_{n=1}^n u'_i(z, t_n)^2 \quad (4.24)$$

After determining the variance of the fluctuating velocity components, the turbulent kinetic energy k can be calculated by adding the variances of the fluctuating velocity components $\sigma_{u_i}^2(z)$ multiplied by 0.5. This is expressed by Equation 4.25:

$$k(z) = \frac{1}{2} \cdot (\sigma_u^2(z) + \sigma_v^2(z) + \sigma_w^2(z)) \quad (4.25)$$

However, due to variations in the definition of turbulent kinetic energy k in the literature, turbulent intensity I_i is utilized for comparison with ESDU (1985) or VDI 3783/12 (2000). The turbulence intensity represents the ratio of the standard deviation $\sigma_i(z)$ of the corresponding velocity component to the mean velocity magnitude $|V|(z)$, as defined by Equation 4.26:

$$I_i = \frac{\sigma_i(z)}{|V|(z)} \quad (4.26)$$

At lower altitudes ($z < 100$), an estimation for the standard deviations σ_i can be used, based on the approximations proposed by Arya (1982) and Lumley and Panofsky (1964):

$$\sigma_u : \sigma_v : \sigma_w = 1 : 0.75 : 0.5 \quad (4.27)$$

Depending on the ground roughness value z_0 , the estimated values of the turbulent intensity I_i vary in magnitude. An illustrative example of turbulent intensity I_i is depicted for the positions of the monitoring lines in Figure 4.44. In addition, reference lines

from ESDU (1985) have been added for slightly rough ($z_0 = 5$ mm), moderately rough ($z_0 = 0.1$ m), rough ($z_0 = 0.5$ m) and very rough ($z_0 = 2$ m) to compare the simulation results with the reference values. The reference from ESDU (1985), which is also presented in VDI 3783/12 (2000) for wind tunnel measurements, are rather conservative in terms of predicting the turbulence intensity, which is why a newer reference will soon be released by VDI. For comparison reasons, the old reference is kept, keeping in mind that values might be slightly over-predicted.

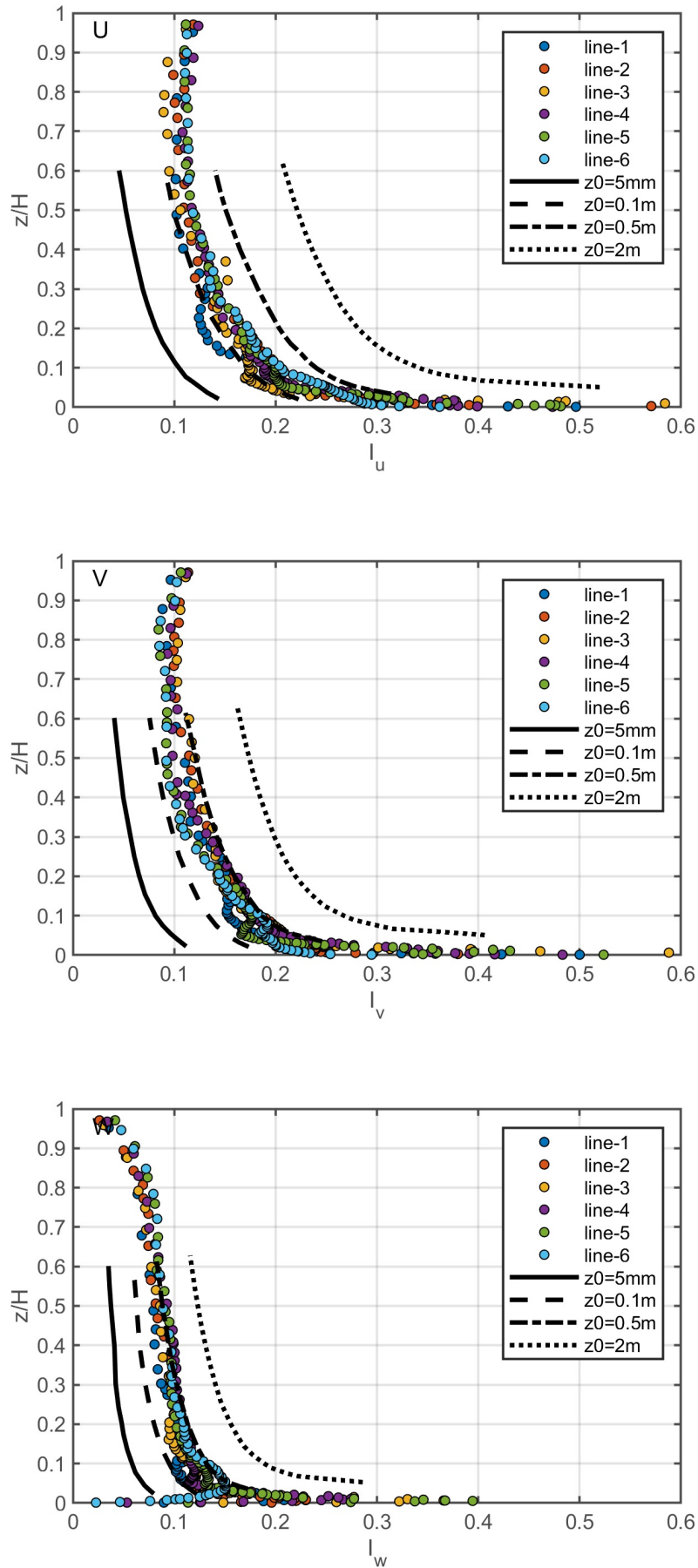


Figure 4.44.: Turbulent intensity profiles I_i , obtained from a LES, performed for the AT-LAS scenario, with wind blowing into North-East direction with $H = 500$ m.

Spectral Distribution of Turbulence Kinetic Energy

The spectral distribution of turbulence kinetic energy represents a crucial metric to assess ABL flow. These spectra can be analyzed in various directions, including along the flow direction (uu), laterally to the flow direction (vv), and vertically to the flow direction (ww). Additionally, co-spectra (uv, uw, vw) can be derived.

Evaluating the spectral distribution of turbulence kinetic energy is essential for examining resolved eddy sizes in large-eddy simulations (LES) and comparing them to established reference values, such as those provided by Kaimal et al. (1972) and Simiu and Scanlan (1986). The procedure described here follows the reference of VDI 3783/12 (2000), which highlights the procedure to plot the spectral distribution of turbulence kinetic energy in the flow. In particular, these references have been adapted to utilize local velocity variances σ_i^2 instead of friction velocity u_*^2 (refer to Equations 4.28 and 4.29), following the empirical relationship established by Counihan (1975). The detailed procedure for obtaining the spectral distribution of turbulence kinetic energy is well documented in Chapter 8 of Stull (1988) and Appendix E of Hertwig (2013). The MATLAB code used in this process underwent thorough validation using standard testing methods, including periodic functions, Gaussian white noise processes, and a first-order autoregressive process, as described in Hertwig (2013).

Kaimal et al. (1972) - modified:

$$\frac{f \cdot E_{uu}}{\sigma_u^2} = \frac{16.8f^*}{(1 + 33f^*)^{5/3}}; \quad \frac{f \cdot E_{vv}}{\sigma_v^2} = \frac{4.8f^*}{(1 + 9.5f^*)^{5/3}}; \quad \frac{f \cdot E_{ww}}{\sigma_w^2} = \frac{1.3f^*}{(1 + 5.3f^{*5/3})} \quad (4.28)$$

Simiu and Scanlan (1986) - modified:

$$\frac{f \cdot E_{uu}}{\sigma_u^2} = \frac{32f^*}{(1 + 50f^*)^{5/3}}; \quad \frac{f \cdot E_{vv}}{\sigma_v^2} = \frac{4.3f^*}{(1 + 9.5f^*)^{5/3}}; \quad \frac{f \cdot E_{ww}}{\sigma_w^2} = \frac{2.2f^*}{(1 + 10f^{*5/3})} \quad (4.29)$$

The spectral distribution of turbulence kinetic energy for the simulations are computed on the basis of the fluctuating velocity terms employing fast Fourier transformation (FFT) to reveal the size of vortices within the simulation. Small eddies or high frequencies can be effectively resolved using a significantly reduced cell size cs and time step size Δt . Conversely, large eddies or low frequencies are typically resolvable, contingent upon the total simulation time, which inherently influences the prediction's uncertainty.

Although detection of large eddies is possible, they occur less frequently. Only a handful of very large eddies could traverse a specific location in several minutes. The limited data sampling time and the infrequent occurrence of these large eddies contribute to higher uncertainty compared to smaller eddies. However, very small eddies also pose a challenge for resolution due to an excessively large time step Δt or cell size cs . The maximal frequency f_{max} resolvable with the corresponding cell size Δx and stream-wise mean velocity U can be estimated using the following relation:

$$f_{max} = \frac{1}{4} \cdot \frac{U}{\Delta x} \quad (4.30)$$

For a complete estimation of the maximal frequency f_{max} at all heights above ground, the factor of 1/4 was determined by iterative testing with various factors. The graphs were visualized for irregularities during factor variations and an optimal value was chosen. To align the maximal frequency f_{max} with the frequency of the spectra plots, normalization is needed by the height z and the mean stream-wise velocity U , after which it can be plotted on the abscissa axis.

$$\begin{aligned} \tilde{f}_{max} &= f_{max} \cdot \frac{z}{U} \\ \tilde{f}_{max} &= \frac{z}{4 \cdot \Delta x} \end{aligned} \quad (4.31)$$

The calculation of the spectral distribution of turbulence kinetic energy adheres to the procedure outlined in Chapter 8 of Stull (1988), which requires the input parameters as follows.

- Instantaneous velocity series along the flow direction u .
- Instantaneous velocity series lateral to the flow direction v .
- Instantaneous velocity series vertical to the flow direction w .
- Equidistant time series t_{eq} .
- Height of each corresponding monitoring point, where u_i are observed.

These parameters are extracted from data recorded for the six monitoring lines during the LES and can be imported into any post-processing tool, where they are then transformed into arrays, such as in MATLAB or Python. For smoothing functions, a non-dimensional frequency of $inc = 0.09$ was chosen. With a corresponding time step size of $\Delta t = 0.2$ s, this results in a time series of approximately $N \approx 2^{15}$ samples. The resulting graphs, shown in Figure 4.45, illustrate the spectral distribution of turbulence kinetic energy for the three main directions and are presented in log-log format. In addition to the simulation results, a reference range is provided following the work of Erdmann (2017), who derived a reference spectra bandwidth from the commonly applied literature in the field of atmospheric boundary layer flows. The reference range includes the research of von Kármán (1948), Kaimal et al. (1972), Simiu and Scanlan (1986), ESDU (1985), and Kaimal and Finnigan (1994) and is defined using the common approach function for spectra 4.32 for five coefficients following VDI 3783/12 (2000).

$$\frac{f \cdot E_{ii}}{\sigma_i^2} = \frac{\mathbf{A} \cdot f^*}{(\mathbf{E} + \mathbf{B} \cdot f^* \mathbf{C})^D} \quad (4.32)$$

The coefficients for the spectral kinetic energy of the turbulence are taken from Erdmann (2017) and can be found in Table 4.7.

In Figure 4.45, the representation of the spectral distribution of turbulence kinetic energy with respect to the sizes of the eddies is presented at an elevation of $H = 10.17$ m.

Table 4.7.: Coefficients for the spectral kinetic energy of the turbulence following Erdmann (2017) and VDI 3783/12 (2000).

Component	A	B	C	D	E
S_{uu} min.	6.57	95.30	1.36	1.24	0.69
S_{uu} max.	37.61	39.74	0.96	1.72	0.74
S_{vv} min.	5.14	27.97	1.17	1.45	1.91
S_{vv} max.	19.22	10.74	0.85	1.92	0.90
S_{ww} min.	0.76	45.32	3.00	0.57	0.50
S_{ww} max.	12.62	11.63	1.48	1.12	1.72

The observed trends in the curves for all three directions exhibit a close resemblance to the reference range at this specific height. In particular, similar frequency ranges, corresponding to the peaks of energy, can be identified across all three components.

However, at the lower end of the frequency spectrum, which corresponds to larger turbulence structures, some disparities emerge for all three components. These deviations are more pronounced because of the infrequency of occurrence of these large eddies in comparison to vortices in the inertial subrange. It is crucial to recognize that the estimation of their spectral content is also influenced by the simulation's limited time duration. The short sampling period in the simulations is reflected in the results.

In the case of the u-component, a characteristic roll-off of the spectral distribution of turbulence kinetic energy is observed, exhibiting a power-law decay of approximately $-2/3$ of the scaled frequency in the inertial subrange for more than one decade. However, for the v and w components, the reduction is more substantial, and this behavior is present for only about a half decade. The chosen time step size of $\Delta t = 0.2$ s, corresponding to a sampling frequency of 5 Hz, imposes limitations on the resolution of high frequencies, restricting the simulation from capturing the same level of detail as field measurements, for example.

Multiple investigations of the distributions of the kinetic energy of turbulence for various simulations have led to the conclusion that the predictions remain accurate up to an altitude of $H = 100$ m. Beyond this altitude, the impact of shear production from ground obstacles diminishes and the turbulence observed at these heights is primarily the result of the turbulent inlet specification method.

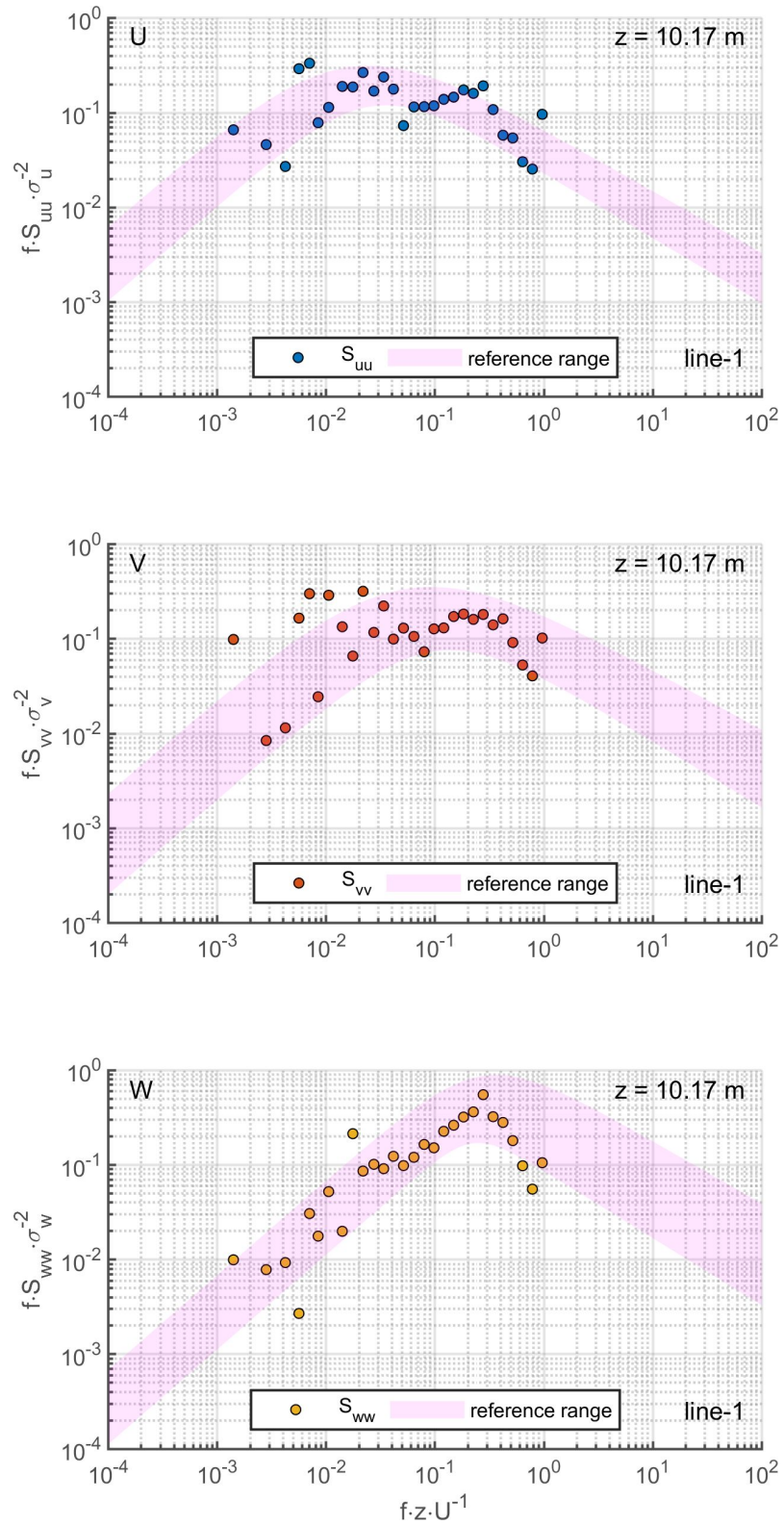


Figure 4.45.: Spectral distribution of turbulence kinetic energy S_{uu} , S_{vv} and S_{ww} , obtained from a LES, performed for the ATLAS scenario, with south-west winds at $H = 10.17$ m. The reference range from Erdmann (2017), covering most common approaches in literature are added as comparison.

5. Discussion - Findings and Guidelines

This chapter presents the results of numerous numerical studies conducted with the modeling approach outlined in Chapter 4, accompanied by a discussion of the results obtained. The primary objective of these investigations is to formulate recommendations for conducting simulations in the context of the FIRIA project at CERN, specifically to obtain accurate pollutant concentration data near release points. Additionally, the chapter aims to discern the behavior associated with urban pollutant dispersion simulations, focusing on the most comprehensive approach in applied modeling of near-ground atmospheric boundary layer flows: Large-Eddy Simulation (LES).

Given the absence of reference data from field or wind tunnel experiments for the validation of results, the LES outcomes are compared with those derived from an analytical Gaussian plume model employed at CERN. These comparative analyzes are detailed in Section 5.1. Then comes Section 5.2, which analyzes boundary conditions and the sensitivity of the results to these.

5.1. Comparison of GPM and LES

This chapter provides a comparative analysis between the Gaussian plume model (GPM) utilized at CERN and the computational fluid dynamics simulations conducted using large-eddy simulation (LES). Given the inaccessibility of validation through field or wind tunnel data, an alternative verification approach is pursued. The strategy involves comparing the numerical simulation results with those obtained through an analytical model, which has been calibrated and validated against real test scenarios. The discussion covers both the similarities and differences inherent in these two modeling approaches. The CFD modeling methodology adheres to the procedure outlined in Chapter 4.

The Gaussian plume model (GPM) employed at CERN primarily adheres to the guidelines outlined in the document "Calculation of radiation exposure in the environment due to emissions of radioactive substances from nuclear facilities - Guidelines for Swiss nuclear facilities" by the Swiss Federal Nuclear Safety Inspectorate (ENSI), as referenced in ENSI-G14 (2009). A concise excerpt from the internal CERN report, documented in Vojtyla (2022), which mentions the utilization of the GPM at CERN, is included in Appendix C. Generally, some models were updated following the state-of-the-art in science and technology and the particularities of CERN facilities.

5.1.1. Similarities of GPM and LES

This section involves a comparison between the results obtained from the large-eddy simulation (LES) and those derived from the Gaussian plume model (GPM). To facilitate this comparison, a straightforward release scenario is selected, minimizing the impact of buildings and other obstacles. The primary objective is to validate the LES approach under simplified conditions before exploring differences in the next section when introducing complexity to the release scenario.

The comparison aims to demonstrate that while analytical GPMs can yield results similar to LES, which requires more computational effort, there are notable differences when the release scenario becomes more intricate. It highlights that GPM may be suitable for straightforward scenarios, but its efficacy diminishes when specific scenario factors are altered.

Although detailed comparison is challenging due to disparities in modeling turbulence, geometry, and other factors, a qualitative evaluation is conducted to gauge whether the models predict results of comparable magnitudes. This comparative analysis also serves as a partial validation of the CFD simulations, given the unavailability of field or wind tunnel data for detailed LES validation within the stipulated time frame.

For this comparative analysis, the ATLAS scenario featuring a door release is selected as a case study. In this particular scenario, the wind flows in two main directions: north-east (NE) and south (S). This creates a flow with distinct landscape characteristics downstream of the release point. In the NE direction, the terrain is relatively flat, characterized by grasslands dominating the surface. In contrast, in the S direction, the flow is interrupted by buildings downstream and the terrain experiences a slight descent.

The expectation is that the plume size and observed concentration in the NE direction for the large-eddy simulation (LES) will exhibit a closer match to the results obtained from the Gaussian plume model (GPM) than in the S direction. This anticipation is grounded in the landscape differences and the influence of buildings on the flow downstream in the S direction.

To facilitate a comparison between GPM and LES, the analysis focuses on concentration values at specific points and plane locations, as illustrated in Figures 4.36 and 4.38. Pollutants are released from the door located on the eastern wall of the ATLAS surface building. The ATLAS building is located north-east of the CERN Meyrin site, as shown in Figure 5.1. Two potential release points are considered. First, a release through the door, where the fire brigade would access the buildings in case of a fire. In this scenario, smoke or pollutants exit without filtration, resulting in a generally higher release of pollutants in a short period of time. The second scenario involves the ventilation stack, where filtration with High-Efficiency Particulate Air/Arrestance (HEPA) filters would drastically reduce the amount of pollutants released. In the fire scenario, the release of smoke through the door is deemed relevant, while in a scenario involving argon gas, extraction through the ventilation stack is more significant.

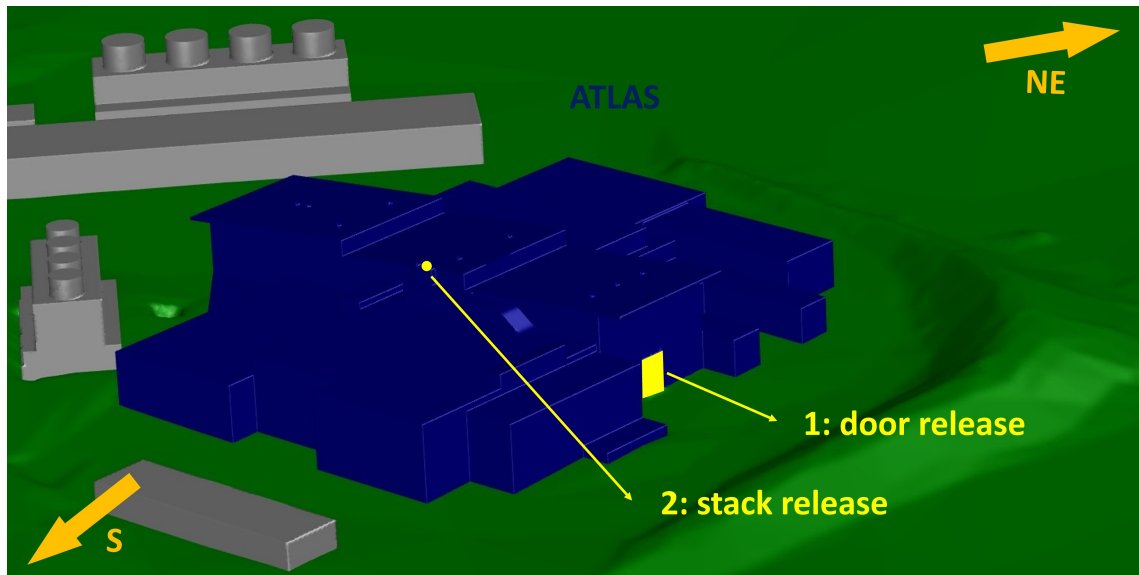


Figure 5.1.: ATLAS surface building in blue and its possible release points from a door (1) for fire brigade access and from a small stack (2) with emergency extraction of gases from the cavern.

Before conducting steady or transient CFD simulations for pollution dispersion release scenarios at CERN, the analytical Gaussian plume model (GPM), in accordance with the Swiss Guideline ENSI G14 as outlined in ENSI-G14 (2009), was used to predict the concentration of pollutants in the surroundings of CERN for specific release scenarios. The primary purpose of using GPMs is to assess the potential impact of pollutant release on the population, predict the direction of the plume, and formulate emergency intervention plans. It is worth noting that, since CERN is not a nuclear power plant, certain parts of the guideline have been adapted. This adaptation is necessary because even in scenarios involving terrorist attacks on CERN, the impact on the population remains at a low level compared to similar events at nuclear power plants, which have a much broader affected area and more significant consequences for the recipients.

It is essential to recognize that GPMs do not explicitly resolve terrain or buildings, nor do they simulate the detailed dynamics of air flow. However, these models incorporate these factors within their framework. In the case of planned short-term releases, the GPM model employs an average wind speed or a reference velocity of $u_{ref} = 1 \text{ ms}^{-1}$, chosen to be conservative but sufficient to transport pollutants to receptors. Although GPMs do not explicitly model airflow and predict its direction, they excel in providing a sufficiently accurate, efficient, and simplified mean dispersion modeling. In addition, important factors such as the decay, deposition, and exposure modeling of pollutants can be integrated for dose assessment. It should be noted that the results of the dose assessment are based on concentration values, which can also be derived from CFD simulations.

To compare the results of CFD and GPM, the integrated concentration values over time are normalized by the total released mass, which, in this specific scenario, was

$m_{release} = 0.931$ kg. In CFD simulations, a species transport model, detailed in Chapter 3.3.2, was used to represent pollutants released as air within the primary phase that represents the wind. Since combustion in this scenario does not significantly alter the density of the released mixture, temperature differences were not considered. The smoke released, at an ambient temperature, and neutral stratification for the atmospheric boundary layer with the Monin-Obukhov mean velocity profile defined at the inlet were assumed. Fluctuations at the inlet were generated using the synthetic turbulence generator (STG), as discussed in Chapter 4.3.1. The CFD simulations used a combination of a digital terrain model (DTM) for terrain elevation and a CAD model for buildings, introduced in Chapter 4.1.

Figure 5.2 illustrates the time-integrated and normalized concentration \tilde{c} in the crosswind plane, located 110 meters from the release point, with the wind blowing in the northeast direction. The coordinate system aligns with the wind direction, and the x coordinate pointing in the wind direction at $x = 110$ meters, as indicated in the top left legend of Figure 5.2. The y-coordinate represents the crosswind direction and is plotted along the abscissa, while the z-coordinate shows the height above sea level and is displayed on the ordinate. Various dispersion parameters can be derived from these crosswind planes, defined for each specific distance:

- \bar{y} [m]: Total displacement of the center line of the plume weighed by concentration in the y direction, indicated in the figure with a vertical black cross.
- \bar{z} [m]: Total displacement of the center line of the plume weighed by concentration in the z direction from sea level, indicated in the figure with a horizontal black cross.
- \bar{z}_0 [m]: Total displacement of the center line of the plume weighed by concentration in the z-direction from ground level.
- A [m²]: Surface of the plume cross-section in the crosswind plane with integrated normalized values of $\tilde{c} > 10^{-5}$.
- \tilde{c}_{max} [m⁻³]: Maximum value of the observed normalized concentration in the crosswind plane.

These parameters facilitate the comparison of different models, allowing the evaluation of plume properties such as size, displacement, maximum observed concentration, and received dose for individuals at specific distances. The concentration of the species in designated areas within the simulation domain is determined either from the species field or the Lagrangian particles located in those areas.

In cases where pollutants are released with constant mass flow and the surrounding air moves slowly, concentration values tend to be higher because of the longer residence time of the particles. These higher concentration values traverse the domain and lead to higher concentration in the monitoring areas. As these particles traverse the domain, particularly as a result of dispersion effects, the concentration typically decreases with an increased distance from the source. However, in specific geometries, such as street canyons, this behavior may not hold, as particles could accumulate close to walls.

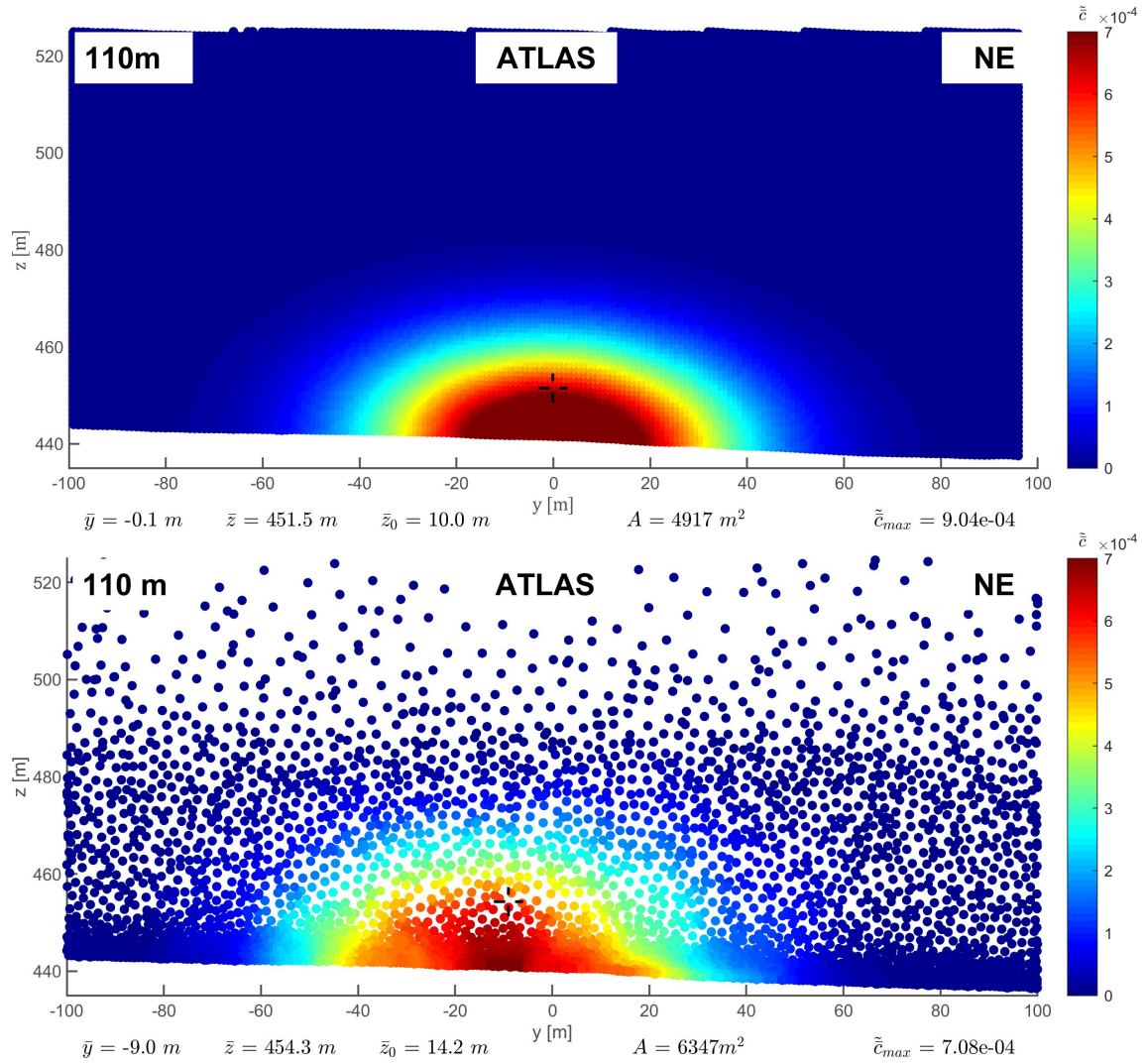


Figure 5.2.: Comparison at the monitoring-planes for the representative distance of 110 m in north-east wind direction from the release point. Air is released from the door of the ATLAS surface building. Integrated normalized concentration are shown at the top for GPM and at the bottom for the LES.

Prior to computing parameters for plume displacement and cross-sectional area, it is essential to post-process the simulation data by transforming the positions of polyhedral cells into a regular shape. Given the irregular nature of these positions, concentration values are assessed on a regular grid with a cell size of $1 \times 1 \text{ m}^2$, resulting in a total of N_{reg} square cells. To assign a concentration to each cell, the following rules are applied:

- If the centroid of only one polyhedral cell falls within a square grid cell, the concentration value of the polyhedral cell is used for that square grid cell.
- In cases where multiple polyhedral cell centroids are located within the same square grid cell, the concentration value is averaged among them.
- If no polyhedral cell centroid falls within a square grid cell, the concentration is linearly interpolated from the values of the surrounding polyhedral cells.

This post-processing step ensures that the solution is independent of the initial mesh size. Subsequently, the parameters for plume displacement and cross-sectional area are calculated based on the concentration and positions of the regular grid cells.

The average plume displacement in the y direction, denoted as \bar{y} , is calculated using the normalized integrated concentration values, denoted as \tilde{c}_i , and their corresponding locations relative to the center of the planes.

$$\bar{y} = \frac{\sum_{i=1}^{N_{reg}} y_i \cdot \tilde{c}_i}{\sum_{i=1}^{N_{reg}} \tilde{c}_i} \quad (5.1)$$

The average rise of the height of the center line of the plume, now called the plume lift, in the z -direction, denoted as \bar{z} , is evaluated using the normalized integrated concentration values, denoted as \tilde{c}_i , and their corresponding altitudes from sea level, denoted as z_i :

$$\bar{z} = \frac{\sum_{i=1}^{N_{reg}} z_i \cdot \tilde{c}_i}{\sum_{i=1}^{N_{reg}} \tilde{c}_i} \quad (5.2)$$

The average plume lift from the ground, denoted as \bar{z}_0 , is determined by the following equation, depending on the terrain altitude $z_{terrain}$ at the corresponding x, y -position:

$$\bar{z}_0 = \bar{z} - z_{terrain} \quad (5.3)$$

In this context, \bar{z} indicates the average lift of the plume in the z direction, as defined earlier, while $z_{terrain}$ denotes the altitude of the terrain at the corresponding y -position. The equation simply subtracts the altitude of the terrain from the average height of the plume, giving the average height of the plume from the ground.

The maximum normalized concentration value, denoted \tilde{c}_{max} , is not derived from the data from the regular grid, as the original concentration values computed in each polyhedral cell are considered the most accurate. Consequently, no averaging or interpolation procedure is employed to determine this value. However, for the uniformity of the result irrespective of the mass released $m_{release}$ [kg], a post-processing step is applied to the concentration values c [kmol m³] obtained from the LES data. Specifically, the concentration values are multiplied by the molar mass of air and divided by the total released mass $m_{release}$ [kg] to obtain the normalized concentration \tilde{c}_{max} [m⁻³]. This post-processing step ensures that the results are independent of the release scenario and can be readily compared.

$$\tilde{c}_{max} = \frac{c \cdot M_{air}}{m_{release}} \quad (5.4)$$

Here, the molar mass of the air released is $M_{air} = 28.966$ kg kmol⁻¹, and the total mass released is $m_{release} = 60505.2$ kg. The mass released $m_{release}$ is calculated using Equation 5.5, which incorporates the smoke release speed $u_{door} = 0.7$ ms⁻¹ at the door of the ATLAS

surface building. The door has a total surface area of $A_{door} = 29.4 \text{ m}^2$ and is located at $z_{door} = 440.06 \text{ m}$, with a total release time of $t_{release} = 40$ minutes.

$$m_{release} = A_{door} \cdot u_{door} \cdot t_{release} \cdot \rho_{air} \quad (5.5)$$

The air density is determined under reference conditions of 1013,2 hPa at 20 °C, with $\rho_{air} = 1.225 \text{ kg m}^{-3}$. In addition to maximum concentration and plume displacement, another crucial parameter is the size of the plume, representing the affected area A [m^2]. For both GPM and LES, lower concentration values are statistically less representative and can obscure a quantitative comparison. Hence, a specific threshold value $\tilde{c} > 10^{-5}$ is defined for comparison. Although this limit remains constant across all planes and simulations, it can be adjusted to a smaller value, such as $\tilde{c} = 10^{-6}$, 10^{-7} , or 10^{-8} , if needed. This adjustment can improve the quality of the assessment, particularly for scenarios with less released mass ($m_{release}$).

Figure 5.3 compares the evaluation parameters for LES and GPM. When examining the CFD results separately, similar trends are observed for the maximum normalized concentration \tilde{c}_{max} , the cross-sectional area of the plume A , and the plume lift \bar{z}_0 . The only parameter showing a different trend is the horizontal displacement \bar{y} of the plume, which varies depending on the direction of the wind in the CFD. This behavior is attributed to the release position, situated on one side of the building, as depicted in Figure 5.1. Consequently, a blocking effect occurs on one side of the building, preventing the species from spreading in both lateral directions relative to the wind direction. Therefore, the plume shifts more in one direction, depending on the wind direction, than in the other in LES. However, in GPM, the plume displacement in the horizontal axis is close to zero ($\bar{y} \approx 0$) at all distances and for both wind directions. Slight differences are noticeable at $x = 40 \text{ m}$, which can be explained by the varying height of the terrain with a slight slope. The height of the center line of the plume \bar{z}_0 increases with a larger distance for both LES and GPM.

Examining the cross-sectional area of the plume A , GPM demonstrates a quicker and wider spread compared to the LES results. It is important to note that the dispersion factors in GPM are determined by the modeling approach and its implementation. Different GPMs may offer varying results, as some are tuned to provide conservative outcomes close to the source, while others predict a wider plume to be conservative with respect to affected areas. Consequently, variations between different GPMs can arise on the basis of the intended use of predicted pollutant concentration.

In contrast, LES results are highly dependent among others on the inlet boundary conditions of the domain, the local dispersion environment, and the type of released gas/pollutant. The turbulent kinetic energy at the inlet plays a crucial role; higher turbulence leads to a higher dispersion factor as larger fluctuations dominate the flow. It should be noted that the parameters for the maximum normalized concentration \tilde{c}_{max} and the cross-sectional area of the plume A are strongly interrelated and any comparison should

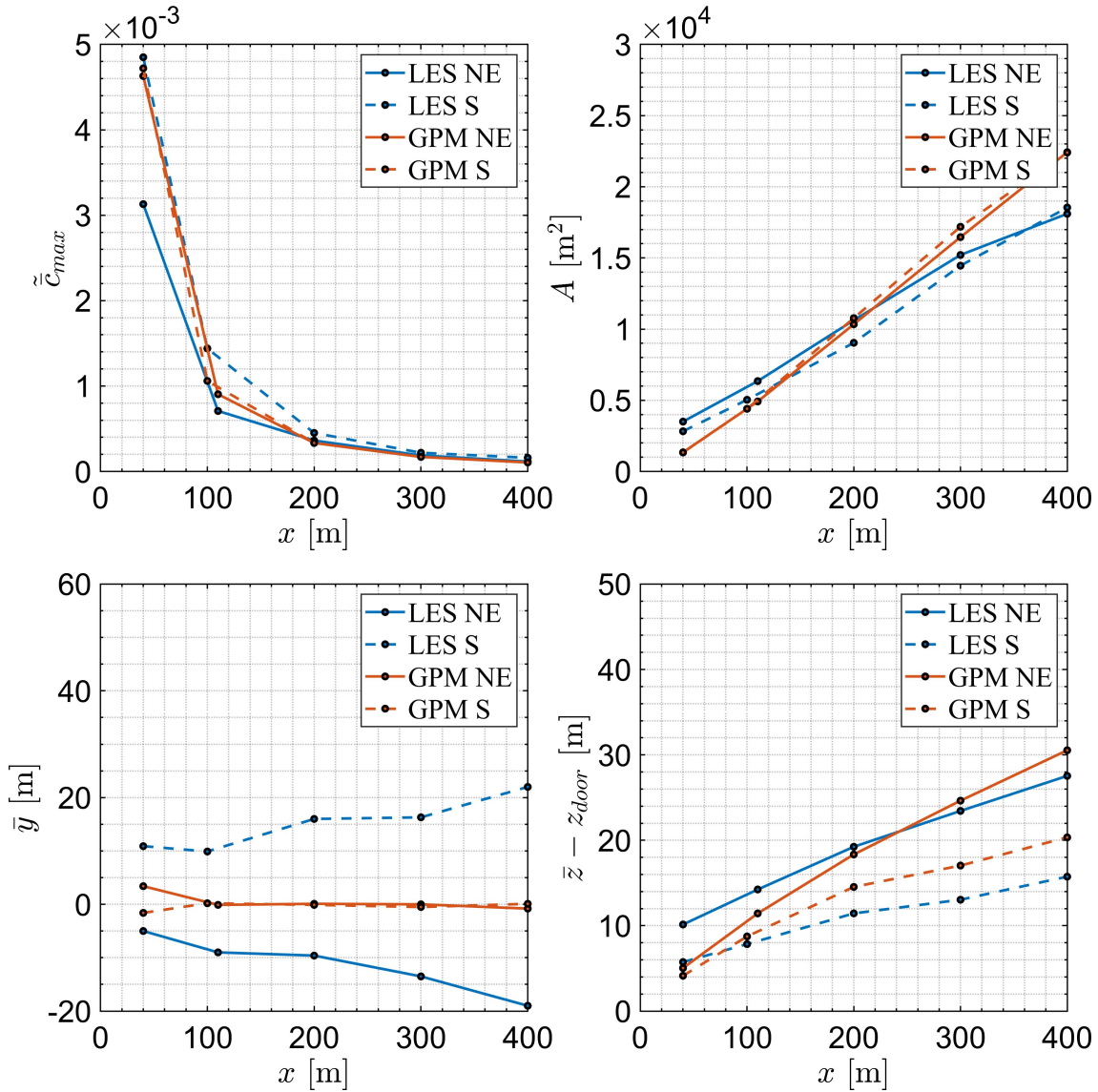


Figure 5.3.: Comparison of displacement parameters \bar{y} and $\bar{z} - z_{door}$, the plume cross-section A and the maximum concentration \tilde{c}_{max} as function of the distance from the release point. All parameters have been evaluated for all monitoring-planes and are compared for LES and GPM for two wind directions (south, north-east).

be approached with caution. However, trends for these parameters can be observed and understood in relation to each other for different wind directions.

As anticipated, a notable distinction between GPM and LES lies in the fact that the CFD solution depends on the wind direction, thereby influencing terrain and geometry considerations. In contrast, GPM yields consistent values for both directions of the wind. Although GPM accounts for terrain height at the evaluated locations, subtle deviations between the two wind directions can be observed. This accounts for a deflection of the plume on the ground with increasing terrain height or a higher rise of the plume centerline above ground with decreasing terrain height.

However, GPM does not factor in terrain slope upstream of the release and its implications on pollutant release. Examining the concentration distributions, it becomes evident that pollutants can accumulate significantly in street canyons or between buildings due to limited mixing or flow channeling. Figure 5.4 illustrates this effect, which GPM is unable to reproduce.

Another notable distinction between GPM and LES lies in the consideration of the impact of building wake on pollutant dispersion. Although GPM typically models the release as a single point or plane, LES treats the release as a more realistic area source. This approach releases pollutants into a larger volume, influenced by the wake flow of the building. Consequently, pollutants can disperse throughout the wake of a building and recirculate in this area before following the mean wind direction. This difference in modeling can result in varied pollutant transport patterns, with significant implications for emergency responders in the event of accidental release. It is crucial to recognize this behavior when conducting risk assessments and formulating emergency response plans.

Despite the fundamental disparities in dispersion modeling, several similarities between the GPM and LES become apparent when examining the cross-wind monitoring planes:

- The maximum normalized concentration \tilde{c}_{max} is remarkably similar for both GPM and LES. The velocity profile at the ATLAS release point remains relatively undisturbed compared to other regions in the domain. Furthermore, plume growth in LES is closely aligned with the results of GPM. While local differences are noticeable, as depicted in Figure 5.4, the overall values exhibit a similar trend.
- The size of the plume A exhibits a behavior similar to the concentration values observed at different distances. GPM and LES predict very similar values, although locally they differ strongly from each other, as illustrated in Figure 5.4. While the GPM shows a semicircular shape at each monitoring plane, the plume shape is much more deformed in LES. This deformation is highly influenced by the interaction with buildings, resulting in a rather irregular shape.

In addition to examining the concentration on the cross-wind planes, the normalized concentration \tilde{c} at the previously defined monitoring points is compared between the GPM and LES models. Monitoring-points are selected according to the flow direction, as shown in an example in Figure 4.36. These points are located at distances ranging from 10 to 160 meters from the release point, each at a height of 1 meter above the ground. The comparison is limited to very close locations only. The results for the normalized concentration \tilde{c} are shown in Figure 5.5 for the north-east and south winds.

The GPM predicts the concentration at $x = 10$ m approximately twice as high as those predicted by LES for both wind directions. The GPM encounters challenges in providing precise predictions at distances smaller than $x = 200$ m, leading to its limited use for distances shorter than 200 m, as stated in ENSI-G14 (2009). Different methods, following

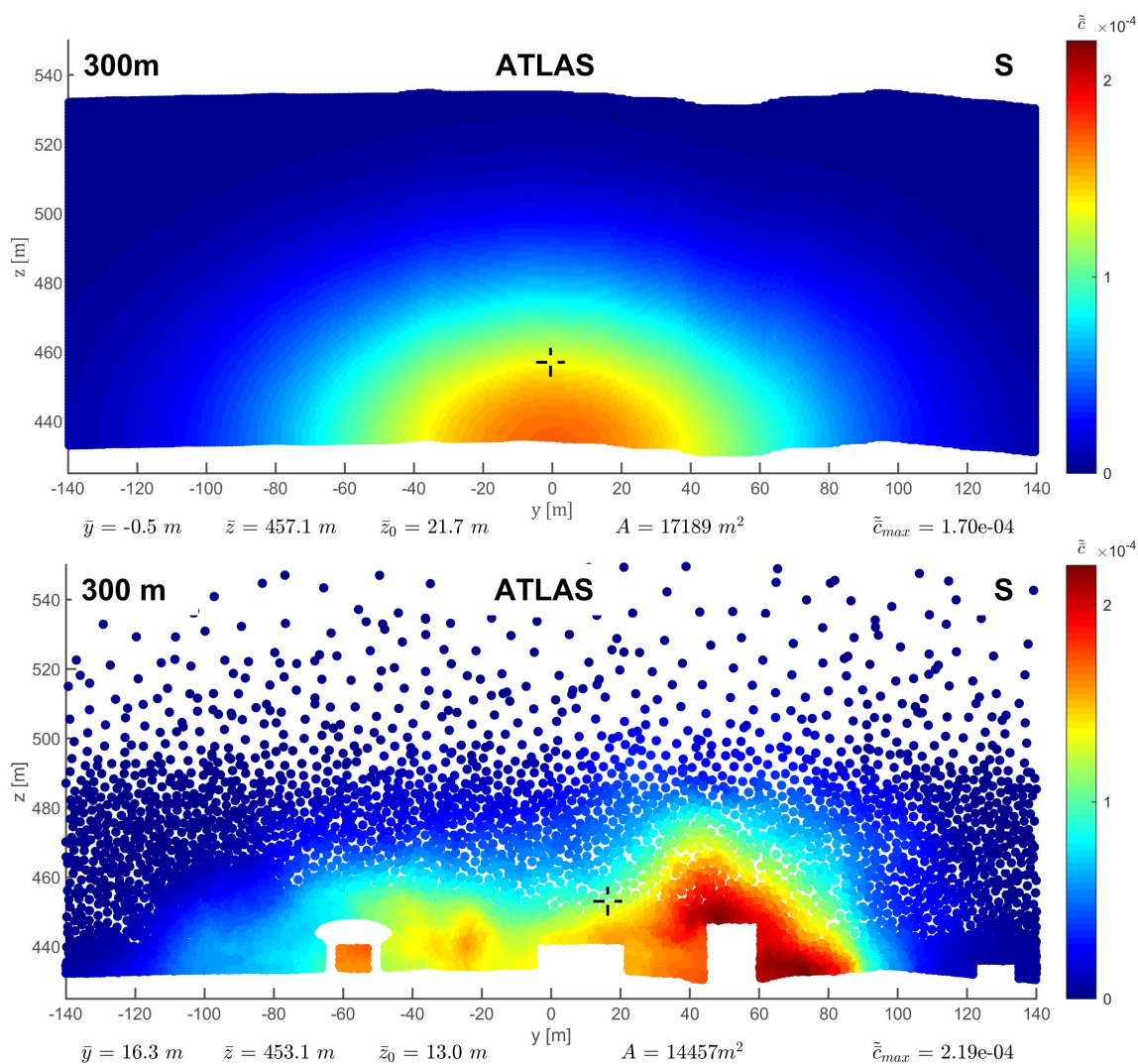


Figure 5.4.: Comparison of the monitoring-planes for the representative distance of 300 m in south direction from the release point. Air is released from the door of the ATLAS surface building. Integrated normalized concentration are shown at the top for GPM and at the bottom for the LES.

Chapter 3 of IAEA (1980) with a minimum distance of 10 m, are utilized in the GPM at CERN. For the direction of the north-east wind, the GPM predicts a higher concentration farther away from the release point compared to the LES results. In the direction of the north-east wind, the CFD plume spreads more, resulting in a lower concentration. The GPM appears to account for these uncertainties, leading to a higher predicted concentration. For the south wind direction, the concentration values farther away from the source, $30 < x < 100$ meters, for both the GPM and LES are very similar. Far from the source, $100 < x$ meters, the concentration values predicted by the GPM align with those predicted by the LES, except for some points close to the buildings. The dispersion coefficients of the GPM seem to exhibit behavior similar to that of the LES.

It can be concluded that, for the chosen scenario, there is good agreement between the results obtained from GPM and LES. Observed concentration values can vary sig-

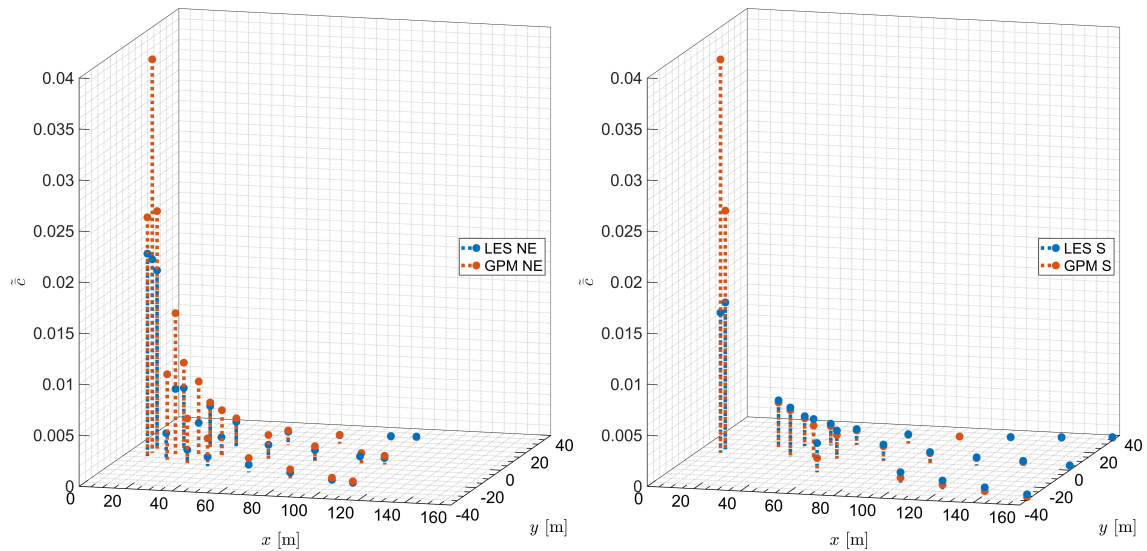


Figure 5.5.: Monitoring-points for the release scenario in north-west flow direction (left) and south direction (right). Air is released from the door of the ATLAS surface building. Normalized concentration are shown for GPM and LES.

nificantly at local levels, but the general tendency is captured with the GPM. The GPM, which is an analytical model based on experimental data and incorporating possible surcharges to ensure conservative results, is widely employed for rapid assessment of accidental scenarios in nuclear power plants. However, because of its simplified nature (cone shape with a point source), the GPM tends to underestimate near-source mixing because of the built environment and overestimates concentration values close to the release point. The monitoring points chosen for comparison were placed in the flow direction with an opening angle, which favors the GPM, which may limit the applicability of the comparison to other scenarios. Locations in the wake of the ATLAS surface building, where the release takes place, have not been considered because the GPM does not indicate any concentration in these areas, while LES predicts the dispersion of pollutants in the wake of the building.

It is crucial to note that when anticipating concentration values in the wake of buildings or within street canyons, the GPM may not be the optimal method. This is because LES can consider the effects of building cavities and forecast areas highly affected by pollutants, which the GPM might not accurately capture. Consequently, LES and CFD, in general, are the preferred solutions for predictions that require a high level of confidence in local areas.

5.1.2. Differences of GPM and LES

In the previous section, the discussion revolves around the similarities between GPM and LES for a simple release scenario where pollutants are released from a door and share the same properties as air. However, this section delves into the differences between GPM and LES for two more complex scenarios. Two modifications are introduced:

- Elevated pollutant release scenario
- Dense gas release scenario

In the first part of this section, the release point is elevated compared to the ground-level release scenario presented in Section 5.1.1. More precisely, the release point is located on the stack of the ATLAS surface building instead of the fire door, as shown in Figure 5.1. This alteration in the simulation setup enables an exploration of the effects of an elevated release on plume behavior and the disparities between the predictions of GPM and LES for this particular scenario.

The volumetric flow through the emergency extraction system stack for the ATLAS cavern is significantly higher than that for the soot scenario. This is attributed to the larger forced extraction in the cavern and the smaller cross-sectional area of the stack, as presented in Table 5.1. The results of the study are deliberated in the first part of this section, which delves into the elevated release scenario and elucidates the various approaches and results derived from GPM and LES.

Table 5.1.: Properties for comparing a ground-level release from the door of the ATLAS surface building to an elevated release from the stack of the same building.

Release Area	Door	Stack
Surface A [m ²]	$A_{door} = 29.4$	$A_{stack} = 1$
Volume flow \dot{V} [m ³ s ⁻¹]	$\dot{V}_{door} = 5.72 \cdot 10^{-3}$	$\dot{V}_{stack} = 8.89$
Velocity u [ms ⁻¹]	$u_{door} = 0.7$	$u_{stack} = 8.89$
Release height z [m]	$z_{door} = 3$	$z_{stack} = 17.7$

In the second part of this section, the scenario of dense gas release is explored, in which fluid is extracted through the stack, but the fluid released is altered according to the properties described in Table 5.2. This scenario highlights the distinctions between the release of neutral and dense gases. Additionally, it demonstrates the constraints of the GPM, which does not consider density variations between the two released gases, illustrating the necessity for simulations capable of forecasting the interaction of distinct fluids.

Table 5.2.: Comparison of release scenarios involving two different fluids (air and argon) released from the stack of the ATLAS surface building.

Fluid	Air	Argon
Density ρ [kg m ⁻³]	$\rho_{air} = 1.23$	$\rho_{Ar} = 1.62$
Molecular weight M [kg kmol ⁻¹]	$M_{air} = 28.97$	$M_{Ar} = 39.95$
Dynamic Viscosity μ [kg m ⁻¹ s ⁻¹]	$\mu_{air} = 17.90 \cdot 10^{-6}$	$\mu_{Ar} = 21.25 \cdot 10^{-6}$

Elevated Release Scenario

In this subsection, a comparative analysis is performed between the representative GPM and LES for an elevated release scenario. Elevated release scenarios often involve re-

lease points in close proximity to buildings or on building rooftops, where various stack lengths can be used to adjust the release height. Theoretical evaluations, such as those of Meroney (1982), and numerous studies, including those conducted by Keshavarzian et al. (2021), have investigated the releases of pollutant emissions toward the windward, leeward and sideward in the vicinity of buildings. This comparison highlights the critical role of LES in precisely forecasting pollutant dispersion in scenarios involving releases in close proximity to buildings.

In the scenario investigated in this dissertation, the release point is situated on the roof of the ATLAS surface building, mimicking a plausible emergency extraction scenario for the ATLAS cavern. The stack is strategically placed near the center of the building, as illustrated in Figure 5.1. The primary focus is on mean pollutant concentration values, which will be systematically compared between the GPM and the LES on multiple monitoring planes at varying distances from the source, along with assessments at specific monitoring points. Furthermore, the comparison will include plume shift and cross-sectional characteristics.

Figure 5.6 displays a crosswind plane at a downwind distance of $x = 75$ meters from the source under conditions of south wind (170°). The evaluated dispersion parameters are located at the bottom of the figure, similar to the evaluation in Section 5.1.1, and indicate the plume's position, size, and the maximum integrated normalized concentration observed. The scatter plot and the color coding reveal that LES predicts a significantly higher concentration ($\tilde{c}_{max,LES} \approx 1.8 \tilde{c}_{max,GPM}$) within the plume cross-section, and the plume is shifted towards the ground ($\bar{z}_{0,LES} \approx 0.63 \bar{z}_{0,GPM}$). This observation aligns with the expected behavior of the suction effect of a leeward release of pollutants. It is also consistent with the statement made in Section 5.1.1 that GPM may not be the preferred method for predicting concentration values when the release point is located in the proximity of buildings or in street canyons, where CFD, in general, has an advantage in predicting the plume trajectory.

As expected, the observed trend in the crosswind plane at $x = 75$ meters under conditions of south wind (170°) becomes more pronounced when the distance of the crosswind evaluation plane increases to $x = 200$ meters, as illustrated in Figure 5.7. The plume exhibits a downward shift, and the CFD simulations continue to generate higher concentration values compared to GPM $\tilde{c}_{max,LES} \approx 2 \tilde{c}_{max,GPM}$. Additionally, the plume started to split up as a result of the interaction with the leeward suction effect of the ATLAS surface building, where the release of air is located on top. This suction effect can be found better in Figure 5.8, where an instantaneous iso-surface is shown for the mass fraction of the air released in $t_{sim} = 1800$ s.

In the comprehensive explanation by Meroney (1982), it was shown that a short stack near the roof of a building might induce a downwash effect, causing a lower effective stack height for the emitted plume. This phenomenon is particularly noticeable when pollutants are released from the roof or the leeward side of a building. In the GPM uti-

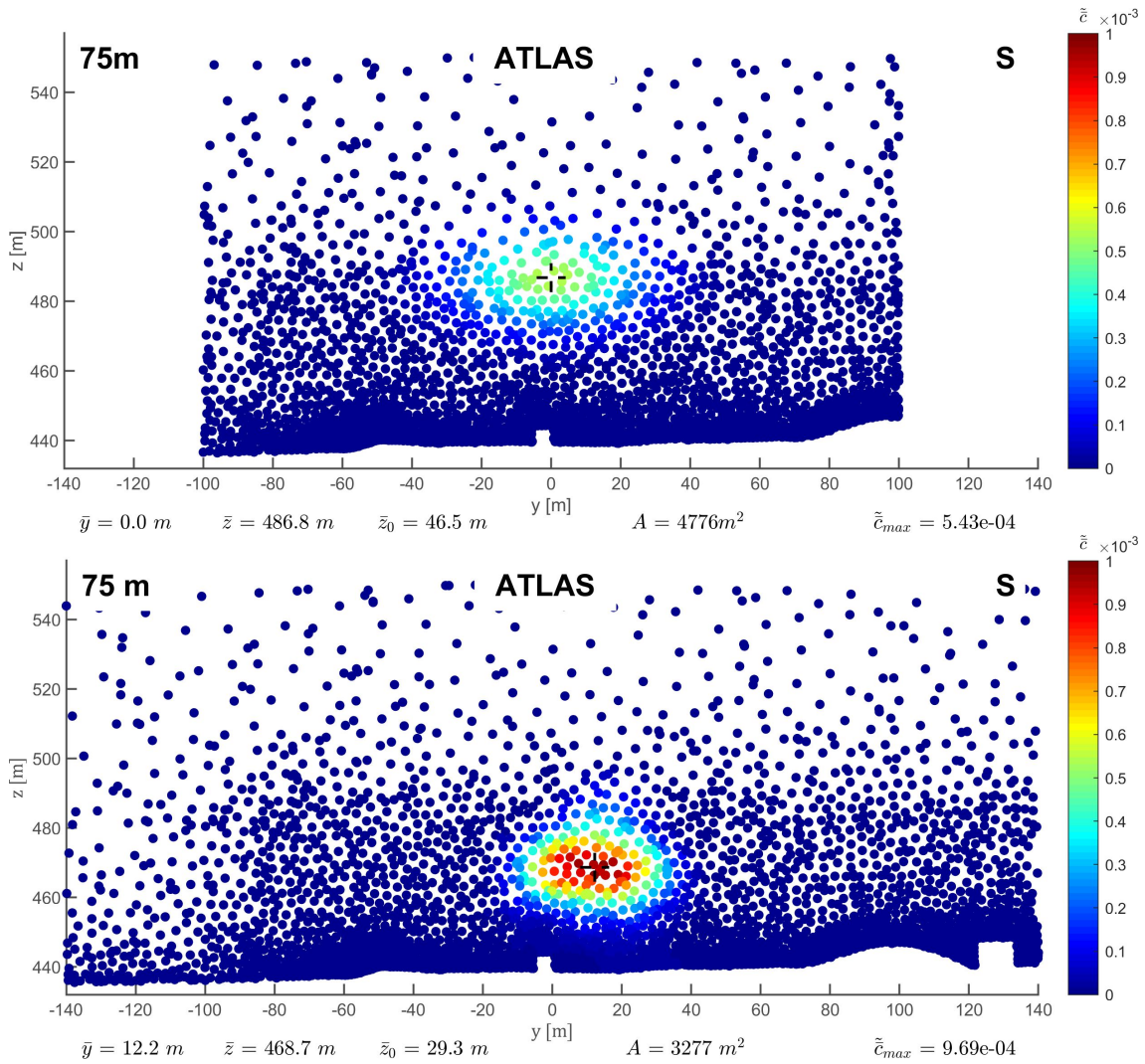


Figure 5.6.: Monitoring-planes at a distance of 75 m downstream in south wind direction from the release point. Air is released from the stack on the rooftop of the ATLAS surface building. Integrated normalized concentration are shown at the top for GPM and at the bottom for the LES.

lized at CERN, a plume rise model is incorporated, enabling the prediction of plume rise for relatively fast exhaust velocities. This model calculates a fictive source location, resulting in an immediate increase in the plume centerline after the release. Similarly, LES also demonstrates this behavior, albeit in a more subdued manner. Figure 5.8 illustrates the movement of the plume in LES at a specific time $t_{sim} = 1800 \text{ s}$, making the trend of the plume clearly visible. In the upper part of Figure 5.8, an iso-surface with a mass fraction of 10^{-3} indicates that the highest concentration is located a few meters from the ground. The lower concentration values, as shown in the lower part of Figure 5.8, reach even higher heights above the ground, but, in particular, also exhibit lower heights close to the ground, attributed to a building-induced downwash effect.

Figure 5.9 provides a comparison of the normalized maximum concentration \tilde{c}_{max} , plume cross-section A , y displacement \bar{y} , and displacement of the release height $\bar{z} - z_{stack}$

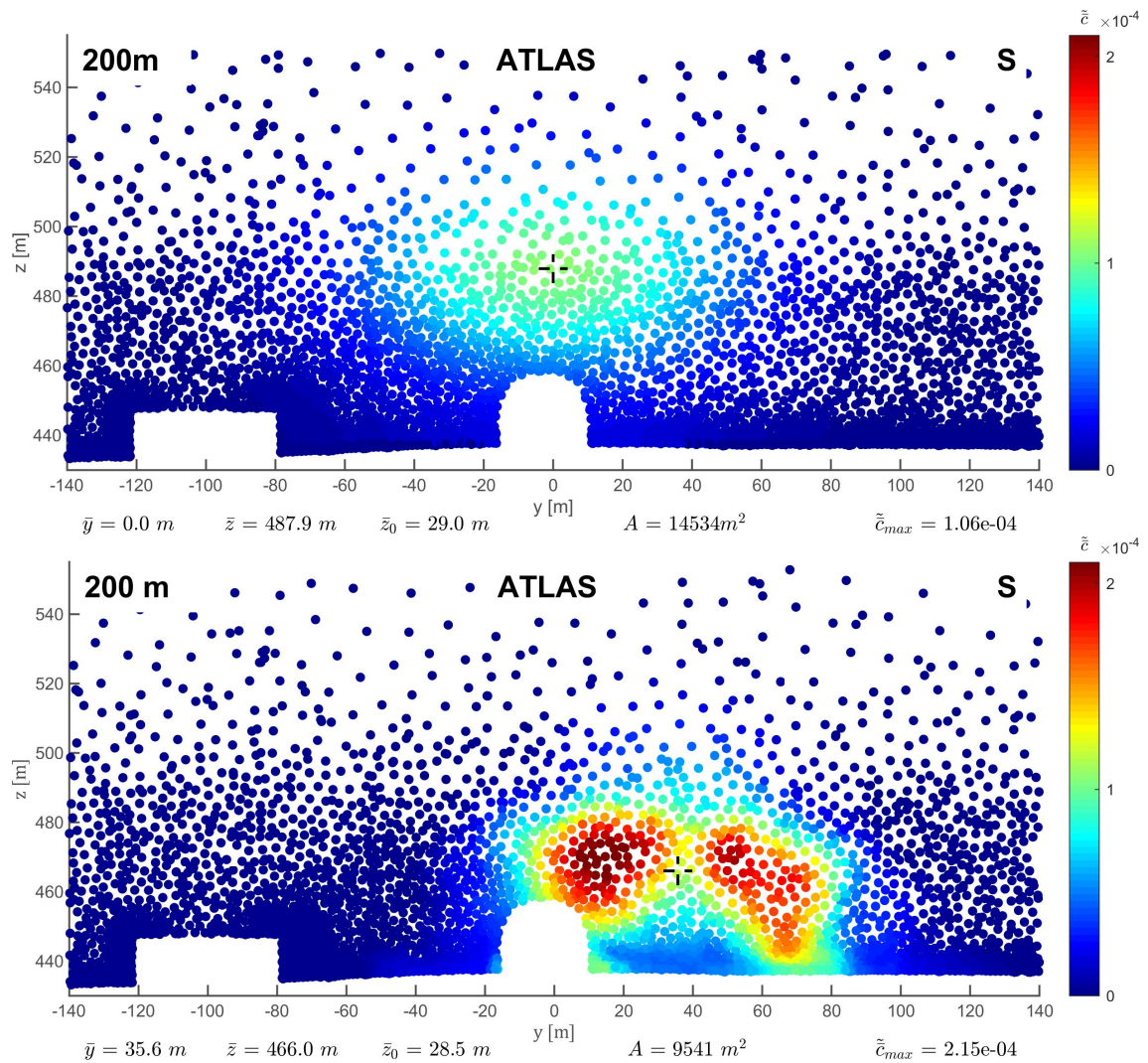


Figure 5.7.: Monitoring-planes at a distance of 200 m downstream in south wind direction from the release point. Air is released from the stack on the rooftop of the ATLAS surface building. Integrated normalized concentration are shown in the top for GPM and at the bottom for the LES.

between GPM and LES. In the cross-wind planes at $x = 75$ m, LES predicts maximum concentration values 20 % higher than those calculated by GPM. In particular, for wind directions southward, this difference is more substantial, with LES showing 77 % higher maximum normalized concentration values. The plume cross-section A shows very similar predictions for all distances and wind directions between GPM and LES. However, the shape of the plume cross-section varies significantly for LES, especially for wind blowing from the south. This variation is attributed to the downwash effect of the source building and the presence of buildings, where the flow needs to navigate between structures, limiting the plume's ability to expand uniformly in all directions, as shown in Figure 5.7.

Another explanation for the higher concentration values predicted by LES when the wind blows from the south can be attributed to the vertical displacement of the center line of the plume $\bar{z} - z_{stack}$. Generally, LES predicts a higher plume centerline compared

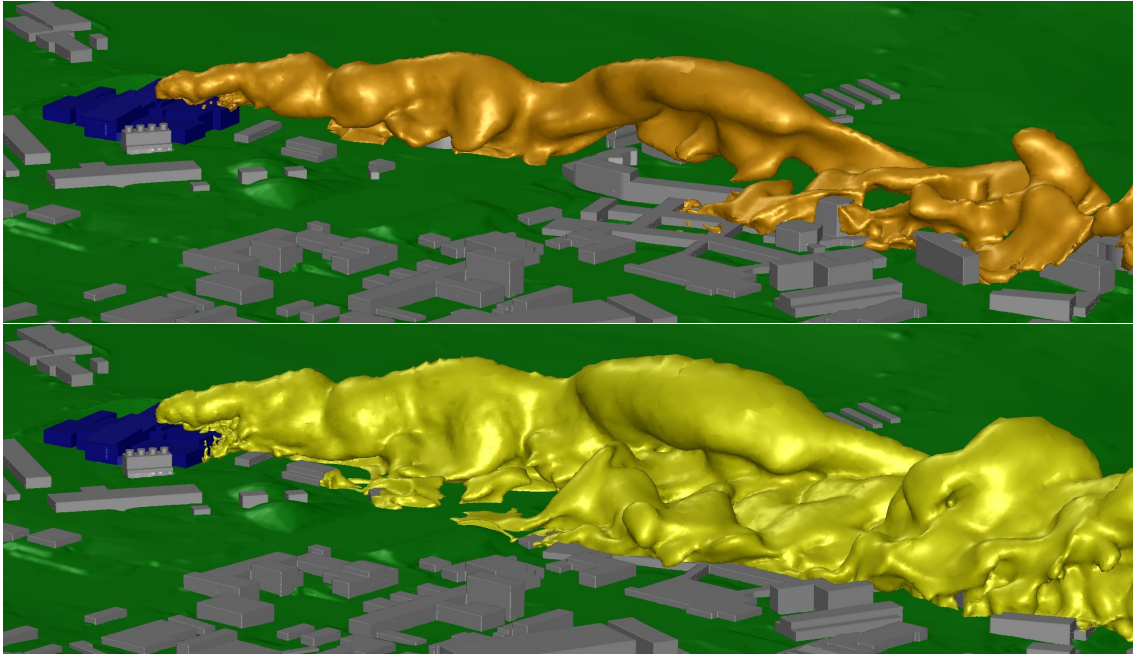


Figure 5.8.: Iso-surface for a mass fraction of polluted air in air $m_{pol}/m_{air} = 10^{-3}$ in the top and $m_{pol}/m_{air} = 10^{-4}$ in the bottom of the released species in south wind direction from the release point at the specific time $t_{sim} = 1800$ s.

to GPM, resulting in a slower movement of pollutants through the air and an extended residence time in specific locations. In LES, this contributes to higher concentrations and a more gradual spreading of the plume, as turbulent diffusion is less pronounced close to the ground than at higher altitudes. Figure 5.9 also presents the results for lateral displacement \bar{y} . A noticeable distinction between GPM and LES is observed, attributed to the influence of surrounding buildings.

In addition, time-integrated normalized concentration values for individuals who reside or work near CERN were investigated for the pollutant release scenario by establishing monitoring points in the south and northeast directions. To assess the concentration predicted by the GPM, monitoring points were defined in a grid. Due to elevated release, the maximum distance of the monitoring points from the release point was increased, compared to the door release scenario in Chapter 5.1.1, or as shown in Figure 5.5. Figure 5.10 displays the time-integrated normalized concentration for wind blowing in the north-east direction on the left and for wind blowing in the south direction on the right. As expected, the results indicate that the concentration values for the stack release scenario do not decrease with increasing distance but instead first increase until they reach a maximum at a certain distance from the release point.

The plume expands as the distance from the release point increases until it makes contact with the ground and undergoes reflection, resulting in relatively higher concentrations. As distance further increases, concentration values gradually decrease as the plume cross-section A expands. This behavior is observable for both wind directions and both models. However, special attention is required for the concentration values, partic-

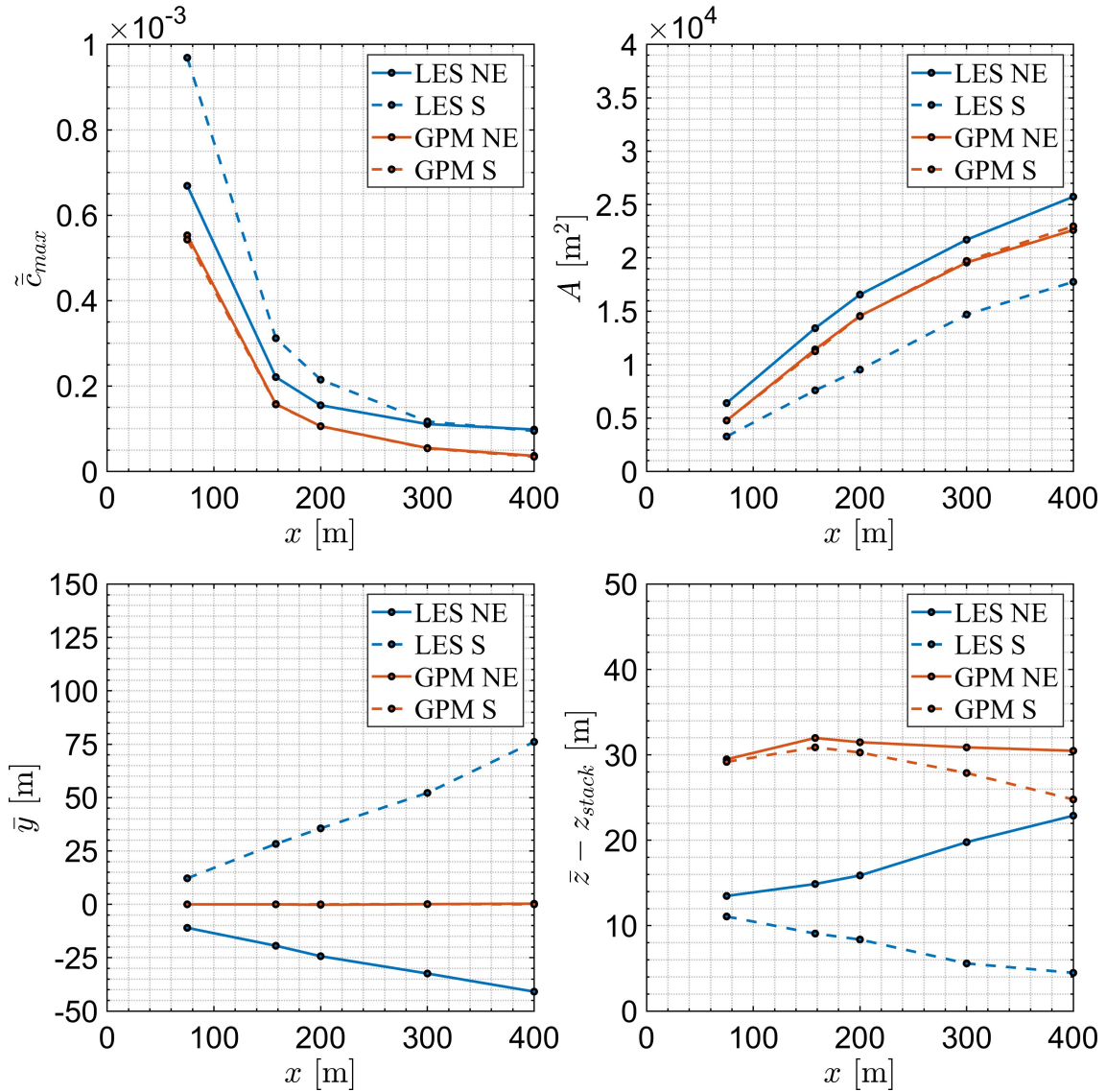


Figure 5.9.: Comparison of displacement parameters \bar{y} and $\bar{z} - z_{stack}$, the plume cross-section A and the maximum concentration \tilde{c}_{max} as function of the distance from the release point. All parameters have been evaluated for all monitoring-planes and are compared for LES and GPM for two wind directions (south, north-east).

ularly in close proximity to the release point, where the differences between GPM and LES are notable. In these plots, the plume downwash predicted by LES becomes evident. The plume first contacts the ground and is narrower compared to the predictions of the GPM. Consequently, the concentration values at these points are significantly higher in magnitude. At a distance of approximately $x = 400$ m, the predictions of GPM and LES converge, generating similar results.

This investigation highlights that the application of a Gaussian plume model (GPM) does not consistently produce results of the same quality as those observed in ground release scenarios, as discussed in Chapter 5.1.1. Although GPM and LES predictions may

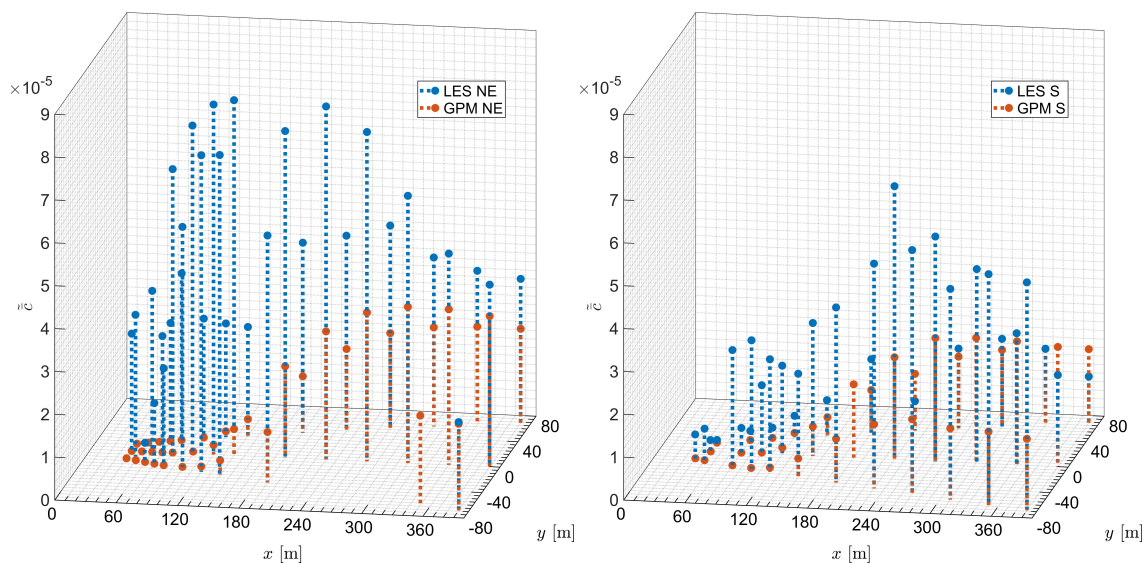


Figure 5.10.: Monitoring-points for the air release scenario in north-west flow direction (left) and south direction (right). Air is released from the stack on the roof of the ATLAS surface building. Time-integrated normalized concentration are shown for GPM and LES.

align in ground release scenarios, variations in the release point, release velocity, or the geometry of the release building and surrounding structures can lead to substantial discrepancies. In contrast, LES offers a more physically realistic representation for release points in close proximity to buildings. The wake field of the building can act as a secondary source in ground release scenarios, influencing the movement of pollutants along the facade of the building. In addition, the wake field can induce a suction effect on pollutants released on the roof. This complex interplay of factors significantly impacts plume size and movement, phenomena to which LES are better equipped to capture compared to GPM, even with dedicated models.

The results obtained from the comparative analysis of GPM and LES in various scenarios, especially those involving an elevated release point on the roof of the ATLAS surface building, highlight significant disparities in their predictive capabilities. GPM, being an analytical model with simplified assumptions, struggles to capture the complex interactions influenced by building wakes, plume rise, and other intricate features of the release environment.

In scenarios where pollutants are released near buildings or from elevated points, LES stands out for its ability to model realistic area sources, simulating the dispersion within a larger volume affected by the building wake flow. Building wakes, which create down-wash effects and impact plume behavior, are crucial elements that GPMs, including the one used at CERN, typically struggle to incorporate accurately. This limitation becomes more pronounced when dealing with complex shapes, varied terrain, and intricate flow physics.

The wake field of a building, acting as a secondary source, affects the size and move-

ment of the plume. LES, with its ability to consider changing terrain, detailed building structures, and dynamic flow physics, captures these effects more realistically. The discrepancy between the GPM and LES predictions becomes evident in scenarios where the wake field leads to a suction effect on rooftop-released pollutants, influencing plume size and dynamics. Although GPMs may employ designated models to approximate such effects, they often do not accurately represent the intricate interplay of factors.

The limitations of GPM become particularly apparent when multiple influencing factors, such as building downwash, plume rise, and dense gas releases, interact. In such cases, GPMs may provide inaccurate predictions, as the simplifications inherent in their models may lead to the elimination of certain influences by others.

In essence, the complexity of real-world scenarios, especially those involving elevated releases and intricate building geometries, demands a more sophisticated and detailed approach provided by CFD simulations, particularly LES. The latter excels in capturing nuanced interactions and flow phenomena that play a crucial role in pollutant dispersion, making it the preferred and more accurate tool for such predictions.

Dense Gas Release Scenario

Using computational fluid dynamics, specifically large-eddy simulations (LES), this study models the dispersion of argon, a noble gas. The scenario is inspired by potential real-life situations, such as the demolition of liquid argon tanks at CERN, which are used to cool the ATLAS detector during the operation of the Large Hadron Collider (LHC). Considering that liquid Argon, used for cooling the detector, becomes activated as a result of radiation from collisions in the detector, the release of gaseous Argon could pose serious health risks to individuals in the vicinity. The release of substantial amounts of argon gas, utilized for detector cooling, could occur during unforeseen events like terrorist attacks or accidents during maintenance downtime of the LHC. In such situations, tank damage can lead to the release of radioactive gaseous argon through the ventilation extraction system. Although HEPA filters can mitigate pollutants, activated argon gas, denser than air (with a density of $\rho_{Ar} = 1.62 \text{ kg m}^{-3}$), would pass unfiltered.

This study involves a comparison between the predictions of LES and the Gaussian plume model (GPM) in the context of the dense gas release scenario described above. It is essential to note that the GPM employed at CERN lacks the capability to specify the density of the released fluid and is consequently utilized with the assumption of neutral gas. The simulation setup used for this investigation is detailed in Chapter 4.3.7.

Figure 5.11 presents scatter plots that illustrate the normalized concentration integrated in time \tilde{c} for both GPM (top) and LES (bottom). Upon inspection of the instantaneous results from LES, it is evident that the plume concentrates near the ground within a short distance from the release point, aligning with a significant dense gas effect, as observed in the experiments conducted by Schatzmann et al. (1995). To dig deeper into the plume dynamics in the dense gas release scenario, iso-surfaces were generated, similar to those

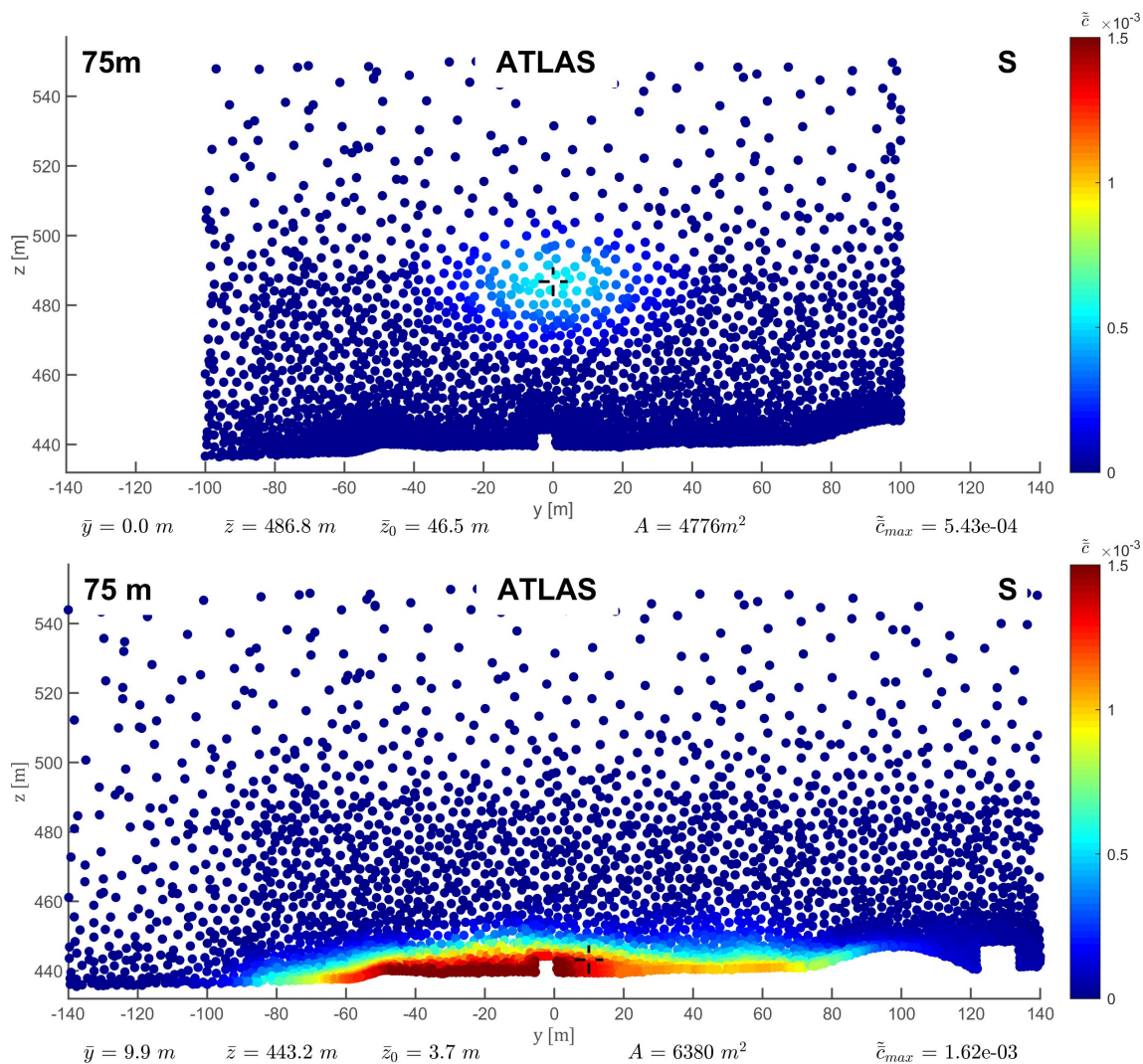


Figure 5.11.: Monitoring-planes at a distance of 75 m downstream in south wind direction from the release point. Argon is released from the stack on the rooftop of the ATLAS surface building. Integrated normalized concentration are shown in the top for GPM and in the bottom for the LES.

in the air release scenario depicted in Figure 5.8. This time, the iso-surfaces represent the same mass fraction of the argon gas in the air, offering a visual depiction of the plume's behavior in Figure 5.12. The visualization reveals that the plume's center line is deflected toward the ground immediately after release because of the higher density of Argon gas. As the plume travels, mixing with ambient air occurs, diminishing the dense gas effect with increasing distance until the plume behavior aligns with that of a neutral release.

Figure 5.13 shows that by evaluating the maximum concentration \bar{c}_{max} , the plume cross-section A , the displacement $y \bar{y}$, and the displacement of the release height $\bar{z} - z_{stack}$ for the GPM and LES for each plane, the behavior described above can be identified.

Table 5.3 provides an overview of the investigated plume dispersion parameters. The two highlighted values have a significant impact on the dose received by potential receptors on site and are therefore crucial in the evaluation. It is especially crucial to carefully

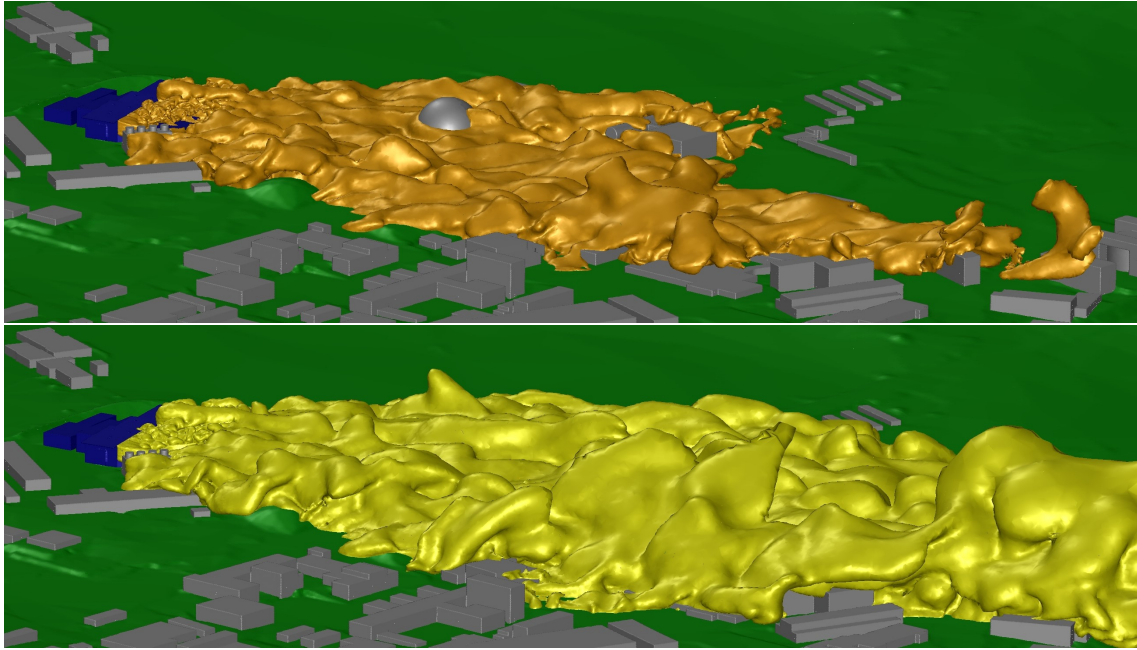


Figure 5.12.: Instantaneous picture of two iso-surfaces for a mass fraction of Argon in air $m_{Ar}/m_{air} = 10^{-3}$ in the top and $m_{Ar}/m_{air} = 10^{-4}$ in the bottom of the released Argon gas at the specific time $t_{sim} = 1200$ s. Wind is blowing into south from the release point at the stack of the ATLAS surface building.

Table 5.3.: Comparison for the dispersion parameters of GPM and LES for the dense gas release scenario.

	GPM	LES	quantity
\tilde{c}_{max}	low	high	max. concentration
A	medium	medium	plume size
\bar{y}	low	medium	lateral displacement
$\bar{z} - z_{stack}$	low	high	vertical displacement

assess maximum concentration and vertical plume displacement for hazmat releases to accurately assess their environmental and human health impact. In the argon release scenario, the largest difference between the GPM and LES predictions can be observed in the vertical plume displacement $\bar{z} - z_{stack}$ and the maximum concentration \tilde{c}_{max} . The maximum concentration observed in LES is approximately four times higher than that observed in GPM. This significant increase in concentration is frightening, as individuals are only exposed by the plume when it is in contact with the ground, leading to an even greater impact on potential receptors.

The monitoring points depicted in Figure 5.14 reveal a significant discrepancy between the two models with respect to the concentration of argon just one meter above the ground. In areas close to the release point, the argon concentration in LES is four times higher, as the dense gas plume is dispersed closer to the ground. The maximum concentrations near the release point range from 3-4 10^{-3} in LES, while in GPM, the high-

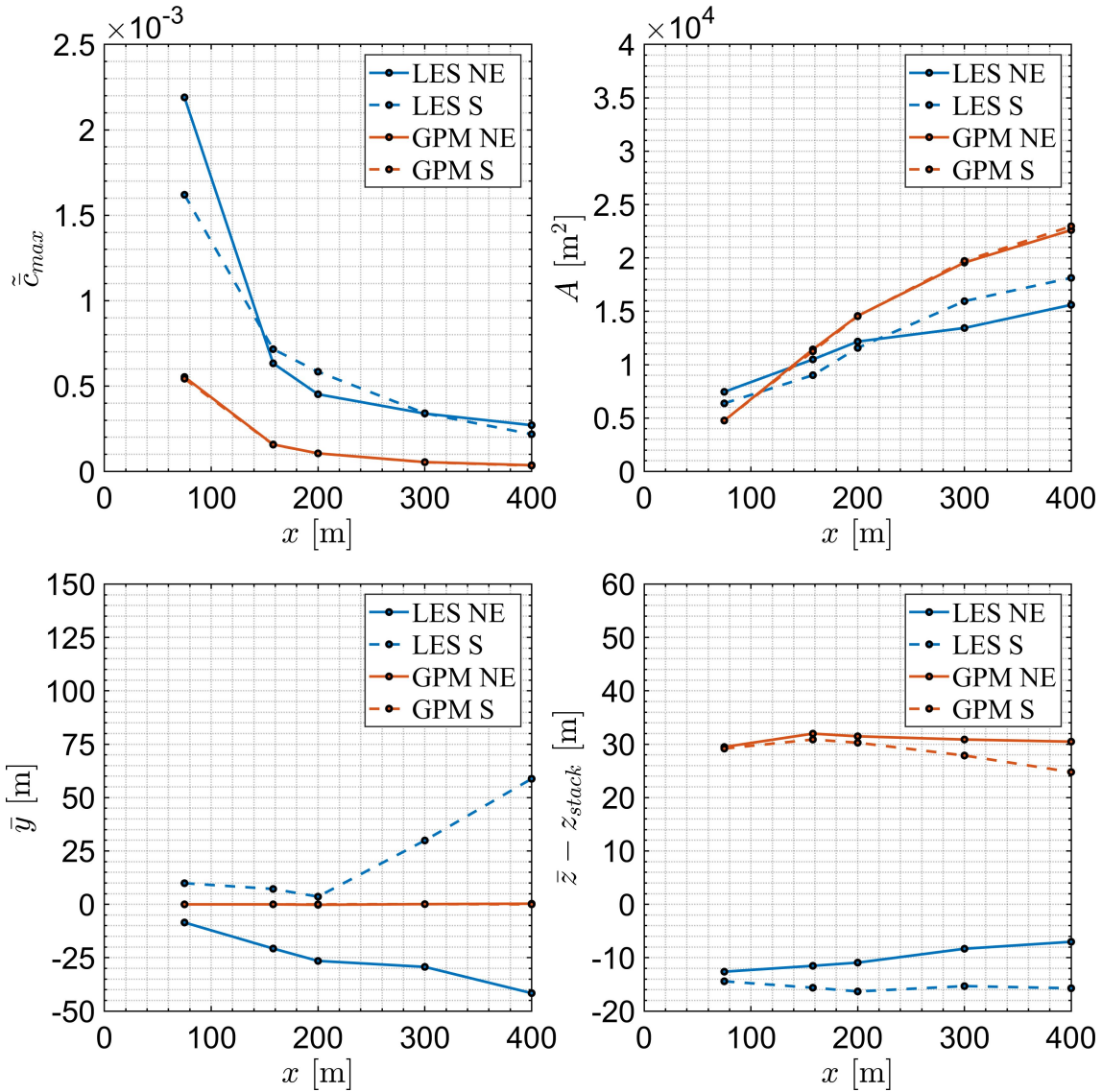


Figure 5.13.: Comparison of displacement parameters \bar{y} and $\bar{z} - z_{stack}$, the plume cross-section A and the maximum concentration \tilde{c}_{max} as function of the distance from the release point. All parameters have been evaluated for all monitoring-planes and are compared for LES and GPM for two wind directions (south, north-east) for the Argon gas release scenario.

est concentrations are observed at a distance of $x = 300$ meters from the release point, ranging from $3-4 \cdot 10^{-5}$. This discrepancy amounts to a difference of two orders of magnitude.

In concluding this chapter, it is essential to acknowledge the inherent complexities associated with modeling dense gas releases using computational fluid dynamics, particularly in the context of large-eddy simulations (LES). The simulated Argon release scenario for the ATLAS facility has provided valuable insight into the strengths and limitations of CFD simulations, shedding light on how the choice of modeling approach can significantly impact the results.

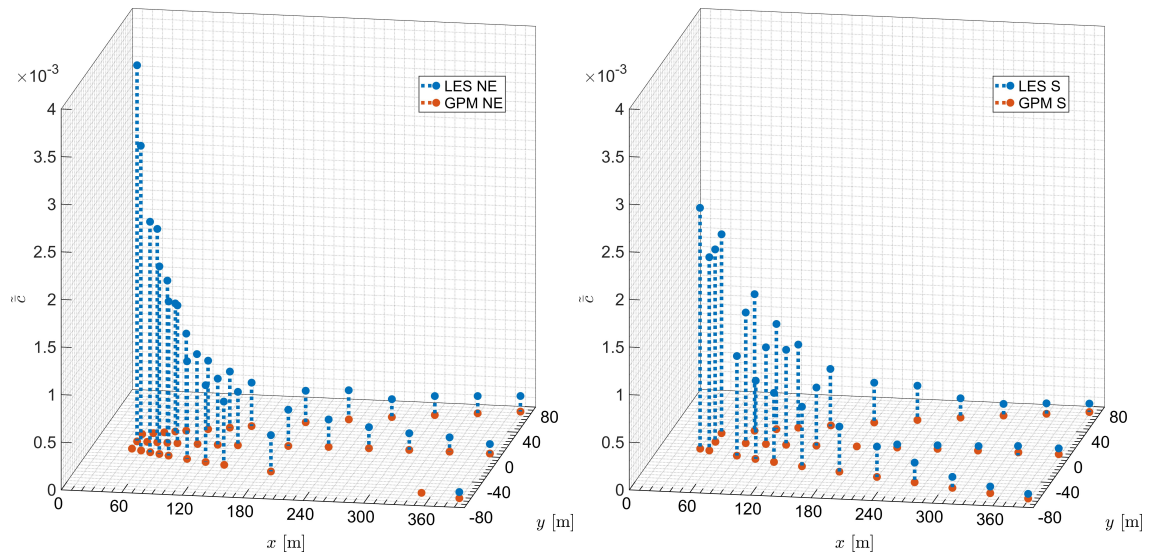


Figure 5.14.: Monitoring-points for the Argon gas release scenario in north-west flow direction (left) and south direction (right). Argon gas is released from the stack on the roof of the ATLAS surface building. Time-integrated normalized concentration are shown for GPM and LES.

The introduction of a release from the stack had a discernible effect on ground concentrations predicted by both the LES and the Gaussian plume model (GPM). In particular, LES exhibited more realistic results, showcasing its ability to capture the intricate dynamics of pollutant dispersion in scenarios involving stack releases. However, real differentiation emerged when the released fluid was changed to the dense noble gas Argon.

The deviations between the LES and GPM predictions were more pronounced in the dense gas release scenario. The GPM, constrained by its assumptions and limitations, could not adequately account for the dense gas effect, resulting in a severe underestimation of Argon concentrations, especially in close proximity to the release point. This observation aligns with experimental findings, such as those documented in Schatzmann et al. (1995), further strengthening the importance of choosing an appropriate modeling approach.

In essence, while the results thus far provide valuable insight, the complexities of dense gas releases warrant a comprehensive understanding of the modeling choices and their implications. Further refinement and validation of the LES model will be crucial in establishing its robustness and reliability in predicting dense gas dispersion scenarios accurately.

This assessment also shows that the choice of modeling approach in CFD plays a pivotal role in accurately capturing the intricacies of pollutant dispersion, particularly in scenarios involving dense gas releases. In this context, Eulerian modeling, and more specifically LES, emerges as a compelling choice because of its inherent capabilities in resolving detailed turbulence features.

Eulerian models, in contrast to Lagrangian models, focus on the continuum represen-

tation of fluid dynamics, where the flow field is discretized into a fixed grid. This approach allows for explicit resolution of turbulent structures and the dynamic interaction between the fluid and the surrounding environment. In the case of LES, large-scale turbulent eddies are resolved directly, while smaller-scale eddies are parameterized, striking a balance between computational efficiency and accuracy.

The advantages of Eulerian modeling become particularly pronounced when dealing with complex scenarios such as dense gas releases. The detailed representation of turbulent structures enables LES to capture phenomena such as plume rise, dispersion patterns, and the interaction with obstacles and terrain. Additionally, the model's ability to account for variable density effects, crucial in scenarios involving noble gases like argon, adds a layer of accuracy that is challenging for other modeling approaches.

Although Eulerian models exhibit strengths in capturing near-wall flows and resolving turbulence in a manner that aligns with real-world physics, it is important to acknowledge the ongoing debates within the scientific community. Challenges, such as the potential sensitivity to grid resolution and the trade-off between resolved and unresolved turbulence, necessitate a cautious approach in interpreting results. The choice of Eulerian modeling, especially LES, is not without its complexities and its appropriateness depends on the specific characteristics of the scenario under investigation.

5.2. Sensitivity Analysis on Boundary Conditions

In this chapter, the sensitivity of the results is analyzed with respect to specific boundary conditions and the topographic model. To carry out this investigation, transient LES simulations were performed using the foundational setup described in Chapter 4.3. Given the dynamic nature of meteorological conditions during pollutant release events, in which factors such as wind direction, wind speed, and stratification can quickly evolve, it becomes imperative to scrutinize the uncertainty of the solution. This involves varying the inlet boundary conditions to gauge the impact of lower wind speeds at higher altitudes or the variability on turbulent scales.

In addition, modifications to the geometric model, particularly the terrain model, were explored. An alteration involved removing the fluctuating component of the inlet boundaries and adopting a mean velocity profile consistent with the Monin-Obukhov theory. This adjustment aimed to mitigate the inlet boundary dependencies, thus minimizing the influence of large vortices on the direction of the pollutant dispersion. Consequently, only small ground-induced fluctuations would affect the dispersion of the pollutant, resulting in a narrower plume cross-section.

Furthermore, the effects of different types of stratification were examined since this variation induces changes in turbulent terms throughout the simulation domain. Another parameter under scrutiny was the selected aerodynamic roughness length z_0 , which determines the mean velocity profile at the inlet boundaries. By altering this value while

maintaining a constant reference wind speed ($u_{ref} = 1 \text{ ms}^{-1}$) and reference height ($z_{ref} = 10 \text{ m}$) where these wind speeds were measured, lower velocities are observed at higher heights above the ground. This relationship is depicted in Figure 5.15.

In simulations, the turbulent inlet plays a critical role in modeling turbulent atmospheric boundary layer flow. However, it is essential to recognize that, at higher altitudes, the flow can approach laminar conditions if the synthetic turbulence introduced by the inlet is removed. This underscores the importance of considering these factors, as they can profoundly impact the accuracy of simulation outcomes. However, it is crucial to acknowledge that turbulent eddies near the ground can still influence the flow, primarily due to shear generated at the walls. By removing the turbulent inlet, insight is gained into the distinct effects of plume dispersion influenced by the inlet turbulence versus those influenced by the flow's direct interaction with obstacles. This distinction allows for a more nuanced understanding of pollutant dispersion dynamics in complex environments.

Selecting the appropriate value for the aerodynamic roughness length z_0 poses a challenge due to its heterogeneous nature, influenced by variations in terrain, buildings, and vegetation in different areas. Compounding this challenge is the fluid definition of aerodynamic roughness length across different levels, making it challenging for users to pinpoint a specific value for mixed scenarios. When the Monin-Obukhov similarity theory is employed to define mean velocity values at inlets, it is imperative to select the reference velocity, reference height, and aerodynamic roughness length appropriately for the specific type of stratification under consideration. By maintaining a reference velocity of $u_{ref} = 1 \text{ ms}^{-1}$ at a height of $z_{ref} = 10 \text{ m}$, which was determined by the ultrasonic anemometer at CERN, and varying the aerodynamic roughness length $z_0 \text{ m}$, different flow velocity profiles of approach are generated for these configurations, as shown in Figure 5.15. In particular, only the wind speed at the reference height of 10 m remains constant. However, altering the aerodynamic roughness length to $z_0 = 0.25 \text{ m}$ results in a similar near-ground wind speed below the height of $z = 10 \text{ meter}$, which does not significantly affect the total volume flow through the domain. In addition, the velocity at heights above $z = 10 \text{ m}$, which is mainly responsible for the total volume flow through the domain, decreases strongly.

Exploring the influence of terrain type on the sensitivity of pollution dispersion sheds light on the impact of shear produced over longer distances from the release point. Specifically, simplifying terrain using a Digital Terrain Model (DTM) for inflows and outflows replaces complex terrain features with a flat surface, neglecting the presence of vegetation such as forests, vineyards, and grasslands. Resolving vegetation with high grid resolution in inflows or outflows requires significantly more polyhedral cells, and direct interaction with released pollutants is limited, especially when vegetation is located far from the release point ($x > 500 \text{ m}$). This approach closely resembles the physical modeling techniques used in wind tunnels, where the equivalent aerodynamic surface roughness

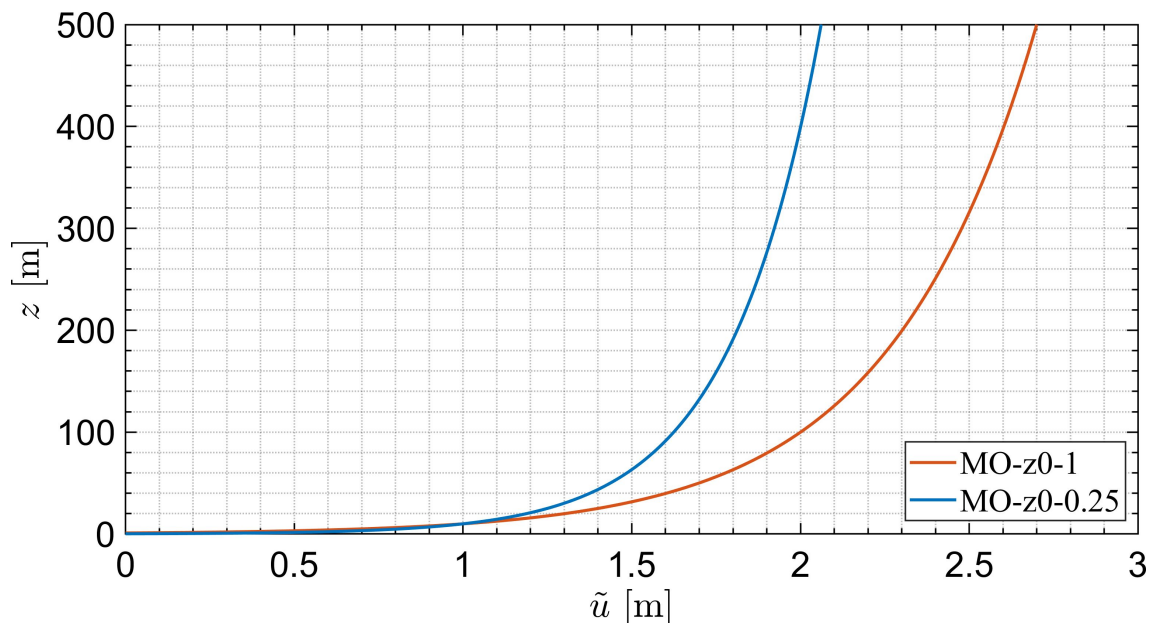


Figure 5.15.: Mean velocity profiles for the reference velocity $u_{ref} = 1$ m/s and reference height $z_{ref} = 10$ m. The aerodynamic roughness length z_0 is altered between the classification for many trees/hedges $z_0 = 0.25$ m and the classification for large towns and cities $z_0 = 1.0$ m, after Stull (1988), while applying the Monin Obukhov similarity theory.

is set using solid obstacles. This approach takes into account the effect of vegetation flow resistance, and the turbulent energy is slightly higher than with the DTM. To model the forest, the DEM can be used to obtain the height of the trees and the volume occupied by them, as shown in Figure 5.16. The equivalent ground surface for the DTM can be found in Figure 4.13. Although the DEM cannot fully account for the turbulence produced in forests, it can still be seen as an initial step toward considering vegetation as a relevant factor that influences airflow near the ground.

An alternative approach, in addition to introducing solid obstacles such as Digital Elevation Models (DEMs) to compensate for momentum sink terms and turbulent energy production, involves employing porous volumes. However, modeling forests as porous zones requires a systematic approach. This starts with identifying forest heights and the corresponding Leaf Area Density (LAD), a crucial factor in the establishment of the model. LAD exhibits significant temporal and spatial variations, especially between summer and winter, and locally, as discussed in Adedipe et al. (2020). Consequently, the corresponding sink or production terms would require adjustments to accurately reflect these variations.

Below, a comparative analysis between the digital terrain model (DTM) and the digital elevation model (DEM) ground surfaces is performed to assess the impact of the absence of vegetation in the DTM model. When differences in flow resistance and turbulence kinetic energy generated by these two approaches are examined, the validity of the results can be assessed. If significant disparities are observed in the areas of interest, it suggests

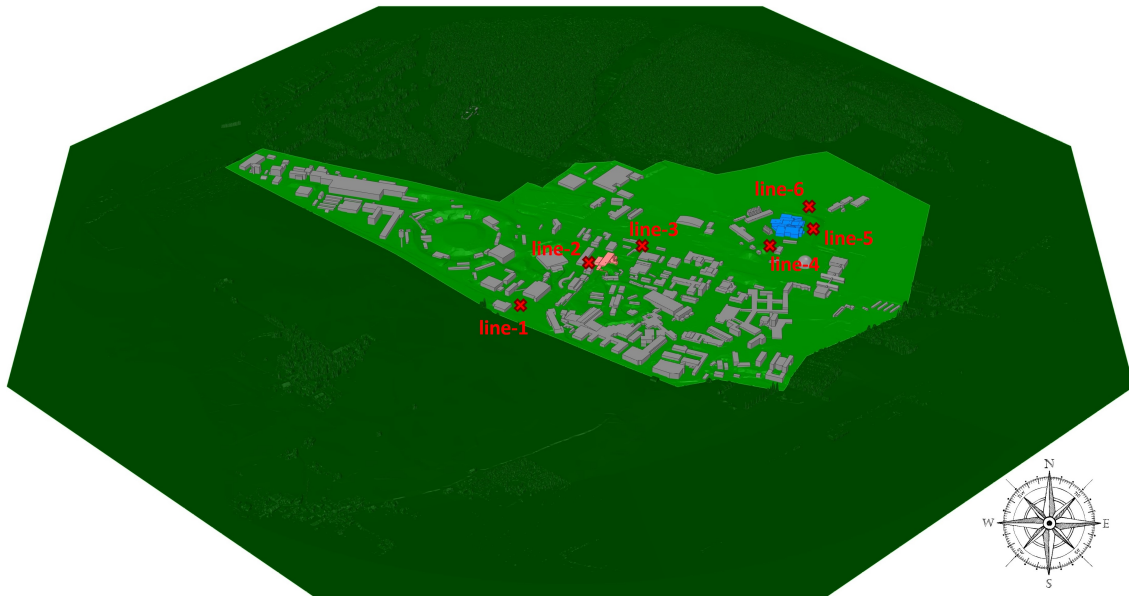


Figure 5.16.: Modelling the geometry with the Digital Elevation Model (DEM) for the surrounding of the CERN Meyrin site. Solid obstacles are shown in green especially in the north of the CERN Meyrin Site and monitoring lines positions are displayed with the red crosses.

that vegetation plays a substantial role in influencing flow dynamics, which warrants adjustments to the model. Conversely, if the results obtained from the DTM and DEM simulations are comparable, it indicates that the presence of vegetation has minimal influence on the turbulence characteristics and the pollutant dispersion, thereby negating the need for vegetation modeling.

In this comparison, the same release scenario as described in Chapter 5.1.1 is used. Using the ANSYS[®] Fluent transport species model, pollutants are released from the ATLAS surface building door, as illustrated in Figure 5.1. To ensure quasi-stationary averaged pollutant concentration values at monitoring planes and points, the release duration is extended to 60 minutes. The resulting time-dependent concentration values are integrated and normalized with the total released mass $m_{released}$ to derive time-averaged normalized concentration values. With the longer release duration and the use of the transport species pollutant tracking method instead of the Lagrangian particle tracking method, a comparison of the concentration values is possible.

In addition to concentration values, two key parameters that govern flow dynamics and, consequently, pollutant dispersion are the mean velocity and turbulence kinetic energy investigated. The characteristics of mean velocity and turbulence kinetic energy near the release point are directly influenced by the prescribed velocity and turbulence conditions at the boundary inlets, as well as by the interaction of the flow with the ground, terrain and buildings upwind of the emission source. Given the alterations in scenarios involving changes in turbulent inlet specifications, mean velocity profiles, or aerodynamic roughness of the ground surface, a significant correlation is anticipated be-

tween these scenarios and the quantities evaluated.

The significance of the zone where the kinetic energy of the turbulence is generated varies depending on the release scenario. In a ground-release scenario, the dispersion of pollutants is heavily influenced by the direct interaction of the flow with the building where the release occurs and the immediate upwind conditions. In contrast, in an elevated release scenario, the specification of turbulence at the inlet can have a greater impact, especially as the plume trajectory extends to higher altitudes where interactions with buildings are limited. The scenario chosen for this study involves a ground release from the ATLAS surface building door, indicating that the highest values of pollutant concentration are expected near the release point. Consequently, the most influential factor that affects pollutant dispersion and plume trajectory is probably the direct interaction of the flow with the buildings rather than the turbulent eddies generated at the inflow boundaries of the entire computational domain.

This study aims to address various inquiries regarding the simulation setup and the consequences of modification in the inlet boundary conditions on the outcomes. These questions encompass:

- Is a turbulent inlet essential for the outcome of the simulations or would it be sufficient to count on a turbulent near ground flow developing in the computational domain upwind of the release location?
- Should the terrain be modeled in both inflow and outflow regions, or could obstacles be relaxed towards the edges of the domain?
- Which boundary conditions yield results that lean towards conservative or realistic outcomes, particularly concerning the analysis of maximum pollutant concentration values and plume size?
- What is the sensitivity of the simulation outcomes to specific boundary condition definitions as, for example, the choice of the aerodynamic roughness length for the definition of the mean velocity profile?

The sensitivity analysis involves four scenarios, identified using the abbreviations listed in Table 5.4 for ease of reference. These abbreviations represent the Digital Terrain Model (DTM), Digital Elevation Model (DEM), No-Fluctuations (NF), synthetic turbulence generator (STG) and Monin-Obukhov (MO) similarity theory, along with the corresponding aerodynamic roughness length z_0 .

Table 5.4.: Convention of four scenarios for simplification reasons.

naming convention	terrain model	turbulent inlet specification	aerodynamic roughness length z_0 [m]
DTM-NF-MO-1	DTM	NF	1.00
DTM-STG-MO-1	DTM	STG	1.00
DTM-STG-MO-025	DTM	STG	0.25
DEM-STG-MO-1	DEM	STG	1.00

5.2.1. Atmospheric Turbulence at Monitoring Lines

To gain deeper insight into the concentration values tracked at the monitoring points and planes, this section delves into the atmospheric flow conditions along designated monitoring lines. These monitoring lines are placed as indicated in Figures 5.16 and 4.37. Positioning the monitoring lines is important for the analysis of the results, particularly for the DTM-NF-MO-1 scenario, which does not include the turbulent inlet condition. When the positions of these monitoring lines would only be centrally between the buildings, the inflow and outflow on the edges of the inner part of the domain could not be investigated. Therefore, positions also on the sides (line-1, line-5, and line-6) have been chosen to incorporate these inflow effects. The locations of the monitoring lines explained in the following list and the elevation of the terrain z_0 are provided at the position of the monitoring line.

- Line-1 ($z_0 = 444$ m):
Located south-west of the inner area of the domain. For south-western wind conditions, there are no buildings in the inflow to the line position. Instead, for north wind conditions, there are several buildings located upstream.
- Line-2 ($z_0 = 443$ m) and line-3 ($z_0 = 438$ m):
Positioned at the center of the buildings and domain, these lines are surrounded by several buildings in both investigated wind directions (south-western and northern wind conditions).
- Line-4 ($z_0 = 441$ m) and line-5 ($z_0 = 440$ m):
Located north-east of the inner part of the domain. For south-western wind conditions there are several buildings upstream of these positions, for northern wind conditions only a few buildings are located at the inflow. The DEM instead models larger areas with forests as solid obstacles upstream also, while for the other terrain models the ground is assumed to be flat.
- Line-6 ($z_0 = 443$ m):
Located north-east of the inner area of the domain. For northern wind conditions, there are no buildings upstream of the line position, similar to lines 4 and 5, but for the DEM terrain, a forest is located at the inflow. For south-western wind conditions, many buildings are located at the inflow to the position of line-6.

In the following subsections of this chapter, the mean velocity profiles will be examined, followed by an analysis of turbulence intensity, and concluding with an investigation of the energy containing eddies with the evaluation using energy cascade plots.

Mean Velocity Profiles

The mean velocity profiles $U(z)$ along each monitoring line are derived by computing the magnitude of the velocity from the time-dependent velocities $u(z, t)$, $v(z, t)$, and $w(z, t)$, and then averaging these values over time. To standardize the results, the mean velocity $U(z)$ is normalized with respect to the reference velocity $u_{ref} = 1 \text{ ms}^{-1}$ at a reference height $z_{ref} = 10 \text{ m}$. The corresponding height z is normalized relative to the height of the domain $H = 500 \text{ m}$. The positioning of the monitoring lines is significant due to the varying altitude of the terrain in the simulation domain.

In addition, this analysis explores two distinct wind directions (NE, S), which affect the observed results due to variations in the presence of obstacles or buildings upwind of the monitoring lines. Lines 1 to 3 are located on slightly elevated terrain, approximately 20 meters above the surrounding area ($\Delta z \approx 20 \text{ m}$). For wind blowing into the north-east (NE), line-1 is completely exposed to the inflow boundary conditions, positioned at the edge of the inner domain (light green). Line-2 is centrally located among the buildings, thus experiencing the strongest deviations in mean velocity and turbulent kinetic energy. With the wind blowing into the south (S), monitoring line-6 is fully exposed to inflow conditions. Lines 3 to 5 should be minimally influenced by surrounding buildings, while lines 1 and 2 have buildings upwind of their positions.

Figure 5.17 illustrates the normalized mean velocity for the DTM-NF-MO-1 scenario, where no fluctuations are defined at the inlet boundary. Across all monitoring lines, the mean velocity values are consistently lower than those defined at the inlet boundary (depicted in black in Figure 5.17). The altitude of the terrain plays a role in the comparison of theoretical values with those extracted from the simulation, as each monitoring line originates from a lower sea level compared to the edges of the domain, which are relaxed to $z = 460 \text{ m}$. Consequently, the domain generally has a higher free cross-section at the center, leading to slightly lower velocities. Within the six monitoring lines, no significant decrease in mean velocity is observed between them. Particularly in the upper part of the domain, where the flow is unaffected by terrain and buildings, the values remain constant as the flow moves from the south-west to the north-east. However, in the bottom layer up to a height of $z/H = 0.2$, the mean velocity profiles exhibit significant variations due to the interaction of the flow with the terrain and buildings.

In the DTM-NF-MO-1 scenario with a wind blowing from north to south (Figure 5.18), the deviation of the mean velocity values between the monitoring lines is minimal. However, a consistent trend is observed, indicating a lower magnitude of mean velocity values. This trend is attributed to the difference in the altitude of the terrain at the monitoring line locations compared to the altitude of the relaxed inflow boundaries.

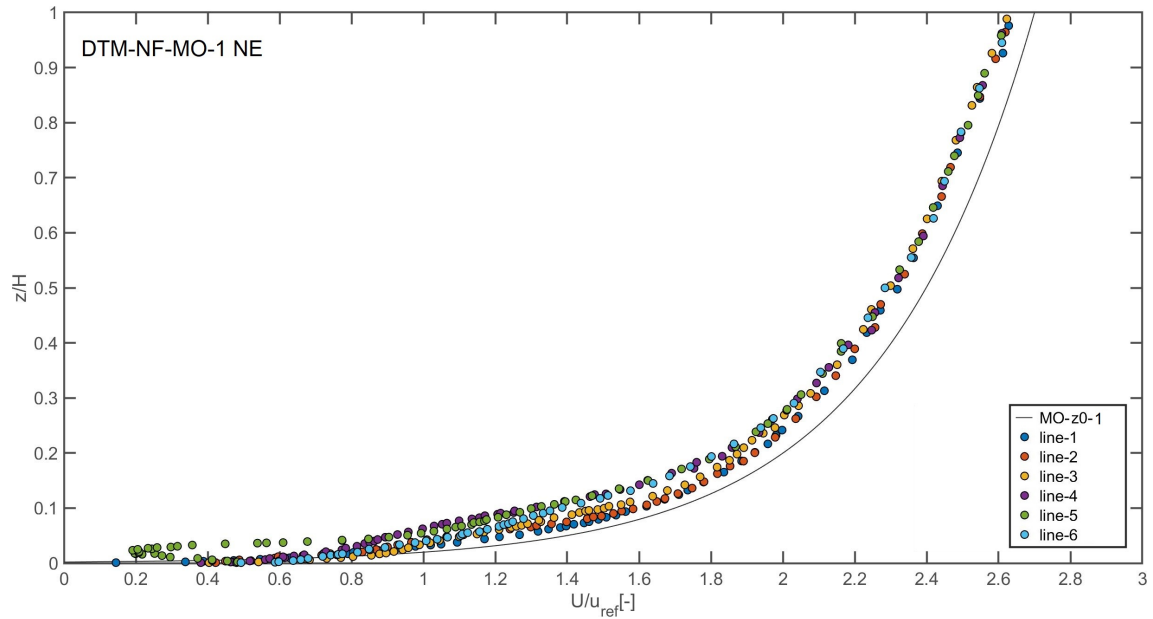


Figure 5.17.: Mean velocity profile for the DTM-NF-MO-1 scenario for wind blowing from south-west to north-east (NE).

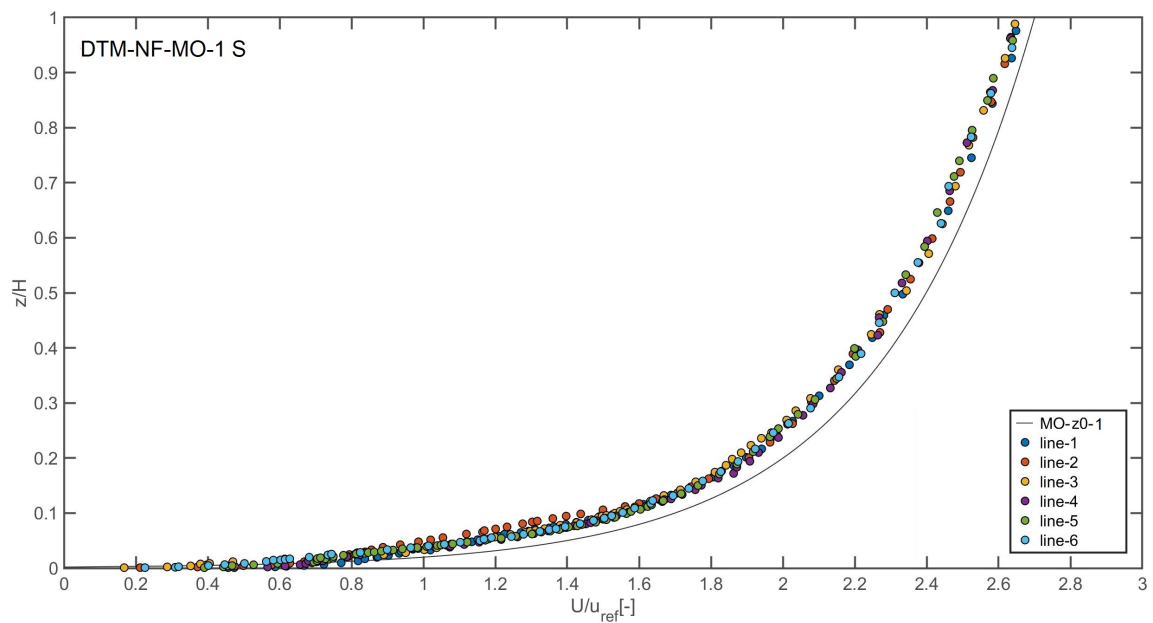


Figure 5.18.: Mean velocity profile for the DTM-NF-MO-1 scenario for wind blowing from north to south (S).

The comprehensive set of mean velocity graphs for each scenario is provided in Appendix D.1. However, in this chapter, the emphasis is placed on the discussion of the results rather than on the exhaustive presentation of all graphs. This selective approach allows for a focused analysis of the findings.

The DTM-STG-MO-1 and DTM-STG-MO-025 scenarios produce results distinct from those of the scenario that lacks turbulent inlet boundary conditions (DTM-NF-MO-1). Specifically, when the wind blows from the north-east, there is notable similarity in the

mean velocity profiles for lines one to three in these scenarios. The flow experiences a slight acceleration on the ground surface from the inflow, reaching its peak at line-1. This behavior can be attributed to the absence of obstacles in the inflow of the DTM terrain and the slope of the terrain in the direction of line-1. Lines four to six instead predict very close mean velocity profiles in the bottom part of the simulation domain as the theoretical curve. In contrast, in the upper part of the simulation domain, lines one to three predict the flow more accurately than lines four to six.

In the case of wind blowing from north to south in the same scenarios (DTM-STG-MO-1 and DTM-STG-MO-025), the velocity profiles generally conform more closely to the theoretical curve and exhibit greater alignment with each other, similar to the DTM-NF-MO-1 scenario. In particular, on line-5, the highest flow velocity is observed close to the ground, while on line-4, the flow is notably slower compared to the other lines, with a discrepancy of up to 20 % from the other positions.

The discrepancy observed in the DTM-STG-MO-1 scenario compared to DTM-NF-MO-1 is mainly attributed to the method of inlet specification. The key distinction between these scenarios lies in the treatment of the inlet boundary: in one case, only the mean velocity is defined, whereas in the other case, a turbulent inlet is specified using the synthetic turbulence generator (STG). In particular, in the upper part of the domain, the differences between each position are pronounced. It appears that relatively large cells may struggle to adequately resolve the vortices generated at the inlet in the upper domain, or that the vortices themselves are of significant size, impacting the mean velocity terms even over extended simulation durations.

Figure 5.19 displays the mean velocity profiles for the DEM-STG-MO-1 scenario with a wind blowing from south-west to north-east. In particular, the prediction of mean velocity close to the ground exhibits a significant increase compared to the DTM scenario, where vegetation is not considered. Including ground roughness, in the form of solid vegetation modeling, in the DEM scenario generally improves the prediction of velocity near the ground. Line-1 in Figure 5.19 exhibits slightly higher values compared to other lines located in the central part of the domain or downstream of the buildings. Moreover, the prediction in the upper domain shows less fluctuation compared to the results obtained with the DTM.

Upon analyzing the mean velocity graphs, it is evident that the predictions for both wind directions exhibit similarities, but also discrepancies of up to 20%. The most accurate predictions are observed in the DEM-STG-MO-1 scenario. In scenarios without fluctuating inlet boundaries, the flow maintains a consistent velocity at different heights, while with fluctuating inlet boundaries and DTM, the velocity profile varies with height and position of the monitoring line. Differences among the six monitoring line locations could be observed not only between the lines but also between the wind directions.

Relaxation of the terrain significantly influences velocity profiles within the inner domain. When the altitude of the terrain at a monitoring position exceeds that at the edge of

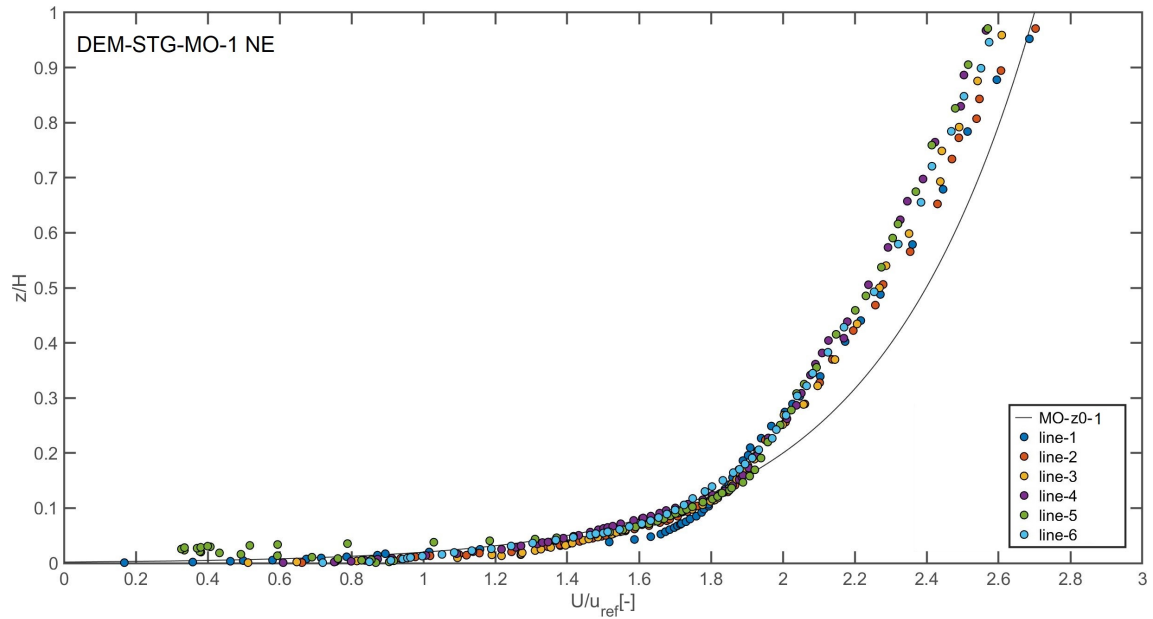


Figure 5.19.: Mean velocity profile for the DEM-NF-MO-1 scenario for wind blowing from south-west to north-east (NE).

the domain, the flow accelerates at that position. In contrast, when the terrain altitude at a monitoring position is lower than that at the domain edges, the flow decelerates. This effect is most pronounced near the ground, where the terrain variations are significant. In particular in DTM scenarios, where the inflow surface is flat, leading to minimal momentum sink terms and turbulence kinetic energy production, the flow tends to accelerate. In contrast, the DEM terrain, characterized by varying geometry due to vegetation, yields more accurate predictions within the inner domain.

In summary, based on the investigation of mean velocity profiles in this section, it can be inferred that the DEM-STG-MO-1 scenario exhibits best results, when comparing them to the theoretical definition at the inlet.

Turbulence Intensity

In the subsequent phase, the fluctuating component of the flow is examined at the specified line positions outlined in the preceding subsection. Choosing turbulence intensity ($I_{u,v,w}$) as the analytical metric enables an independent examination of the streamwise, lateral, and vertical directions. The findings in the four scenarios under investigation are juxtaposed and differences are discussed.

In Figure 5.20, the results of the DTM-NF-MO-1 scenario are shown. Regardless of the direction of the wind, turbulent fluctuations are observed up to heights of $z/H = 0.3$, equivalent to 150 meters above the ground. This scenario serves not as a realistic release scenario, but rather investigates up to which height from the ground mechanical turbulence is produced due to surface friction and obstacles. The results imply that mechanical turbulence primarily affects the lower portion of the simulated domain, suggesting that

microscale modeling should be limited to lower heights, since higher areas are only influenced by the inlet specification method. However, when pollutants approach the limit $z/H = 0.3$ for elevated release scenarios, which are not required at CERN, it may be necessary to expand the size of the domain to encompass distant obstacles influencing the dispersion of these higher-altitude pollutants or to rely on validated turbulence inlet specification methods. This observation also hints at a potential limitation of micro-scale modeling across all four scenarios. The current configuration, which features flat flow conditions at ground level and lacking synthetic fluctuations at the inlet, interacts with ground-level obstacles within the inner domain, generating eddies in the lower layer ($z < 150$ m). Also, for the other scenarios, the on-the-ground generated eddies affect only the lower layer. Eddies above 150 meters from the ground will then solely depend on the fluctuations defined at the inlet.

In Figure 5.20, significant variations in the turbulence intensity in the three directions $I_{u,v,w}$ are evident for both directions of the wind. There are significant differences in turbulence values between line-1 and line-6. When the wind originates from the north-east, line-1 records the lowest values of turbulence intensity, with line-2 and line-3 showing a gradual increase in turbulence intensity in the lower layer. In contrast, line-4, line-5, and line-6 show comparable levels of turbulence intensity. A similar trend is observed for the wind from the south, with line-6 registering the lowest turbulence intensity values, while line-5, line-4, and line-3 demonstrate increasing turbulence intensity values, and line-2 and line-1 exhibit similar turbulence intensity levels. These findings underscore the necessity of specifying a turbulent inlet to accurately capture vortices at higher heights of the atmospheric boundary layer. Additionally, it is essential to note that the directed and non-turbulent inlet condition, which is very rare and for most of the time unrealistic flow conditions in general, does not realistically represent atmospheric conditions. To understand the flow dynamics and the ground-produced vortices with their propagation, this scenario without specifying a turbulent inflow is valid and serves as a basis for further understanding the other more realistic scenarios.

Figure 5.21 shows the intensity of the turbulence $I_{u,v,w}$ for the DTM-STG-MO-1 scenario. This scenario exhibits turbulence intensity levels above 10 % for both wind directions at most heights above ground. Eddies are observed even at higher altitudes, generated by the synthetic turbulence generator (STG). Similarly to scenarios with steady inlet conditions, line-1 and line-6 display extreme turbulence intensity values for both wind directions. In the case of wind blowing into the north-east, line-1, being the first location reached by the flow, exhibits the lowest turbulence intensity. In contrast, for wind blowing to the south, line-6 shows the lowest turbulence intensity near the ground. The discrepancy between the monitoring lines is less than 10 %, suggesting low energy dissipation at higher elevations.

Figure 5.21 also reveals that the eddies in the vertical flow direction, represented by the intensity of the turbulence in the z direction (I_w), generally contain less energy compared

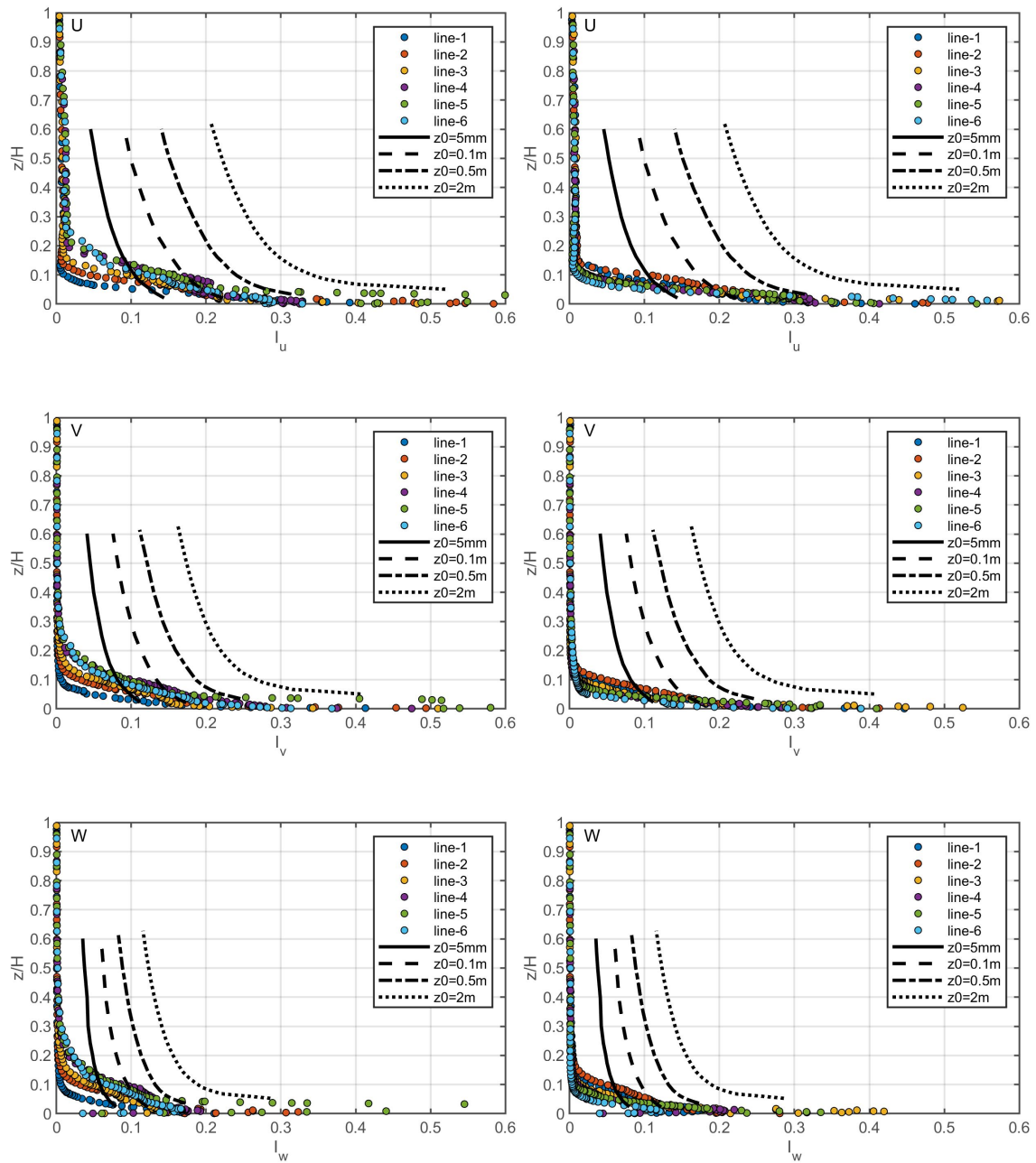


Figure 5.20.: Turbulence intensity shown for the DTM-NF-MO-1 scenario evaluated at six monitoring lines for wind blowing into north-east (left) and south (right).

to the eddies in the x and y directions ($I_{u,v}$). Additionally, eddies in this direction contain slightly decreased energy towards the top part of the domain. This trend suggests that the top layer of the flow is influenced by the boundary condition at the top, where a velocity-inlet without flow perturbations is defined. Although this boundary condition does not significantly affect pollutant dispersion simulations in scenarios with elevated release, where the plume only reaches $z = 100$ m (normalized to $z/H = 0.2$), it does affect eddies in the vertical direction down to $z/H = 0.8$. However, for the scenarios investigated in this dissertation, this effect does not adversely impact pollutant dispersion.

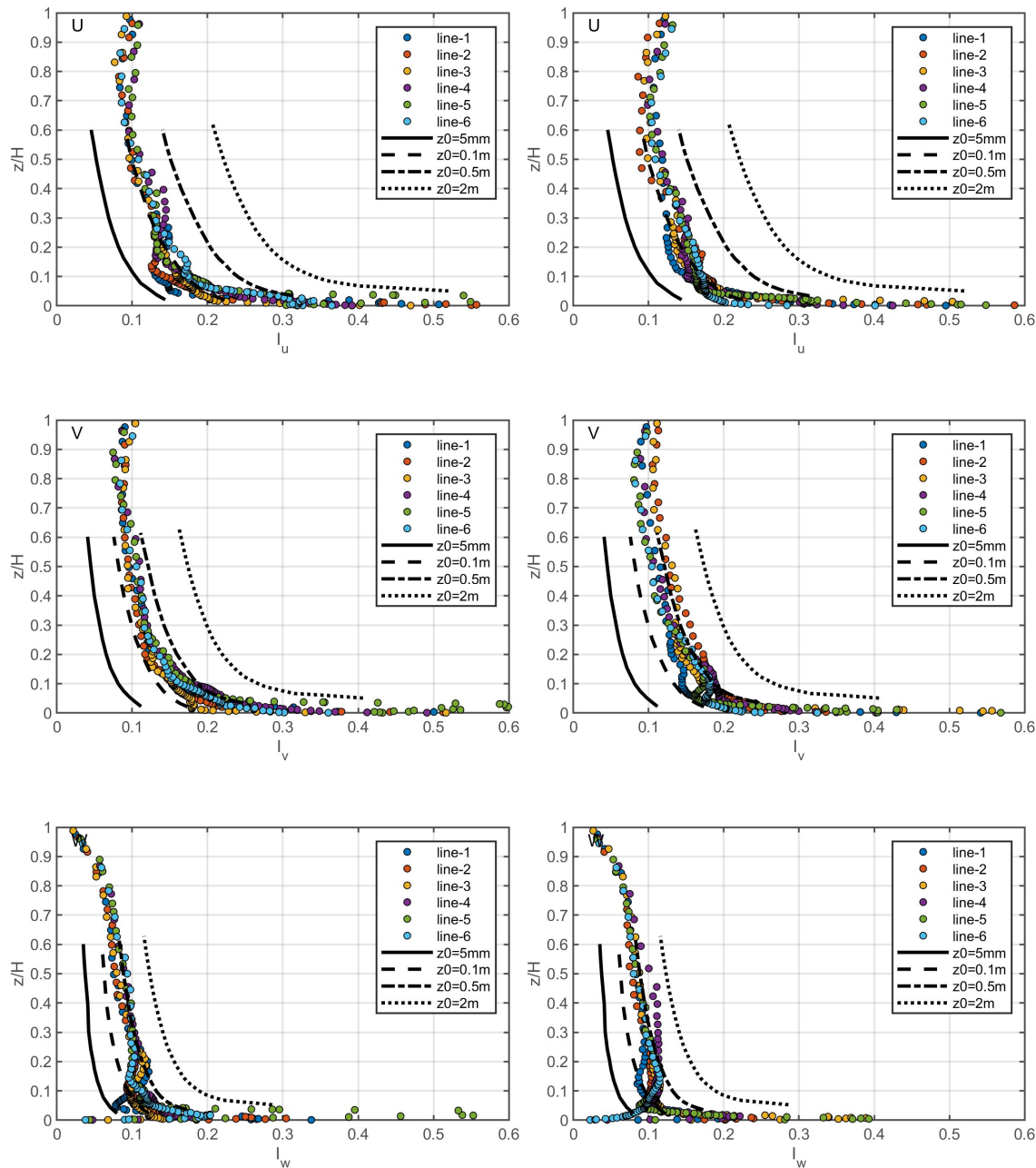


Figure 5.21.: Turbulence intensity shown for the DTM-STG-MO-1 scenario evaluated at six monitoring lines for wind blowing into north-east (left) and south (right).

Figure 5.22 shows the intensity of the turbulence ($I_{u,v,w}$) in the three directions for the DTM-STG-MO-025 scenario, where the turbulence is generated with the STG at the inlet, resulting in a generally lower mean velocity compared to the DTM-STG-MO-1 scenario. The turbulence intensity trends for both scenarios are similar. However, within the DTM-STG-MO-025 scenario, higher turbulence intensity values ($I_{u,v}$) are observed, approximately 10% higher, for every line position with the south wind direction compared to the north-east wind direction. This discrepancy in the intensity of the turbulence might be due to the smaller velocity at heights exceeding 10 meters within the domain.

A lower velocity generally leads to a lower rate of dissipation of energy because there is less internal friction.

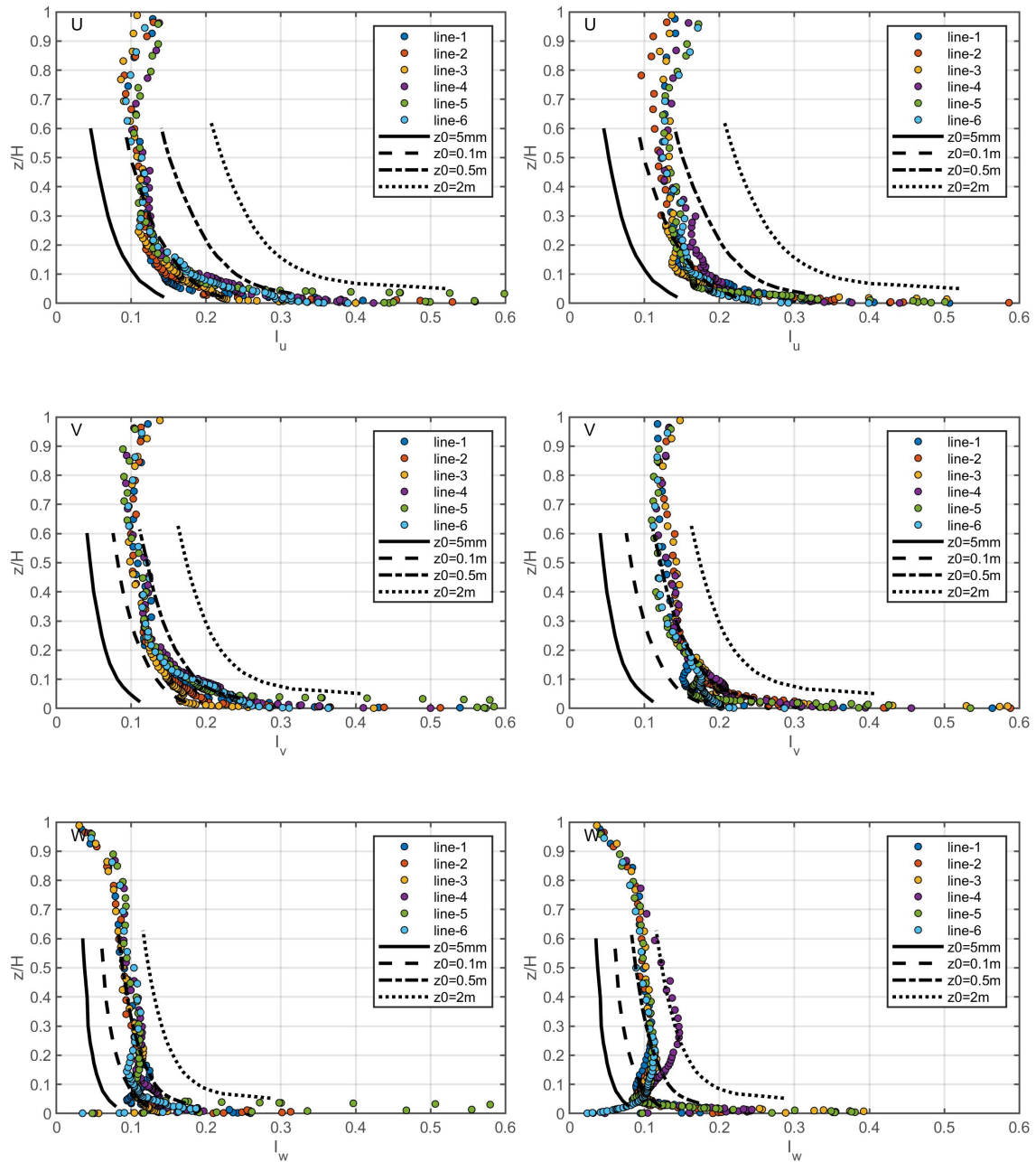


Figure 5.22.: Turbulence intensity shown for the DTM-STG-MO-025 scenario evaluated at six monitoring lines for wind blowing into north-east (left) and south (right).

In Figure 5.23, the intensity graphs of the turbulence for the DEM-STG-MO-1 scenario exhibit similar behavior at the top of the domain compared to the corresponding scenario with DTM. However, a notable difference is observed in the turbulence intensity values across different line positions. Unlike DTM scenarios, where significant discrepancies were observed between line-1 and line-6, the DEM scenario shows much closer agreement among all line positions, typically within a range of around 5%. This suggests that

the DEM scenario performs better overall, probably because of the presence of obstacles distributed throughout the outer part of the domain. These obstacles introduce flow resistance, leading to the production of turbulent kinetic energy, which aligns more closely with real-world conditions.

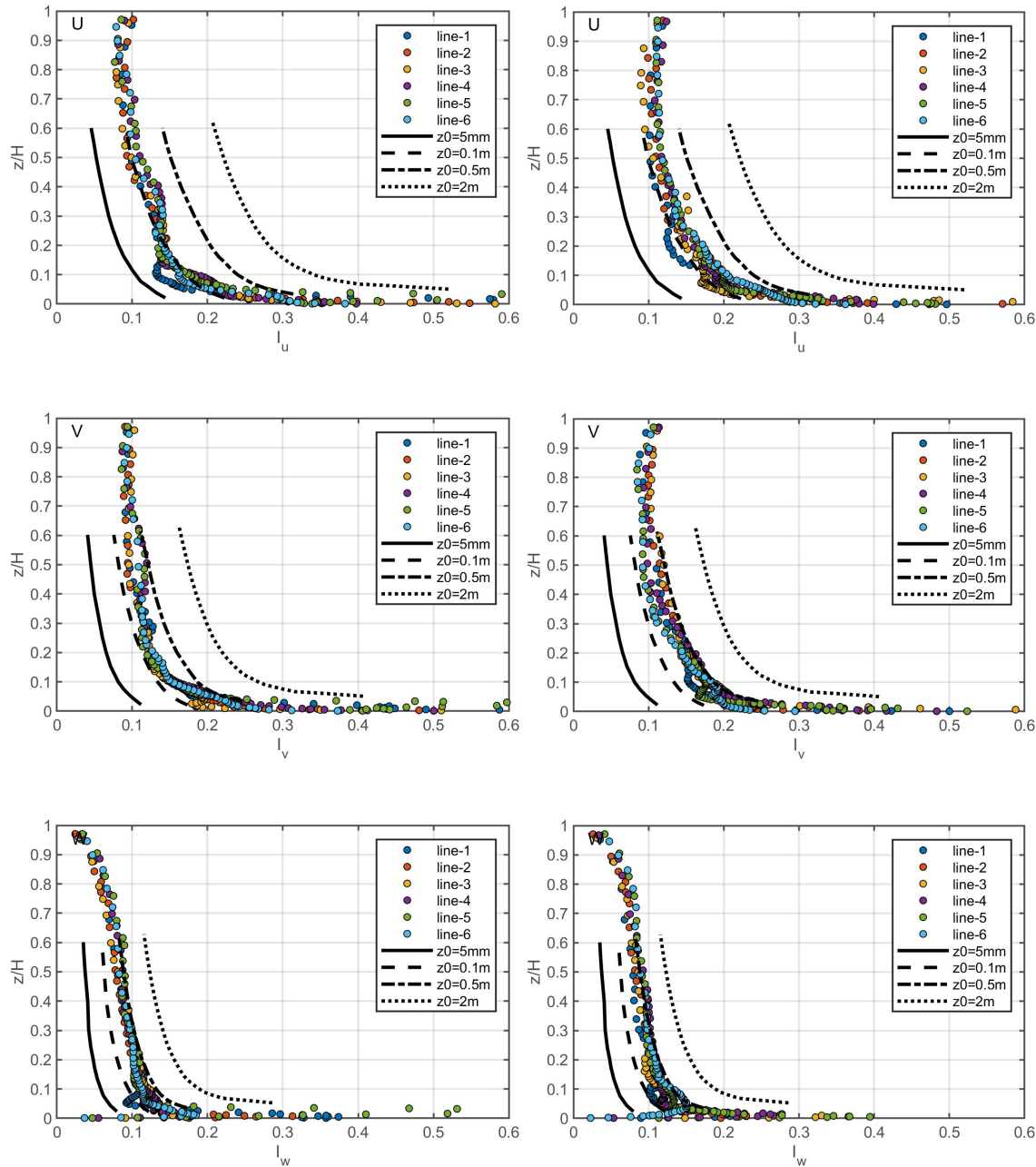


Figure 5.23.: Turbulence intensity shown for the DEM-STG-MO-1 scenario evaluated at six monitoring lines for wind blowing into north-east (left) and south (right).

The turbulence intensity graphs underscore the necessity of employing a turbulent inlet, such as the STG, to generate turbulent flow not only in the lower layer but also in the medium to upper layers of the atmospheric boundary layer. In simulations using the synthetic turbulence inlet model (STG), the intensity of the turbulence reaches values of

approximately 10% between heights of 150 and 500 meters, except I_w in the top domain section. At ground level ($z < 150$ m), the turbulence intensity $I_{u,v,w}$ generally exceeds 10%. These findings are consistent with those of the reference ESDU (1985), which is pertaining to rough or very rough terrain.

Furthermore, DEM emerges as the preferred terrain modeling approach for the outer region of the domain, since it incorporates vegetation and buildings as solid obstacles. However, it should be noted that the DEM model used in the simulation setup is a combination of DEM and DTM. Although the outer part of the domain utilizes DEM, the inner part relies on DTM with a flat surface, augmented by CAD-modeled buildings. Although a full DEM ground was tested, its results were not presented due to significant alterations in ground flow patterns when using non-straight walls in the inner part of the domain. Therefore, caution is advised when configuring the geometry. The presence of solid obstacles, particularly in distant areas from the pollutant release point, aids in modeling flow resistance more accurately and generates eddies in these regions.

Energy Cascade

In this section, the results of the spectral distribution of turbulence kinetic energy of the four scenarios are presented. The time-dependent velocity at each monitoring line was used to compute the spectral distribution of turbulence kinetic energy for each cell intersecting the geometric line. For each scenario, six monitoring lines (5.16 and 4.37) were analyzed, with each line producing between 63 and 105 figures. Across the four scenarios, this process resulted in a total of 1800 figures or 5400 graphs for the three components of the spectral distribution of turbulence kinetic energy. The analysis followed the methodology described in Chapter 4.5.3.

In the preceding subsection on the intensity of the turbulence, certain trends were identified, particularly regarding the artificial behavior observed at the top boundary of the domain in specific directions. Additionally, the influence of no turbulent inlet conditions suggested that few or no vortices are present at heights above 150 meters and that eddy production on the ground reaches a height of around 150 meters. These trends were similarly observed in the plots for the spectral distribution of turbulence kinetic energy. Consequently, the analysis in this subsection will focus on examining the correlation between vortex size and energy. Although this analysis is most relevant near the ground where pollutants disperse, attention was also paid to heights up to 120 meters.

The significance of employing a turbulent inlet to simulate atmospheric flow, which better reflects real wind behavior, is confirmed by the findings from the plots for the spectral distribution of turbulence kinetic energy. Figure 5.24 illustrates that turbulent energy near the ground is better modeled even in a scenario without turbulent fluctuations at the inlet. However, the modeling of energy at higher altitudes is notably insufficient. The decrease in energy starts at approximately 70 meters and diminishes to very low levels around 120 meters.

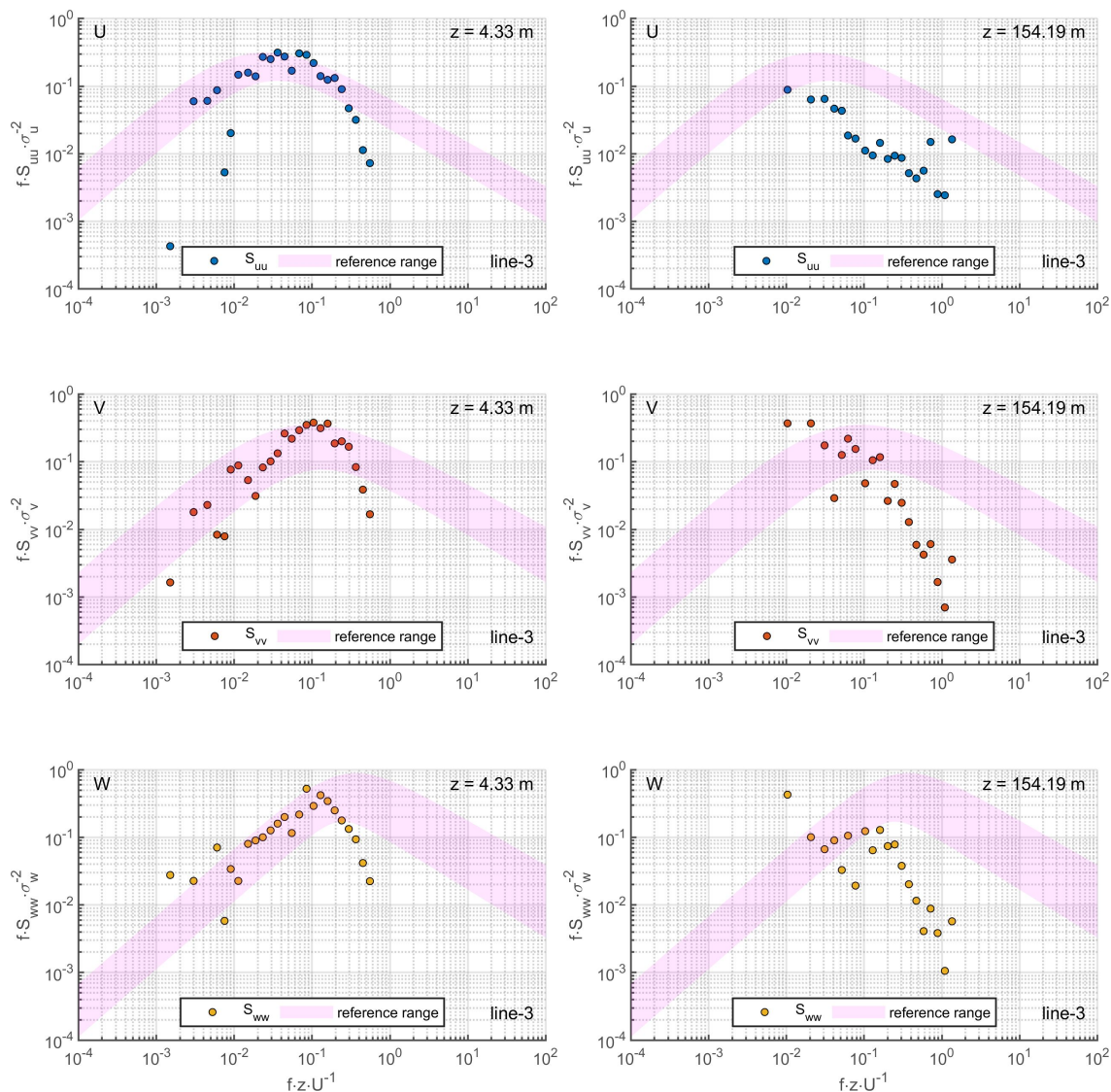


Figure 5.24.: Spectral distribution of turbulence kinetic energy shown for the DTM-NF-MO-1 scenario evaluated at line-3 for wind blowing into south at a height of $z = 4.33$ m on the left and $z = 154.19$ m on the right. References of Simiu and Scanlan (1986) and Kaimal et al. (1972) have been added to the plot.

The transition from an inlet with no perturbation to one that introduces fluctuations using the STG model significantly alters the aforementioned behavior. In the DTM-STG-MO-1 scenario, there is a notable increase in energy for each height for small and medium vortices compared to the DTM-NF-MO-1 scenario, as shown in Figure 5.25. However, very small vortices or high frequencies still appear to be underestimated at a height of $z = 154.19$ m, in contrast to references provided by Simiu and Scanlan (1986) and Kaimal et al. (1972). However, the plume does not extend vertically even close to these altitudes, which means that the dispersion of pollutants in these heights is rather unexpected and, therefore, smaller and medium-sized vortices cannot influence the dispersion of the pollutants. Instead, large vortices at this height may still influence the flow in the lower layer, making them more significant. The scattering of the low frequency band in the

graphs of Figure 5.25 is caused by the relatively short simulation period, and the sampling frequency with 0.2 seconds has definitely affected the high frequency band. The curves are shifted to the reference curves.

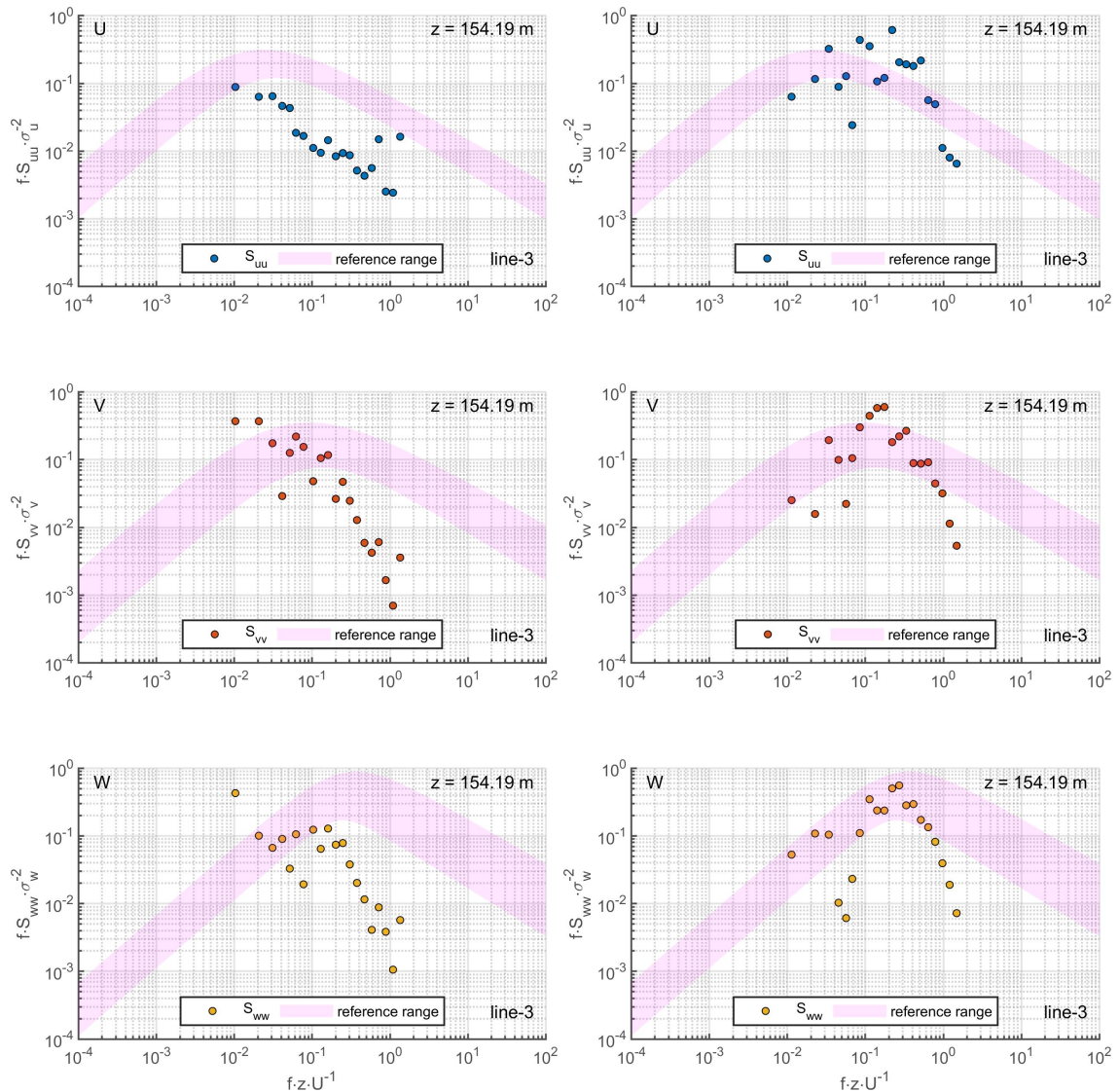


Figure 5.25.: Spectral distribution of turbulence kinetic energy shown for the DTM-NF-MO-1 scenario on the left and DTM-STG-MO-1 scenario on the right, evaluated at line-3 for wind blowing into south at a height of $z = 154.19$ m.

When analyzing the results for the DTM-STG-MO-1 scenario, it becomes evident that the predicted spectral distribution of turbulence kinetic energy closely matches the reference range, particularly at lower altitudes. Similarly, the DTM-STG-MO-025 scenario also exhibits favorable values at lower altitudes, as depicted in Figure 5.26. When comparing these two scenarios with different roughness specifications z_0 in the Monin-Obukhov similarity theory, it is apparent that the mean velocity has no discernible impact on the non-dimensional turbulence observed in the simulation results. Therefore, the previously observed behavior in the turbulence intensity graphs is further supported by the spectral

distribution of turbulence kinetic energy.

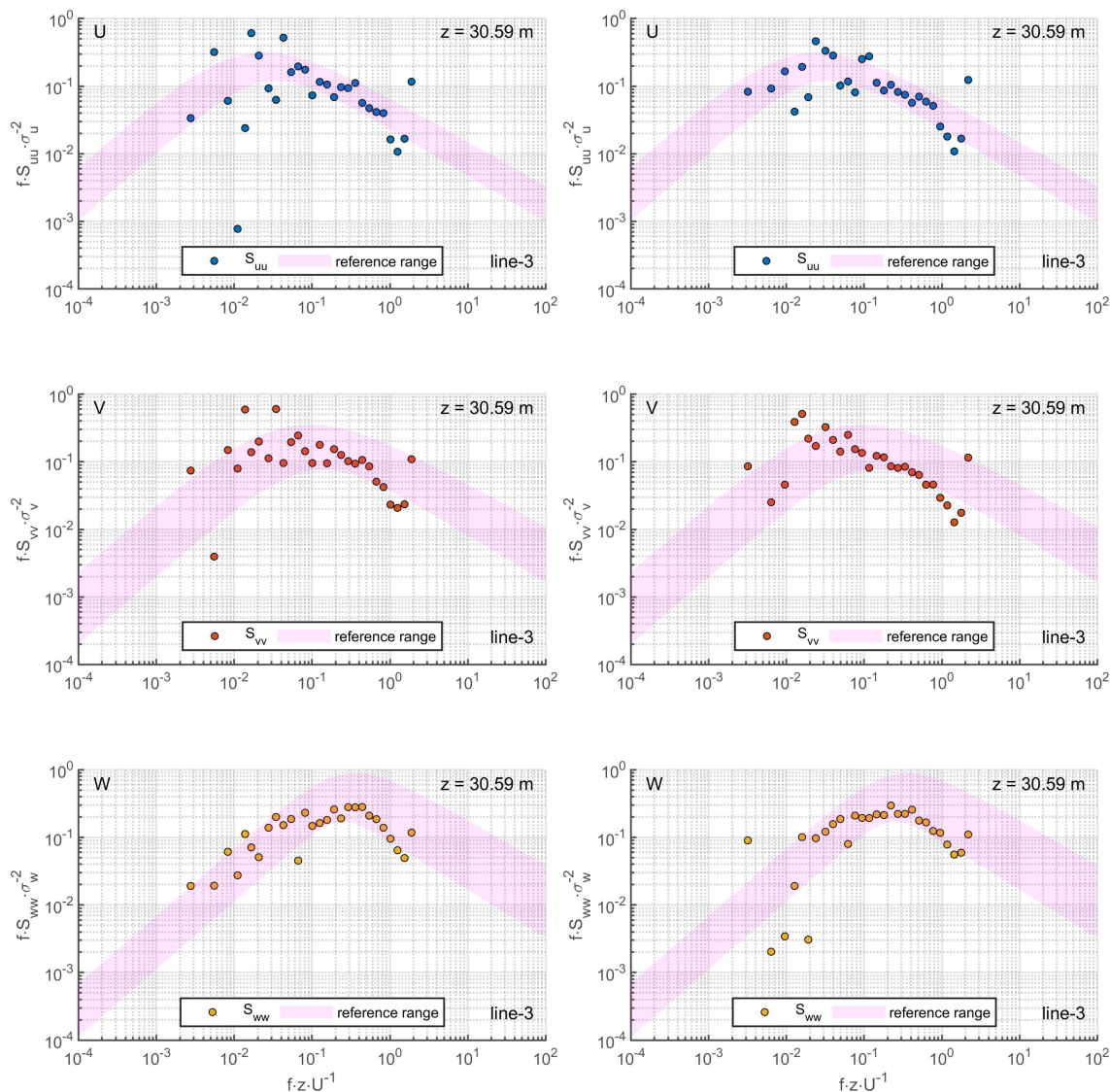


Figure 5.26.: Spectral distribution of turbulence kinetic energy shown for the DTM-STG-MO-1 scenario on the left and DTM-STG-MO-025 scenario on the right, evaluated at line-3 for wind blowing into south at a height of $z = 30.59$ m.

However, Figure 5.27 illustrates the spectral distribution of turbulence kinetic energy for line-5 under conditions of the south wind direction at a height of approximately $z \approx 23$ m. Figure 5.28 shows the spectral distribution of turbulence kinetic energy for line-5 under conditions in the direction of the south wind at a height of approximately $z \approx 30$ m. The figures compare the DTM-STG-MO-1 scenario on the left with the DEM-STG-MO-1 scenario on the right. The turbulent energy levels in the fourth scenario, DEM-STG-MO-1, exhibit even greater consistency with the reference curves provided by Simiu and Scanlan (1986) and Kaimal et al. (1972) than in the DTM-STG-MO-1 scenario, particularly evident in the results for line-5, as illustrated in Figure 5.27. In contrast, for line-3, the DTM and DEM scenarios match closely in predicting the spectral distribution

of turbulence kinetic energy. For example, at a height of approximately $z \approx 30$ m along line-3, the differences between the two scenarios are negligible, as shown in Figure 5.28. This finding aligns with observations from the turbulence intensity graphs, indicating that solid obstacles at the inflow to the inner part of the domain, notably the forests, contribute significantly to the production of energy over distances greater than 500 meters from the inner part of the domain. These eddies are subsequently transported to the central part of the domain, leading to a more realistic resolution of the turbulence in the simulation with the DEM terrain.

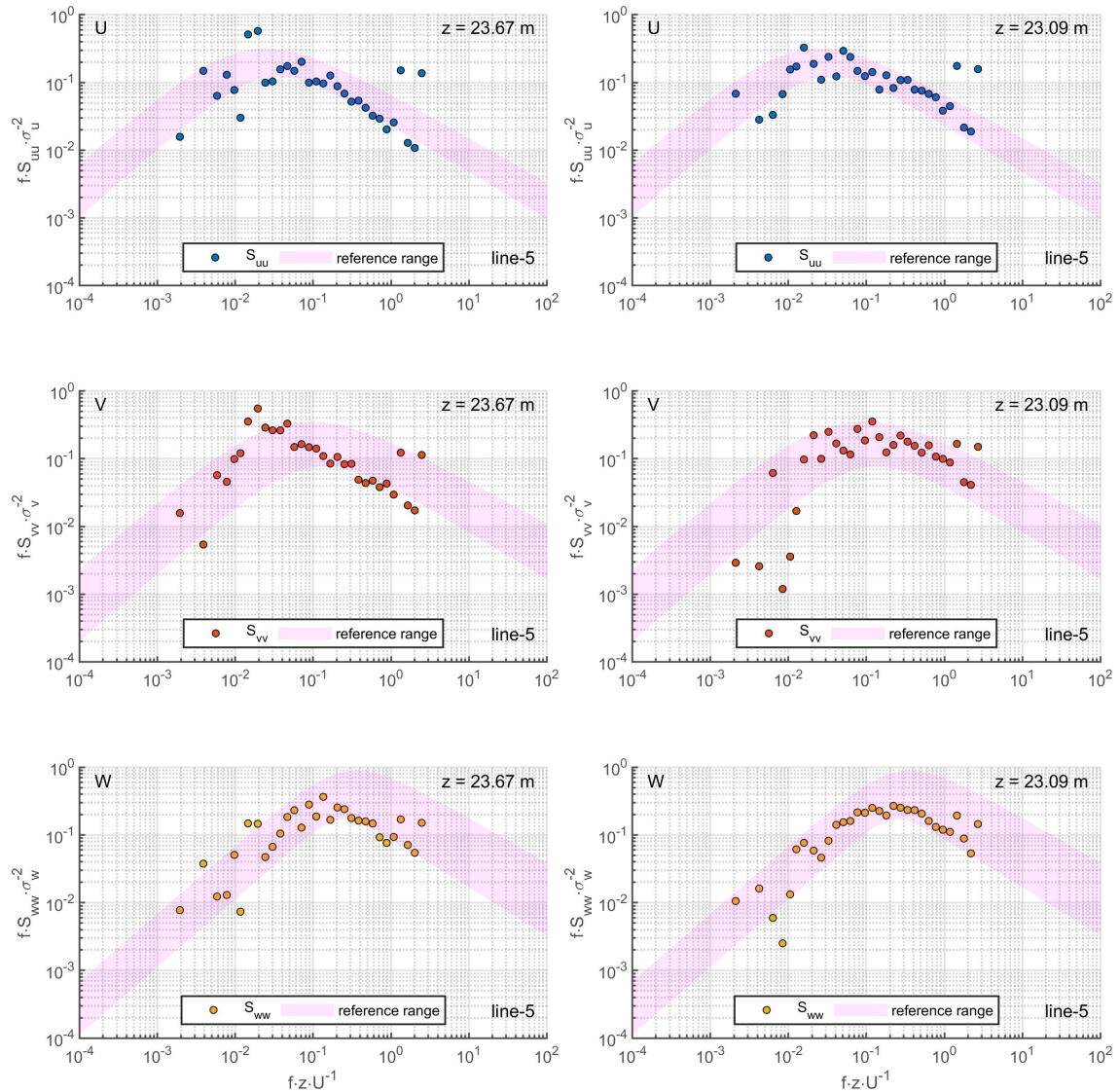


Figure 5.27.: Spectral distribution of turbulence kinetic energy shown for the DTM-STG-MO-1 scenario on the left and DEM-STG-MO-1 scenario on the right, evaluated at line-5 for wind blowing into south at a height of $z \approx 23$ m.

It can be concluded that the DEM, which incorporates obstacles' surfaces in the outer region of the domain, offers slightly closer predictions of the spectral distribution of turbulence kinetic energy due to the additional dynamics contributed by distant obstacles.

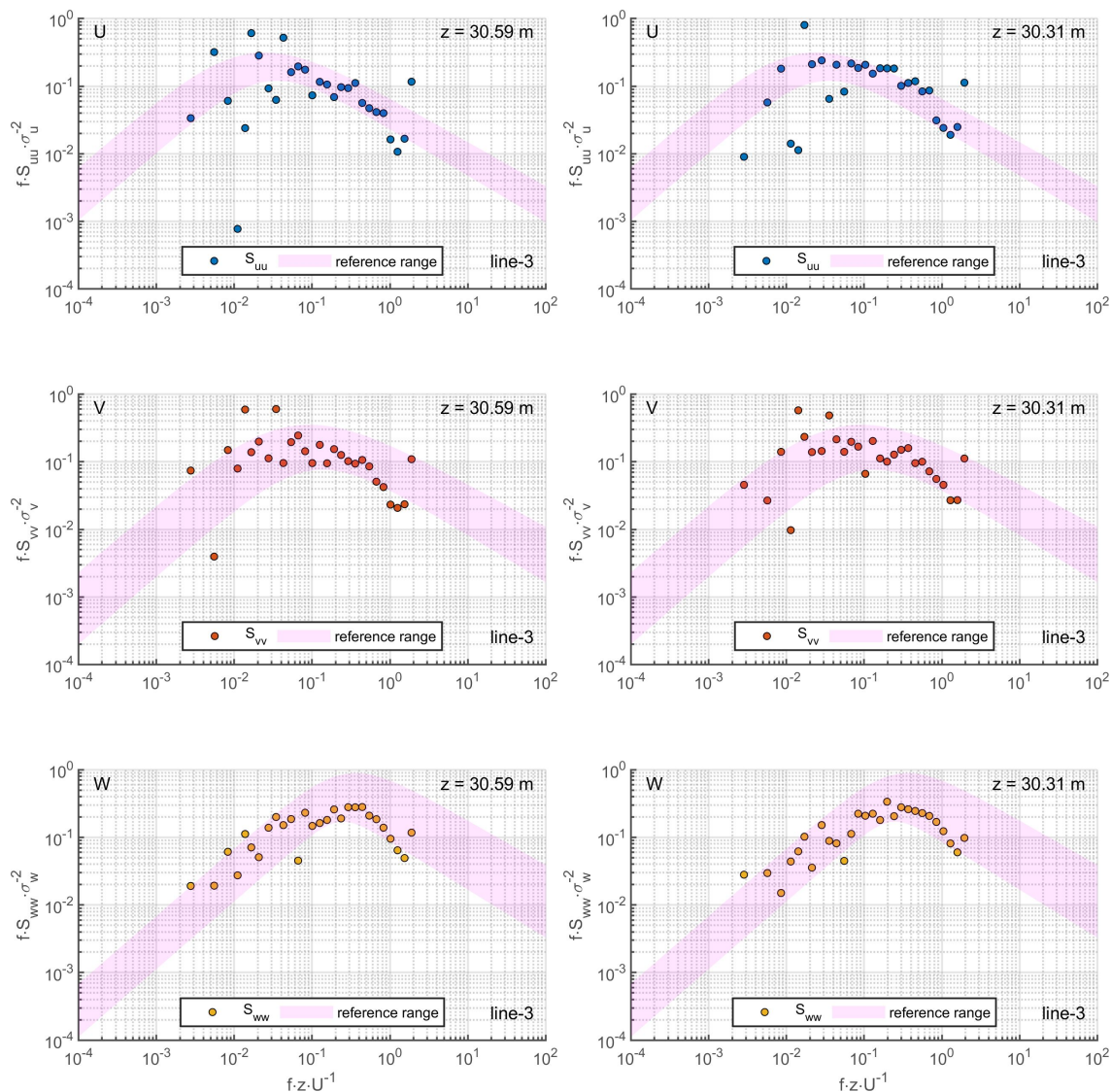


Figure 5.28.: Spectral distribution of turbulence kinetic energy shown for the DTM-STG-MO-1 scenario on the left and DEM-STG-MO-1 scenario on the right, evaluated at line-3 for wind blowing into south at a height of $z \approx 30$ m.

In contrast, the DTM assumes a flat surrounding area, neglecting shear effects generated in areas such as woodlands or suburbs. Consequently, particularly at the periphery of the inner domain with the DTM, the flow tends to underestimate the turbulence generated by vegetation. Small vortices with high frequencies cannot be adequately predicted in the same manner for these two scenarios. As illustrated in Figure 5.27, the DEM significantly outperforms the DTM in capturing high-frequency turbulence.

Analysis of the four scenarios suggests that the DEM-STG-MO-1 model offers a realistic representation of atmospheric flow conditions throughout the entire domain. However, if the release point and the area of interest for pollutant dispersion are located within a built-up area, the DTM yields results comparable to those of the DEM. In such scenarios, employing the DEM may not be essential, and instead, increasing the mesh resolution

in the outer domain could serve as a more efficient approach to minimize computational costs. Instead, when the pollutant source is located at the edge of a built area, considering vegetation in any way might make sense.

Comparison between DTM with and without perturbations at the inlet boundary underscores the importance of synthetic turbulence generators or alternative specification methods. The synthetic turbulence generator notably increases the presence of turbulent eddies in the inflow, which are then conveyed from the domain boundaries to the center, consequently elevating the overall turbulent energy throughout the entire domain height, as observed in the turbulence intensity graphs. The influence of turbulent energy on plume size will be discussed in the following section.

5.2.2. Monitoring-Planes - Dispersion Parameter

In this section, the attention shifts to the dispersion of pollutants and their propagation within the domain, monitored across various monitoring planes, as shown in Figure 4.38. Rather than delve into the dispersion data for each individual plane, the four dispersion parameters outlined in Chapter 5.1.1 are employed to assess maximum concentration, plume size, and plume displacement. The parameters are evaluated for five monitoring planes located at distances x of 40, 110, 200, 300, and 400 meters from the release point.

- \tilde{c}_{max} [m^{-3}]: Maximum mean normalized concentration.
- A [m^2]: Cross-sectional area of the plume with a mean normalized concentration greater than $\tilde{c} > 10^{-5}$.
- \bar{y} [m]: Total mean concentration-weighted displacement of the centerline of the plume in the y direction.
- $\bar{z} - z_{door}$ [m]: Total mean concentration-weighted displacement of the centerline of the plume in the z -direction from ground level.

After evaluating the retrieved data for both wind directions, it becomes evident that slight variations in the boundary conditions can influence the pollutant concentration, although without a strong impact on the dispersion parameters. Figure 5.29 presents the evaluated parameters at five distances from the release point for south-western wind conditions.

Based on the results of the previous section, it is expected that scenarios with higher turbulence intensity, using synthetic turbulent inlet conditions, will generally lead to greater dispersion of pollutants, while the scenario without turbulent inlet conditions (DTM-NF-MO-1) is expected to exhibit a smaller plume size. Furthermore, the inflow condition, which leads to a low mean velocity (DTM-STG-MO-025) is expected to result in a higher concentration compared to scenarios with a higher mean velocity.

As expected, the plume cross-section (A) expands less for the nonfluctuating inlet condition (DTM-NF-MO-1), and the observed concentration is higher than for the other scenarios with the synthetic turbulence inlet condition (DTM-STG-MO-1). This trend per-

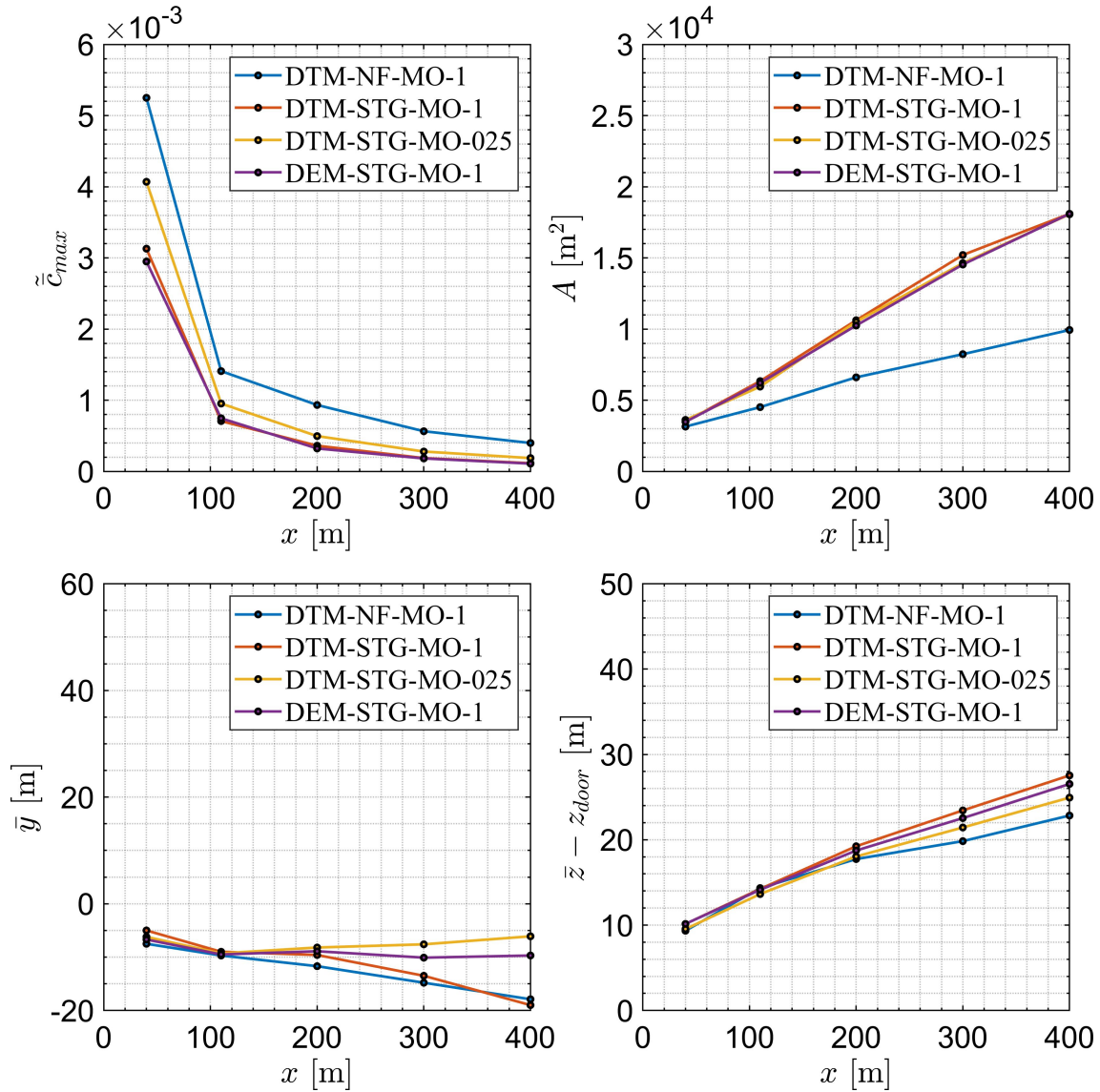


Figure 5.29.: The maximum mean normalized concentration \tilde{c}_{max} , the plume cross-section A and displacement parameters \bar{y} , $\bar{z} - z_{stack}$ are shown as functions of the distance from the release point. These parameters have been evaluated across all monitoring planes and are compared across the four scenarios for south-western wind conditions.

sists from close to the release point to the maximum distance of $x = 400$ m. The mean maximum normalized concentration for the non-fluctuating inlet condition (DTM-NF-MO-1) is approximately 1.73 times higher at close distances and up to 3 times higher for far distances compared to the synthetic turbulence inlet condition (DTM-STG-MO-1). The difference in relative values increases with greater distances, underscoring the importance of appropriately selecting boundary conditions and modeling turbulent inflow conditions.

The plume size is correspondingly up to two times smaller for the scenario without fluctuating inlet conditions (DTM-NF-MO-1) compared to the scenario with synthetic

turbulent inlet conditions (DTM-STG-MO-1). Furthermore, the model without fluctuations at the inlet (DTM-NF-MO-1) predicts the lowest vertical displacement $\bar{z} - z_{door}$, resulting from the lower vertical gradient of turbulence within the boundary layer. This illustrates the expected relationship between turbulence, plume size, and concentration.

The scenarios DTM-STG-MO-1 and DTM-STG-MO-025 exhibit similar performance in terms of turbulence intensity and plume cross-section A . However, the maximum mean concentration is up to 30 % higher for the scenario with lower mean velocity (DTM-STG-MO-025) compared to the scenario with higher mean velocity (DTM-STG-MO-1). This underscores the importance of selecting the appropriate surface roughness parameter (z_0) or, more broadly, ensuring an accurate vertical profile of the mean velocity at the inflow boundary of the domain to obtain realistic concentration estimates.

The differences between the DEM and DTM models are minor, the primary distinction being the slightly less pronounced horizontal plume displacement \bar{y} for the DTM-STG-MO-1 scenario (1.4 degrees). This variation could be attributed to the influence of obstacles on the inflow of the wind.

Figure 5.30 illustrates the results for northern wind conditions, where similar patterns emerge as for the south-western wind condition. The main differences between the four scenarios are as follows:

- DTM-STG-MO-1 and DTM-NF-MO-1: As expected, higher maximum mean normalized concentration is observed when no perturbations are defined at the inlet (120-200 %). The plume cross-section is larger for the scenario with a fluctuating inlet condition.
- DTM-STG-MO-1 and DTM-STG-MO-025: Up to 20 % higher maximum mean normalized concentration are observed for the scenario with a lower velocity.
- DTM-STG-MO-1 and DEM-STG-MO-1: Up to 15 % higher maximum mean normalized concentration can be observed for the flat terrain (DTM), since the turbulence intensity is higher for the DEM, which was discussed in Section 5.2.1.

Despite the consistency of the results for the four scenarios between both wind directions, there are notable differences in the predicted magnitudes. Specifically, the maximum mean normalized concentration for northern wind conditions is approximately twice as high as that for south-western wind conditions. These discrepancies can be attributed to variations in inflow conditions and terrain characteristics.

In the case of south-west wind conditions, airflow encounters several buildings before reaching the release point, resulting in a higher turbulence intensity at the release point. Additionally, the area downwind of the release point is more open compared to the northern wind condition. In contrast, for the northern wind condition, the presence of buildings downstream restricts the movement of the wind, leading to higher concentrations even when the plume cross-sectional area is similar for both wind directions.

If the roughness values and atmospheric turbulence vary in the surrounding area or

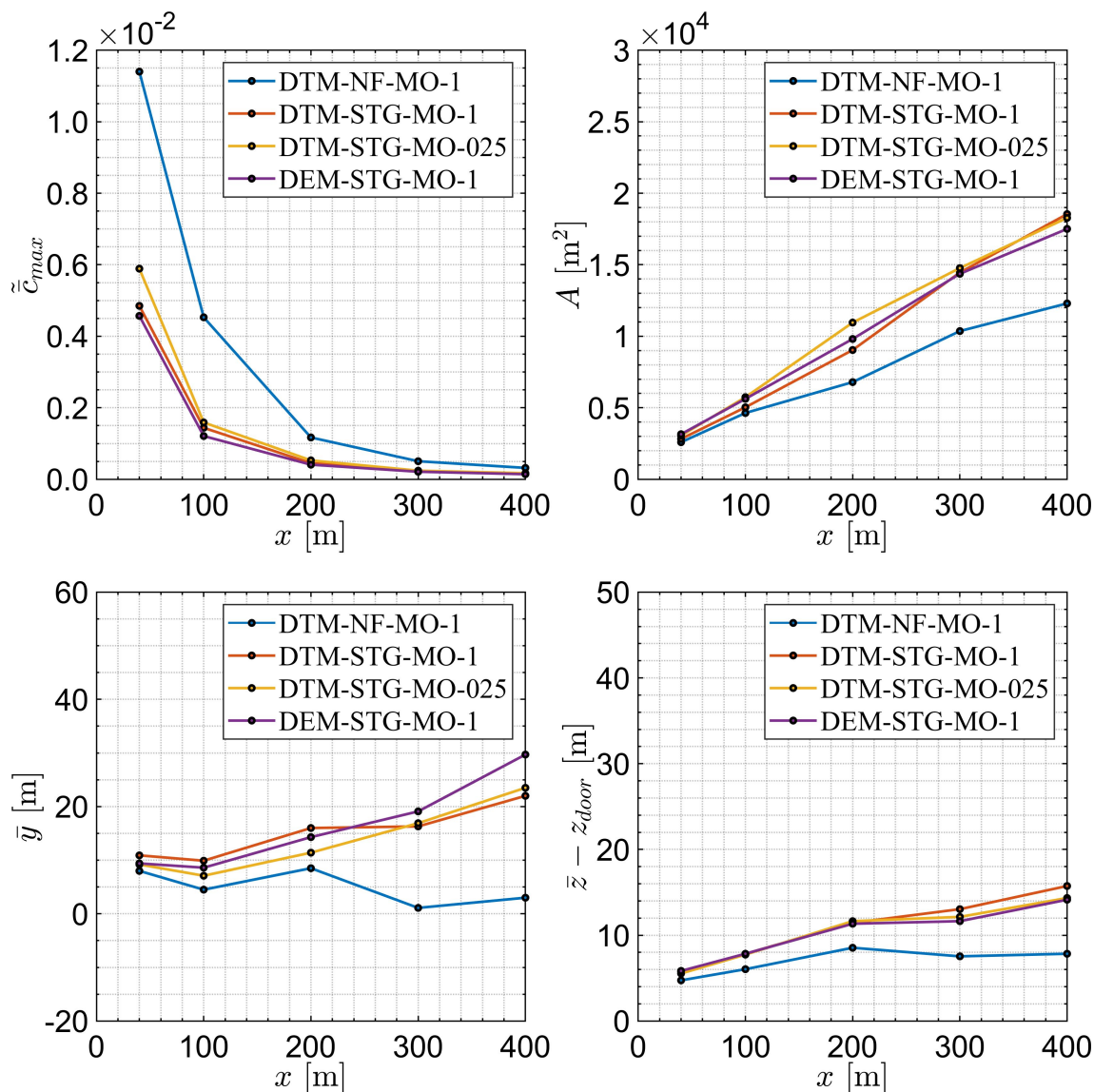


Figure 5.30.: The maximum mean normalized concentration \bar{c}_{max} , the plume cross-section A and displacement parameters \bar{y} , $\bar{z} - z_{stack}$ are shown as functions of the distance from the release point. These parameters have been evaluated across all monitoring planes and are compared across the four scenarios for northern wind conditions.

cannot be clearly defined, the following procedure is recommended for pollutant dispersion simulations.

For scenarios where the assessment focuses on maximum concentrations for individuals very close to the release point ($x < 10$ m), a conservative approach is warranted. In such cases, it is recommended to select a lower surface roughness value (z_0) and the intensity of the turbulence at the inlet.

In contrast, for situations where a greater amount of pollutants is released and the goal is to evaluate exposed or safe areas more thoroughly, higher surface roughness values (z_0) and the turbulence intensity at the inlet should be chosen. This approach ensures

that the plume affects a wider range of regions, facilitating a more thorough assessment.

The results demonstrate a direct dependence on several factors, including turbulence intensity, surface roughness specification, and inlet fluctuations. For high-fidelity simulations of pollutant dispersion, LES should be prioritized over RANS, particularly for safety-critical evaluations. The ability to capture transient phenomena in dispersion scenarios is paramount, aiding in the careful planning of emergency response strategies at facilities such as CERN.

Although RANS modeling can offer similar predictions, it has limitations in accurately representing transient phenomena, such as the wake field of buildings and the interaction of eddies with structures. However, it can still provide valuable insight into the observed trends in maximum concentration for different wind directions.

This investigation shows that it is crucial to define the inlet boundary, including the velocity profile and turbulence intensity, as closely to reality as possible. Although simplifying boundary conditions may yield more conservative results in some aspects, it comes at the cost of a decreased accuracy. Balancing these considerations is essential to obtain reliable predictions in pollutant dispersion simulations.

5.2.3. Monitoring-Points - Ground Concentration

This section presents the results for the monitoring points in the four scenarios of the sensitivity analysis. These monitoring points are 1 meter above the ground, as illustrated in Figure 4.36, to track the concentration of pollutants close to the ground. The concentration values are integrated over the total release time and normalized with the total released mass. Figure 5.31 displays the results for the four scenarios under south-western wind conditions, while Figure 5.32 presents the results for northern wind conditions.

For the scenario without turbulent inlet conditions (DTM-NF-MO-1), higher concentration values are observed for most distances from the release point due to the lower atmospheric turbulence compared to the scenario with turbulent inlet conditions (DTM-STG-MO-1), as discussed in Chapter 5.2.1. Analyzing the ground concentration for both wind directions reveals significant differences, particularly farther from the release point. Under northern wind conditions, the flow interacts with only a few buildings before reaching the release point, resulting in lower ground turbulence and a narrower dispersion of pollutants, especially for the scenario without turbulent inlet conditions. This effect intensifies further away from the release point for the DTM-NF-MO-1 scenario. In contrast, under south-west wind conditions, the flow must pass several buildings before reaching the release point, leading to a higher turbulence intensity at ground level and a generally wider dispersion compared to the other wind direction. This effect is particularly pronounced in scenarios without inlet fluctuations. Although the impact of non-fluctuating inlet conditions is less noticeable for north-east wind direction, it is still advisable to use a turbulent inlet, especially for positions where the release point is located at the edge of built-up areas.

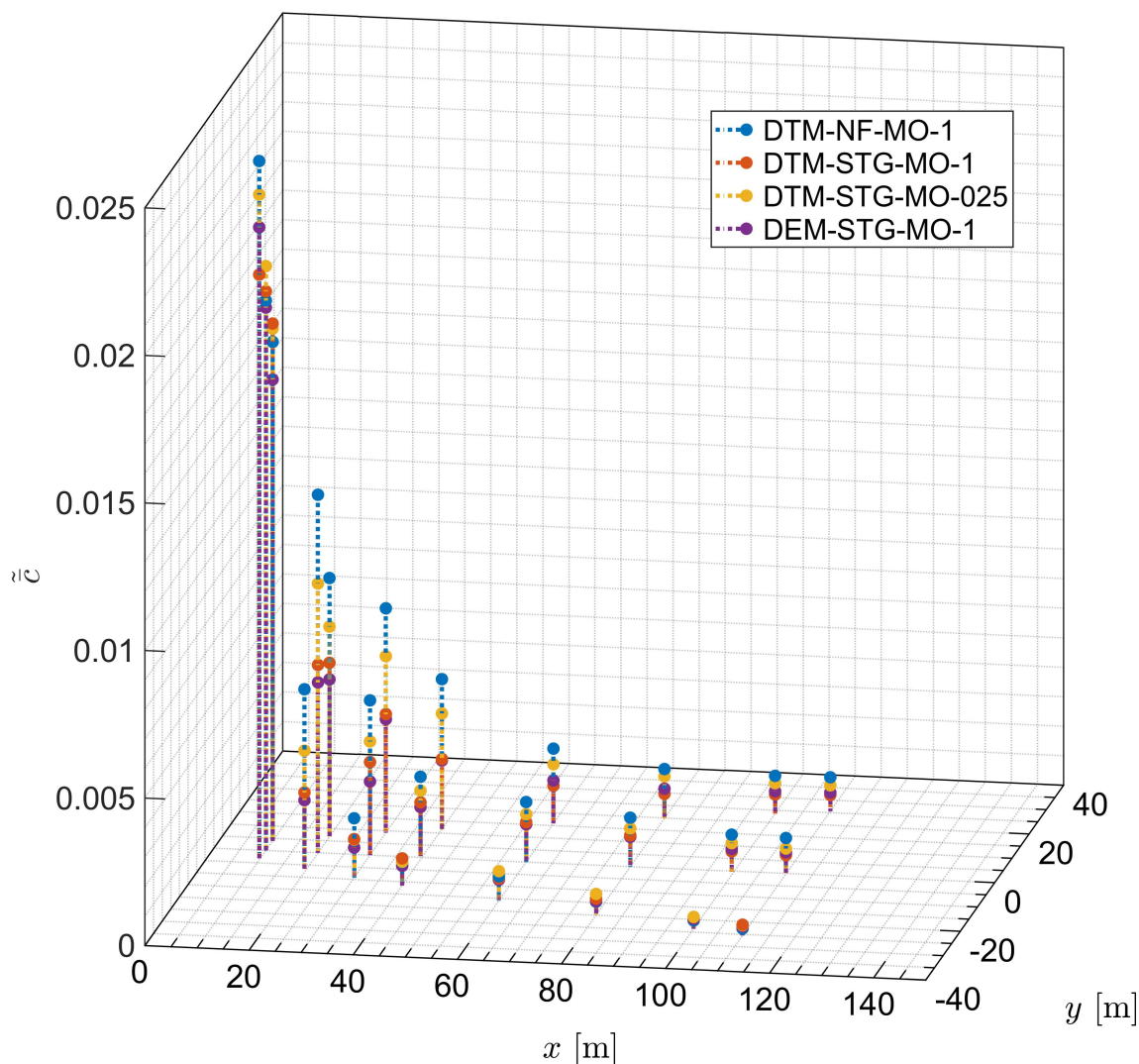


Figure 5.31.: Mean normalized ground concentration values with south-western wind conditions are shown.

For south-western winds, as shown in Figure 5.31, all scenarios at a distance of $x = 10$ m from the release point are within a range of 20 percent for a single lateral position (i.e. $y = 0$ m). Instead, between the different lateral positions ($\pm y$) at the same distance $x = 10$ m are predicting up to 80 percent different concentration values. This behavior can also be observed for further distances, but generally gets less strong. The highest concentration is obtained with the DTM-NF-MO-1 scenario, followed by the DTM-STG-MO-025 scenario, which has a lower mean flow velocity in the inflow (as shown in Figure D.5 and Figure D.6). The scenario with the lowest concentration values is DEM-STG-MO-1. This solution has a higher turbulence intensity, as additional obstacles in the DEM terrain generate supplementary turbulence for both wind directions and lead to a more dispersed plume, both vertically and horizontally, which leads to lower concentration values close to the ground.

For south-western winds, shown in Figure 5.31, all scenarios exhibit concentration val-

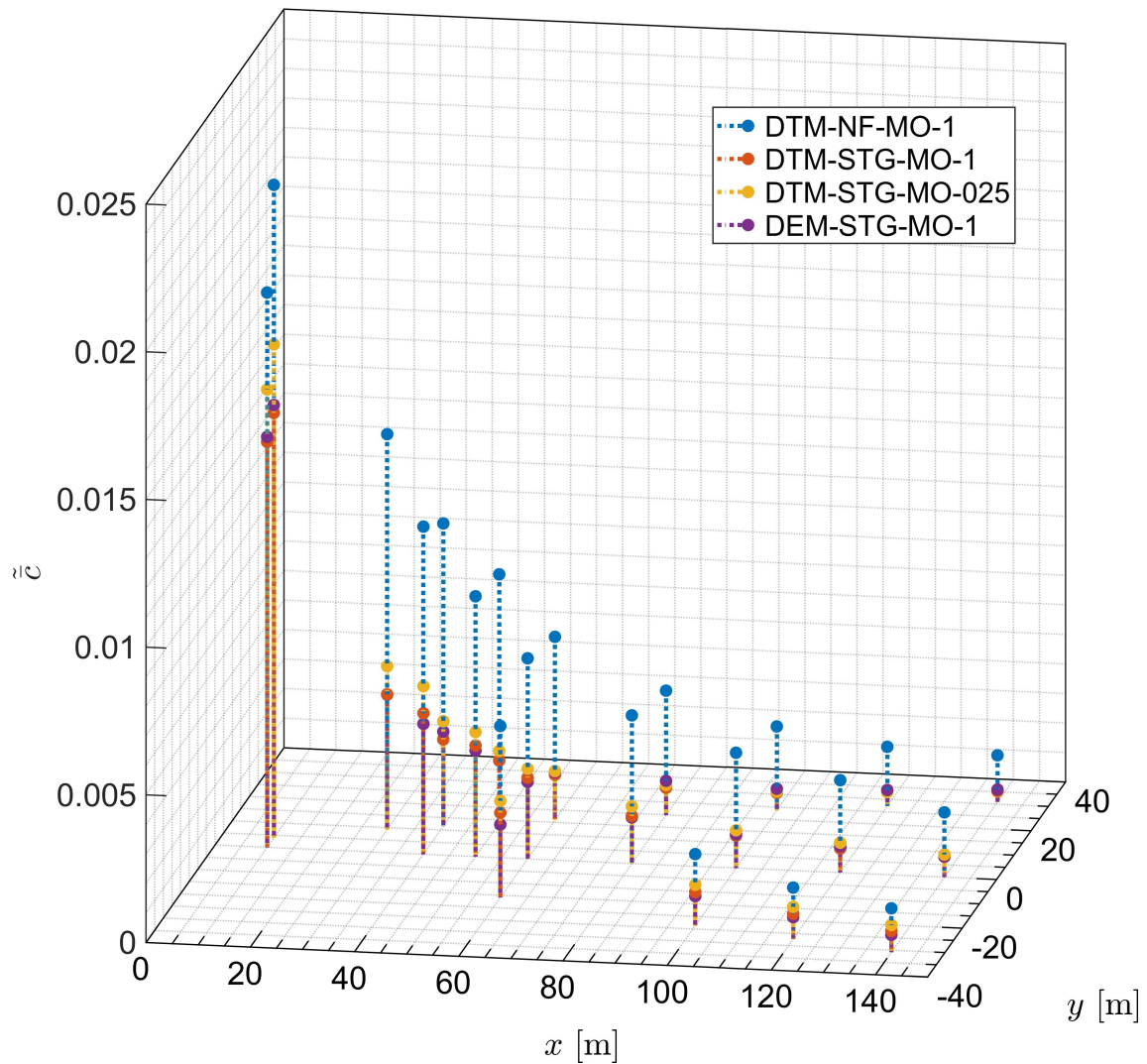


Figure 5.32.: Mean normalized ground concentration values with northern wind conditions are shown.

ues within a 20 percent range at a distance of $x = 10$ m from the release point for a single lateral position (i.e. $y = 0$ m). However, there is considerable variation between different lateral positions ($\pm y$) at the same distance of $x = 10$ m, with concentration values differing by up to 80%. This trend persists for further distances, albeit to a lesser extent. The highest concentration values are observed with the DTM-NF-MO-1 scenario, followed by the DTM-STG-MO-025 scenario, which has a lower mean flow velocity at the inflow (as illustrated in Figure D.5 and Figure D.6). In contrast, the scenario with the lowest concentration values is DEM-STG-MO-1. This solution exhibits a higher turbulence intensity due to additional obstacles in the DEM terrain, resulting in supplementary turbulence for both wind directions and leading to a more dispersed plume, both vertically and horizontally, resulting in lower concentration values close to the ground. The following conclusions can be drawn from the results presented in this section:

- DTM-STG-MO-1 vs. DTM-NF-MO-1:
Fluctuations defined at the inlet of the computational domain result in decreased concentrations close to the ground. Therefore, it is necessary to define turbulent inlet conditions even if the scope of the simulation is to evaluate concentration values only close to the ground.
- DTM-STG-MO-1 vs. DTM-STG-MO-025:
Decreasing the mean velocity of the flow, or in this case selecting a smaller surface roughness parameter z_0 , leads to higher concentration values close to the ground.
- DTM-STG-MO-1 vs. DEM-STG-MO-1:
The transition from flat terrain at the inflow to terrain with solid obstacles slightly decreases the concentration values observed close to the ground because of higher turbulent inflow to the central area of the computational domain.

In unrealistic scenarios lacking turbulent inlet conditions, such as DTM-NF-MO-1, pollutant concentration values can be up to three times higher than in scenarios with turbulent inlet conditions. The definition of the surface roughness parameter is critical not only for concentration values in cross-wind planes, as shown in the previous section, but also for ground concentration values. With the same reference wind speed at the reference height and lower surface roughness values z_0 , the velocity profile, defined by formula 4.9, influences the mean velocity of the flow. This behavior can result in up to 20 percent higher concentration values at specific locations, as illustrated in Figure 5.32. Lower surface roughness values z_0 further exacerbate these effects.

To achieve realistic results, careful selection of the surface roughness parameter z_0 when applying the Monin-Obukhov similarity theory is crucial. This involves determining appropriate reference height and velocity values. Employing a turbulent inlet boundary condition is indispensable for realistic predictions. For more conservative estimates of ground concentration near the release point, a smaller surface roughness parameter z_0 with constant input parameters (reference height z_{ref} and reference velocity u_{ref}) can be chosen. Although using a perturbation-free inlet reduces the computational efforts of the simulations, it also decreases turbulence, especially at the domain inlet. It is important to note that this approach underestimates the impact of turbulent kinetic energy on the dispersion of pollutants, particularly for release scenarios in rural areas.

5.2.4. Sensitivity Analysis - Conclusions

The conclusions derived from the results of the sensitivity analysis on the monitoring lines, monitoring planes, and monitoring points are generally consistent. Simplifying the inlet boundary condition or omitting turbulent inlets results in decreased turbulence within the domain. This decrease in turbulence consequently leads to a more localized dispersion of the pollutants because pollutants are less influenced by turbulent movements that would otherwise disperse them more widely. It should be noted that all

scenarios accurately capture the generation of turbulence by geometric obstacles, which contributes to the propagation of vortices throughout the domain.

The questions posed in the Introduction to this chapter have been thoroughly investigated, leading to the following conclusions.

- Is a turbulent inlet necessary to correctly predict concentration values close to the ground and in close proximity to the release point?
 - **YES** - a turbulent inlet is necessary to simulate a neutral stratification of the atmospheric boundary layer flow with realistic turbulent characteristics.
 - Should the terrain be modeled in the inflow and outflow of the domain?
 - **NEUTRAL** - Including terrain features as obstacles at the inlet and outlet can significantly enhance the realism of the simulation results, as demonstrated in the evaluation of the energy cascade plots for the DEM-STG-MO-1 scenario. However, if modeling complexity needs to be reduced, a flat terrain (DTM) may suffice, particularly when the release point is centrally located within the domain and surrounding obstacles or buildings are accurately modeled. In such cases, choosing an appropriate surface roughness length is crucial to ensure realistic simulation outcomes.
 - How can conservative but still realistic results be achieved in terms of maximum concentration values observed in the close vicinity?
 - **NO PERTURBATION** - Not capturing turbulent motions at the inlet can lead to conservative results in dispersion scenarios. However, it is important to note that, depending on the specific dispersion scenario, concentration values may be overestimated by a factor of two or more. In the scenarios examined in this thesis, an overestimation factor of up to two is applicable.
 - How sensitive are simulation results to the definition of individual boundary conditions?
 - **HIGHLY SENSITIVE** - Simulation results can exhibit high sensitivity to the definition of individual boundary conditions, resulting in concentration predictions that can vary significantly, sometimes by a factor of three for the scenarios investigated in the thesis. Therefore, it is crucial to define the boundary conditions carefully.
-

6. Summary and Conclusion

The research investigates the transient flow and dispersion of hazardous materials (hazmat) at CERN, with a focus on predicting the dispersion of radioactive substances as a consequence of a fire, accident, or terrorist attack. The study develops a methodology for simulating the release of radioactive pollutants or gases using computational fluid dynamics simulations, particularly using large-eddy simulation (LES) to model complex interactions between released pollutants and their environment. This methodology aims to improve safety and environmental assessments in industrial and research settings, with CERN as the main focus.

6.1. Comprehensive Approach to Domain Setup

A comprehensive methodology was devised to develop CFD simulations of ABL flows, which covered the entire process, from the acquisition of terrain data from CERN sites to the manipulation and integration of detailed obstacles and buildings for obstacle-resolved simulations. The optimal domain configuration was identified as an octagon with a medium diagonal of 3 km and a height of 500 m. The octagonal shape was determined to facilitate the establishment of a consistent flow at the transition from velocity inlets to pressure outlets. The recommended topography integrates a digital terrain model (DTM) in the center of the domain and a digital elevation model (DEM) in the outer domain. This configuration allows the induction of eddies in the outer domain by porous structures such as forests, while the combination of CAD-modeled buildings with the DTM ensures a seamless transition between the two domain segments. Accurate modeling of buildings with straight walls is needed for correct flow dynamics representations close to walls.

Relaxation of the terrain at the edges is another critical aspect for the efficacy of CFD simulations. When employing velocity inlets at the walls, a smooth transition from the edges to the inner domain is preferable. Relaxation at the edges of the domain is beneficial in ensuring that the flow defined at the boundaries does not accelerate or decelerate up to the release point. Consequently, the relaxation height should match the height at the release point to maintain a vertical velocity profile consistent with that defined at the edges. A slope of 5.1 degrees or less was found to exert a negligible influence on the flow pattern in the domain. CAD software or programming tools, such as ANSYS SpaceClaim or Python, may be utilized for relaxation implementation.

Modeling challenges, such as backflow, particularly in the domain corners due to fluctuating inlets, need to be addressed. The risk of backflow can be mitigated by opting for an octagonal shape instead of a quadratic shape for the domain. It is also crucial to ensure the absence of large hills or mountains near the domain edges, as they may induce vortices and cause backflow issues, which will expand in size over time and might lead to termination of the simulation. Domain boundaries aligned with the flow direction should ideally be defined without fluctuating velocity terms, while boundaries perpendicular to or at an angle greater than 15 degrees to the flow direction should employ fluctuating inlets, preferably with a synthetic turbulence generator to enhance the accuracy of pollutant dispersion. Vegetation should be accurately modeled if it is proximate to the release point, whereas for vegetation distant from the release point, a detailed modeling approach may not be necessary because the eddies formed in those areas will dissipate before reaching the point of interest. Larger obstacles, particularly hills, distant from the point of interest should be considered as they may generate large vortices that take longer to dissipate.

6.2. Meshing Strategy

The mesh employed in this investigation demonstrated comparable efficacy in terms of turbulence kinetic energy, pollutant concentration, and turbulence energy spectrum for LES simulations with a ground resolution of one meter. This resolution proved particularly effective in regions with buildings and proximal to the release point. Polyhedral cells exhibited superior performance in LES simulations due to their inherent inability to form high aspect ratios. Vortices could develop within merely four cells, allowing coarser meshing relative to other cell types near walls. Beyond their advantageous cell shape, polyhedral cells also provided adaptability to the geometry of buildings, with faces aligned with building walls and fully resolving the geometry. Local refinements could be implemented near surfaces or within specific volumes, facilitating a fine mesh resolution in areas of interest while maintaining a minimal overall number of cells. For instance, the release buildings and adjacent areas could be resolved with a cell size of 0.5 m, while the total cell count in the volume remained below 16 million within a volume of approximately 3.75 km³ throughout the domain. Owing to the extensive domain size, the application of wall-resolved large-eddy simulation was impracticable, necessitating explicit modeling of the ground and building walls. Consequently, a coarser mesh resolution was selected to remain within the range of $0 < y^+ < 300$ for cells close to the ground, with the maximum cell size in the domain set at 80 meters and the region surrounding the release point modeled with cells of a maximum of three meters.

Significant challenges were encountered in the endeavor to partition the computational domain into multiple regions to facilitate the generation of a new mesh for a specific area. For instance, when examining various release scenarios with only the release point vary-

ing, it would be optimal to refine one region while coarsening the previous region. However, achieving an adequate mesh for the ground while maintaining a low total count of polyhedral cells proved to be problematic. Furthermore, the wrapping procedure in ANSYS® Fluent Meshing, required by the input of various data types (such as .stl, .step, etc.), precluded the creation of a conformal mesh at the boundaries. Consequently, it was infeasible to define non-overlapping surfaces even if the CAD geometry of these faces was entirely conformal, as the wrapping procedure misaligned these surfaces, preventing full matching. Therefore, the use of surface wrapping should be avoided whenever possible.

6.3. Crucial Role of Boundary Conditions

In conclusion, the specification of boundary conditions is essential for the precise characterization of flow dynamics and pollutant dispersion in CFD simulations. The analysis of localized meteorological data proximal to the emission source is indispensable for estimating wind vectors, stratification regimes, and surface thermal effects. Adherence to pertinent regulatory frameworks is equally imperative. The Monin-Obukhov similarity theory is extensively employed to delineate the velocity profile of the atmospheric boundary layer, particularly its logarithmic nature proximate to the surface. Meticulous parameter selection for the velocity profile is critical for an accurate representation of the wind patterns, while even minor deviations in surface roughness can substantially influence ground-level pollutant concentrations. The integration of velocity inlets and pressure outlets is effective in preserving mass conservation within simulations. Walls are optimally defined using a no-slip condition to encapsulate their influence within the computational domain. The boundary central differencing (BCD) method is favored over central differencing (CD) due to its expedited convergence and mitigation of backflow phenomena at boundary outlets. Overall, the meticulous definition of boundary conditions is essential for the fidelity of simulation outcomes. Thorough consideration of meteorological data, regulatory compliance, and flow attributes is requisite for an authentic representation of the release scenario and its implications on flow and concentration fields.

6.4. Dispersion Modeling: Lagrangian vs. Eulerian Models

The selection of modeling methodologies for pollutant dispersion is dependent on the characteristics of the pollutants in question. For pollutants with a larger diameter ($d_p > 10\mu m$), the Lagrangian particle model is advocated, given the significant influence of gravitational forces on particle trajectories. Within the Lagrangian particle model, individual parcels (aggregates of particles) can be monitored with a specific range in particle diameter. Furthermore, in scenarios where particle sedimentation and deposition are

substantial, this model may surpass the species model in computational fluid dynamics simulations. In such instances, a wall-resolved large-eddy simulation is advisable, albeit at the expense of elevated computational costs. In contrast, for passive pollutants with diameters ($d_p < 10\mu m$) or gaseous pollutants, these tend to adhere to the streamlines of the primary fluid phase. The species model conceptualizes pollutants as scalar quantities within the flow field and employs concentration equations to elucidate their dispersion.

For the Lagrangian particle model, it has been observed that the total number of parcels introduced is a critical factor, as the movement of the pollutants is directly influenced by the instantaneous velocity field, which varies with each time step. As pollutants attain different positions at each time step, they disperse in multiple directions, resulting in substantial fluctuations in mass flux at considerable distances from the source. Consequently, if the impact in regions remote from the release point is of interest, the application of the Lagrangian particle model is not advisable.

6.5. Simulation Methods and Models

The simulation methods and models must be selected with careful consideration of several factors. Initially, a pristine geometric configuration should be established by integrating terrain data with CAD data at a suitable resolution to achieve optimal outcomes. Subsequently, the mesh and its sizing functions must be delineated, employing a combination of evaluation using Reynolds-Averaged Navier-Stokes equations, where feasible, and remeshing as a prudent strategy. This facilitates the estimation of the mesh for the subsequent large-eddy simulation run based on parameters such as turbulent kinetic energy and local velocities, aiding in the determination of the minimum cell size proximal to the ground. Following mesh preparation, an adaptive Courant-Friedrichs-Lewy-based time-stepping method can be selected to ensure $CFL < 1$, with the time-step size being estimable and potentially increased upon further investigation. In the context of pollutant release, defining the initiation of pollutant injection poses challenges due to atmospheric flow fluctuations, particularly when the release duration is brief, such as in puff releases or short-term discharges. Larger eddies reaching the release point directly influence the initial trajectory of pollutants, thereby affecting their dispersion over extended distances. These substantial eddies may intersect the release point only every 30 minutes or even less frequently. Consequently, if the simulation and release duration are not extensive, these large eddies will intersect the release point only sporadically, leading to potential variability in the results.

6.6. Gaussian Plume Models and Large-Eddy Simulations

The results of pollutant release scenarios derived from analytical Gaussian plume models, as elucidated in Chapter 5.1.1, and large-eddy simulations can exhibit similarities

depending on the chosen scenario. For elementary ground-level smoke releases, the dispersion patterns may align closely for specific wind directions. In contrast, for other wind directions, the observed concentrations near the ground may be affected by proximate structures, which the large-eddy simulation accommodates by incorporating the topography and edifices, thereby enhancing the fidelity of the results. In scenarios involving relatively flat terrain with minimal buildings in the flow path, the dispersion of pollutants can be comparably predicted by both Gaussian plume models and large-eddy simulations. However, for release surfaces exceeding 1 m^2 , Gaussian plume models tend to overestimate concentrations near the release point due to the assumption of a point source, whereas large-eddy simulations generally yield superior and more reliable results by integrating the actual geometry into the simulations. For Gaussian plume models with area sources these are usually modeled by multiple single point releases. These release area must be carefully determined beforehand.

For more intricate release scenarios, such as stack emissions or dense gas releases, it becomes particularly challenging for analytical models to replicate the results obtained from CFD simulations. Large-eddy simulation, in contrast, can deliver significantly more realistic outcomes, as it accurately resolves the flow around structures, accounting for the plume downwash induced by the building's wake. Gaussian plume models, on the other hand, cannot capture this level of detail, and although some models endeavor to simulate similar effects, they fall short of the precision of large-eddy simulations. Furthermore, dense gas releases pose substantial predictive challenges for analytical models, whereas large-eddy simulations can markedly outperform other simulation methods and simpler models in these contexts. Consequently, the results derived from Gaussian plume models and large-eddy simulations can diverge considerably for these types of scenarios.

However, the limitations faced by Gaussian plume models in the near-field become advantageous in the far-field. The computational efficiency of Gaussian plume models is significantly better, facilitating straightforward assessments over extended distances. Large-eddy simulations, on the contrary, are particularly advantageous for regions proximate to the release point and in densely built environments where Gaussian plume models may not accurately predict the flow. Large-eddy simulations are especially valuable for evaluating the affected area surrounding a potential release point for emergency preparedness and estimating the dosimetric impact on receptors in the affected area. Thus, the potential impacts of pollutants on the population or receptors in the affected vicinity at the time of release can be estimated with greater certainty.

6.7. Sensitivity on Boundary Conditions

Concentration values at various positions are significantly influenced by boundary conditions, which include not only the released mass but also the inlet conditions. More turbulent flow at the inlet facilitates a wider spread of pollutants. Furthermore, elements

such as trees within the geometry induce turbulent fluctuations in the flow, thereby enlarging the plume and diminishing the concentration downstream of the release point. The selection of the Monin-Obukhov roughness parameter for the ground also modulates the logarithmic mean wind profile, subsequently impacting pollutant dispersion. The prolonged residence time of pollutants in a specific location due to the reduced air velocity results in combination with the same release mass flow rate to higher time-integrated concentration in a specific cell.

To achieve realistic predictions of flow and pollutant trajectories, it is advisable to employ a turbulent inlet condition. For studies aiming to ascertain the maximum concentration of receptors in the vicinity, a non-fluctuating inlet can be utilized for a conservative outcome, while underestimating the plume size. This approach mitigates the formation of larger eddies at the inlet surfaces, as only smaller to medium-sized eddies typically develop en route to the domain center due to the influence of forests, buildings, or ground shear forces. For a relatively straightforward methodology yielding mean pollutant trajectory predictions, a combination of large-eddy simulation and a non-perturbation inlet may be selected.

The impact of vegetation on pollutant dispersion was examined and should be modeled with the utmost diligence whenever possible. The proximity of vegetation to the release point necessitates precise modeling, as it can substantially affect pollutant dispersion. Given the impracticality of resolving individual trees and their leaves due to computational demands and seasonal variations in their impact on flow, careful consideration is warranted in deciding the modeling approach. When vegetation is proximal to the release point and directly influences pollutant dispersion, it is recommended to model it as a porous zone, incorporating leaf area density based on tree type and seasonal variations, or as a rough solid structure if the leaf area density estimation is infeasible.

6.8. Turbulent Inlet Specification Method

It can be demonstrated that the synthetic turbulence generator integrated within ANSYS® Fluent operates at a superior level relative to the more traditional vortex method found in the literature. The synthetic turbulence generator not only matches or surpasses the vortex method in terms of evaluation metrics, but also markedly reduces computational time. Specifically, the vortex method necessitates nearly three times the computational time to resolve an equivalent simulation setup. Consequently, it is advisable to employ the synthetic turbulence generator for future analyses of pollutant release scenarios when utilizing ANSYS® Fluent.

6.9. Outlook

Following preliminary investigations conducted for the FIRIA project at CERN, the project has advanced into its second phase, wherein the developed tools will be deployed in the production stage across multiple scenarios. The foundational work presented in this dissertation is pivotal for the efficient generation of further results through the implementation of the described methodologies. Large-eddy simulation has demonstrated considerable potential for modeling pollutant dispersion in the scope of atmospheric boundary layer flows at CERN, and the partial validation of the investigated scenarios could yield valuable insights for future applications extending beyond the scope of CERN. However, due to travel restrictions and limitations imposed by the University in response to the COVID-19 pandemic, complete validation during this work was not feasible. Consequently, conducting validation studies would significantly improve the reliability and applicability of the developed methods.

6.10. Scientific Summary

This dissertation presents a comprehensive approach to modeling atmospheric boundary layer flows and pollutant / gas dispersion using computational fluid dynamics, specifically tailored for hazardous material releases at CERN research facilities. The core scientific questions addressed in this research include:

1. How to optimize the simulation domain configuration for accurate ABL flow and pollutant dispersion modeling?
2. What is the impact of detailed terrain and structural modeling on the fidelity of CFD simulations?
3. How to effectively implement and compare various boundary conditions to enhance simulation accuracy?
4. What meshing strategies are most effective for large-eddy simulations in complex environments?
5. How do different types of pollutants and release scenarios affect the selection of modeling techniques?

Key Developments and Establishments

1. **Optimal Domain Configuration:**

Developed an octagonal simulation domain with a medium diagonal of 3 kilometers and a height of 500 meters. This configuration ensures robust flow transitions and minimizes backflow issues.

2. **Detailed Terrain and Structural Modeling:**

Integrated digital terrain models (DTM) and digital elevation models (DEM) to represent terrain characteristics.

Employed CAD software to model buildings and vegetation, ensuring high-fidelity replication of turbulent structures and flow interactions with obstacles.

3. Boundary Conditions and Flow Characterization:

Conducted a thorough analysis of weather data and regulatory standards to define velocity profiles, surface roughness, and inlet / outlet conditions.

Demonstrated that the combination of velocity inlets and pressure outlets is effective for mass conservation and accurate flow representation.

4. Meshing Strategy for LES:

Implemented a meshing strategy with a ground resolution of one meter and polyhedral cells near surfaces of interest, achieving a balance between high resolution and computational efficiency.

Highlighted the benefits of using polyhedral cells for their ability to form vortices within fewer cells, facilitating coarser meshing without compromising accuracy.

5. Modeling Techniques for Pollutant Dispersion:

Recommended the Lagrangian particle model for larger pollutants (diameter $>10\mu\text{m}$) due to its ability to account for gravitational forces.

Advocated the species model for smaller pollutants and gaseous releases, where gravitational effects are negligible, and dispersion follows fluid streamlines.

Achievements

- **Enhanced Simulation Accuracy:**

By incorporating detailed terrain and structural data, the developed models provide highly accurate simulations of ABL flows and pollutant dispersion, surpassing the capabilities of traditional Gaussian plume models (GPMs).

- **Improved Computational Efficiency:**

Demonstrated the effectiveness of the synthetic turbulence generator in ANSYS® Fluent, which not only matches the evaluation metrics of traditional methods but also significantly reduces computational time.

- **Practical Applications:**

The methodologies and models developed have direct applications in environmental assessments, emergency preparedness, and air quality management at CERN and similar research facilities.

- **Dense Gas Dispersion Analysis:**

Investigated the dispersion of dense gases, such as argon, using CFD simulations, highlighting the superior predictive capabilities of large-eddy simulations under various environmental conditions.

Contributions to Safety and Environmental Assessments

- **Enhanced Hazard Scenarios Analysis:**

Developed a methodology to simulate the release of radioactive pollutants or gases,

focusing on improving safety and environmental assessments in industrial and research settings at CERN.

- **Evaluation of Methodology and Modeling Challenges:**

Addressed challenges such as managing backflow issues, selecting appropriate simulation detail levels, and accurately modeling buildings and vegetation.

- **Sensitivity Analysis of Boundary Conditions:**

Conducted sensitivity analyses to understand the impact of different boundary conditions, wind directions, and turbulence intensities on the dispersion of pollutants.

- **Realistic Inlet Boundary Conditions:**

Emphasized the necessity of defining turbulent inlet conditions to obtain realistic simulations and reliable predictions for hazmat dispersion scenarios.

In conclusion, this dissertation significantly advances the field of hazmat dispersion modeling by providing robust, accurate, and computationally efficient methods to simulate complex environmental scenarios. These contributions not only improve the understanding of pollutant behavior in realistic settings but also offer practical tools for mitigating the impact of hazardous releases, thereby improving safety and environmental assessments at CERN and similar facilities.

A. Python Relaxation Procedure

Listing A.1: Insert code directly in your document

```

1  # Script to convert ascii grid elevation data to stl file ,
2  # coarsed the grid and relax elevation to a fixed height on boundaries
3
4  # Relaxation based on:
5  # Balogh and Kristof
6  # Fine scale simulation of turbulent flows in urban canopy layers
7  # Quarterly Journal of the Hungarian Meteorological Service
8  # Vol 114. No. 1-2. January 2010 pp. 135-148
9
10 # Created for CERN Meyrin site
11 # Author: Uwe Kaeuflin , 17-04-2020
12
13 import matplotlib.pyplot as plt
14 import numpy as np
15 from scipy import interpolate
16 from linecache import getline
17 #if stl generation is needed
18 #from stl_tools import numpy2stl
19 from scipy.ndimage import gaussian_filter
20
21 ##### User modifiable part #####
22 # File name of ASCII digital elevation model
23 # this is a 5 x 5 tile
24 source_00 = "MN_Surface_2017_GRID.asc"
25 x_tile = 1
26 y_tile = 1
27 # File name of resulting ascii file , if needed
28 do_write_ascii = True
29 result_ascii = "3km-meyrin-relaxed-500m.asc"
30
31 # Relaxation length: distance from boundary where relaxation starts , in m
32 relaxation_length = 500
33 # Coarsening factor , if needed
34 do_coarsen = False
35 coarsen = 10
36 ##### End of user modifiable part #####
37
38 # Parse the header using a loop and the built-in linecache module
39 hdr = [getline(source_00, i) for i in range(1,6)]
40 values = [float(h.split("_")[-1].strip()) for h in hdr]

```

```

41 cols , rows , lx , ly , cell = values
42
43 print(values)
44
45 print("Loading_ ascii_ files_ to_ arrays")
46
47 # Load the into a numpy array
48 array = np.loadtxt(source_00 , skiprows=5)
49 #array_NW = np.loadtxt(source_00 , skiprows=5)
50 #array_SW = np.loadtxt(source_01 , skiprows=5)
51 #array_NE = np.loadtxt(source_02 , skiprows=5)
52 #array_SE = np.loadtxt(source_03 , skiprows=5)
53
54 print("Merging_arrays")
55
56 # Merge arrays
57 #merged_array = np.concatenate([np.concatenate([array_NW, array_SW], axis=0),
58 # np.concatenate([array_NE, array_SE], axis=0)],axis=1)
59 merged_array = array
60
61 # Put some sensible data to the missing one,
62 # this must be checked with the visualization first!
63 merged_array[merged_array == 0] = 460
64
65 # Array dimensions and vectors
66 x_length = x_tile*cell*cols
67 y_length = y_tile*cell*rows
68 x = np.arange(0, x_length, cell)
69 y = np.arange (0, y_length, cell)
70
71 if do_coarsen:
72     print("Coarsening_array")
73     #Linear interpolate to a less dense and smaller array to deal with
74     I2 = interpolate.interp2d(x, y, merged_array, kind='linear')
75     x_coarse = np.arange(0, x_length, coarsen*cell)
76     y_coarse = np.arange(0, y_length, coarsen*cell)
77     merged_array_coarse = I2(x_coarse , y_coarse)
78     merged_array = merged_array_coarse
79     x = x_coarse
80     y = y_coarse
81 else:
82     print("No_coarsening")
83
84 if do_coarsen:
85     cell = cell*coarsen
86     print("Cell_size_changed_to_%s" % cell)
87 else:
88     print("Cell_size_remained_original_%s" % cell)
89
90 # Constants

```

```

91 # Domain relaxation extents
92 x_min = relaxation_length
93 x_max = x_length + cell - relaxation_length
94 y_min = relaxation_length
95 y_max = y_length - relaxation_length
96
97 # Choosing the lowest value on the edge of the domain
98 edge_value1 = min(merged_array[0,:].min(), merged_array[-1,:].min(),
99     merged_array[:,0].min(), merged_array[:, -1].min())
100 print(edge_value1)
101 edge_value2 = max(merged_array[0,:].min(), merged_array[-1,:].min(),
102     merged_array[:,0].min(), merged_array[:, -1].min())
103 print(edge_value2)
104 edge_value = (edge_value1+edge_value2)/2
105 print(edge_value)
106 edge_value = 460
107
108 # Grid arrays
109 xx, yy = np.meshgrid(x, y)
110
111 print("Creating_distance_array")
112
113 # Distance array
114 Rarray = np.zeros(np.shape(xx))
115 Rarray[np.logical_and((xx < x_min),(yy > y_max))] =
116     np.sqrt((xx[np.logical_and((xx < x_min),(yy > y_max))]-x_min)**2 +
117     (yy[np.logical_and((xx < x_min),(yy > y_max))]-y_max)**2)
118 Rarray[np.logical_and((xx < x_min),(yy < y_min))] =
119     np.sqrt((xx[np.logical_and((xx < x_min),(yy < y_min))]-x_min)**2 +
120     (yy[np.logical_and((xx < x_min),(yy < y_min))]-y_min)**2)
121 Rarray[np.logical_and((xx > x_max),(yy > y_max))] =
122     np.sqrt((xx[np.logical_and((xx > x_max),(yy > y_max))]-x_max)**2 +
123     (yy[np.logical_and((xx > x_max),(yy > y_max))]-y_max)**2)
124 Rarray[np.logical_and((xx > x_max),(yy < y_min))] =
125     np.sqrt((xx[np.logical_and((xx > x_max),(yy < y_min))]-x_max)**2 +
126     (yy[np.logical_and((xx > x_max),(yy < y_min))]-y_min)**2)
127
128 Rarray[np.logical_and(np.logical_and((xx >= x_min),(xx <= x_max)),(yy > y_max))]
129     = np.absolute(yy[np.logical_and(np.logical_and((xx >= x_min),
130     (xx <= x_max)),(yy > y_max ))] - y_max)
131 Rarray[np.logical_and(np.logical_and((xx >= x_min),(xx <= x_max)),(yy < y_min))]
132     = np.absolute(yy[np.logical_and(np.logical_and((xx >= x_min),
133     (xx <= x_max)),(yy < y_min ))] - y_min)
134 Rarray[np.logical_and(np.logical_and((yy >= y_min),(yy <= y_max)),(xx > x_max))]
135     = np.absolute(xx[np.logical_and(np.logical_and((yy >= y_min),
136     (yy <= y_max)),(xx > x_max )]) - x_max)
137 Rarray[np.logical_and(np.logical_and((yy >= y_min),(yy <= y_max)),(xx < x_min))]
138     = np.absolute(xx[np.logical_and(np.logical_and((yy >= y_min),
139     (yy <= y_max)),(xx < x_min )]) - x_min)
140

```

```

141 Rarray[Rarray > relaxation_length] = relaxation_length
142
143 # Normalize distance to pi
144 Rarray = np.pi * Rarray / relaxation_length
145
146 print("Relaxing_array")
147
148 # Sigma relaxing array
149 sigma_array = (1 + np.cos(Rarray)) / 2
150
151 # Relaxing the original array
152 relaxed_array = ((merged_array - edge_value) * sigma_array) + edge_value
153
154 print(np.shape(relaxed_array))
155
156 # Do some plotting to make sure it looks ok
157 # Original merged tiles
158 CP = plt.contourf(x, -y, merged_array, levels=[380,400,420,440,460,480,500,520])
159 nm, lbl = CP.legend_elements()
160 plt.legend(nm, lbl, title= 'Elevation', fontsize= 8)
161 plt.show()
162 # Distance from the domain of interest
163 CP = plt.contourf(x, -y, Rarray)
164 nm, lbl = CP.legend_elements()
165 plt.legend(nm, lbl, title= 'Distance', fontsize= 8)
166 plt.show()
167 # Relaxation smoother based on distance
168 CP = plt.contourf(x, -y, sigma_array)
169 nm, lbl = CP.legend_elements()
170 plt.legend(nm, lbl, title= 'Sigma', fontsize= 8)
171 plt.show()
172
173 # Relaxed elevation
174 CP = plt.contourf(x, -y, relaxed_array, levels=[380,400,420,440,460,480,500,520])
175 nm, lbl = CP.legend_elements()
176 plt.legend(nm, lbl, title= 'Elevation', fontsize= 8)
177 plt.show()
178
179 # write new ascii file based on:
180 # http://geospatialpython.com/2013/12/python-and-elevation-data-ascii-grid.html
181
182 if do_write_ascii:
183     print("Writing_ascii_file")
184     header = "ncols_%s\n" % relaxed_array.shape[1]
185     header += "nrows_%s\n" % relaxed_array.shape[0]
186     header += "xllcorner_%s\n" % lx
187     header += "yllcorner_%s\n" % ly
188     header += "cellsize_%s\n" % cell
189     np.savetxt(result_ascii, gaussian_filter(relaxed_array,1), header=header,
190               fmt="%4.2f")

```

```
191 else:  
192     print("No_ascii_file_written.")
```

B. ANSYS Fluent Meshing Functionalities

In the initial stages of mesh generation, after the surfaces and CAD models have been imported, the critical task is wrapping the surfaces to create a unified and connected surface for meshing. Scoped sizing controls come into play both in this wrapping process and subsequently in mesh definition. Importantly, the terrain's resolution in the volume meshing phase is determined by the minimum sizes assigned. Therefore, it is essential that the wrapping procedure aligns with these volume mesh sizes.

The terrain, represented in .stl-data, and the buildings/walls available in the ANSYS® SpaceClaim CAD format need to be amalgamated into a single domain. This involves identifying intersections and extracting fluid regions from existing surfaces. The wrapping procedure in ANSYS® Fluent Meshing is a relatively straightforward process, which is why there it is not detailed here.

In ANSYS® Fluent, mesh sizes are governed by scoped sizing controls, which can be applied to surfaces or specific volumes known as Body-of-Influence (BOI). To utilize these controls effectively, one must create named selections for surfaces in ANSYS SpaceClaim, where size functions will be configured during the meshing process. ANSYS Fluent Meshing provides a variety of scoped sizing control options for managing mesh sizes on surfaces.

- **Curvature:** This control permits you to set the minimum and maximum sizes for the normal angle for circular edges or faces. Smaller values for these parameters result in improved resolution of curved faces and edges.
- **Hard:** With this control, you can maintain a uniform specified size, and the growth rate influences cell growth on adjacent faces. The hard sizing takes the highest priority among all size functions.
- **Soft:** This control defines the maximum size of the selected face and the growth rate influences cell growth in adjacent zones. Soft sizing has a lower priority when other size functions with higher priority are adjacent to the selected face.
- **Body-of-Influence:** This control enables you to specify a maximum cell size for a certain region within the domain, while the minimum mesh size is determined by other size controls.

In summary, there is a specific function for addressing circular faces to ensure their accurate resolution. Additionally, there are two face size functions that allow you to define the cell surface size. Finally, there is a function to control the size within a particular region or volume.

C. GPM at CERN - Differences from the Swiss Guideline ENSI G-14

The Swiss Guideline ENSI-G14 (2009) served as the most important source of models and their parameters used in the methodology described in this report. Yet, some models were updated following the state of the art of science and technology, and the particularities of CERN facilities. This section lists such alterations as they appear in the previous text.

C.1. Assumptions

The Guideline, ENSI-G14 (2009), is primarily intended for prospective assessments to fix discharge limits valid during the whole lifetime of a facility, which may extend to 50 years. Assumptions concerning the land-use and habit data are therefore very conservative.

Places at distances from the source shorter than 200 m in normal operation and shorter than 500 m in failures occurring with a frequency lower than 10^{-6} y^{-1} shall not be considered according to the Guideline, ENSI-G14 (2009). Members of the population often reside at shorter distances around CERN's site, which do not have fenced exclusion areas. The Gaussian dispersion model with extrapolated dispersion coefficients is not used for source-receptor distances shorter than 200 m except point-kernel integrals for evaluation of submersion doses. In situations, when the receptor is closer than 200 m to the discharge point, alternative methods are applied.

C.2. Gaussian Atmospheric Dispersion Model

1. In topological corrections, only the altitudes of the source and the receptor are considered. If the source is topologically higher than the receptor, the altitude difference source-receptor (positive) is added to the stack height. If the receptor is topologically higher, both receptor and source are put on the same altitude. It is assumed that air moving towards a hill will be pushed up, deflected or even split in two separate streams. The modelled concentration would not be lower around the hill but certainly higher than the real concentration on the top of the hill, US Environmental Protection Agency (2018). Detailed modelling of all buildings and
-

obstacles on and around sites, like in this reference Rakai (2015), is time consuming, hardly feasible for fluctuating wind directions during short-term discharges, and technically impossible for long-term discharges.

2. The stable atmospheric turbulence conditions occur very frequently. In some facilities, the vertical momentum flux of the discharged air can lead to a high plume-rise. The limitation of the plume to the boundary layer of the atmosphere by the inversion effect may be frequent. Hence, the stability-class dependent boundary layer height, Mavall (2003), is introduced into the model. Mathematically it is treated as a series of multiple plume reflections from the ground and from the top of the layer, Smith and Simmonds (2009). The height of the plume centerline cannot be higher than the height of the mixing layer. The boundary layer effect is not considered in the Guideline, ENSI-G14 (2009).
 3. The wind-speed height profile, such as defined by default in reference ENSI-G14 (2009), is applied to the plume centerline rather than to the discharge height (stack height). This seems to be more logical and it is the case in similar models in the literature.
 4. The ultrasonic anemometers offer reliable wind speed data down to wind speeds around 0.02 ms^{-1} . When using cup anemometers, situations with wind speeds smaller 1 ms^{-1} are classified as calms and wind directions for winds of this category are distributed in the same way as the wind directions of the first reliable wind speed bin, IAEA (1980). The plume may be meandering during situations with low wind speeds, or the measured wind speed may be a statistical fluctuation of true calm conditions. The availability of ultrasonic anemometers at present enables us to refrain from this method adopted by the Swiss Guideline ENSI-G14 (2009) through reference, IAEA (1980).
 5. The segmentation of meteorological data is not prescribed in the guideline except for the number of wind sectors (72). The same number of wind sectors is used in the present model. There are 47 wind speed sectors spaced by 0.3 ms^{-1} with central bin values evaluated as reciprocal of the average of (u^{-1}).
 6. The long-term dispersion factor is not formulated through a sum of 3D matrix elements, but using a vector of situations that occurred during the data collection period associated with their probabilities. This method is mathematically equivalent but more computationally efficient.
 7. Correction factors for short-term discharges lasting more than 8 hours used in ENSI-G14 (2009) were abandoned because they are not traceable. The CERN model is more conservative in this respect.
-

C.3. Deposition Factors

The dry and the wet deposition during short-term discharges is treated exactly the same way as in the Guideline ENSI-G14 (2009), the model parameters included. Long-term wet deposition factors, which require integration of the dispersion factor over the height, are not calculated by summing elements of a 4D matrix with mostly 0 elements, but through summing short-lived wet deposition factors represented by quadruplets of relevant data as they occurred during the whole weather statistics collection period. This way is more efficient computationally, but more importantly, it avoids binning of precipitation rates, which can occur in a large value interval, (e.g. 0.1 mm h^{-1} to 50 mm h^{-1}). This method is mathematically equivalent.

D. Sensitivity Analysis on Boundary Conditions

Here plots, which could not be presented in Chapter 5.2 are presented. They are divided into similar sections as in the original chapter. First the mean velocity profiles for the different scenarios are shown.

D.1. Mean Velocity Profiles

D.1.1. DTM-NF-MO-1

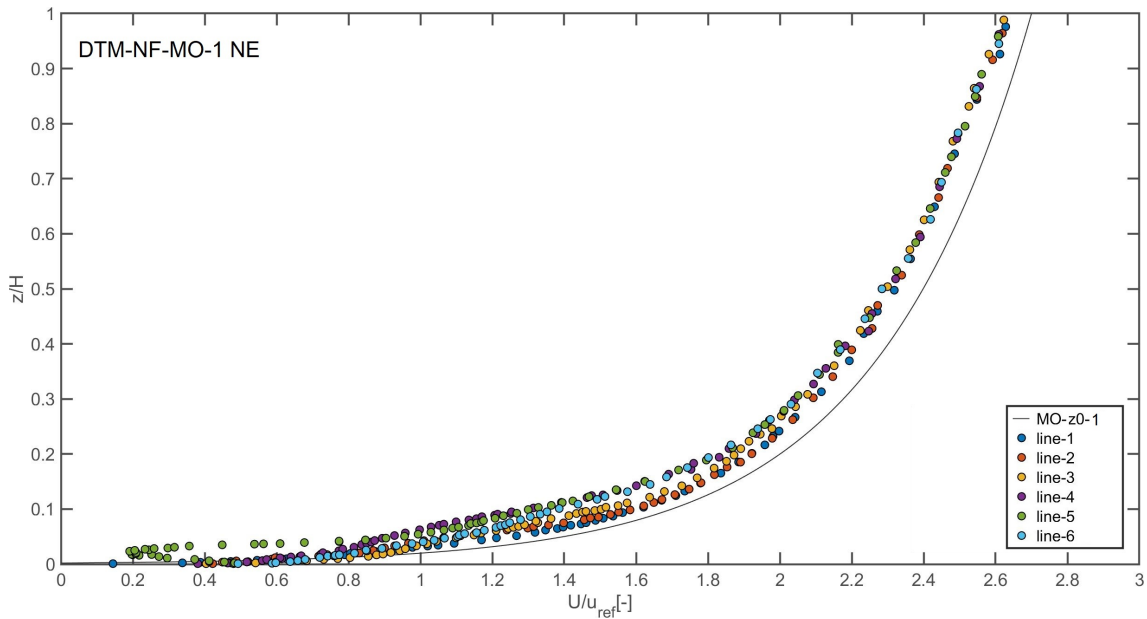


Figure D.1.: Mean velocity profile for the DTM-NF-MO-1 scenario for wind blowing from south-west to north-east (NE).

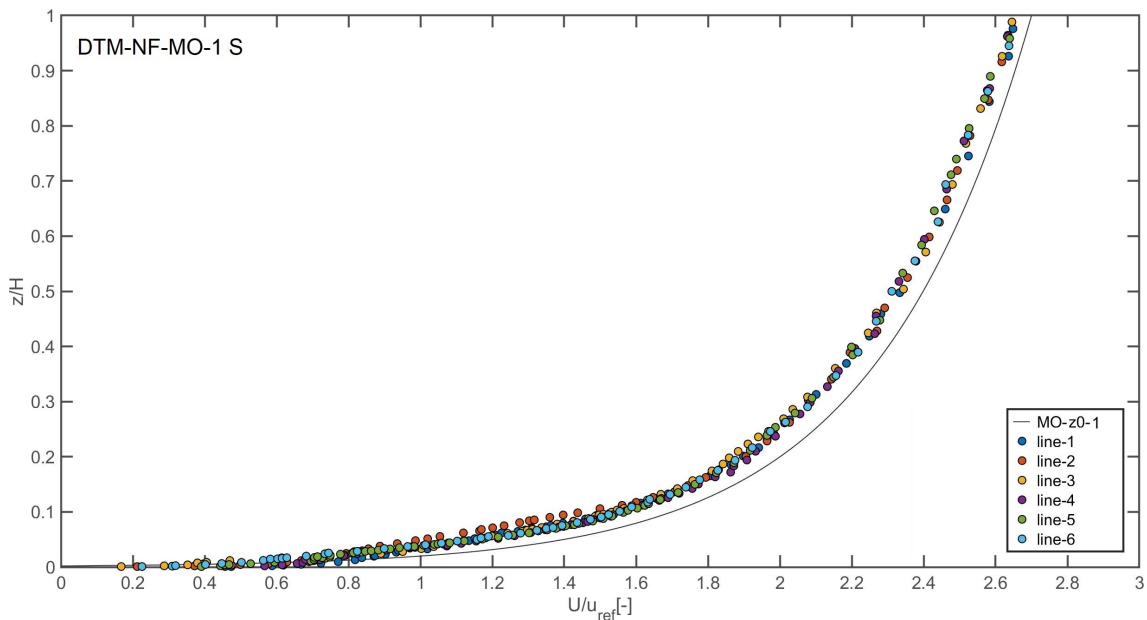


Figure D.2.: Mean velocity profile for the DTM-NF-MO-1 scenario for wind blowing from north to south (S).

D.1.2. DTM-STG-MO-1

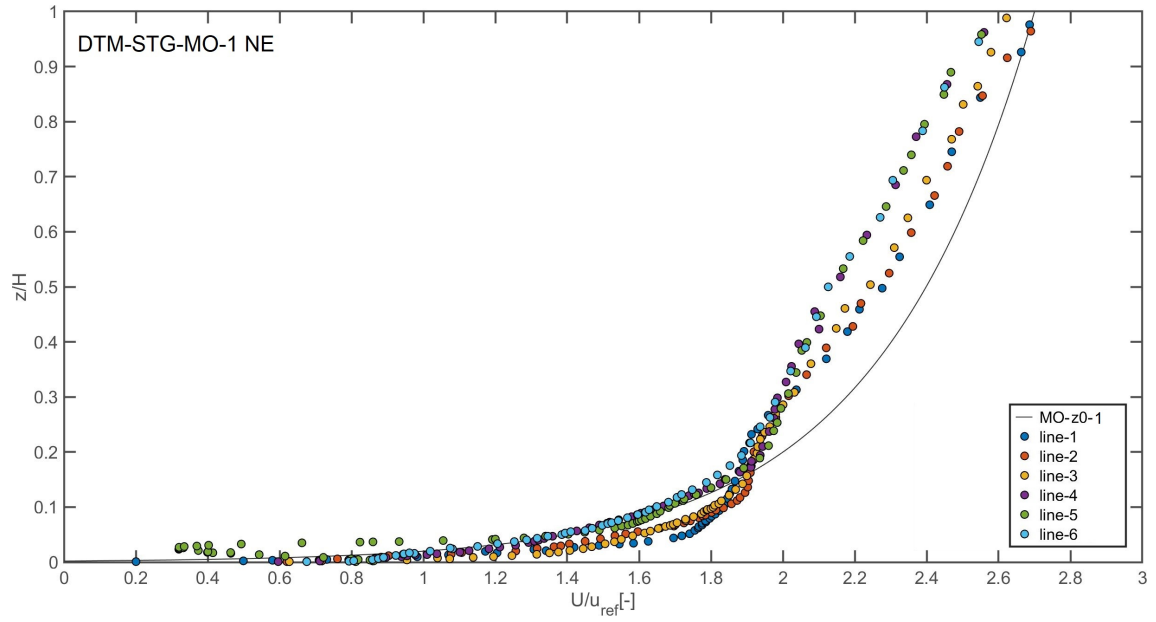


Figure D.3.: Mean velocity profile for the DTM-STG-MO-1 scenario for wind blowing from south-west to north-east (NE).

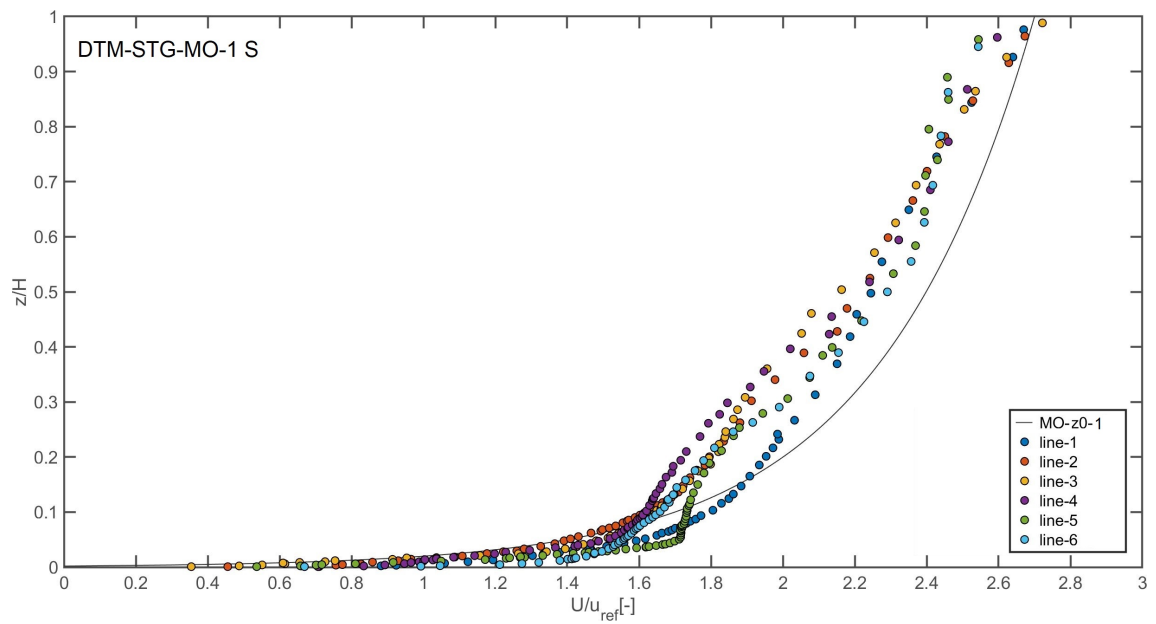


Figure D.4.: Mean velocity profile for the DTM-STG-MO-1 scenario for wind blowing from north to south (S).

D.1.3. DTM-STG-MO-025

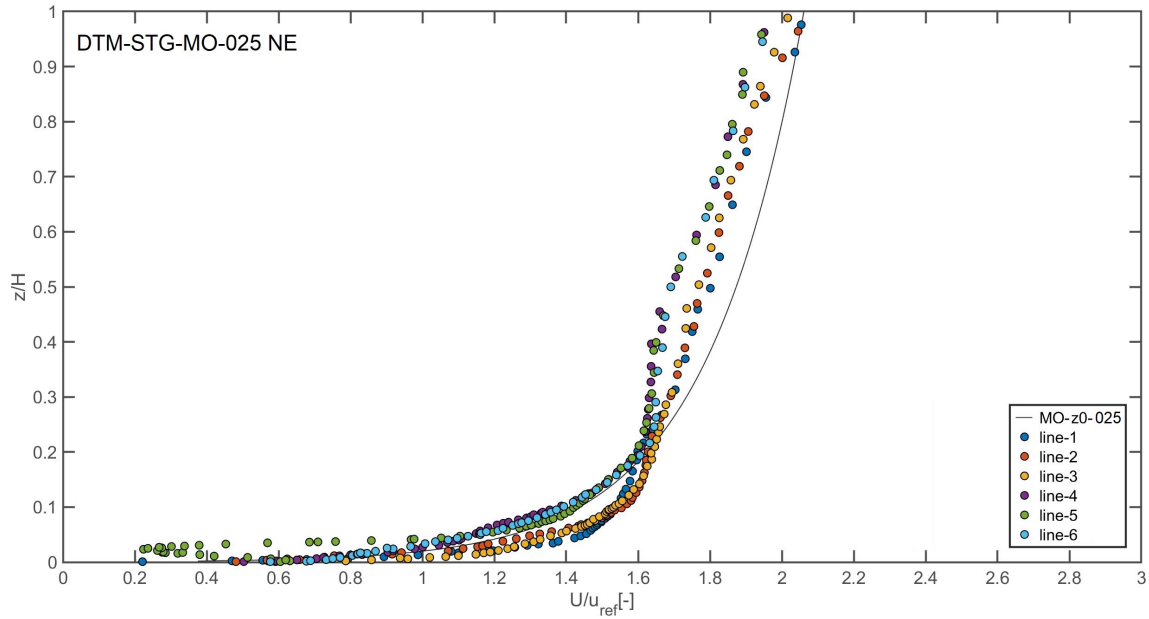


Figure D.5.: Mean velocity profile for the DTM-STG-MO-025 scenario for wind blowing from south-west to north-east (NE).

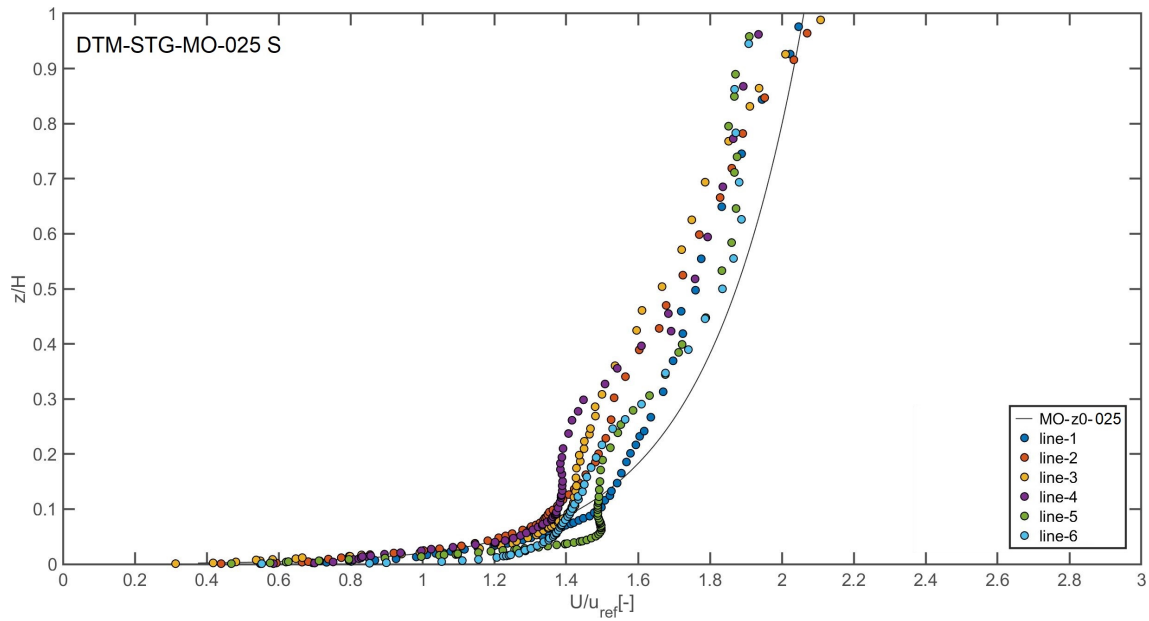


Figure D.6.: Mean velocity profile for the DTM-STG-MO-025 scenario for wind blowing from north to south (S).

D.1.4. DEM-STG-MO-1

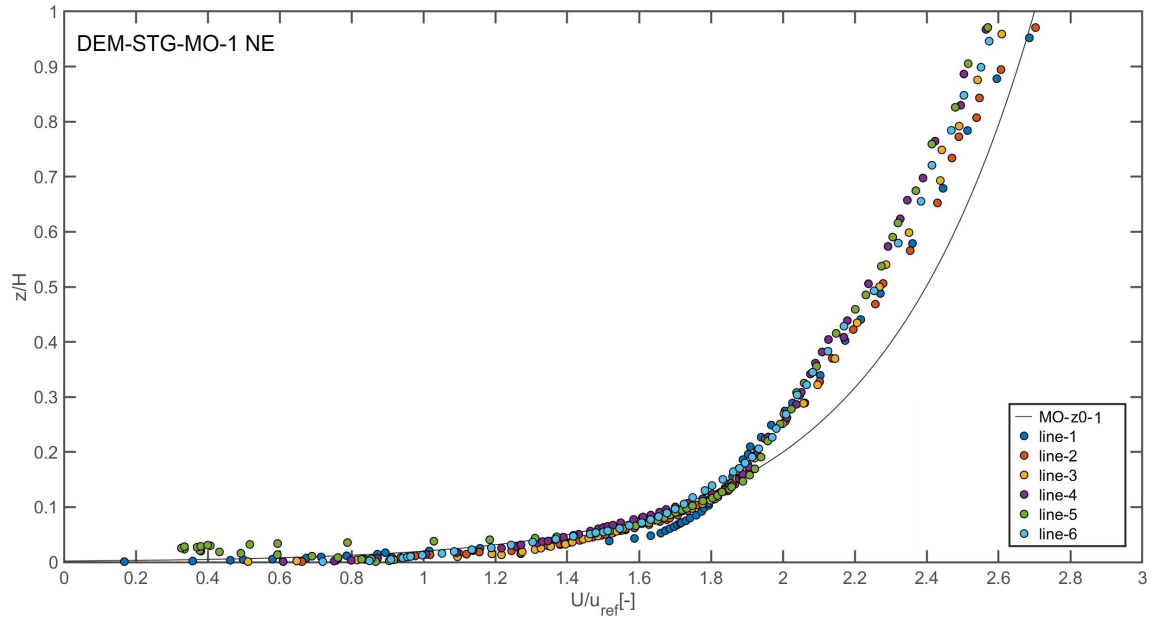


Figure D.7.: Mean velocity profile for the DEM-STG-MO-1 scenario for wind blowing from south-west to north-east (NE).

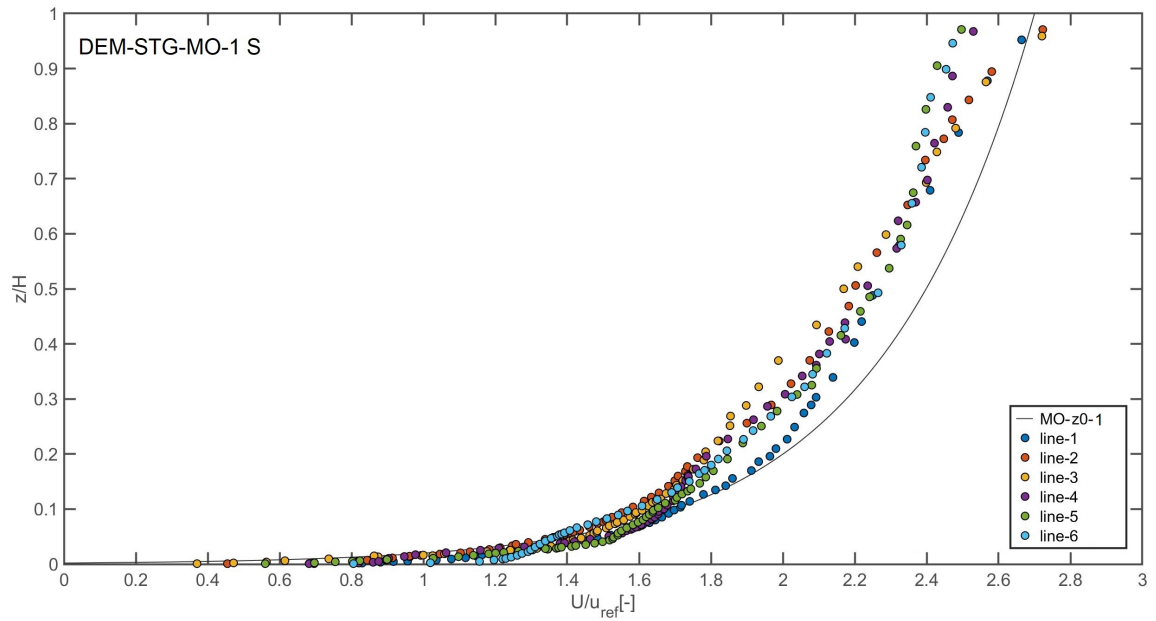


Figure D.8.: Mean velocity profile for the DEM-STG-MO-1 scenario for wind blowing from north to south (S).

Bibliography

- T. A. Adedipe, A. Chaudhari, and T. Kauranne. Impact of different forest densities on atmospheric boundary-layer development and wind-turbine wake. *Wind Energy*, 23(5):1165–1180, 2020.
- D. G. Andrews. *An Introduction to Atmospheric Physics*. Cambridge University Press, 4 2010. ISBN 9780521872201. doi: 10.1017/CBO9780511800788.
- ANSYS Inc. *Ansys® Academic Research CFD, Release 2020 R2, Fluent Theory Guide*. ANSYS, 2022.
- N. Antoniou, H. Montazeri, H. Wigo, M. K. Neophytou, B. Blocken, and M. Sandberg. CFD and wind-tunnel analysis of outdoor ventilation in a real compact heterogeneous urban area: Evaluation using “air delay”. *Building and Environment*, 126:355–372, 12 2017. ISSN 03601323. doi: 10.1016/J.BUILDENV.2017.10.013.
- S. P. Arya. *Introduction to micrometeorology*. Academic Press, 1st edition, 1982.
- S. P. Arya. *Introduction to Micrometeorology*, volume 79 of *International Geophysics*. Academic Press, 2001.
- G. K. Batchelor. *An Introduction to Fluid Dynamics*. Cambridge University Press, 2 2000. ISBN 9780521663960. doi: 10.1017/CBO9780511800955. URL <https://www.cambridge.org/core/product/identifier/9780511800955/type/book>.
- F. Bazdidi-Tehrani, M. Kiamansouri, and M. Jadidi. Inflow turbulence generation techniques for large eddy simulation of flow and dispersion around a model building in a turbulent atmospheric boundary layer. *Journal of Building Performance Simulation*, 9(6): 680–698, 2016.
- J. Boussinesq. *Essai sur la théorie des eaux courantes, Mémoires présentés par divers savants à l’Académie des Sciences*. 23, Paris, France, 1877.
- A. Chaudhari, B. Conan, S. Aubrun, and A. Hellsten. Numerical study of how stable stratification affects turbulence instabilities above a forest cover: Application to wind energy. *Journal of Physics: Conference Series*, 753(3), 2016.
- W. C. Cheng and F. Porté-Agel. Large-eddy simulation of atmospheric boundary layer flow and passive scalar dispersion over idealized urban surfaces, 2015. URL <https://infoscience.epfl.ch/record/207745>.
-

- COST Action 732. *Best Practice Guideline for the CFD Simulation of Flows in the Urban Environment*. COST Office, 2007.
- COST Action 732. *Model Evaluation Case Studies: Approach and Results*. COST Office, 2010.
- J. Counihan. Adiabatic atmospheric boundary layers: A review and analysis of data from the period 1880-1972. *Atmospheric Environment*, 9(10):871–905, 1975. ISSN 00046981. doi: 10.1016/0004-6981(75)90088-8.
- R. Courant, K. Friedrichs, and H. Lewy. Über die partiellen Differenzgleichungen der mathematischen Physik. *Mathematische Annalen 1928 100:1*, 100(1):32–74, 12 1928.
- C. T. Crowe, J. D. Schwarzkopf, M. Sommerfeld, and Y. Tsuji. *Multiphase Flows with Droplets and Particles*. CRC Press, 8 2011. ISBN 9780429106392. doi: 10.1201/b111103.
- D. Direction de l'information du territoire. SITG - Le Territoire Genevois à la Carte, 12 2022. URL <https://ge.ch/sitg/donnees>.
- A. J. Dyer. A review of flux-profile relationships. *Boundary-Layer Meteorology*, 7(3):363–372, 11 1974.
- S. Elghobashi. On predicting particle-laden turbulent flows. *Applied Scientific Research*, 52 (4):309–329, 6 1994. ISSN 00036994. doi: 10.1007/BF00936835/METRICS. URL <https://link.springer.com/article/10.1007/BF00936835>.
- ENSI-G14. Berechnung der Strahlenexposition in der Umgebung aufgrund von Emissionen radioaktiver Stoffe aus Kernanlagen - Richtlinie für die schweizerischen Kernanlagen, 2009.
- F. Erdmann. *Wind tunnel study of terrain induced flow modification and spatial resolution effects*. PhD thesis, Universität Hamburg, Hamburg, 2017.
- ESDU. Characteristics of atmospheric turbulence near the ground. Part II: single point data for strong winds (neutral atmosphere). In *ESDU 85020*. SAE International, London, UK, engineering edition, 1985.
- A. Fick. Ueber Diffusion. *Annalen der Physik und Chemie*, 170(1):59–86, 1855. ISSN 00033804. doi: 10.1002/andp.18551700105.
- M. Germano, U. Piomelli, P. Moin, and W. H. Cabot. A dynamic subgrid-scale eddy viscosity model. *Physics of Fluids A: Fluid Dynamics*, 3(7):1760–1765, 7 1991. ISSN 0899-8213. doi: 10.1063/1.857955.
- A. D. Gosman and E. Ioannides. Aspects of Computer Simulation of Liquid-Fueled Combustors. *Journal of Energy*, 7(6):482–490, 11 1983. ISSN 0146-0412. doi: 10.2514/3.62687.
-

-
- P. Gousseau, B. Blocken, T. Stathopoulos, and G. J. van Heijst. CFD simulation of near-field pollutant dispersion on a high-resolution grid: A case study by LES and RANS for a building group in downtown Montreal. *Atmospheric Environment*, 45(2):428–438, 1 2011. ISSN 1352-2310. doi: 10.1016/J.ATMOENV.2010.09.065.
- D. Hargreaves and N. Wright. On the use of the k– model in commercial CFD software to model the neutral atmospheric boundary layer. *Journal of Wind Engineering and Industrial Aerodynamics*, 95:355–369, 1 2007.
- D. Hertwig. *On Aspects of Large-Eddy Simulation Validation for Near-Surface Atmospheric Flows*. PhD thesis, Universität Hamburg, 2013.
- IAEA. *Atmospheric Dispersion in Nuclear Power Plant Siting*, 1980.
- A. Innocenti, C. Marchioli, and S. Chibbaro. Lagrangian Filtered Density Function for LES-Based Stochastic Modelling of Turbulent Particle-Laden Flows. *Physics of Fluids*, 28(11), 11 2016. ISSN 10897666. doi: 10.1063/1.4967800.
- J. C. Kaimal and J. J. Finnigan. *Atmospheric Boundary Layer Flows*. Oxford University Press, 3 1994. ISBN 9780195062397. doi: 10.1093/oso/9780195062397.001.0001. URL <https://academic.oup.com/book/40882>.
- J. C. Kaimal, J. C. Wyngaard, Y. Izumi, and O. R. Coté. Spectral characteristics of surface-layer turbulence. *Quarterly Journal of the Royal Meteorological Society*, 98(417):563–589, 1972.
- E. Keshavarzian, R. Jin, K. Dong, and K. C. Kwok. Effect of building cross-section shape on air pollutant dispersion around buildings. *Building and Environment*, 197:107861, 6 2021. ISSN 0360-1323. doi: 10.1016/J.BUILDENV.2021.107861.
- W.-W. Kim and S. Menon. Application of the localized dynamic subgrid-scale model to turbulent wall-bounded flows. In *35th Aerospace Sciences Meeting and Exhibit*, Reston, Virginia, 1 1997. American Institute of Aeronautics and Astronautics. doi: 10.2514/6.1997-210.
- A. N. Kolmogorov. Equations of turbulent motion in an incompressible fluid. *Dokl. Akad. Nauk SSSR*, 30:299–303, 1941.
- M. T. Landahl and E. Mollo-Christensen. *Turbulence and Random Processes in Fluid Mechanics*. Cambridge University Press, 2 edition, 1992.
- L. D. Landau and E. M. Lifshitz. *Fluid Mechanics*. Institute of Physical Problems, U.S.S.R. Academy of Sciences, 2nd edition, 1987.
- J. Larsson, S. Kawai, J. Bodart, and I. Bermejo-Moreno. Large eddy simulation with modeled wall-stress: recent progress and future directions. *Mechanical Engineering Reviews*, 3(1):15–00418, 2016. doi: 10.1299/mer.15-00418.
-

- M. Lateb, R. N. Meroney, M. Yataghene, H. Fellouah, F. Saleh, and M. C. Boufadel. On the use of numerical modelling for near-field pollutant dispersion in urban environments - A review. *Environmental Pollution*, 208:271–283, 1 2016. ISSN 18736424. doi: 10.1016/J.ENVPOL.2015.07.039.
- B. E. Launder and D. B. Spalding. The Numerical Computation of Turbulent Flows. *COMPUTER METHODS IN APPLIED MECHANICS AND ENGINEERING*, 3:269–289, 1974.
- A. Li and G. Ahmadi. Dispersion and deposition of spherical particles from point sources in a turbulent channel flow. *Aerosol Science and Technology*, 16(4):209–226, 1992.
- D. K. Lilly. The Representation of Small-Scale Turbulence in Numerical Simulation Experiments. In *National Center for Atmospheric Research*, 1966. doi: 10.5065/D62R3PMM.
- D. K. Lilly. A proposed modification of the Germano subgrid-scale closure method. *Physics of Fluids A: Fluid Dynamics*, 4(3):633, 9 1998. ISSN 0899-8213. doi: 10.1063/1.858280. URL <https://aip.scitation.org/doi/abs/10.1063/1.858280>.
- R. Longo, A. Bellemans, M. Derudi, and A. Parente. A multi-fidelity framework for the estimation of the turbulent Schmidt number in the simulation of atmospheric dispersion. *Building and Environment*, 185:107066, 11 2020.
- J. L. Lumley and H. A. Panofsky. *The Structure of Atmospheric Turbulence*, 1964.
- V. Malmberg. Fire-Induced Radiological Integrated Assessment - Aerosol Characterization. Technical report, Division of Ergonomics & Aerosol Technology, Lund University, 2019.
- C. Marchioli. Large-Eddy Simulation of Turbulent Dispersed Flows: a Review of Modelling Approaches, 3 2017. ISSN 00015970.
- F. Mathey, D. Cokljat, J. P. Bertoglio, and E. Sergent. Assessment of the vortex method for large eddy simulation inlet conditions. *Progress in Computational Fluid Dynamics*, 6 (1-3):58–67, 2006.
- A. Mavall. Chapter 2: Modelling the dispersion of radionuclides in the atmosphere. *Radioactivity in the Environment*, 4(C):13–54, 2003. ISSN 15694860. doi: 10.1016/S1569-4860(03)80058-X.
- K. McGrattan, S. Hostikka, R. McDermott, J. Floyd, C. Weinschenk, and K. Overhold. Sixth Edition Fire Dynamics Simulator User’s Guide (FDS). *NIST Special Publication 1019*, Sixth Edit, 2020.
- R. N. Meroney. *Turbulent Diffusion near Buildings*. Engineering Meteorology: Fundamentals of Meteorology and Their Application to Problems in Environmental and Civil Engineering, 1982. ISBN 0-444-41972-1.
-

-
- A. Monin and A. Obukhov. The Basic Laws of Turbulent Mixing in the Surface Layer of the Atmosphere. *Tr. Akad. Nauk SSSR Geophys. Inst.*, 24(151):163–187, 1954.
- S. A. Morsi and A. J. Alexander. An investigation of particle trajectories in two-phase flow systems. *Journal of Fluid Mechanics*, 55(2):193–208, 1972.
- B. Nebenführ and L. Davidson. Large-Eddy Simulation Study of Thermally Stratified Canopy Flow. *Boundary-Layer Meteorology*, 156(2):253–276, 2015.
- F. Nicoud and F. Ducros. Subgrid-Scale Stress Modelling Based on the Square of the Velocity Gradient Tensor. *Flow, Turbulence and Combustion*, 62(3):183–200, 1999. ISSN 13866184. doi: 10.1023/A:1009995426001/METRICS. URL <https://link.springer.com/article/10.1023/A:1009995426001>.
- B. R. Pascual, G. Gai, O. Rios, and S. La Mendola. FIRIA-FDS Modelling of a Large Underground Cavern of CERN’s LHC Accelerator Complex. In *Fire and Evacuation Modeling Technical Conference (FEMTC) 2020*, 2020.
- L. Patruno and M. Ricci. A systematic approach to the generation of synthetic turbulence using spectral methods. *Computer Methods in Applied Mechanics and Engineering*, 340: 881–904, 10 2018. ISSN 00457825. doi: 10.1016/j.cma.2018.06.028.
- S. B. C. U. Pope. *Turbulent Flows*. Cambridge University Press, 2000. ISBN 978-0521598866.
- A. Rakai. Project report on atmospheric modelling with CFD around CERN sites, EDMS 1705285. Technical report, CERN, Geneva, 2015.
- P. Richards. Appropriate boundary conditions for computational wind engineering models using the k- ϵ turbulence model. *Journal of Wind Engineering and Industrial Aerodynamics*, 46-47(1993):145–153, 1993.
- Roberts R. C. *Molecular Diffusion of Gases*. American Institute of Physics Handbook, third edition edition, 1963.
- P. G. Saffman. The lift on a small sphere in a slow shear flow. *Journal of Fluid Mechanics*, 22(2):385–400, 1965.
- M. Schatzmann, W. H. Snyder, and R. E. Lawson, Jr. Building effects on heavy gas jet dispersion. *U.S. Environmental Protection Agency*, pages 1–1033, 12 1995.
- S. Schütz, M. Piesche, G. Gorbach, M. Schilling, C. Seyfert, P. Kopf, T. Deuschle, N. Sautter, E. Popp, and T. Warth. CFD in der mechanischen Trenntechnik. *Chemie Ingenieur Technik*, 79(11):1777–1796, 11 2007. ISSN 0009-286X. doi: 10.1002/cite.200700109.
- E. Sergent. *Vers une méthodologie de couplage entre la Simulation des Grandes Echelles et les modèles statistiques*. PhD thesis, Ecole Centrale de Lyon, 2002.
-

- M. L. Shur, P. R. Spalart, M. K. Strelets, and A. K. Travin. Synthetic turbulence generators for RANS-LES interfaces in zonal simulations of aerodynamic and aeroacoustic problems. *Flow, Turbulence and Combustion*, 93(1):63–92, 2014.
- E. Simiu and R. H. Scanlan. Wind effects on structures - Part A: The Atmosphere. *An Introduction to Wind Engineering*, 1986.
- P. Sjöholm, D. B. Ingham, M. Lehtimäki, L. Perttu-Roiha, H. Goodfellow, and H. Torvela. GAS-CLEANING TECHNOLOGY. *Industrial Ventilation Design Guidebook*, pages 1197–1316, 1 2001.
- J. Smagorinsky. General circulation experiments with the primitive equations: I. The basic experiment. *Monthly weather review*, 91(3):99–164, 1963.
- J. G. Smith and J. R. Simmonds. *The Methodology for Assessing the Radiological Consequences of Routine Releases of Radionuclides to the Environment Used in PC-CREAM 08*. UK Health Protection Agency, Oxfordshire, 2009. ISBN 9780859516518.
- P. Spalart and S. Allmaras. A one-equation turbulence model for aerodynamic flows. In *30th Aerospace Sciences Meeting and Exhibit*, Reston, Virginia, 1 1992. American Institute of Aeronautics and Astronautics. doi: 10.2514/6.1992-439.
- R. B. Stull. Mean Boundary Layer Characteristics. In *An Introduction to Boundary Layer Meteorology*, pages 1–27. Springer Netherlands, 1988.
- L. Sufra and H. Steiner. A Priori Assessment of Subgrid-Scale Models and Numerical Error in Forced Convective Flow at High Prandtl Numbers. *Flow, Turbulence and Combustion*, 105(2):377–392, 8 2020. ISSN 15731987. doi: 10.1007/s10494-019-00107-y.
- O. G. Sutton. The theoretical distribution of airborne pollution from factory chimneys. *Quarterly Journal of the Royal Meteorological Society*, 73:426–436, 1 1947.
- H. Tennekes, J. L. Lumley, J. L. Lumley, and others. *A first course in turbulence*. MIT press, 1972.
- W. Tollmien, H. Schlichting, H. Görtler, and F. W. Riegels. Bericht über Untersuchungen zur ausgebildeten Turbulenz. In F. W. Riegels, editor, *Ludwig Prandtl Gesammelte Abhandlungen: zur angewandten Mechanik, Hydro- und Aerodynamik*, pages 714–718. Springer Berlin Heidelberg, Berlin, Heidelberg, 1961.
- US Environmental Protection Agency. AERMOD Model Formulation and Evaluation, EPA-454/R-18-003, 2018.
- I. Van der Hoven. Power Spectrum of Horizontal Wind Speed in the Frequency Range from 0.0007 to 900 Cycles Per Hour. *Journal of Atmospheric Sciences*, 14(2):160–164, 4 1957. ISSN 0022-4928. doi: 10.1175/1520-0469(1957)014.
-

-
- E. R. Van Driest. On Turbulent Flow Near a Wall. *Journal of the Aeronautical Sciences*, 23(11): 1007–1011, 1956. doi: 10.2514/8.3713. URL <https://doi.org/10.2514/8.3713>.
- R. Vasaturo, I. Kalkman, B. Blocken, and P. J. van Wesemael. Large eddy simulation of the neutral atmospheric boundary layer: performance evaluation of three inflow methods for terrains with different roughness. *Journal of Wind Engineering and Industrial Aerodynamics*, 173(November 2017):241–261, 2018. ISSN 01676105. doi: 10.1016/j.jweia.2017.11.025.
- VDI 3783/12. Environmental meteorology – Physical modelling of flow and dispersion processes in the atmospheric boundary layer – Application of wind tunnels. *VDI guideline 3783, Part 12*, 2000.
- P. Vojtyla. Models for assessing the dosimetric impact of discharges of radioactive substances from CERN facilities to the environment - Air. Technical report, CERN - European Organisation for Nuclear Research, Geneva, Switzerland, 2022.
- T. von Kármán. Mechanische Ähnlichkeit und Turbulenz. *Nachrichten von der Gesellschaft der Wissenschaften zu Göttingen*, 1930.
- T. von Kármán. Progress in the Statistical Theory of Turbulence. *Proceedings of the National Academy of Sciences*, 34(11):530–539, 11 1948. ISSN 0027-8424. doi: 10.1073/pnas.34.11.530.
- W. Wang, Y. Cao, and T. Okaze. Comparison of hexahedral, tetrahedral and polyhedral cells for reproducing the wind field around an isolated building by LES. *Building and Environment*, 195(February):107717, 2021.
- J. Wei and Y. Li. Enhanced spread of expiratory droplets by turbulence in a cough jet. *Building and Environment*, 93(P2):86–96, 11 2015.
- D. Wilson. Flow patterns over flat roofed buildings and application to exhaust stack design. *ASHRAE Transactions*, 85:284–295, 1979.
- J. Wyngaard. *Turbulence in the Atmosphere*. Cambridge University Press, Cambridge, UK, 2010.
- D. F. Young, B. R. Munson, T. Okiishi, and W. Huebsch. *A brief introduction to fluid mechanics*. Wiley (Asia) Pte, 5th edition, 2010. ISBN 978-0-470-90215-8.
- X. Zheng, H. Montazeri, and B. Blocken. Large-eddy simulation of pollutant dispersion in generic urban street canyons: Guidelines for domain size. *Journal of Wind Engineering and Industrial Aerodynamics*, 211:104527, 4 2021. ISSN 0167-6105. doi: 10.1016/J.JWEIA.2021.104527.
- Y. Zhiyin. Large-eddy simulation: Past, present and the future. *Chinese Journal of Aeronautics*, 28(1):11–24, 2015.
-

List of Figures

1.1. Number of Publications with the keywords "large-eddy simulation"	2
2.1. ABL Stability Class	8
4.1. TerrainDataSITG	37
4.2. Domain Extends Bird's Eye View	39
4.3. Raw-DEM	41
4.4. Geometry Relaxation	42
4.5. Relaxation Steps	43
4.6. Terrain Altitude	44
4.7. Impact Geometry Shape on Backflow	45
4.8. Flow Around A Sharp-Edged Building	46
4.9. CERN Meyrin Site	48
4.10. Mesh Refinement Study Concentration Deviation S	53
4.11. Mesh Refinement Study Results NE	57
4.12. Mesh Refinement Study Results S	59
4.13. Geometry-DTM	62
4.14. Geometry-DTM-BOI-Buildings	62
4.15. Geometry-DTM-BOI-ATLAS-ISOLDE	63
4.16. Final-Mesh-Cross-Section	64
4.17. Final-Mesh-Cross-Section-Enlarged-View	64
4.18. Mesh-Quality-Illustration	65
4.19. Mesh-Final-Quality	66
4.20. Integral Length Scale	67
4.21. TKE Integral Length Scale Relationship	68
4.22. Numerically Resolvable Length Scale	69
4.23. L0 to Delta Ratio	70
4.24. Wind-Rose	73
4.25. Atmospheric-Stability-Classes	74
4.26. STG VM Comparison ATLAS S TKE	78
4.27. STG VM Comparison ATLAS S TI	80
4.28. STG VM Comparison ATLAS S TKE	81
4.29. STG VM Comparison ATLAS S Energy Cascade ML-6	82
4.30. STG VM Comparison ATLAS S Displacement Parameter	83

4.31. Averaged Aerosol Size Distributions	89
4.32. Source Term Graphs	90
4.33. Velocity Magnitude Final Steady Solution	93
4.34. Initialized Velocity Field Including Fluctuations	94
4.35. Velocity Magnitude Flushed Transient Solution	94
4.36. Monitoring Points	96
4.37. Monitoring Lines	96
4.38. Monitoring Planes	98
4.39. Time Step Size	99
4.40. Time Step Size	100
4.41. Law of the Wall	102
4.42. Yplus Values	102
4.43. Mean Velocity Profile	104
4.44. Turbulent Intensity Profile	107
4.45. Spectral Energy Density Plots	111
5.1. ATLAS Facility	115
5.2. GPM vs LES NE 110m	117
5.3. Comparison GPM vs LES	120
5.4. GPM vs LES S 300m	122
5.5. GPM vs LES Monitoring Points	123
5.6. GPM vs LES Air S 75m	126
5.7. GPM vs LES Air S 200m	127
5.8. GPM vs LES Air S 1800s Iso Surface	128
5.9. Comparison GPM vs LES	129
5.10. GPM vs LES Monitoring Points Air Scenario	130
5.11. GPM vs LES Argon S 75m	132
5.12. GPM vs LES Air S 1200s Iso Surface	133
5.13. Comparison GPM vs LES	134
5.14. GPM vs LES Monitoring Points Argon Scenario	135
5.15. Mean Velocity Profile Aerodynamic Roughness Length Specification	138
5.16. Sensitivity Analysis Terrain Type DEM	139
5.17. Sensitivity Analysis Mean Velocity DTM-NF-MO-1 NE	143
5.18. Sensitivity Analysis Mean Velocity DTM-NF-MO-1 S	143
5.19. Sensitivity Analysis Mean Velocity DEM-NF-MO-1 NE	145
5.20. Sensitivity Analysis Turbulence Intensity DTM-NF-MO-1	147
5.21. Sensitivity Analysis Turbulence Intensity DTM-STG-MO-1	148
5.22. Sensitivity Analysis Turbulence Intensity DTM-STG-MO-025	149
5.23. Sensitivity Analysis Turbulence Intensity DEM-STG-MO-1	150
5.24. Sensitivity Analysis Energy Cascade DTM-NF-MO-1	152
5.25. Sensitivity Analysis Energy Cascade Comparison NF STG	153

5.26. Sensitivity Analysis Energy Cascade Comparison NF STG	154
5.27. Sensitivity Analysis Energy Cascade Comparison DTM DEM	155
5.28. Sensitivity Analysis Energy Cascade Comparison DTM DEM	156
5.29. Sensitivity Analysis Monitoring Planes NE	158
5.30. Sensitivity Analysis Monitoring Planes S	160
5.31. Sensitivity Analysis Export Points Concentration NE	162
5.32. Sensitivity Analysis Export Points Concentration S	163
D.1. Sensitivity Analysis Mean Velocity DTM-NF-MO-1 NE	190
D.2. Sensitivity Analysis Mean Velocity DTM-NF-MO-1 S	190
D.3. Sensitivity Analysis Mean Velocity DTM-STG-MO-1 NE	191
D.4. Sensitivity Analysis Mean Velocity DTM-STG-MO-1 S	191
D.5. Sensitivity Analysis Mean Velocity DTM-STG-MO-025 NE	192
D.6. Sensitivity Analysis Mean Velocity DTM-STG-MO-025 S	192
D.7. Sensitivity Analysis Mean Velocity DEM-STG-MO-1 NE	193
D.8. Sensitivity Analysis Mean Velocity DEM-STG-MO-1 S	193

List of Tables

3.1. Characteristics of different transport modelling approaches	35
4.1. Mesh Refinement Properties	52
4.2. Resolvable Energy From Mesh Size	69
4.3. Obukhov Length	73
4.4. Computing Efficiency VM-STG	84
4.5. Solver settings	87
4.6. Solution Controls	88
4.7. Coefficients for spectral kinetic energy of turbulence	110
5.1. Properties Door and Stack Release	124
5.2. Properties Argon Air	124
5.3. Dense Gas Release Scenario Comparison	133
5.4. Identification of Scenarios	141
